

OSCILLATIONS IN MICROVASCULAR FLOW: THEIR
RELATIONSHIP TO TISSUE OXYGENATION, CELLULAR
METABOLIC FUNCTION AND THEIR DIAGNOSTIC
POTENTIAL FOR DETECTING SKIN MELANOMA

CLINICAL, EXPERIMENTAL AND THEORETICAL INVESTIGATIONS

Gemma Lancaster, MPhys

THESIS SUBMITTED FOR THE DEGREE OF
DOCTOR OF PHILOSOPHY



DEPARTMENT OF PHYSICS
LANCASTER UNIVERSITY
LANCASTER, UK

September 2015

ACKNOWLEDGEMENTS

First and foremost, I would like to thank my supervisor Prof. Aneta Stefanovska, first for giving me the opportunity to work in such an interesting field, and with a pioneer in that field, and second for her support and guidance during the last four years, which has allowed me to grow not only as a researcher, but also as a person. Thank you also to Prof. Peter V. E. McClintock for his kindness, and being willing to help throughout.

Dr. Alan Bernjak introduced me to the laser Doppler flowmetry recording equipment, and some of the fundamental time series analysis techniques which have served me throughout my studies, for which I am very grateful. Thanks to Prof. Marco Rossi, who managed the melanoma study in Pisa, and Dr. Margherita Pesce who recorded the LDF data analysed in chapter 5. Thanks also to the dermatologists and pathologists involved in the study, Dr. Gian Marco Vezzoni, Dr. Barbara Loggini, Prof. Raffaele Pingitore, Dr. Fabrizio Ghiara, Prof. Paulo Barachini, Prof. Gregorio Cervadoro and Dr. Marco Romanelli.

Thanks to Dr. Norman Turner for providing the free diver data analysed in Chapter 6, and to all of the volunteers in my recruited control group. Thanks also to Dr. Yevhen Suprunenko for his initial work on the cellular energy metabolism model with Kirsten Jenkins, and our collaboration in the development into the presented results. Dr. Philip Clemson has been very helpful throughout my studies, from answering analysis questions in the early days, to proofreading parts of this thesis, for all of which I am very thankful. I am also grateful to Dr. Robert Young for his work on the laser speckle system.

I would also like to thank everybody that has made the department, and the office, a nice place to be: Dr. Tomislav Stankovski, Dr. Spase Petkoski, Dr. Dmytro Iatsenko, Will Gibby, Valentina Ticcinelli, Miroslav Barabash and Phil Furneaux.

Finally, I would like to thank the members of my family who have always been there for me, and the friends who understood when I could not always be around.

DECLARATION

This thesis is my original work and has not been submitted, in whole or in part, for a degree at this or any other university. Nor does it contain, to the best of my knowledge and belief, any material published or written by another person, except as acknowledged in the text.

ETHICS DECLARATION

The data recorded and analysed within this work were collected in accordance with the appropriate permissions from their respective institutions or committees, as detailed below.

- The electroencephalography (EEG) data recorded from a patient under anaesthesia used in Chapter 4 was recorded as part of the Brain, Respiration and Cardiac Causalities in Anaesthesia (BRACCIA) study, contract No. 517133 (NEST). The approval of the relevant Research Ethics Committees (Lancaster, UK and Oslo, Norway) were obtained before the study commenced. Data collection took place before registration of studies into trials registries was required. Written informed consent was obtained on the day of surgery.
- The blood flow data analysed in Chapter 5 were recorded in the Hospital of Pisa after obtaining written consent. The protocol was approved by the Ethical Committee of the University of Pisa and was in accordance with the Declaration of 1975, as revised in 2000. The project was funded by Tuscany Region.
- The protocol used for the data recorded from free divers which are analysed in Chapter 6 was approved by the University of Lancaster Ethics Committee, as was the protocol used in the recruitment of control subjects. All volunteers gave their informed written consent.

LIST OF PUBLICATIONS

Parts of the work presented in this thesis have been published in the following papers and proceedings:

- G. Lancaster, A. Stefanovska, M. Pesce, G. M. Vezzoni, B. Loggini, R. Pingitore, F. Ghiara, P. Barachini, G. Cervadoro, M. Romanelli & M. Rossi. Dynamic markers based on blood perfusion fluctuations for selecting skin melanocytic lesions for biopsy. *Sci. Rep.*, 5, 12825, 2015. (Work from Chapter 5).
- G. Lancaster, P. Clemson, Y. Suprunenko, T. Stankovski & A. Stefanovska. Detecting chronotaxic systems from single-variable time series with separable amplitude and phase. *Entropy*, 17, 6, 4413–4438, 2015. (Work from Chapter 4).
- G. Lancaster & A. Stefanovska. Central control of vasomotion. *J. Vasc. Res.* 52, supp 1, 7–8, 2015.

The following manuscripts are currently under review or in preparation:

- P. Clemson, G. Lancaster & A. Stefanovska. Reconstructing time-dependent dynamics. *Proc. IEEE* 2015. Accepted.
- G. Lancaster, Y. Suprunenko, K. Jenkins & A. Stefanovska. Modelling nonautonomous oscillatory dynamics of cellular energy metabolism to facilitate the identification of altered metabolic states. In Preparation. (Work from Chapter 7).

Parts of the work have also been presented at the following scientific meetings and workshops:

- G. Lancaster & A. Stefanovska. Central control of vasomotion. *Joint European Society for Microcirculation and European Vascular Biology Organisation Meeting. 3–6 June 2015. Pisa, Italy.* Oral presentation.

-
- G. Lancaster, Y. Suprunenko, K. Jenkins & A. Stefanovska. Chronotaxic dynamics of cell metabolic oscillations. *Random Walks and Nonlinear Dynamics in the Life of Cells, International Workshop. 18–22 May 2015. Dresden, Germany.* Poster presentation.
 - G. Lancaster, M. Rossi & A. Stefanovska. Blood flow dynamics in the diagnosis of malignant melanoma. *SET for Britain. 17 March 2014. London, UK.* Poster presentation.
 - G. Lancaster & A. Stefanovska. Can single cancer cell behaviour be related to local blood flow dynamics? *Let's Face Chaos Through Nonlinear Dynamics, Conference and Summer School. 22 June – 6 July 2014. Maribor, Slovenia.* Poster presentation.
 - G. Lancaster, M. Rossi & A. Stefanovska. What can blood flow dynamics in melanoma tell us about the tumour microenvironment? *Faculty of Science and Technology Christmas Conference. 17 September 2013. Lancaster, UK.* Oral & poster presentation.
 - G. Lancaster, M. Rossi, M. Pesce & A. Stefanovska. Identifying malignant melanoma through unique signatures in blood flow dynamics. *Physics of Cancer, 4th Annual Symposium. 24–27 September 2013. Leipzig, Germany.* Oral & poster presentation.
 - G. Lancaster, M. Rossi, M. Pesce & A. Stefanovska. Diagnosis of malignant melanoma through identification of changes in blood flow dynamics. *Post-graduate Research Conference. 13 July 2013. Lancaster, UK.* Oral & poster presentation.

ABSTRACT

Tumour vasculature is known to be inefficient and abnormal due to poorly regulated angiogenesis during tumour growth. This leads to irregular patterns of blood flow which are spatially and temporally heterogeneous. Many investigations into the characteristics of tumours are invasive and performed on animal models. However, continuous technological and theoretical advancement is leading to the use of non-invasive imaging techniques, providing *in vivo* information on humans.

Here, data recorded using laser Doppler flowmetry (LDF) in malignant melanoma and control lesions are analysed using techniques designed for application to non-stationary, time-varying data. Many studies utilising LDF have previously revealed increased blood flow in malignant lesions, but very little attention has been paid to the *dynamics* of this blood flow, or how it changes over time. As it has been demonstrated previously that the oscillations observed within blood flow data are physiologically significant, failure to extract these characteristics loses information about the underlying dynamical system from which the blood flow data were recorded. Significant differences in blood flow dynamics are revealed and used in the development of a diagnostic test for melanoma.

In addition to the characterization of the blood flow dynamics in melanoma, possible causes for the observed changes are investigated and related to two widely observed characteristics of cancer, intermittent hypoxia and altered cellular energy metabolism. The former is explored through the analysis of blood flow and oxygenation data recorded during dry static apnoea, whilst the latter is modelled using coupled phase oscillators.

Contents

Glossary & Abbreviations	xiv
1 Introduction	1
1.1 Outline of thesis	3
2 Physiology	5
2.1 The circulatory system	6
2.1.1 The cardiovascular system	6
2.1.2 The heart	6
2.2 Vascular structure and function	8
2.2.1 The microvasculature	9
2.2.2 The endothelium	11
2.2.3 Vasomotion and flowmotion	13
2.2.4 The relationship between vasomotion and tissue oxygenation	16
2.3 Evaluation of microvascular function	18
2.3.1 Skin microvascular blood flow	18
2.3.2 Blood flow dynamics for the evaluation of skin microvascular function	21
2.3.3 Skin microvasculature as a model for the microvasculature .	25
2.4 Microvascular blood flow in cancer	26
2.4.1 Tumour angiogenesis	27
2.4.2 Angiogenesis in melanoma	30
2.4.3 Blood flow in cancer	31
2.4.4 Noninvasive diagnosis of melanoma	32
2.4.5 Blood flow in skin cancer	34
2.4.6 Renormalization of the vasculature	36
2.5 Potential microenvironmental influences on microvascular blood flow	37
2.5.1 Metabolic and microvascular responses to hypoxia	38
The role of hypoxia in melanoma development	39
2.5.2 Cellular energy metabolism	40
Metabolic oscillations in health and diseases	42
Metabolic alterations in cancer	44
Effects of altered energy metabolism on microvasculature . .	45
2.6 Summary	46
3 Physiological measurement	47
3.1 Systemic processes	47
3.1.1 Electrocardiogram	47
3.1.2 Heart rate variability	48

3.1.3	Respiration	49
3.2	Blood flow	50
3.2.1	Laser Doppler flowmetry	50
3.2.2	Laser Doppler perfusion imaging	52
3.2.3	Laser speckle contrast imaging	53
3.3	Blood oxygenation	54
3.4	Summary	57
4	Dynamical systems	58
4.1	Introduction	58
4.1.1	Nonautonomous systems	59
4.1.2	Chronotaxic systems	60
4.2	Inverse approach to dynamical systems	63
4.2.1	Time domain	64
Instantaneous frequency and phase	64	
Preprocessing	65	
Detrended fluctuation analysis	66	
4.2.2	Frequency domain	67
The Fourier transform	67	
4.2.3	Time-frequency analysis	70
Short time Fourier transform	70	
Continuous wavelet transform	70	
Wavelet types	72	
Cone of influence	73	
Implementation	73	
4.2.4	Interactions	74
Wavelet phase coherence	74	
Synchronization	75	
Dynamical Bayesian inference	76	
4.3	Identifying chronotaxic systems	78
4.3.1	Extracting the phase estimates	80
4.3.2	Detecting chronotaxicity	81
4.4	Further development of the inverse approach to chronotaxic systems	84
4.4.1	Numerical simulations	84
4.4.2	Practical considerations	88
4.4.3	Application to brain dynamics	92
4.5	Summary	98
5	Blood flow dynamics in skin melanoma	101
5.1	Cancer	101
5.1.1	Skin cancer	102
5.1.2	Hypotheses	104
5.2	Experimental protocol	104
5.2.1	Exclusion criteria	106
5.3	Analysis	107
5.3.1	Pre-processing	107
5.3.2	Statistics	107
5.3.3	Time domain analysis	108
Heart rate and heart rate variability	108	

	Mean blood flow	109
5.3.4	Histological results	112
5.3.5	Time-frequency analysis	114
5.3.6	Wavelet phase coherence	117
5.3.7	Non-invasive diagnosis of melanoma	120
5.4	Summary	121
6	Oxygenation and blood flow dynamics	126
6.1	Hypothesis	126
6.2	Experimental protocol	127
6.2.1	Measured parameters	128
	Electrocardiogram	128
	Arterial oxygen saturation	128
	Respiration	129
	Blood flow	129
	Oxygenation parameters	130
6.3	Results	130
6.3.1	Statistics	130
6.3.2	Comparison of divers and controls at rest	131
	Systemic comparisons	131
	Local comparisons	135
6.3.3	Blood flow and oxygen dynamics during apnoea	140
	Systemic changes during apnoea	144
	Systemic changes during naive apnoea	145
	Local changes during apnoea following breathe-up	146
	Local changes during naive apnoea	151
	Involuntary chest contractions	152
	Blood flow and oxygenation dynamics during naive apnoea	155
6.4	Summary	160
7	Modelling metabolic oscillators	166
7.1	Modelling cellular energy metabolism	167
7.1.1	Determining metabolic states through chronotaxicity	170
7.2	Numerical simulations	171
7.2.1	Detection of chronotaxicity via the inverse approach	176
7.2.2	Experimental verification	180
7.2.3	Verification of the glycolytic oscillator	181
7.2.4	Links to carcinogenesis	183
7.3	Summary	185
8	Concluding remarks	188
8.1	Summary	188
8.2	Original contributions	190
8.3	Future work	192
	Appendices	194
	A Diagnostic test values	195

B Sample size and statistical power calculations	197
Power of significance tests	198
Effect size	199

List of Figures

2.1	Capillary structure	10
2.2	Typical LDF signal	22
2.3	Diagram of the different stages of melanoma	30
2.4	Diagram of cellular energy metabolism	41
3.1	Typical ECG trace	48
3.2	Diagram of laser Doppler flowmetry	50
3.3	Scattering of a photon by a moving red blood cell	51
3.4	Example wavelet transform of a LDF signal	52
3.5	Laser speckle contrast imaging (LSCI) image of fingers	55
3.6	Absorption spectra for haemoglobin and water	57
4.1	Moving point attractor in a chronotaxic system	61
4.2	Removal of artefacts using linear interpolation	65
4.3	Detrending data before analysis	66
4.4	Comparison of the Fourier transforms of simulated low frequency oscillations and $1/f$ noise	69
4.5	Chirp signal transformed to frequency and time-frequency domains	71
4.6	Diagram showing the main principles of the wavelet transform	72
4.7	Time averaged wavelet transform vs. Fourier transform	73
4.8	Example showing the difference in noise distributions in chronotaxic and non-chronotaxic systems	83
4.9	Identifying chronotaxicity in signals with more than one oscillatory mode	85
4.10	Identifying chronotaxicity in a system of bidirectionally coupled oscillators	86
4.11	Identifying intermittent chronotaxicity using dynamical Bayesian inference	89
4.12	Determination of the minimum number of oscillations required in a time series to reliably detect chronotaxicity	92
4.13	Application of PFA to brain dynamics during anaesthesia	94
5.1	Diagram of the skin	102
5.2	Diagram of LDF recording setup on a melanoma lesion	106
5.3	Boxplots and scatter plots of mean heart rate and standard deviation of heart rate	110
5.4	Mean blood flows in all lesion types	111
5.5	Anti CD34 Mab highlighted vessels in melanoma and vessel counts	113
5.6	Histological correlations	114

5.7	Comparison of absolute powers between all groups	115
5.8	Normalized time-averaged wavelet power of all groups	116
5.9	Comparison of mean blood flows and normalized wavelet power spectra between lesion centres and contralateral skin	117
5.10	Wavelet phase coherence between blood flow recorded in lesion centres and contralateral skin	119
5.11	Evaluation of the discriminatory power of ratios between cardiac and myogenic/neurogenic power	120
5.12	Sensitivity and specificity ranges for melanoma diagnostic parameters	122
6.1	Location of probes	128
6.2	Diagram of the two tissue depths measured by the O2C	131
6.3	Comparison of heart rate between divers and controls	132
6.4	Comparison of heart rate variability between divers and controls . .	132
6.5	Comparison of S_pO_2 between divers and controls	133
6.6	Example of the interaction between S_pO_2 and respiration	134
6.7	Wavelet phase coherence between S_pO_2 , respiration and heart rate variability	136
6.8	Normalized wavelet power for all recorded blood flow signals	138
6.9	Comparison of S_TO_2 wavelet power between groups	140
6.10	Timeline of free diver breath-hold protocol	141
6.11	Example of physiological signals recorded from a free diver during the breath-hold protocol	142
6.12	Example wavelet transforms of physiological signals recorded from a free diver during the breath-hold protocol	143
6.13	Heart rate and S_pO_2 compared during breathe-up and breath-hold periods	144
6.14	Heart rate and S_pO_2 compared during rest periods 1 and 2 and breath-hold 6	146
6.15	Examples of blood flow, S_TO_2 and rHb signals during breathe-ups and breath-holds	149
6.16	Example of the effect of involuntary contractions on LDF signals . .	152
6.17	Time averaged wavelet power of blood flow compared during rest and the final breath-hold in all blood flow recordings	157
6.18	Boxplots of absolute wavelet power in frequency intervals I–IV during rest and during breath-hold 6 in all S_TO_2 recordings	158
6.19	Example blood flow signal during rest and breath-hold	159
7.1	Diagram of cellular metabolism model of coupled oscillators	170
7.2	Phase trajectories of the 7 types of dynamics observed in the model	174
7.3	Numerical chronotaxicity plot for ε_1 vs. ε_2	175
7.4	Varying the influence of drivers in the phase oscillator model	175
7.5	Varying the natural frequencies in the phase oscillator model	177
7.6	Effect of a time-varying driver on the chronotaxic dynamics of the phase oscillator model	178
7.7	Phase fluctuation analysis of simulated ATP dynamics	179
7.8	Example of the detection of chronotaxicity from a single ATP time series using phase fluctuation analysis	180
7.9	Testing real metabolic oscillations for chronotaxicity	184

List of Tables

3.1	Overview of techniques for the measurement of blood flow	56
5.1	Type, gender, age and location information for all subjects studied .	105
5.2	Average blood flow in melanoma and control lesions	109
5.3	Rank sum comparisons of mean blood flow between all groups . . .	111
5.4	Histological characteristics of melanoma lesions	112
5.5	Normalized power values for all studied frequency intervals	118
6.1	Age and sex matching of controls	129
6.2	Mean blood flows at all locations for freedivers and controls	137
6.3	Results of significance testing on blood flow intervals	139
6.4	$S_T O_2$ and rHb means at all locations for freedivers and controls . .	139
6.5	Mean and standard deviation of blood flow compared between states	148
6.6	Mean and standard deviation of $S_T O_2$ and rHb compared between states	150
6.7	Mean and standard deviation of blood flow recorded at rest and during breath-hold 6	153
6.8	Mean and standard deviation of oxygenation parameters recorded at rest and during breath-hold 6	154
6.9	Lengths of breath-holds five and six for all subjects	156
7.1	Characteristic frequencies of oscillators in different metabolic states	172
A.1	Results of the melanoma diagnostic test for all subjects	196

Glossary & Abbreviations

ACh Acetylcholine. Vasodilator which acts indirectly to relax the smooth muscle cells via endothelial cells.

Action potential A rapid rise and fall in the membrane potential of an excitable cell, occurring when the membrane potential reaches a threshold value.

ADP Adenosine diphosphate. Precursor to ATP synthesis. ADP and phosphate are required to synthesize ATP.

Aerobic respiration Energy producing reactions which require oxygen to generate ATP.

Anaerobic respiration Less efficient mechanism of energy production which does not use oxygen.

Apnoea Suspension of breathing.

Apoptosis A very organised and controlled mechanism of cell death, abnormally avoided by cancer cells.

Atherosclerosis An arterial disease characterized by the presence of fatty deposits on the vessel walls.

ATP Adenosine triphosphate, energy currency of the cell. ATP is used as an energy source for protein synthesis, signalling and cell division, among many other processes.

Autonomic nervous system The control system that regulates unconscious actions such as heart rate, breathing and digestion.

BF Blood flow.

Breslow depth A prognostic factor in melanoma of the skin related to how deep the tumour has invaded the tissue.

Carcinogenesis The transformation of normal cells to cancer cells.

Clark level A descriptor for the level of invasion of melanoma in the skin, split into 5 levels, where level 1 is the least invasive, and 5 is the most severe.

Cytosol The liquid inside cells in which the cellular organelles reside. Surrounded by the plasma membrane.

-
- Dermoscopy** A method for the noninvasive inspection of skin lesions using a magnifier, a light source and a liquid medium.
- DFA** Detrended fluctuation analysis. A method to determine the statistical self similarity of a signal at different timescales.
- ECG** Electrocardiogram. Method of recording the electrical activity of the heart.
- EEG** Electroencephalogram. Method of recording brain activity via electrical signals.
- FFT** Fast Fourier transform. A fast algorithm for the computation of the Fourier transform, which transforms a signal from the time domain to the frequency domain.
- FRET** Fluorescence resonance energy transfer.
- Haemoglobin** An oxygen carrying protein found in the red blood cells.
- HRV** Heart rate variability. A measure of how the heart rate fluctuates over time.
- Hypoxaemia** An abnormally low level of oxygen in arterial blood i.e. haemoglobin oxygen saturation below 90%.
- Hypoxia** A localized deprivation of oxygen in the body.
- in vitro* Studies of biological organisms or cells outside their usual context, e.g. in test tubes or petri dishes.
- in vivo* Studies on intact biological organisms.
- Lactate** The end product of self-functioning glycolysis, i.e. when glycolysis is the only energy source within the cell.
- LDF** Laser Doppler flowmetry. Method of blood flow measurement based on the Doppler shift of incident light by moving red blood cells.
- LSCI** Laser speckle contrast imaging. Method of monitoring blood flow by exploiting speckle contrast patterns.
- Membrane potential** The difference in electric potential between the inside and outside of a cell.
- NADH** Reduced form of nicotinamide adenine dinucleotide (NAD). Donates electrons during redox reactions in cellular energy metabolism.
- NIRS** Near infrared spectroscopy. A method used to measure the changes in concentration of oxy- and deoxy-haemoglobin in the blood.
- NMD** Nonlinear mode decomposition. A method for the extraction of oscillatory modes from time series using time-frequency representations and surrogate methods.

-
- NO** Nitric oxide. Powerful vasodilator, i.e. relaxes smooth muscle cells surrounding blood vessels.
- OXPHOS** Oxidative phosphorylation. A highly efficient pathway for the formation of ATP which requires oxygen.
- PFA** Phase fluctuation analysis. Method of identifying chronotaxicity from a single time series.
- PFK** Phosphofructokinase. Performs the committed step in glycolysis, the conversion of fructose-6-phosphate to fructose-1,6-biphosphate.
- Plasma membrane** A selectively permeable phospholipid bilayer surrounding the cell, separating it from its surroundings.
- PORH** Post occlusive reactive hyperemia. A method of inducing increased blood flow following occlusion of a limb.
- Proliferation** An increase in cell number as a result of cell growth and division.
- PU** Perfusion unit. Arbitrary unit used in laser Doppler flowmetry.
- Pyruvate** An end product of glycolysis which can be converted to lactate or acetyl-CoA to be used in the Krebs cycle.
- rHb** Relative haemoglobin. Value which varies with fluctuations of haemoglobin, not an absolute value.
- RSA** Respiratory sinus arrhythmia. The natural variation of the heart rate during each respiration cycle.
- S_TO₂** Venous oxygen saturation.
- SNP** Sodium nitroprusside. A vasodilator which not does require the presence of endothelial cells to function.
- Systemic** In the context of the human body, a systemic process is one which affects the whole body, for example the beating of the heart. The effects of these processes may be observed at large distances from where they originate.
- VEGF** Vascular endothelial growth factor.

1. Introduction

The human body is an incredibly complex biological machine, which, unlike many man-made machines, functions continuously for the duration of its lifetime. The number of simultaneously occurring chemical, physical and biological processes within the body at any one time is almost impossible to comprehend, and yet these continue without any conscious input. This facilitates not only basic essential functions, such as breathing, eating and sleeping, but also intelligence, memory and countless others. These processes occur on all spatial scales within the body, from the creation of new individual molecules in protein synthesis to the collective behaviour of whole organs, such as the beating of the heart. Taking the heart as an example, it is clear that the heart beat is an oscillatory process, without which oxygen and other essential nutrients could not be delivered to tissues, or waste products collected. Despite the importance of this oscillation, the existence of such time-varying behaviour is not always appreciated at smaller scales. In fact, whilst they may not initially appear as obvious as the heart beat or breathing, oscillations have been observed throughout the body, in cellular energy metabolism [1], blood vessels [2], neurons [3], intracellular calcium [4], plasma membrane potential [5], adenosine triphosphate (ATP) concentrations [6] and mitosis [7], to name a few. It is therefore very important to understand the nature of these oscillations, and crucially, how they are affected by their environment. Due to the complexity of the body, many studies focus on isolated subsystems, removed from the body, to extract information about biological functions. However, whilst this has resulted in huge leaps forward in terms of our knowledge of the underlying

mechanisms of many processes, it cannot be known how much information is lost, or even how the behaviour is changed, by removing these subsystems from their natural environment. Considering that they are no longer functioning as part of a whole, the natural behaviour of these subsystems, and their interactions, cannot be observed. An example of this can again be seen in the heart. Outside the body, the pacemaker cells of the heart will contract around 100 times per minute, much higher than the average resting heart rate. However, once the heart is within the body it is influenced by the autonomic nervous system, which lowers this rate to around 60 beats per minute. Thus, it is clear that only observing the activity of individual heart cells does not provide a realistic picture of the behaviour of the heart in its natural environment within the body.

The continuous development of noninvasive imaging techniques is enabling the collection of increasing amounts of data *in vivo*, providing functional information about the human body in its natural state. Using the method of laser Doppler flowmetry, at least six distinct oscillations have been observed in microvascular blood flow, and have been attributed to various physiological functions, from the systemic cardiac and respiratory functions down to local regulation of blood flow at lower frequencies [2]. Knowledge of these oscillations and their physiological origins allows pathological states to be investigated in terms of abnormalities in blood flow dynamics, and this approach has been used in many studies of various pathologies, including type 2 diabetes [8], obesity [9] and hypertension [10]. The noninvasive nature of these studies means that spontaneous oscillations in blood flow can be observed in health and disease, and attributed to alterations in physiological processes depending on the observed dynamics.

One disease in which blood flow is expected to be altered is cancer, due to the recruitment of new blood vessels by tumours in a process known as angiogenesis. Usually, cancers are difficult to observe within their natural environment, due to their location within the body, or the requirement for their swift removal. However, as previously demonstrated [11, 12], skin cancer provides an opportunity to observe

and characterise noninvasively the blood flow dynamics in malignant lesions using laser Doppler flowmetry (LDF).

1.1 Outline of thesis

The main goal of this thesis is to utilise oscillations in microvascular blood flow to investigate skin malignant melanoma, in order to test the hypothesis that blood flow dynamics are altered in malignant melanoma when compared with atypical lesions and normal skin. The data and analysis methods are also used to assess whether local or systemic regulatory processes are altered in this state, and to extract as much information as possible about the regulation of tumour vasculature from these observations for use in the development of a diagnostic test. These oscillations are also investigated in terms of their relationship to tissue hypoxia and cellular energy metabolism.

Chapter 2 provides an introduction to the physiology of the cardiovascular system and oscillations in microvascular flow in the context of skin malignant melanoma. Chapter 3 describes the relevant measurement techniques used to acquire the data presented in this thesis.

Chapter 4 introduces dynamical systems and highlights the importance of the consideration of living systems as nonautonomous. This chapter also presents the inverse approach techniques used to extract the results presented in this thesis, and provides a brief review of the inverse approach as applied to the newly-defined class of chronotaxic systems.

Chapter 5 investigates the blood flow dynamics in skin malignant melanoma, as compared to controls. The results provide insights into the pathophysiology of tumour vasculature and are also used in the development of a diagnostic test. Analysis of data previously recorded during apnoea in free divers is presented in chapter 6, which provides an opportunity to measure physiological parameters during oxygen deprivation. The aim of this chapter is to investigate blood flow and oxygenation dynamics during hypoxia, which has been implicated in cancer.

Finally, chapter 7 seeks to investigate the altered cellular energy metabolism observed in the majority of cancer cells using a model of coupled chronotaxic phase oscillators.

2. Physiology

Of all observable processes occurring within the body, very few may be considered as stationary. The vast majority vary with time, continuously reacting with each other and their environment. These variations form the very basis of life. Whilst studying the dynamics of whole systems, for example the cardiovascular and respiratory systems, we must also consider the single cell and its organelles, and everything in between. Only when all scales, and thus all oscillators, are considered, may we truly begin to understand life.

Practical difficulties often make the observation of biological oscillations *in vivo* impossible, therefore many studies have focussed on the separation of different parts of biological dynamical systems which are readily accessible. Problems arise here with the assumption that biological systems can be characterized by the sum of their parts, i.e. that they are linear. In fact, the opposite is almost always true. Living systems on all scales are subject to continuous perturbations, which may be deterministic or stochastic and may arise from adjacent dynamical systems or random fluctuations. Isolation of a single component of this large scale system results in the loss of very important information about its behaviour within the whole, which is likely to be fundamentally different, limiting the viability and applicability of any resultant conclusions. To retain all available information, we must consider living systems in their natural state as far as is possible. It is also very important to observe their spontaneous dynamics, rather than introducing unnatural perturbations to the system.

However, before beginning to study the interactions between physiological pro-

cesses, it is important to understand their basic physiology and the techniques which are used to observe them.

2.1 The circulatory system

The circulatory system comprises the cardiovascular system and the lymphatic system, but here the focus will be on the cardiovascular system.

The origins of our current understanding of the cardiovascular system began in 1628, when William Harvey showed that arteries and veins are functionally connected, and that blood circulates [13]. This was in stark contrast to the previous model presented by the Ancient Greeks, in particular Galen, who viewed the arteries and veins as two distinct networks, and concluded that the blood was food that had been transformed in the liver for the nourishment of the body [14].

There are around 100,000 miles of blood vessels in the human body [15]. Without this transport and feedback system, it would be impossible for the body to function. Problems arise within the vasculature in many disorders. Thus, it is of vital importance to understand the mechanisms and processes involved in the regulation and growth of the vasculature.

2.1.1 The cardiovascular system

We now know that the cardiovascular system is a connected system which includes the heart, blood, blood vessels and the lungs, and its primary function is to deliver nutrients continually and efficiently, via blood circulation, to the whole body and to remove metabolic waste from the body effectively.

2.1.2 The heart

The heart pumps blood around the body, beating around 2.5 billion times in an average lifetime [16]. The five litres of blood found in the average human body is continuously circulated, with a whole cycle taking around one minute. The

heart is made up of three layers: the pericardium, a thin outer protective sack, the myocardium, the specialized cells that make up the thick muscular wall of the heart, and endocardium, which is the thin inner lining of the heart. The heart has four chambers: two atria and two ventricles. The atria, at the top of the heart, are smaller than the ventricles, which are located in the lower heart. The stronger left ventricle pumps oxygenated blood to the whole body. Deoxygenated blood returns to the heart into the right atrium, and is then pumped into the right ventricle, through the tricuspid valve. From the right ventricle, blood is pumped through the pulmonary valve, through the pulmonary artery to the lungs. The oxygenated blood returns from the lungs through the pulmonary vein, into the left atrium. From here, the blood is pumped through the mitral valve into the left ventricle, where it is once again ready to be pumped to the tissues of the body, via the aortic valve and the aorta. The heart contains valves to prevent the backflow of blood. The heart also contains a muscular wall which divides the left and right sides, called the septum. This prevents mixing of oxygenated and deoxygenated blood. The heart itself, as a particularly demanding muscle, also requires its own oxygen supply, obtained from coronary arteries, which branch from the aorta.

The heart generates regular electrical pulses in order to coordinate pumping by instructing the cells to contract. The concept of the heart as an electrical conducting system was first appreciated by Sunao Tawara in his 1906 monograph [17, 18]. Soon after, Keith and Flack discovered the sinoatrial (SA) node [19], providing an answer to the fundamental question: why does the heart beat? The SA node, the primary pacemaker of the heart, is located in the right atrium, and generates a normal sinus rhythm by generating impulses which then spread through the cells of the heart. This gives rise to the most familiar biological oscillation, the heart beat.

2.2 Vascular structure and function

Blood flow, the movement of the blood through the cardiovascular system, is an essential process for survival. If blood flow stops, the brain can only survive without damage for up to three minutes at physiological temperatures, due to the lack of oxygen delivery resulting in the irreversible death of neurons [20]. Other tissues will also die following prolonged periods of inadequate perfusion, known as ischemia [21].

The blood is the medium by which nutrients are delivered to all cells within the body, and their waste collected for removal. Blood contains many different cells, the most abundant being red blood cells, or erythrocytes, the carriers of oxygen. White blood cells, or leukocytes, are also important for the immune system.

Blood flow is incredibly complex. Macrovascular flow dynamics, arising from large and small arteries, depends on many factors, including the velocity of the blood, the geometric properties of the vessel and the influence of the blood on the vessel wall. Whilst complicated, these have been used to develop models in which the main observed characteristics of arterial flow can be accurately recovered [22]. These models are based on the assumption that the vessel walls are impermeable. Thus, it immediately becomes clear why different approaches must be used in the case of the microcirculation, containing capillaries which are necessarily permeable, allowing the passive diffusion of dissolved gases, ions and solutes across the vessel wall [23]. This permeability arises from the arrangement of endothelial cells, and varies with location and function [23]. Consideration of the intrinsic behaviour and function of the blood vessels, and the role played by the endothelium is therefore critical for the understanding of the regulation of blood flow. To assess the relationship between macro- and microvascular blood flow dynamics Urbančič-Rovan *et al.* performed measurements of blood pressure and basal skin blood flow in diabetic patients and controls [24]. They found that except from a significant positive correlation between systolic pressure and the endothelial frequency interval in dia-

betic patients on the right side of the body, macro- and microvascular changes do not progress simultaneously. This highlights the requirement for models of macro- and microvascular blood flow to be specific to each system.

Arteries carry oxygenated blood from the heart to the rest of the body. Two exceptions to this are the pulmonary artery and umbilical arteries which carry deoxygenated blood. Arteries are under the most pressure in the vascular system, as the blood they are transporting is required at large distances from the heart. They withstand the pressure generated by the heart with their strong muscular walls. The largest artery is the aorta, directly connected to the left ventricle of the heart. This then branches into smaller arteries, arterioles, and finally capillaries.

Arterial walls are made up of many layers. The outer layer, the tunica adventitia (or externa), is a strong outer covering composed of connective tissue as well as collagen and elastic fibres. These fibres allow the arteries to stretch to prevent overexpansion due to the pressure of the blood flow. The middle layer, the tunica media, is composed of smooth muscle and elastic fibres. The inner layer, the tunica intima, is composed of an elastic membrane lining and smooth endothelium that is covered by elastic tissues.

Veins transport deoxygenated blood back to the heart and are under less pressure than arteries. Consequently, the muscular middle layer of a vein is thinner than in an artery. Because of the lower pressure, and the required movement of blood against gravity, veins contain valves to prevent the back flow of blood. The largest veins are the vena cava, the superior vena cava and inferior vena cava, which transport blood directly to the right atrium of the heart. Smaller veins are called venules, and are also connected to the capillaries.

2.2.1 The microvasculature

The groundbreaking work of Harvey, whilst proving that arteries and veins were connected, did not demonstrate *how* they were connected. In fact, the capillaries which serve this purpose were observed by Leonardo da Vinci, but he did not link

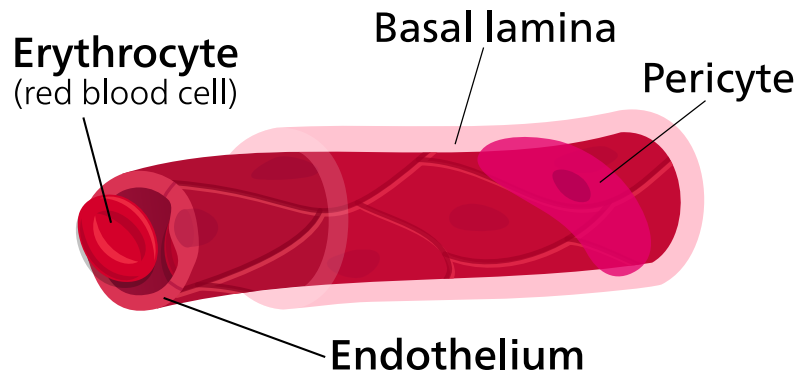


Figure 2.1: Capillary structure. Modified from [28].

them to their role in linking arterioles and venules [25]. The mystery was solved in 1661 by Marcello Malpighi, when he observed blood coursing through a network of small tubes on the lung surface and in the distended urinary bladder of the frog, and speculated that these capillaries were the connection between arteries and veins [26, 25]. Independently, Van Leeuwenhoek also observed red blood cells and their movement through the capillaries in 1688 [27]. These findings constitute the earliest observations of blood flow in the microvessels.

Capillaries are the smallest vessels in the body, usually measuring around 5-10 μm . They connect arterioles and venules to complete the blood transport network.

The flow of blood from an arteriole, through a capillary bed and into a venule is known as microcirculation. The capillary bed is a collection of capillaries which form an interweaving network, and contains two types of vessels; vascular shunts and true capillaries. True capillaries are where exchange of substances occurs. Depending on vasomotor nerves and chemical conditions, the blood can bypass the capillary bed through the vascular shunt, also called a metarteriole, to divert blood to another area of the body. At their smallest, capillaries are made up of only a layer of endothelial cells, to allow fast diffusion of water, oxygen and carbon dioxide through their walls, amongst other substances.

2.2.2 The endothelium

Initially considered only as tunnels, in the 1800s Reckinghausen observed that blood vessels are actually canals lined with cells [29]. These cells were identified and termed endothelial cells by Wilhelm His in 1865, who differentiated the inner lining of body cavities from epithelium [30, 31], yet the detailed study of the endothelium only began in the 1950s with Howard Florey describing their structure but not realising the magnitude of their importance [32].

The realization by Jaffe, Nachman and members of their laboratory that endothelial cells were the key to understanding how the vascular wall worked in health and disease led to them culturing human umbilical endothelial cells for the first time in 1973 [33] leading to an explosion in the field of vascular biology [34].

Vascular endothelial cells form a continuous monolayer in all blood vessels. Once viewed as an inert barrier between blood and tissues, it is now known that this vital organ has many essential functions, including maintaining the fluidity of the blood [35], regulation of the flow of nutrients and biologically active molecules [36], and signalling [37]. The endothelium varies between sites, with almost every organ having its own adaptation of endothelial structure depending on functional requirements [38]. The endothelium also plays an essential role in angiogenesis, the development of new blood vessels from existing vasculature, by dividing and migrating in response to growth factors such as vascular endothelial growth factor (VEGF) [39] (see below).

However, the first crucial role of the vascular endothelium to be discovered was its effect on vascular tone, and thus blood flow regulation, through the release of vasoactive substances [36]. This began in 1976, when Moncada and colleagues discovered that blood vessels secrete a vasodilatory substance, prostacyclin [40]. In 1980, Furchgott and Zawadzki [41] discovered that the vasodilator acetylcholine (ACh), a very potent vasodilator *in vivo*, did not always induce the same response *in vitro*. They discovered that the reason was that endothelial cells had been accidentally removed during preparation, and deduced that their presence is essential

for vasodilation to occur using ACh. They also demonstrated that ACh stimulates the release of a substance termed endothelium-derived relaxing factor (EDRF). EDRF was later identified as nitric oxide (NO) by Ignarro *et al.* [42] and independently by Palmer *et al.* [43], both in 1987. A third vasodilator was discovered when vasodilation was still observed after blocking NO and prostacyclin production, and named endothelium-derived hyperpolarizing factor (EDHF) [44], and shown to be distinct from EDRF by Chen *et al.* [45]. In 1989, another endothelial secretion was discovered, this time a vasoconstrictor named endothelin [46].

Substances secreted by endothelial cells induce responses within the vascular wall, resulting in vessel constriction or dilation to modulate the blood flow as required. For example, NO acts to relax the smooth muscle cells by activating guanylyl cyclase, which then raises the cyclic guanosine monophosphate (cGMP) concentration [47]. This increases the activity of cGMP-dependent protein kinase (PKG) which in turn activates myosin light-chain phosphatase (MLCP)[47]. This then induces relaxation by reducing the concentration of phosphorylated myosin regulatory light-chain subunits in vascular smooth muscle [47]. Via sensing of the shear stress induced by blood flow by the anionic polyelectrolyte heparan sulphate proteoglycan (HS-PG), the endothelial cells act on the smooth muscle cells to induce a flow-dependent vasodilation in response to increased blood flow, whilst a decrease in blood flow will induce vasoconstriction [48]. This flow-dependent regulation by the endothelium was first demonstrated in dogs *in vivo* by Pohl and colleagues in 1986 [49]. Endothelial dysfunction, mainly characterized through impaired sensing by a reduction in the availability of vasodilators and an increase in endothelium-derived contracting factors, has now been associated with many pathologies, including atherosclerosis [50], other chronic inflammatory diseases such as psoriasis, rheumatoid arthritis and inflammatory bowel diseases [51], hypertension [52], diabetes [53], impaired renal function [54], erectile dysfunction [55], Alzheimer's disease [56], preeclampsia [57] and obesity [58]. Thus, it is clear that a focus on vascular regulation is very important in the understanding of the

development of many diseases, especially at the level of the microvasculature.

2.2.3 Vasomotion and flowmotion

Vasomotion is the rhythmical change in tone exhibited within arteries, predominantly within the microcirculation [59], but also demonstrated in large muscular arteries [60, 61]. The mechanisms and physiological importance for vasomotion are still not fully understood, thus it remains an intense area of research.

Vasomotion was observed for the first time by Jones in 1852 in the circulation of a bat wing [62], and has been widely observed in both humans and animals ever since, both *in vivo* and *in vitro*. Both the *in vivo* and *in vitro* approaches provide their own benefits. Studying vasomotion *in vivo* allows the behaviour of the vessel walls to be studied in their natural environment, as affected by systemic and local regulatory processes. In contrast, *in vitro* studies have provided information about the *intrinsic* behaviour of the vessels themselves, and allows experimental conditions to be finely tuned in order to pinpoint directly the cause of different phenomena, whilst *in vivo* their origins may not be so clear due to difficulties in measurement. *In vivo*, it is a challenge to observe vasomotion directly, but it has been demonstrated to be possible using intravital microscopy [63], optical-resolution photoacoustic microscopy [64], and optical coherence tomography [65].

In vitro, vasomotion with a frequency ranging from 0.01 to 0.3 Hz is seen in isolated arteries from various species and in blood vessels from different areas of the body [66, 67]. It has been observed that the frequencies of vasomotion observed *in vitro* correspond well with those observed in the myogenic frequency interval (around 0.1 Hz) *in vivo* [67, 68], providing evidence for the automated nature of oscillations observed at myogenic frequencies, and the local *in vivo* regulation that the neurogenic and endothelial contributions provide (see below).

The first studies of vasomotion in different conditions *in vivo* used intravital microscopy, and demonstrated that vasomotion frequency and amplitude are affected by pH, temperature and partial pressure of oxygen changes [69], and arterial

pressure [70]. Another way to observe vasomotion indirectly *in vivo* is by measuring the effects of these variations in the vascular wall on the blood flowing through them, which will be oscillatory as a result. This is known as flowmotion [71], and has since been widely utilised via the application of laser Doppler flowmetry to study vasomotion noninvasively.

For vasomotion to occur, i.e. for macroscopic oscillations in a blood vessel to be observed, the oscillations in individual smooth muscle cells must be synchronised [72]. The origins of these individual cellular oscillations are debated, and could arise from membrane potential oscillations, cytosolic oscillations (i.e. calcium oscillations) or metabolic oscillations [72]. On a completely automated level, in response to increased blood pressure, a dilation of vessels will act so as to decrease the pressure [73].

Vasomotion occurs at a wide range of frequencies, which have been shown to vary depending on vessel size by Colantuoni *et al.* [74], with the frequency of vasomotion higher in small arteries than larger vessels in hamsters. This conclusion was based on the frequency with the largest amplitude in the Fourier transform of the vessel diameter time series, and thus does not take into account variations in this frequency, which were clearly present. This study also demonstrated that vasomotion was strongly suppressed during anaesthesia [74]. This effect was later confirmed in humans *in vivo* by Landsverk *et al.* who found significant reductions in oscillatory activity associated with myogenic, sympathetic and endothelial related vasomotion [75] during general anaesthesia, as measured by laser Doppler flowmetry (see below).

Most available *in vivo* data on the prevalence of vasomotion has been obtained using LDF [67], but care must be taken in the interpretation of these results, due to the single point nature of LDF and the fact that it is not possible to visualise the underlying blood vessels. As a result, it is difficult to know whether the measurement area contains only capillaries, or a mixture of vessel types. Another issue is the systemic influences on LDF, and care must be taken to avoid record-

ing locations at which the cardiac component is very strong and will overpower more subtle, locally generated oscillations. New techniques which allow imaging of blood flow, such as laser Doppler perfusion imaging (LDPI) and laser speckle contrast imaging (LSCI) may provide solutions to these issues, but LDF has been shown to be sufficient to study vasomotion non-invasively [76] as long as care is taken to minimise variability through optimal probe placement and sufficiently long recording times.

A large proportion of the current knowledge on vasomotion is derived from animal studies. Vasomotion in humans has been found to depend heavily on experimental conditions and pathology. Alterations in vasomotion have been observed in many pathological states. Reduced vasomotion has been observed in type 2 diabetes [8], obesity [9] and hypertension [10]. In the case of type 2 diabetes, it was shown that microcirculation could be improved by synchronizing smooth muscle cell activity and thus increasing vasomotion [8]. Vasomotion induced by electrical stimulation of the cervical sympathetic nerve was also shown to be abolished at high and low temperatures [77]. The same study provided evidence that vasomotion enhances tissue perfusion, highlighting its vital role in oxygen delivery to tissues. The effects of temperature on spontaneous vasomotion in humans *in vivo* was investigated by Sheppard *et al.* using local skin cooling and heating in combination with LDF [78]. They found that local cooling increased the myogenic response, yet lowered the frequency of vasomotion in this interval, whilst heating the skin decreased myogenic activity whilst significantly increasing blood flow, which demonstrates the maximum, sustained vasodilation of the local vessels during heating. The effects of different dynamics of the temperature change were also investigated by Vuksanović *et al.* who found that a steady level of skin blood flow must be significantly perturbed by a thermal shock to cause vasodilation/constriction [79]. They also found that the temperature flow curves obtained during heating and cooling demonstrated hysteresis, indicating bistable or multistable blood flow levels for a given temperature stimulus [79].

Many efforts have been made to identify the exact mechanisms involved in vasomotion, but it is also important to understand why vasomotion occurs, if it provides any physiological advantages, and if so, what are they? It is strongly believed that vasomotion provides important benefits, particularly for oxygen, ion and nutrient delivery via the blood, and thus it remains an intense area of research.

2.2.4 The relationship between vasomotion and tissue oxygenation

Although not universally demonstrated, there is strong evidence to suggest that there are benefits of vasomotion for tissue oxygenation.

In 1991, Bertuglia *et al.* induced hypoxia and hyperoxia in hamsters and observed the effects on vasomotion, by using an edge detection algorithm to track changes in the diameter of microvessels observed within a skinfold window preparation and applying the Fourier transform and autoregressive modelling to the resultant time series to find the dominant vasomotion frequency [80]. They found that hypoxia (8,11, and 15% O₂ gas mixture inspiration) increased the frequency of vasomotion and decreased mean diameters of vessels, whilst hyperoxia (100% O₂) reduced the frequency of vasomotion and also decreased mean diameters in the smallest vessels. Rucker *et al.* studied the response of the microvasculature in tissues to reduced perfusion, and found that these conditions induced vasomotion in muscle capillaries but not in the periosteum, subcutis or the skin [81]. They concluded that this demonstrated a beneficial effect of vasomotion on the oxygenation of local tissues.

Theoretical modelling has shown that in well oxygenated tissue, vasomotion appears to have little effect on tissue oxygenation [82]. However, in tissue with hypoxic regions, blood flow oscillations with high amplitude and low frequency (0.025–0.05 Hz) significantly reduced tissue hypoxia [82], but importantly only when myoglobin was not present, though myoglobin is usually not present under physiological conditions. This verifies what was previously modelled by Tsai & In-

taglietta, that low frequency oscillations are beneficial for local tissue oxygenation [83]. This supports vasomotion as an induced response to tissue hypoxia. Using combined LDF and optical reflectance spectroscopy (ORS), Thorn *et al.* revealed an association between vasomotion at low frequencies associated with endothelium and oxygen extraction; this does not, however, imply causality [84].

The extensive study of blood flow dynamics has led to universally accepted frequency bands of oscillatory activity in blood flow, as discussed in detail below. However, the dynamics of resting blood oxygenation are not so well characterised, but oscillations in oxygenation at rest have recently been demonstrated in skeletal muscle [85]. Skin blood oxygenation can be studied using optical techniques based on the absorption spectra of oxy- and deoxygenated haemoglobin, in methods such as near infrared spectroscopy (NIRS) and optical reflectance spectroscopy (ORS). Skin blood oxygenation reflects the activity of the underlying tissue, which is likely to result in relatively slow changes due to finite diffusion times. ORS has been used to non-invasively study skin oxygenation at rest, and provides a measure of mean blood oxygen saturation, $S_{T}O_2$, at a recording depth dependent on the spacing of the probe fibres. By recording LDF and ORS simultaneously, Bernjak *et al.* demonstrated significant phase coherence at frequencies below around 0.1 Hz between oscillations in blood flow and blood oxygen saturation in the skin microcirculation recorded at the same skin site [86], which may indicate causal connections between them. It was found that the value of oxygen saturation alone cannot be accepted as a definitive marker of tissue oxygenation, as two different types of oxygenation ‘swings’ were observed, which were indistinguishable in terms of $S_{T}O_2$, but different in terms of oxygenated haemoglobin (HbO_2) and deoxygenated haemoglobin (Hb) behaviours [87]. HbO_2 and Hb can be calculated from $S_{T}O_2$ and relative haemoglobin (rHb) using the relation $S_{T}O_2 = HbO_2 \times 100 / (HbO_2 + Hb)$ [84], where $rHb = HbO_2 + Hb$. Recently, a study in which blood flow and blood oxygenation were measured simultaneously showed that the relationship between microvascular blood flow and $S_{T}O_2$ at rest and during var-

ious physiological perturbations, including breath-holds, can be described by a one-phase association curve fit with a plateau in $S_{T}O_2$ of 84% for blood flow (BF) > 50 perfusion units (PU) [88]. This study also showed strong evidence for multiple, synchronized, time-varying oscillations in both microvascular BF and tissue oxygenation in healthy skin [88], but that although they appear to be modulated by similar processes, this is not simultaneous.

In summary, vasomotion is a highly variable phenomenon, affected by many different parameters, including blood flow, blood pressure, tissue oxygenation, endothelial secretions, local and systemic innervation, temperature and health. It has been widely observed in many settings, and physiological advantages are emerging. It is therefore of great importance to be able to observe and characterise vasomotion *in vivo* in humans.

2.3 Evaluation of microvascular function

2.3.1 Skin microvascular blood flow

The most widely used technique for the assessment of skin microvascular blood flow is laser Doppler flowmetry (LDF), also known as laser Doppler fluxmetry. Based on the Doppler effect, LDF uses laser light to measure the velocity of red blood cells, identified by how much the frequency of the incident light is shifted. LDF was used to measure blood flow *in vivo* in the undisturbed microcirculation for the first time in human skin by Stern *et al.* [89, 90], following its use in the rabbit retinal artery [91]. The resulting signal, the blood flow, flux or perfusion, represents not only the velocity of the red blood cells, but also their concentration. This technology was further expanded in the technique of laser Doppler perfusion imaging (LDPI) [92], based on the same principles but scanning a larger area of interest rather than a single point as in LDF, which can measure only a volume of 1 mm^3 or less, depending on the incident wavelength [93]. LDPI decreases spatial variability, but the scanning involved means that it cannot match the temporal resolution

of LDF. Used interchangeably, depending on requirements, these advances paved the way for a whole new field of noninvasive investigation of blood flow in the microcirculation in health and disease, which has been shown to vary widely in different pathologies.

The ability to directly measure the blood flow in the microcirculation using LDF has been exploited in many investigations which seek to assess microvascular function [94]. The most basic tests involve the calculation of mean blood perfusion, and comparison between different states of health and disease. However, it has been shown that basal flux values are highly variable and depend on many factors, including recording site and skin temperature [93]. Even when taking these factors into account, microvascular blood flow is constantly fluctuating in a non-constant way, as will be discussed below, and thus average flow values do not provide an accurate representation of the underlying dynamics.

In an attempt to improve the reliability of results, many studies have used LDF to evaluate the reactivity of the skin microcirculation by quantifying its response to well characterised provocations, for example during postocclusive reactive hyperemia (PORH). PORH involves a period of arterial occlusion by a cuff. This cuff is then released following a specified amount of time, and the resulting initial peak followed by sustained hyperemia in skin blood flux measured with LDF. Various parameters are measured, including maximum flux and time to resting flux, the latter of which was shown to have the best discriminative power in distinguishing between patients with peripheral arterial obstructive disease and healthy controls [95]. PORH has also been used to demonstrate microvascular dysfunction in many other pathologies, including diabetes [96], hypertension [97] and chronic renal failure [98]. The popularity of PORH arises from its apparent high reproducibility when considering absolute values [99]. Four major factors have been proposed to be involved in the PORH response: metabolic vasodilators, endothelial vasodilators, the myogenic response and sensory nerves [93], highlighting the complexity of this response. Thus care should be taken when attributing this to a single

mechanism, particularly endothelial function. The assessment of the behaviour of the endothelium is often the end goal of these studies, as it is known to regulate vascular smooth muscle tone, for example by the release of nitric oxide (NO). Regardless of the reason for the response observed in PORH, it is useful for the assessment of the efficacy of pharmacological interventions, such as the treatment of hypertension [10].

PORH is often performed along with iontophoresis and thermal hyperemia. All three provocations provide a characteristic flux response, but they do so by different physiological mechanisms. Iontophoresis involves drug delivery across the skin by using a local electric current. Two drugs commonly used in the assessment of the microcirculation with iontophoresis are acetylcholine (ACh) and sodium nitroprusside (SNP). ACh indirectly induces smooth muscle relaxation, and therefore vasodilation, via the stimulation of the release of NO, vasoactive prostanoids and endothelium derived hyperpolarizing factor from the vascular endothelium [100]. Importantly, ACh will only have a vasodilatory effect in the presence of endothelial cells, as discussed previously [41]. In contrast, SNP is a nitrovasodilator, acting directly on the smooth muscle cells [101], and therefore does not rely on the presence of endothelium to induce vasodilation. These different mechanisms allow the evaluation of endothelial function by comparing ACh and SNP induced vasodilation during iontophoresis [102], as measured by changes in blood flow using LDF. However, it has been shown that the current used during iontophoresis may induce increased blood flow even in the absence of drugs [103], for example when using water [104] or NaCl solution [105] as electrolytes. This highlights the importance of the careful planning of iontophoresis protocol for the purposes of endothelial assessment, to minimise these effects. To investigate the effects of voltage on skin blood flow, Bandrivskyy *et al.* studied the varying voltages required during iontophoresis to maintain a constant current, and found no correlation between voltage and changes in blood flow with any of the electrolytes used (deionised H₂O, NaCl solution, ACh and SNP) [103].

Thermal hyperemia involves local heating of the skin and measurement of the subsequent increase in cutaneous blood flow, with the maximum dilation of the vessels reached at around 42°C in healthy humans [106]. Again, the reproducibility of thermal hyperemia depends on the parameter studied [107], but when used correctly provides a simple method for the examination of microvascular and endothelial function [108].

Whilst these provocation techniques for the evaluation of skin microvascular function are well established and widely used, the exact mechanisms by which they alter skin blood flow are still debated, and are known to vary between recording locations. This leads to uncertainty in exactly which processes are being induced, and to what extent each one is affecting the vasculature, especially in completely noninvasive studies. Therefore, whilst they remain useful in studies of systemic conditions and pharmacological testing, where a global difference is assessed, they are not completely reliable in separating specific underlying mechanisms of microvascular regulation, including endothelial function. The perturbations also remove any information about the resting state dynamics of the underlying area, and thus the effects of spontaneous vasomotion.

2.3.2 Blood flow dynamics for the evaluation of skin microvascular function

Although LDF studies initially only considered average perfusion values or responses to various stimuli, it was soon discovered that LDF signals contained much more information than originally thought. Longer recordings led to conclusions that data recorded with LDF is highly variable and not reproducible. In fact, the opposite is true, once these variations are treated in the correct way. In healthy skin, sustained oscillations have consistently been observed in blood flow signals arising from the microcirculation as recorded by LDF [109, 110, 2]. In light of this fact, studies were performed in which the Fourier transform was used to extract information about the frequency of these oscillations, but this ap-

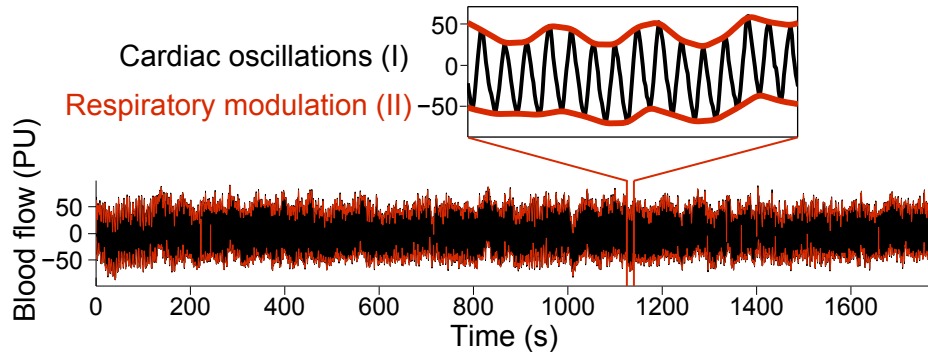


Figure 2.2: Typical blood flow signal obtained with laser Doppler flowmetry, with cardiac oscillations and respiratory modulation shown. PU = perfusion units (arbitrary).

proach is not suitable for such time-varying data. The breakthrough came when Stefanovska *et al.* applied the *wavelet transform* (see Chapter 4.2.3) to LDF signals [110], allowing the accurate simultaneous observation in time and frequency of these biological oscillations and their continuously varying characteristics. This approach is also ideal for the observation of low frequency oscillations, due to the logarithmic scale of the wavelet transform. This led to many studies which sought to further characterise the oscillations present in skin blood flow, and their physiological origins.

Whilst it is obvious that the beating of the heart has a huge influence on the blood flow, particularly in larger vessels, the dynamics of blood flow is also governed by many other physiological processes. A crucial influence, independent of the systemic heart and respiratory influences, is the local phenomenon of vasomotion. In addition to the intrinsic movement of the vessels, and the effects of the vascular endothelium as detailed in section 2.2.2, the amplitude and frequency of vasomotion is also influenced by neurogenic factors. A typical LDF blood flow signal is shown in Figure 2.2.

Extensive spectral analysis of signals obtained using LDF has provided a deeper understanding of the oscillations found in these signals, and their physiological origins. To date, six distinct frequency intervals have been identified, containing different oscillatory processes corresponding to various functions within the body [68, 111, 112, 113]:

Interval I – Cardiac interval (0.6–2 Hz). A dominant oscillation around 1 Hz can be detected at all points on the body, and can reliably be attributed to cardiac function by comparisons with a simultaneously recorded ECG. Depending on the proximity of the LDF probe to large vessels in addition to the capillaries, the effective contribution of the heart will vary. It is therefore recommended to avoid LDF measurements in the proximity of these large vessels, to allow observation of the dynamics at lower frequencies, which generally have lower power contributions.

Interval II – Respiration interval (0.145–0.6 Hz). A slower oscillation around 0.3 Hz has also been observed, and was shown to originate from respiration by Bollinger *et al.* in 1993 [114, 115]. The contribution of the respiration to LDF signals is not as strong as in the cardiac oscillations, and is not always detectable.

Interval III – Myogenic interval (0.052–0.145 Hz). This interval contains oscillations resulting from intrinsic myogenic activity of vascular smooth muscle cells, as previously discussed in the context of vasomotion. This means that oscillations in this frequency are inherent to the vessel wall, and have been observed both *in vivo* and *in vitro* [67]. Proof of this classification was shown when oscillations in the region of 0.11 Hz were unchanged during local and ganglionic nerve blockade [116]. The myogenic response is the passive local regulation of blood flow by the smooth muscle cells, in reaction to increased blood pressure [73]. One debated topic in this area currently is the observation and characterization of waves around 0.1 Hz which are deemed to be of a different origin to the myogenic response, sometimes known as Mayer waves, and observed in arterial pressure signals. Although these waves are usually enhanced during states of sympathetic activation, an underlying mechanism has still not been identified [117]. The origin of oscillations at this frequency is still uncertain, and is likely to consist of a combination of different physiological processes depending on vessel type.

Interval IV – Neurogenic interval (0.021–0.052 Hz). This is where neurogenic (sympathetic) activity manifests. The involvement of the sympathetic nervous system (SNS) in this interval was proven by Söderström *et al.* using LDF recordings

on skin flaps in which it is known that there is no sympathetic activity, as compared to LDF recordings on intact skin [73]. Differences were observed between 0.02-0.05 Hz, and thus these can be attributed to sympathetic nerve activity. This activity provides another fundamental mechanism for the control of blood flow by rhythmically discharging and influencing the relaxation and contraction of the blood vessels [73], as described by Malpas [118]. Landsverk *et al.* provided further evidence for the origin of the oscillations in this interval when evaluating the effects of brachial plexus block on the skin microcirculation [119], which is known to induce sympathetic impairment [120]. Using LDF and the wavelet transform they found that the relative amplitude of the oscillations within the 0.0095 to 0.021 and 0.021 to 0.052 Hz range was reduced, indicating an inhibitory effect on both endothelial and sympathetic activity. The sympathetic origin of oscillations in this interval was also demonstrated in rats by Bajrovic *et al.* when the relative energy of blood flow significantly decreased in the neurogenic interval (4 times higher frequency in rats) following partial denervation of the hind limb [121].

Intervals V & VI – Oscillations arising from endothelial activity. This has been tested using various vasoactive substances, in the presence of endothelial cells, and following their removal [122, 67]. Interval V, from 0.0095 to 0.021 Hz, was first found to contain oscillations due to endothelial activity through the use of the endothelial dependent vasodilator acetylcholine (ACh) and the endothelial independent vasodilator sodium nitroprusside (SNP) [123]. This endothelial activity was found to be partly mediated by nitric oxide (NO) [102]. In a later study, even lower frequency oscillations in the frequency interval 0.005 to 0.0095 Hz were observed [68], forming interval VI. In contrast to interval V, oscillations in this interval were found not to be NO dependent, arising instead from other endothelial mechanisms such as endothelium-derived hyperpolarizing factor (EDHF) [68]. To ensure that these conclusions based on iontophoresis arose as a result of endothelial activity and not as a result of current induced blood flow increases, Veber *et al.* performed iontophoresis using the same protocol as used by Kvandal *et al.*

[102] but replacing ACh and SNP with deionised water and NaCl solution [124]. They found that although in iontophoresis with deionised water (a low conductance electrolyte), cathodal current stimulates more than anodal current, this does not affect a specific frequency interval more than the others. They also showed no difference in blood flow when using iontophoresis with NaCl, a high conductance solution, and concluded that the differences observed previously using ACh and SNP, both highly conductive solutions, were indeed a result of endothelial activity [124].

The complexity of blood flow signals arises from the coupling between all of these physiological processes, and likely other additional effects. Locally, these manifest through the modulation of vasomotion by the contributions discussed above. The introduction of this coupled oscillator model of the cardiovascular system by Stefanovska & Bračič in 1999 [125, 2] meant that skin blood flow recordings could be used to extract information about underlying processes in states with altered microvascular regulation by calculating the contributions of the oscillations in each frequency interval, usually using time-frequency analysis methods such as the wavelet transform, and comparing between states and subjects. This approach has been shown to be reliable and reproducible [76]. The characterisation of blood flow dynamics at rest continues to be used to investigate the skin microvasculature in many studies, including in hypertension [10], congestive heart failure [113], ageing [112], obesity [9], athletes [126], diabetes [127] and critical limb ischemia [128]. The method has also been extended to the study of blood flow in cancer, which will be discussed in detail below.

2.3.3 Skin microvasculature as a model for the microvasculature

Studies of the skin microcirculation have been used in the assessment of skin microvascular dysfunction in many pathologies due to the noninvasive nature of the techniques and the ease with which signals can be recorded using LDF [129]. How-

ever, many of these studies seek to use the skin microvasculature as a model for generalized microvascular function, particularly in systemic diseases such as hypertension, diabetes and atherosclerotic coronary artery disease [130]. Although this approach is seen by some to require more investigation [131, 132], the rationale behind this assumption is that the circulatory system behaves as a single entity, with the dynamics observed in skin blood flow providing a tool for the investigation of both local and global mechanisms [133], and that the methodologies used to evoke an integrated vascular response represent physiology that is not unique to the cutaneous microvascular bed [130]. Therefore, the noninvasive evaluation of local skin microvascular function in cancer may provide insights into cancer microvasculature in general.

2.4 Microvascular blood flow in cancer

Cancer is a large group of diseases, characterized by unregulated cell growth. In normal, healthy cells, the balance between the creation of new cells by cell division and the natural death of cells, apoptosis, is tightly regulated. A cell can become cancerous when the genetic information that it contains is changed in some way, or mutated. Many cell mutations can occur, but it is those which cause accelerated or uncontrolled growth which are particularly dangerous. Most cells contain tumour suppressor genes, to prevent cell growth from becoming out of control, but mutations can cause the loss of this gene, and thus the apoptosis signalling pathway is disrupted, effectively resulting in immortal cells [134]. Carcinogenesis is not usually the result of just one mutation, but several [135]. Potentially cancerous cells are present in most humans, but the immune system usually recognises damaged cells and destroys them before they can proliferate. Problems arise when a cancer cell is allowed to divide. The cells then very efficiently evolve to adapt to their surroundings. Cancer cells express growth factors, for the purpose of creating ideal surroundings and establishing a blood supply, whilst remaining unaffected by any growth factor inhibition control directed toward them by the host. This

uncontrolled growth will result in a tumour which could potentially grow indefinitely, diverting the vital nutrients required by the body away from healthy cells and toward its own cells, stimulating further growth. Once a tumour has a blood supply, the possibility of the cancer spreading around the body, or metastasizing, greatly increases. During metastasis, cancer cells can settle anywhere in the body served by vasculature, and proliferate to form secondary tumours. Therefore, understanding of tumour vasculature and the flow dynamics of the blood supply is of critical importance in the fight against cancer.

2.4.1 Tumour angiogenesis

Once cancerous cells begin to proliferate, a point will eventually be reached when this tumour growth cannot be sustained without extra resources from the body. In order to obtain these resources, and also to effectively dispose of the high levels of waste products produced by the cells, a new blood supply to the tumour must be established. A tumour can grow up to 1-2 mm before it requires its own blood supply [136]; at sizes beyond this, diffusion is no longer adequate to satisfy the demands of the rapidly proliferating cells. At this critical point, the cancer cells will begin signalling to the body, requesting a greater volume of blood. The existing blood vessels will then sprout new branches toward the signals, at rates of up to 1mm per day [137]. This process is known as *angiogenesis*, and is separate to vasculogenesis, which is the formation of new vessels where there were originally none.

The origins of angiogenesis research were in the early 20th century. When observing the growth of blood vessels around tumours in 1939, Ide *et al.* were the first to suggest that tumours release specific factors for the purposes of stimulating the growth of blood vessels from observations of tumour tissue transplanted into the rabbit ear [138, 139]. Then, in 1945 Algire & Chalkley demonstrated that tumours actively attract new blood vessels [140]. In 1968, Greenblatt & Shubik showed that following tumour transplantation in the hamster cheek pouch stroma,

a vasoproliferative effect was observed even when the tumour was separated from the vessels by a barrier which blocked the passage of cells [141], confirming that there was indeed a diffusible substance which induced angiogenesis.

Judah Folkman, known by many as the father of angiogenesis research [142], proposed in 1971 that tumour growth is angiogenesis dependent, and that angiogenesis inhibitors could be used in the treatment of cancer [143], a theory which was initially not very well received. Also in 1971, in another paper, Folkman *et al.* isolated a growth factor responsible for tumour angiogenesis for the first time from human and animal neoplasms [144].

Since this pioneering work led to a huge interest in angiogenesis research, many angiogenic growth factors have been discovered, with vascular endothelial growth factor (VEGF) being of particular importance [145]. VEGF was first discovered in 1983 by Senger *et al.*, and was initially called vascular permeability factor [146], due to its observed effects on the permeability of the microvessels in guinea pigs, hamsters and mice. VEGF is expressed in most types of human cancer, with increased expression associated with a less favourable prognosis in various cancer types [147, 148]. In addition to VEGF, many other angiogenic growth factors have been observed, including: acidic fibroblast growth factor (aFGF), angiogenin, basic fibroblast growth factor (bFGF), heparinase, hepatocyte growth factor, interleukin-8, placental growth factor (PGF), platelet-derived endothelial cell growth factor, pleiotropin, prostaglandins E₁, E₂, transforming growth factor α (TGF α), transforming growth factor β (TGF β) and tumour necrosis factor α (TNF α) [149]. These growth factors then activate receptors in the endothelial cells of the surrounding vasculature. The endothelial cells in the parent capillary produce enzymes to break down the basement membrane (a thin sheet of fibres underlying the epithelium). The endothelial cells then escape from the original vessel, proliferate, and form sprouts, elongating the vascular tree, migrating through the extra-cellular matrix in the direction of the signals until the required blood supply is established [150]. This process is known as sprouting angiogenesis, and

was initially considered exclusively as the mechanism by which tumour vasculature is established. However, more recently other processes of neovascularization have been discovered in tumours [151]. Intussusceptive angiogenesis, in which preexisting vessels may split in two by the formation of transvascular tissue pillar into the lumen of the vessel, requires much less time and energy than the proliferation of endothelial cells. New vessel growth may also be aided by the recruitment of endothelial progenitor cells which circulate in the blood stream, but this occurs less in humans than in mouse models where they may contribute up to 100% of the vasculature [152].

Another interesting, and unexpected, observation arises in some cancer cases. Folkman *et al.* observed that while a primary tumour is thriving, it actually releases angiostatin into the circulation. Angiostatin is an angiogenesis inhibitor, being investigated for anticancer therapy. This angiostatin prevents metastatic tumours from forming whilst the primary tumour thrives. Unfortunately, if this tumour is removed, then so is the source of angiostatin, and metastatic tumours are much more likely to appear [153].

It has also been found that tumours may develop a secondary circulation system of vasculogenic structures lined not by endothelial cells, but tumour cells [151]. This ‘vasculogenic mimicry’ has been observed in melanoma, suggesting that aggressive melanoma cells may generate vascular channels devoid of endothelium, independently of angiogenesis [154].

Although angiogenesis is a major factor in the development of a tumour from dormant to malignant, it is not associated only with tumour growth. It also plays an important role in growth and the healing of wounds. Angiogenesis can also be used to treat cardiovascular disease, as well as many other conditions characterized by insufficient angiogenesis, including chronic wounds [155] and peripheral arterial disease [156].

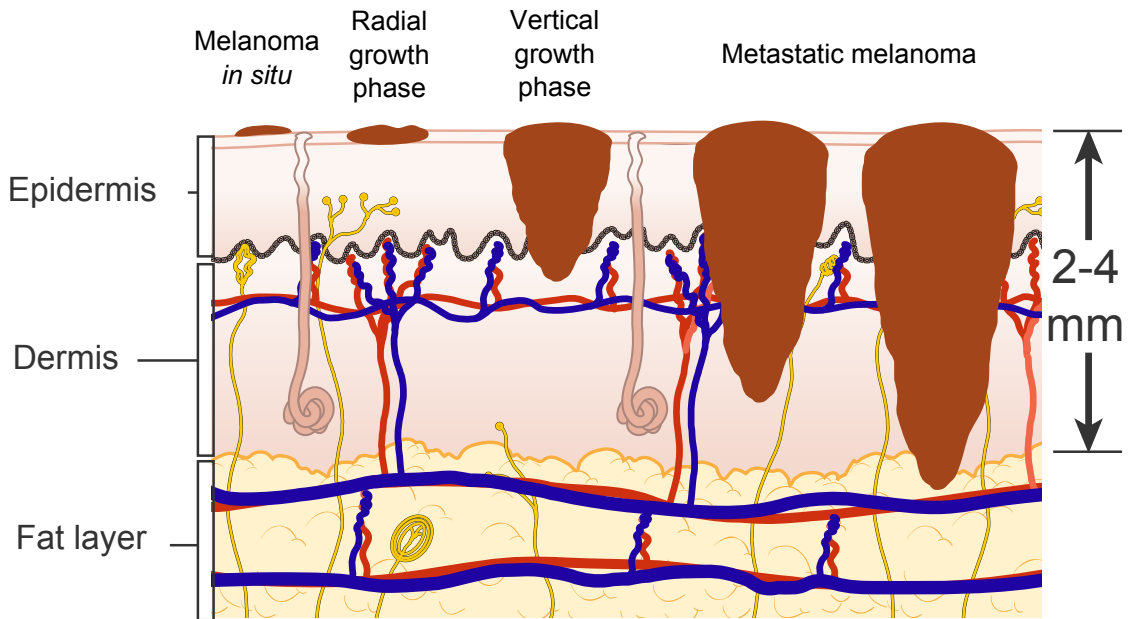


Figure 2.3: Diagram of the different stages of melanoma. Modified from [158]

2.4.2 Angiogenesis in melanoma

Human malignant melanoma, the most deadly skin cancer, is a highly metastatic tumour, with poor prognosis. Initially, melanoma *in situ* undergoes a radial growth phase. The onset of angiogenesis during this radial growth phase then leads to the development of the vertical growth phase, with tumour thickness and stage of invasion determining prognosis [157]. This then leads to metastatic melanoma (see Figure 2.3).

Angiogenesis in melanoma is initiated by growth factors including VEGF, bFGF, aFGF, platelet derived growth factor (PDGF), PGF and transforming growth factors α and β (TGF- α and β), and is essential for melanoma tumour growth and metastasis [159]. It has been shown that the secretion of VEGF by melanoma cells has been correlated to the transition from the radial to the vertical growth phase [160, 161].

Increased vascularity of cutaneous melanomas has previously been shown to be an important prognostic factor [162], but this has not been universally observed [163].

2.4.3 Blood flow in cancer

Blood flow in tumours has long been known to be spatially and temporally heterogeneous, for an early review see [164]. Overall perfusion rates vary widely depending on the recording location within the tumour, the size and stage of the tumour, and the tumour microenvironment.

Although the functional aim of angiogenesis is to increase tissue perfusion via the development of new vessels, the process is rarely efficient in tumours, i.e. increased microvascular proliferation does not necessarily mean an increase in blood flow, due to deregulated tumour angiogenesis. It was demonstrated in endometrial carcinomas that microvascular proliferation was negatively correlated with tumour blood flow, and also that low tumour blood flow is a poor prognostic factor [165].

Once angiogenesis has been initiated by a tumour, new vessels will be rapidly formed as a result of the release of the growth factors discussed previously. The imbalance between pro- and anti-angiogenic growth factors that allows this angiogenic switch results in immature, dysfunctional, dilated, tortuous vessels [166]. Whilst normal vessels possess a well organized architecture with dichotomous branching, tumour vessels are disorganized, with trifurcations and branches with uneven diameters [167]. Unlike normal vessels, there is no relationship between vessel size and red blood cell velocity in tumours [167].

The abnormalities, both in structure and function, of tumour vessels leads to heterogeneous, intermittent blood flow [168], and highly permeable vascular walls, due to fenestration of the endothelium [169], resulting in leaky vessels. These characteristics may vary across the tumour and even in the same location over time. Although smooth muscle cells do surround some tumour vessels, usually the local co-opted vessels rather than the newly formed ones [164], they do not function as normal contractile cells, thus directly affecting their blood flow regulatory mechanisms [136].

Physical pressure from the growing tumour also restricts blood flow [170], and is also the main reason for the lack of functional lymphatics within tumours [171],

as lymphatic vessels are not suited to such high pressures.

The endothelial cells which result from angiogenesis may be also distinctly different to normal endothelial cells, being disorganized, loosely connected, branched, overlapping and sprouting [172, 169], and with fundamental differences in terms of gene expression [173], all of which may limit their ability to act as vascular regulators, and therefore have an impact on blood flow.

The combination of inadequate vascular function and altered endothelial cells found in tumours will inevitably influence the dynamics of the blood flow in tumours due to changes in blood flow regulation, both intrinsic to the vessel wall and via endothelial mechanisms.

Various techniques have been used to study blood flow in tumours *in vivo*, including nuclear magnetic resonance imaging [168] and Doppler ultrasound [174]. Recently, laser Doppler techniques such as laser Doppler perfusion imaging (LDPI) and laser Doppler flowmetry (LDF), traditionally used to characterise microvascular function, have been applied to the study of blood flow in many cancer types, including, but not limited to, breast cancer [175], gastric adenocarcinomas [176] and colorectal cancer [177]. Kragh *et al.* demonstrated that angiogenic activity can be estimated *in vivo* using LDF and NIRS [178].

2.4.4 Noninvasive diagnosis of melanoma

Melanoma is currently diagnosed and treated depending on a number of factors, including its size, shape and level of metastasis (if any). An initial examination of melanoma seeks to evaluate the following characteristics [179]:

Asymmetry - Ordinary moles are usually symmetrical, whereas a melanoma will usually be irregular in shape.

Border - Moles also generally have a well defined border, in melanoma, this can be jagged and irregular.

Colour - A mole rarely has more than one shade of brown. A telltale sign of melanoma is the presence of different colours, such as brown mixed with black,

pink, red, white or blue.

Diameter – Normal moles are usually no bigger than 6mm, but a melanoma will usually be more than 7mm across.

Evolving – Most moles do not change over time, so if any changes in size, colour or shape are noticed, this could be an indication that the mole has developed into a melanoma.

The prognosis of melanoma depends on various factors, the main ones being the thickness of the tumour, and whether it is ulcerated (broken skin). The thickness of the tumour is measured on the Breslow scale [157], with a thickness greater than 4mm leading to a poor prognosis; ulceration also reduces chances of survival. Any lesion presented which meets one or more of the clinical features above is considered clinically atypical, and is usually further investigated by means of pattern analysis using a microscopy based technique known as dermoscopy [179]. Dermoscopy is a widely used, non-invasive method of further inspection of an atypical lesion, and has been shown to reduce the number of biopsies required [180] and improve diagnostic accuracy of skin malignant melanoma compared to inspection by the unaided eye [181], but this accuracy strongly depends upon the expertise of the examiner [182]. With the aid of dermoscopy, vascular structures can be observed in skin lesions. Despite the improved specificity provided by dermoscopy, many biopsies are still performed unnecessarily, causing discomfort and distress to patients. Therefore, non-invasive techniques for the diagnosis of skin melanoma remain an active area of research. Various techniques have been developed based on quantification of changes in colour, shape, size and blood flow; for a review see [183]. A high proportion of these are based on digital imaging and other imaging tools, including magnetic resonance imaging (MRI) and positron emission tomography (PET) scans, gene profiling, and laser based technologies.

In this thesis, it is the blood flow, as measured by laser Doppler flowmetry, that is investigated for the non-invasive characterisation and diagnosis of skin malignant melanoma.

2.4.5 Blood flow in skin cancer

The accessible nature of skin cancer in particular has led to many studies of blood flow using laser Doppler techniques in basal cell carcinoma [184, 185, 186, 187] and melanoma [184, 12, 188]. Compared to other methods [189, 183, 190], laser Doppler flowmetry is relatively cheap, simple to use, requires little training and is not subjective, in contrast to many imaging techniques. It is also superior to Doppler ultrasound, which does not register blood flow until tumours reach a thickness of around 0.8mm [191].

In 1992, Tur *et al.* demonstrated elevated average blood flow in basal cell carcinoma and melanoma when compared to non-cancerous skin lesions using LDF [192], providing a basis for its role in the characterization of tumour blood flow and diagnostic potential. Enejder *et al.* demonstrated how LDPI could be used to follow the perfusion of BCCs over time following treatment, showing a reduction in perfusion with healing [185].

The elevated blood flow observed in melanoma was correlated with vascularization [174], which has been shown to rise gradually during tumour progression [193].

Stücker *et al.*, due to concerns about the applicability of single point LDF in pigmented lesions, used LDPI to study blood flow in benign melanocytic naevi, malignant melanomas, and basal cell carcinomas, and found significantly higher flow values in melanocytic naevi than in basal cell carcinomas, and highlighted the role of inflammation in these results [184]. They also concluded that LDPI was not sensitive enough to distinguish between inflamed melanocytic naevi and malignant melanomas, based on average perfusion values. In a later study, Stucker *et al.* further elaborated on their findings in an attempt to evaluate LDPI average perfusion values for differential diagnosis of pigmented skin tumours [11]. They compared malignant melanomas to clinically suspicious dysplastic melanocytic naevi and basal cell carcinomas, again finding elevated blood flow in melanomas. Unfortunately, this method only provided a specificity of 48% when distinguishing

malignant melanoma from clinically suspicious naevi.

Whilst average blood perfusion values may provide some insight into the tumour blood flow, it is clear that single point LDF has a relatively low reproducibility when using average values alone, due to the inherent time-variability of the blood flow signal, as discussed above. PORH has been performed on basal cell carcinoma lesions and imaged using laser speckle contrast imaging (LSCI), but this method limits the recording site to locations on the body in which perfusion can be successfully occluded, namely the limbs [187].

As skin cancer may occur anywhere on the body, more robust results may be obtained by measuring perfusion in the lesion and in the contralateral site on healthy skin, to allow location specific effects to be taken into account. Analysis of these signals using techniques for the characterization of their intrinsic dynamics then allows an assessment of the underlying vasculature by investigating the frequency intervals known to correspond to vascular regulatory processes. Based on this approach, Häfner *et al.* directly addressed the question of how to distinguish between inflammation and tumour induced angiogenesis by applying wavelet analysis to LDF signals recorded from basal cell carcinomas and psoriasis [186]. Basal cell carcinomas were used as a model of tumour associated angiogenesis, whilst psoriasis was used as a model of inflammatory associated angiogenesis. They found that the blood flow dynamics observed in both cases were completely different, with reduced sympathetic activity observed in basal cell carcinomas but not in psoriasis, demonstrating that even though inflammation is present and average blood perfusion is increased, psoriasis maintains its vascular regulatory mechanisms, whilst BCC does not.

Häfner *et al.* [12] also combined laser Doppler flowmetry with wavelet analysis in order to quantify altered vasomotion in malignant melanoma and to facilitate diagnosis between benign and malignant melanocytic lesions *in vivo*. The conclusion was reached that melanoma blood vessels likely exist independently of autoregulatory processes by which they would usually be governed. They also found

arterial pulsation was a dominant feature in blood flow signals and that this causes more homogeneous blood flow and reduces the contributions of other blood flow oscillations. However, blood flow recordings in this study were for only 3.3 minutes, which according to previously defined criteria only allows oscillations to be reliably viewed down to a frequency of around 0.03 Hz. Indeed, the lowest considered frequency was 0.15 Hz, excluding part of the myogenic, and all of the neurogenic and endothelial related frequency intervals. It has been shown previously that characteristic oscillations in blood flow can be found at frequencies much lower than this, but these will not be visible in such a short recording time. This study also did not include dysplastic naevi as controls, so the very high sensitivity and specificity are likely to be reduced in less clear-cut cases of diagnosis. This provides an opportunity to further improve understanding of blood flow dynamics in melanoma by increasing the length of recording time and including atypical dysplastic naevi.

2.4.6 Renormalization of the vasculature

The vital role that angiogenesis plays in the development of cancer makes it an ideal target for anti-cancer drugs. Anti-angiogenic therapy is a highly active area in cancer research and treatment since it was introduced by Folkman [143, 194]. The aim is to halt tumour growth by preventing angiogenesis, thus starving the tumour of oxygen, whilst poisoning it with its own waste. The most successful approach is to target endothelial cells and inhibit their growth [195]. In comparison with cancer cells, the endothelial cells lining the vasculature are genetically more stable. This stability means that targeting endothelial cells with anti-angiogenic therapy will be more advantageous than targeting the cancer cells directly with chemotherapy, as endothelial cells are less likely to mutate, or acquire drug resistance [196]. As with most areas of cancer research however, there are conflicting theories. While the idea sounds promising, genetic abnormalities have been shown in endothelial cells, which means they could also acquire resistance, albeit probably not as quickly. This cancer of the endothelial cells, or haemangiosarcoma, is a very

common occurrence in dogs, rare in cats, and very rare in humans [197]. Another direction of anti-angiogenic therapy is interference with angiogenic factors such as VEGF and fibroblast growth factor (FGF) [195]. Despite promising results, the effects of anti-VEGF therapy in human solid tumours have not been as successful as expected [166].

Although lots of treatments focus on destroying the tumour vasculature, it has also been shown that normalization of the vasculature is sometimes possible and can increase treatment efficacy. The inability of the blood and lymphatic vasculature to work efficiently results in the widely observed characteristics of the tumour microenvironment, hypoxia and low pH [198]. Hypoxia will arise from the poor blood perfusion of the area resulting in limited oxygen delivery, while low pH will be induced by the build up of waste products of the increased metabolism of rapidly proliferating cells, further exacerbated by a metabolic switch to glycolysis. The presence of hypoxia reduces the efficacy of radiation treatment for tumours, as oxygen is a potent chemical radiosensitizer. Therefore, normalizing tumour vasculature, whilst perhaps seeming counterintuitive, has been investigated as a promising direction for the improved effectiveness of cancer treatment in hypoxic tumours by reinstating a functional blood supply and thus facilitating the delivery of therapeutic agents and normalizing the tumour microenvironment [199, 166]. This suggests that the ability to regulate blood flow in vessels formed during tumour angiogenesis may not be completely absent, but may be influenced or suppressed by microenvironmental factors.

2.5 Potential microenvironmental influences on microvascular blood flow

It is becoming more apparent to cancer researchers that only considering cancer cells outside of their microenvironment results in the loss of valuable information and may give rise to unrealistic models. Any cell or collection of cells *in situ* will be

continuously interacting with the surrounding cells and tissues. Failure to account for environmental interaction effects is likely the reason that 90% of drugs which exhibit preclinical activity are relative failures in human models [200]. It is now accepted by modern cancer biologists that cancer is not only an accumulation of genetic mutations leading to excessive proliferation, but is also heavily dependent on the growth environment [200].

2.5.1 Metabolic and microvascular responses to hypoxia

As discussed above, hypoxia is a major feature of solid tumours [201]. Hypoxia results from inadequate perfusion and contributes to cancer treatment resistance [202]. It also results in a phenotype which favours tumour progression [202, 203]. As a result, tumour hypoxia is a poor prognostic factor in many malignancies [135].

Severe hypoxia can result in a failure to generate enough energy to maintain cellular functions. If prolonged, hypoxia will result in cell death. Therefore, cells have many mechanisms in place to respond efficiently to hypoxia, and thus try to regulate cellular oxygen concentration within a narrow range [204]. The main response to hypoxia in cells is the expression of hypoxia-inducible factors such as HIF-1 α , first identified in 1992 by Semenza & Wang [205], which then play a role in cell proliferation, angiogenesis, metabolism and apoptosis [206]. Significant effects of hypoxia on the microcirculation have recently been demonstrated in rabbits [207], highlighting the need for further investigation into the dynamics of this response and the possible links to carcinogenesis.

The expression of hypoxia-inducible factors in response to hypoxia in tumours has been implicated in the widely observed metabolic switch to glycolysis in cancer cells [208] (see below). In hypoxic conditions, glycolysis will be the main source of adenosine triphosphate (ATP) within the cell, even though it is much less efficient than oxidative phosphorylation (OXPHOS), which requires oxygen in order to produce ATP. Local hypoxia may also induce angiogenesis in a tumour through VEGF-A expression [149, 39], in an attempt to increase blood perfusion, thus

altering the structure of the tumour microvasculature.

Hypoxia has been implicated as one of many possible causes of cancer [209, 210], with cancer cells taking advantage of some of the hypoxic responses, e.g. angiogenesis and cell proliferation, whilst suppressing others, e.g. apoptosis [206]. Although hypoxia can be crucial in the evolution and survival ability of tumours [211], through stimulation of angiogenesis, its role in carcinogenesis is not so clear, as some cancer cells appear to switch to glucose metabolism before exposure to hypoxic conditions [212].

The role of hypoxia in melanoma development

The primary microenvironment of melanoma, the skin, is unusual in that it is known to be hypoxic (1.5-5% O₂), at least in some areas. Although highly heterogeneous, it has been shown that while the dermis is well oxygenated, the epidermis is sometimes modestly hypoxic [213]. This hypoxia could be a consequence of the relatively large distance from superficial blood vessels, as oxygen will only travel a finite distance from capillaries to cells before it is completely metabolized, estimated to be around 180 μm [206]. Knowing the oxygenation status of the skin and other tissues allows us to reasonably assume that any experiments carried out on cancer cells above these levels, e.g. in atmospheric oxygen conditions, may not provide meaningful results. Indeed, it has been shown that cells grow better in mildly hypoxic environments than in atmospheric levels of O₂, with atmospheric conditions actually causing cellular ageing, and human melanocytes benefiting from growing in a more physiological environment [214]. Combining this knowledge with the tendency of tumours to be hypoxic allows us to begin to build up a picture of the early stages of melanoma. It appears that the skin provides an optimal microenvironment for melanoma progression, with ideal proliferation conditions and promotion of avoidance of apoptosis. Physiologically normal hypoxia, as present in the skin, is not cause for concern. HIF-1 activates many oxygen responsive genes involved in survival, apoptosis, glucose metabolism and angiogenesis [214]. These

functions are finely balanced in normal skin, but are disrupted during severe hypoxia ($<0.5\%$ O_2). This leads to the hypothesis that melanoma may be promoted by low oxygen conditions in the skin [215].

2.5.2 Cellular energy metabolism

Cellular energy metabolism encompasses many processes, ultimately resulting in the production of ATP, the fuel continuously used by cells for many essential functions, such as maintenance of ionic balance across their membranes, signalling and protein synthesis. Every day, we turnover the equivalent of our body weight in ATP [216]; thus our understanding of every stage of cellular energy metabolism is of crucial importance. A diagram of cellular energy metabolism can be seen in Figure 2.4. Novel imaging techniques have provided insights into the function of metabolic pathways, including methods based on pH changes [217, 218], measurements of nicotinamide adenine dinucleotide (NADH) levels in glycolysis [219], measurements of mitochondrial membrane potential [220], and direct measurements of ATP release [221]. These have led to the growing understanding that many diseases can be associated with metabolic dysfunction, including diabetes [222] and cancer [223, 210, 224, 225].

Two main pathways are involved in the production of ATP: glycolysis, and oxidative phosphorylation (OXPHOS). The balance between these energy pathways is tightly regulated through their mutual interactions, according to supply and demand [226, 1, 227]. Both processes are required for normal energy production within a cell; however in a healthy cell, OXPHOS dominates [212]. In contrast, in a dysfunctional cell, ATP production via glycolysis may increase and dominate even in the presence of oxygen [228]. This effect has been shown to be favoured in cancer cells [224], known as the Warburg effect [229, 212, 230].

ATP may be produced in two cellular locations. Glycolysis occurs in the cytoplasm of the cell, and the Krebs cycle and oxidative phosphorylation (OXPHOS) occur in the mitochondria, considered as the powerhouses of the cell. ATP is pro-

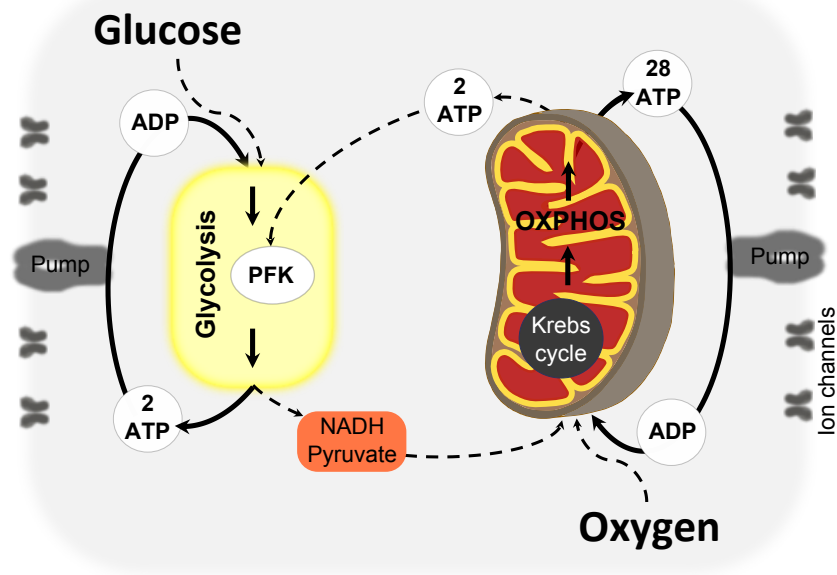


Figure 2.4: Diagram of cellular energy metabolism. ATP production in a cell (thick lines) occurs via glycolysis using glucose, and when oxygen is present ATP is produced via oxidative phosphorylation (OXPHOS) using the products of glycolysis. Both processes are oscillatory, and can influence each other. Couplings between these processes, as well as external influences are shown by dashed lines.

duced by each process in differing ratios depending on cell type and current energy requirements.

For example, in the absence of oxygen, or in cells with low energy requirements, such as endothelial and yeast cells, glycolysis may be the primary source of energy metabolism [231]. Glycolysis is much less efficient than OXPHOS, producing only 2 ATP molecules for each glucose molecule, compared to 38 ATP molecules resulting from the combined processes of glycolysis, the Krebs cycle and OXPHOS [206]. Therefore, for cells which consistently require larger amounts of energy and have functional mitochondria, e.g. cardiac myocytes, the latter pathway is used. In this case, 88% of the total cellular energy is produced via OXPHOS due to its efficiency, with the other 12% being produced equally from glycolysis and the Krebs cycle [224].

ATP synthesis occurs through complex interactions between metabolic processes. Glycolysis converts glucose to pyruvate, and produces ATP and NADH.

The pyruvate is used during pyruvate decarboxylation, the products of which are used in the Krebs cycle. This releases more ATP and leads to production of substrates which are used to create a hydrogen ion gradient across the inner mitochondrial membrane. This gradient then drives the production of ATP from ADP and inorganic phosphate, in the process of oxidative phosphorylation [225].

Evidently, energy metabolism via glycolysis and OXPHOS are complex processes, subject to many feedback mechanisms at different points in their respective cycles. This allows the cell continuously to meet energy demands even when subjected to external perturbations. In order to gauge their required rates, based on current production and requirements, the two processes must be coupled to maintain the correct balance between supply and demand.

Metabolic oscillations in health and diseases

Metabolic oscillations are dynamical processes dominated by two main components, mitochondrial and glycolytic oscillations. These oscillations can be observed using different techniques, some based on changes in glycolytic intermediates [219], and some based on observation of changes in mitochondrial membrane potential [232].

Oscillations attributed to glycolysis have long been observed in many types of cells, including yeast [233], pancreatic β cells [234, 235, 226] and muscle cells [1]. Glycolytic oscillations were first observed by Duysens & Ames in 1957 whilst studying the fluorescence of glycolytic intermediates in yeast [236]. The source of these oscillations was first proposed by Ghosh & Chance [237] as an enzymatic step catalyzed by phosphofructokinase (PFK) [7]. This is still debated, however. There is now lots of evidence to suggest that the reaction involving PFK is responsible for their origin [238, 226, 219], but not exclusively, as glycolytic oscillations in yeast have been found to have frequencies that are also dependent on glucose transport across the cell membrane [239]. Interestingly, the metabolic switch observed in cancer cells results in a metabolism which has been shown to have features

in common with yeast metabolism [228]. In addition to the observation of the existence of glycolytic oscillations, their presence has been shown to provide an advantage in maintaining a high ATP/ADP ratio [240].

Oscillations in the mitochondria have been observed since almost 50 years ago [241], and it was Chance & Yoshioka who demonstrated that they could be sustained over many cycles [242].

Mitochondrial oscillations can be considered in two separate cases. In the physiological, or healthy, domain, small amplitude oscillations can be observed in mitochondrial membrane potential $\Delta\psi_m$. These have been associated with cycles of oxidation [243, 241], and extramitochondrial factors, such as the plasma membrane potential $\Delta\psi$ or Ca^{2+} [226]. In cases of oxidative stress or substrate deprivation, the inner mitochondrial membrane potential may destabilise, causing depolarization and oscillation [220, 244], forcing synchronous oscillations within the mitochondrial network [232, 245, 220].

Independent of their cause, metabolic oscillations may manifest as ATP oscillations. ATP oscillations have been observed in the cytosol of human single islet β cells, which were shown to be affected by glucose concentration, with oscillations present at both low and high glucose concentrations, with those at high concentrations exhibiting an increase in their period of oscillation [246]. Kwon *et al.* observed ATP oscillations during chondrogenesis, which is the process by which cartilage is developed, which were found to depend on glycolysis and mitochondrial respiration, which in turn were revealed to depend on Ca^{2+} oscillations with an anti-phase relationship [6]. Measurements in yeast cells with oscillatory glycolysis revealed oscillations in ATP and also a slow decrease in ATP [247, 248]. It has also been demonstrated that oscillations in ATP concentration are tightly coupled to intracellular water dynamics, affecting the overall state of the cytoskeleton of the cell, coupling the chemistry and physics of the system [249].

Metabolic alterations in cancer

In the 1920s, Otto Warburg discovered that cancer cells display a metabolic switch to glycolysis, even in the presence of oxygen, a phenomenon now known as the Warburg effect [229]. From these observations, Warburg concluded that the respiration of all cancer cells is damaged; a conclusion which is still debated [230].

Two of many universal observations in cancer cells are: 1) their metabolism is altered, and 2) genetic mutations are present [250]. Which, if any, of these is responsible for carcinogenesis is still unknown, but increasing evidence suggests that mitochondrial dysfunction plays a key role [212, 251, 225]. Most other properties observed in cancer cells can be explained as consequences of this dysfunction [224].

The metabolism of a cancer cell has to meet the increased energy requirements of a constantly proliferating cell, whilst still maintaining the correct balance of ATP. Too little ATP and the cell will not have enough energy to function, whilst over-production of ATP will disrupt cellular processes [224]. The excess lactate secreted by cancer cells can be explained by upregulation of glycolysis, following increased glucose uptake. Decreased mitochondrial activity has also been observed in cancer cells [225]. This preference for glycolysis even in the presence of oxygen can be explained either by mitochondrial dysfunction, or a survival advantage provided by a switch to glycolysis [251]. Cellular energy metabolism within tumours is highly heterogenous, with both oxygenated and hypoxic regions [252], depending on the distance to the local blood supply.

It has been shown that tumour mitochondria are structurally and functionally abnormal, and incapable of meeting cellular energy requirements [224]. The mitochondrial proton gradient required for OXPHOS is disrupted, which may force the cell to rely on glycolysis for ATP production, even when oxygen is abundant. If healthy cells spend prolonged periods of time in this state, without repair of the mitochondria, it may lead to genetic instability and disorder within the cell [224]. This may cause mutations to arise, and facilitate the onset of carcinogenesis.

Within such complex metabolic processes, in normal and cancer cells, it is un-

feasible to assume stationarity of the balance between supply and demand; it is inevitably time-dependent. Indeed, it has been shown that oscillations are present in cellular metabolism. Understanding these oscillations and their interactions, and considering how they are altered during the metabolic transition to a glycolysis dependent state may prove extremely useful in the characterization of carcinogenesis.

Effects of altered energy metabolism on microvasculature

The global effects of the metabolic switch to glycolysis may directly affect the microvasculature, either through alterations in signalling (i.e. initiation of angiogenesis, as described above) or by changes to the tumour microenvironment.

During aerobic and/or anaerobic glycolysis and ATP hydrolysis, hydrogen ions are formed and are actively transported out of the cell, through the interstitial space, to the blood vessels, where they can be transported away from the site [253]. The altered metabolism in cancer cells, i.e. the high glycolytic rate, coupled with reduced drainage of waste products due to inadequate tumour vasculature leads to a build-up of H^+ ions which decreases the extracellular pH, i.e. the microenvironment becomes more acidic [198, 253, 254, 255].

In 1880, Gaskell demonstrated that acid solutions evoke vascular smooth muscle cell relaxation [256, 257]. Changes in pH modulate the responsiveness of the smooth muscle cells to vasoconstrictor stimuli [258]. It has since been shown that altered pH can promote changes in vascular smooth muscle tone, with low pH values inducing vessel dilation [257]. A reversible abolition of vasomotion has also been demonstrated outside of a very narrow pH range in hamster cheek pouch arterioles [69], providing evidence of the importance of microenvironmental stability for effective vascular regulation. Acidic extracellular pH in melanoma was shown to promote angiogenesis [255].

The reactivity of the blood vessels within a tumour may depend on their origin. Those which already existed in the host but have been co-opted by the tumour

[151] may still retain their ability to regulate blood flow in the right conditions, whilst vessels arising from tumour induced angiogenesis may never be capable of such responses due to their inadequate structure [259]. Therefore, the exploitation of potentially functional and mature blood vessels in tumours by introducing vasodilators is an active area of research [259], highlighting the necessity of vascular regulation.

2.6 Summary

Oscillations in microvascular blood flow can be quantified in health and disease, providing a tool for the investigation of pathologies in which vascular regulation is altered. One such pathology is cancer, which is likely to demonstrate altered blood flow dynamics due to many simultaneous factors: the development of new, yet dysfunctional, vessels via angiogenesis, alterations in cellular energy metabolism to become more robust to limited nutrient availability, and the subsequent effects of these factors on the tumour microenvironment resulting in reduced vessel reactivity and inadequate tissue perfusion due to hostile conditions.

3. Physiological measurement

The observation and measurement of spontaneous dynamics within living systems is becoming increasingly feasible with the introduction of new measurement techniques based on various physical principles from optical to electrical effects. This chapter describes the techniques used for the acquisition of the data presented in this thesis.

3.1 Systemic processes

3.1.1 Electrocardiogram

The heart is one of the most important oscillators in the human body. The electrical activity of the heart can be non-invasively monitored in time using an electrocardiogram (ECG). An ECG tracks the electrical changes in the heart during a heartbeat. The average resting heart rate is between 60 and 90 beats per minute (BPM), with a resting heart rate outside of these boundaries indicative of an underlying medical condition. In athletes, the resting heart rate is generally lower, due to an increased stroke volume, which is the volume of blood pumped out of the heart with each beat. As cardiac output is the product of heart rate and stroke volume, an increase in the latter allows the required resting cardiac output to be maintained with a lower heart rate. In addition to monitoring changes in heart rate, the specific waveform observed during one cardiac cycle may provide valuable information on the health of the heart. A typical heartbeat ECG is shown in Figure 3.1. The small upward P wave indicates atrial depolarization, with the

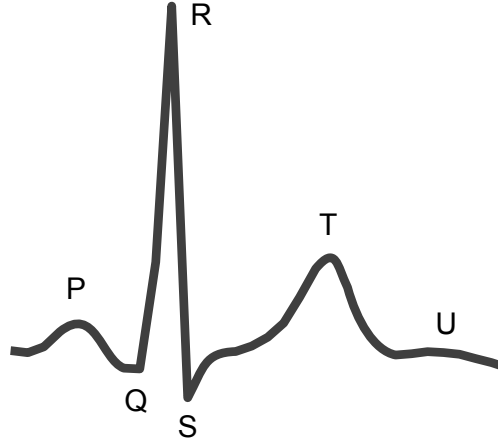


Figure 3.1: Typical one-cycle ECG trace

initial part representing right atrial depolarization and the terminal portion the left atrial depolarization. A fraction of a second after the P wave begins, the atria contract. The Q wave is a downward deflection after the P wave and represents septal depolarization. The R wave is usually the easiest wave to identify, and can thus be used to calculate heart rate, and heart rate variability. It represents early ventricular polarization. The S wave represents the late ventricular depolarization. The T wave represents repolarization of the ventricles [260]. All these waves can differ in shape, and in some cases be absent, and are used in the early detection and diagnosis of heart conditions.

3.1.2 Heart rate variability

Heart rate variability (HRV) can be calculated directly from an ECG signal by marking the locations of the R-peaks, and considering the distance between them as a complete period of oscillation with phase between 0 and 2π . The instantaneous frequency is then the reciprocal of the time period between each pair of R-peaks. R-peaks are chosen because they are the most prominent component of the heart beat, and are present in every cycle. A disadvantage of this method is that the resolution depends on the period of oscillation, i.e. no instantaneous frequency or phase information is available between events. As the sampling frequency of the HRV obtained from this method will vary depending on the period, linear interpolation

must be performed on the signal. To retain the same resolution as the original time series, the instantaneous frequency can also be extracted from the wavelet transform of the ECG signal using ridge extraction methods, as in nonlinear mode decomposition (NMD) [261]. HRV can be investigated by studying the obtained signal using methods which will characterise the temporal fluctuations, for example the continuous wavelet transform.

Heart rate varies naturally within a breathing cycle; it will slightly increase during inspiration and slightly decrease during expiration. This variation is known as respiratory sinus arrhythmia (RSA) [262]. The presence of RSA indicates efficient feedback mechanisms in the heart, it is evidence of the heart constantly responding to the needs of the body. Whilst the heart rate can be an indicator of general health, with a low resting heart rate generally associated with a high level of physical fitness, e.g. in athletes, and a prolonged high resting heart rate, or tachycardia (>100 bpm) a possible indicator of cardiac problems, it is the variability of the heart rate which provides us with the most information. For example it has been shown that heart rate variability decreases with age [112].

Heart rate variability is widely considered as a measure of the performance of the autonomic nervous system. Lower HRV has been implicated in many physiological conditions, such as congestive heart failure, diabetic neuropathy, susceptibility to sudden death, atherosclerosis and hypertension. It has also been shown to be a predictor of mortality after myocardial infarction [263]. Decreased HRV has also been found in major depressive disorder and coronary heart disease, both of which are hypothesized to be linked to vagal function [264].

3.1.3 Respiration

Respiration can be measured either mechanically, i.e. direct measurement of chest displacement, or via analysis of expired carbon dioxide levels. Respiratory rate can be calculated using the marked events method explained above. Using respiration and heart rate signals it is possible to investigate cardiorespiratory coupling [265].

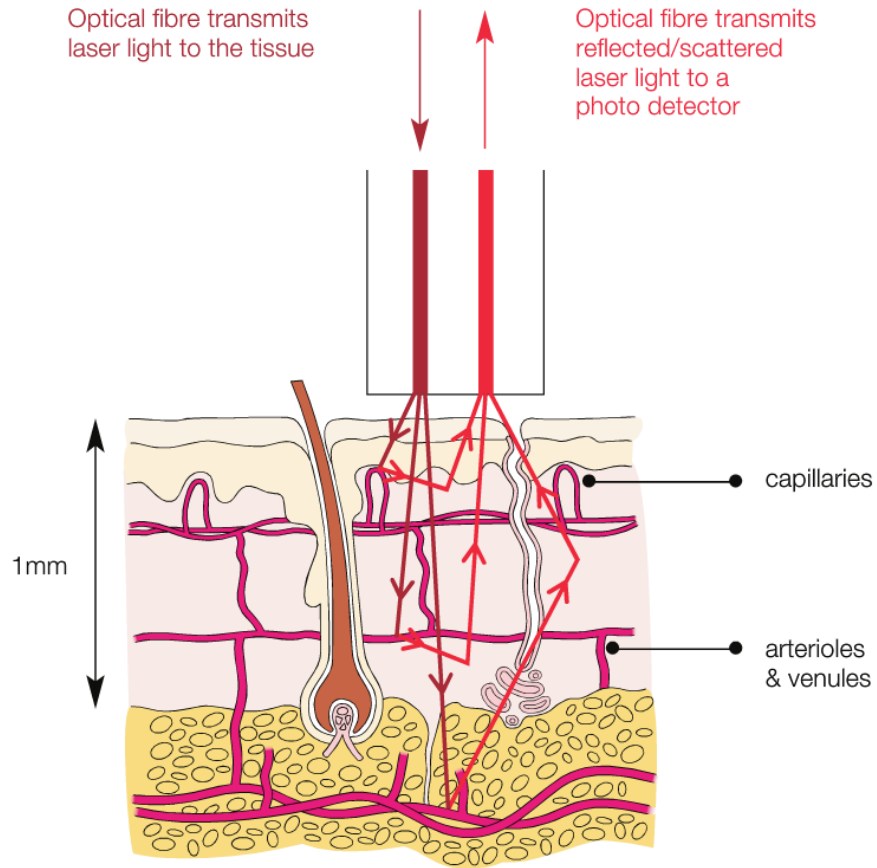


Figure 3.2: Diagram demonstrating the principles and recording area of laser Doppler flowmetry. From [266]

3.2 Blood flow

3.2.1 Laser Doppler flowmetry

Laser Doppler flowmetry (LDF), exploits the Doppler effect to calculate blood flow (or flux) in laser illuminated microvessels (see Figure 3.2). The photons from a beam of light directed into the tissue will be scattered by both static and moving particles. The moving red blood cells impart a Doppler shift to the photon, depending on the scattering angle, the wavelength, and the velocity vector of the cell [267]. If a wave with frequency ω is scattered from a moving particle with velocity \mathbf{v} , the Doppler shift is

$$\Delta\omega = |\mathbf{v}| |\mathbf{k}_i - \mathbf{k}_s| \cos \beta, \quad (3.1)$$

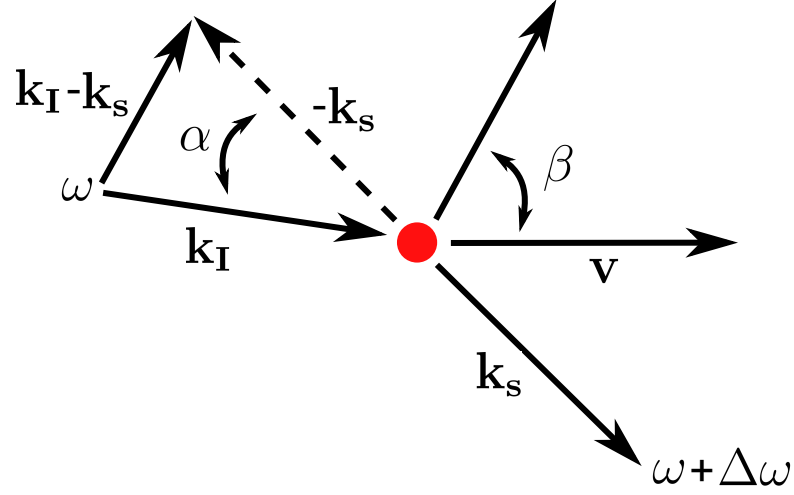


Figure 3.3: Scattering of a photon with a wave vector \mathbf{k}_I by a moving red blood cell with velocity \mathbf{v} .

where \mathbf{k}_I is the incident wave vector, \mathbf{k}_S is the wave vector of the scattered wave, and β is the angle between the velocity vector and the scattering vector, defined as $\mathbf{k}_I - \mathbf{k}_S$ (see Figure 3.3). If α is the scattering angle, and λ the wavelength of the light, the Doppler shift can then be written as [267]

$$\Delta\omega = 2(2\pi/\lambda)|v| \sin(\alpha/2) \cos \beta. \quad (3.2)$$

The large number of vessels and moving particles in the microcirculation means that the photons will inevitably undergo multiple Doppler shifts, giving a range of shifts even if all particles have the same speed [267]. The Doppler shifted light will interfere with non-Doppler shifted light on the photodetector, generating a dynamic speckle pattern, causing the current signal of the detector to fluctuate. The power spectrum of these fluctuations then provides information about the flux and concentration of the red blood cells [267], as the first moment of order, or mean frequency, of the power spectrum is linearly proportional to these values. These methods do not provide absolute velocity values, therefore blood flow, or flux, is measured in perfusion units (PU). The perfusion signal is the average concentration multiplied by the average root mean squared velocity of moving red blood cells.

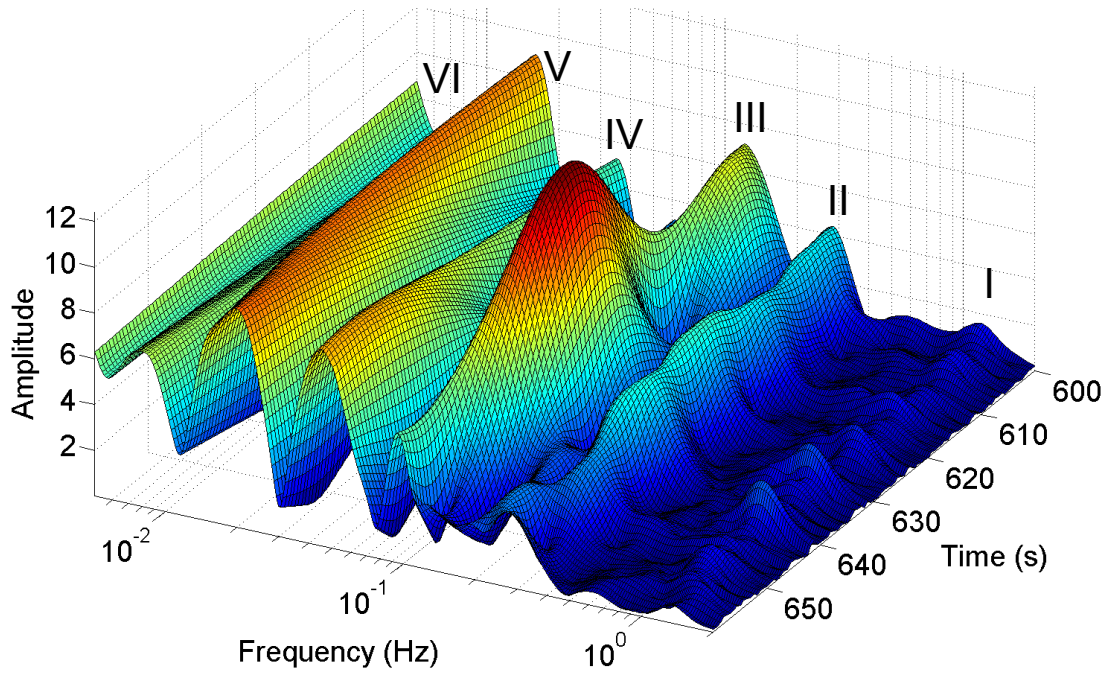


Figure 3.4: Example wavelet transform of a laser Doppler flowmetry blood flow signal, demonstrating peaks in the six frequency intervals described in Section 2.3.2.

A LDF probe contains an optical fibre, through which laser light propagates, with an emitter and detector, spaced according to the depth of light penetration required. This technique has been used extensively to study the microcirculation, providing essential insights into the oscillations present in blood flow. Of particular importance was the discovery of six characteristic peaks in the frequency spectrum of LDF signals [68] (see Figure 3.4). These peaks have been reliably attributed to various physiological oscillatory processes as described in Section 2.3.2.

The advantage of LDF is its non-invasiveness, and its ability to measure the microcirculatory blood flow in real time, with a high sampling frequency. A disadvantage is that it provides only a single point measurement, and therefore no spatial information from the surrounding tissue.

3.2.2 Laser Doppler perfusion imaging

Laser Doppler perfusion imaging (LDPI) is based on the same principles as LDF, but scans many points to create a blood flow image rather than the single point information provided by LDF. LDPI is ideal for the spatial imaging of blood flow

at the same depth afforded by LDF, but the scanning time results in relatively poor temporal resolution.

3.2.3 Laser speckle contrast imaging

When illuminating a diffuse object, laser light will produce a random interference effect known as a speckle pattern. If the illuminated object moves, or consists of moving parts, the speckles over the moving area(s) will fluctuate in intensity in a manner related to the velocity of the movement. This velocity information can be extracted by imaging the speckle pattern and calculating the local speckle contrast, a measure of the blurring caused by intensity fluctuations [268].

Since the discovery of lasers, speckle patterns caused by random interference have resulted in much research into methods to reduce their effects. More recently, this phenomena has been studied in its own right, and has been found to be applicable to many different areas of science. One area in which it has proven particularly useful is in biomedical imaging of blood flow [268, 269]. Laser speckle contrast imaging (LSCI) provides superior temporal resolution to LDPI, but cannot penetrate as far into the tissue.

LSCI is based on the fact that movement in an area on which a speckle pattern is projected will cause blurring upon image capture, to an extent which depends on the velocity of the movement and the exposure time of the camera [270]. High velocities will cause the most blurring, and areas in which there is no movement will retain a static speckle pattern. This blurring is quantified as speckle contrast, K ,

$$K = \frac{\sigma}{\langle I \rangle}, \quad (3.3)$$

where σ and $\langle I \rangle$ are the standard deviation and mean, respectively, of the intensity of a grid of pixels from the image. This value can be calculated spatially or temporally, depending upon the application. A window (typically 5×5 or 7×7 pixels) is moved across the imaged speckle pattern, and its central value set to the speckle contrast value for the window. Low speckle contrast values correspond to

high blood perfusion values.

To represent these speckle contrast values in terms of flux values, Brownian motion with a Lorentzian power spectrum of the velocity distribution can be assumed, leading to [271]

$$K = \frac{\sigma}{\langle I \rangle} = \left\{ \frac{\tau_c}{2T} \left[1 - \exp\left(\frac{-2T}{\tau_c}\right) \right] \right\}^{1/2}, \quad (3.4)$$

where τ_c is correlation time (time taken for the autocorrelation to fall to a pre-determined low level), and T is camera integration time. In theory, the speckle contrast, K , should vary between 0 (high perfusion) and 1 (very low perfusion), but in practice it never exceeds 0.5. This allows the simplification of the previous equation to [271]

$$K = \frac{\sigma}{\langle I \rangle} = \left(\frac{\tau_c}{2T} \right)^{1/2}. \quad (3.5)$$

If we assume that perfusion is proportional to the mean velocity of scatterers then perfusion is inversely proportional to the correlation time. Applying this assumption gives blood flow in terms of speckle contrast (for fixed exposure time) [271]:

$$\text{Flux} \propto \left(\frac{\langle I \rangle}{\sigma} \right)^2. \quad (3.6)$$

LSCI systems are commercially available, but a system can be built at a much lower cost [272]. A system was developed within the Department of Physics at Lancaster University using a Raspberry Pi with an infrared camera and an IR laser diode, with processing performed in MatLab. A raw image and the corresponding laser speckle image from this system can be seen in Figure 3.5.

3.3 Blood oxygenation

The colour difference between oxygenated and de-oxygenated blood can be exploited via their differing absorption spectra to observe relative changes in blood oxygenation and volume. Blood oxygenation measurements will vary depending on whether they are measured in an artery or vein. Pulse oximetry measures the

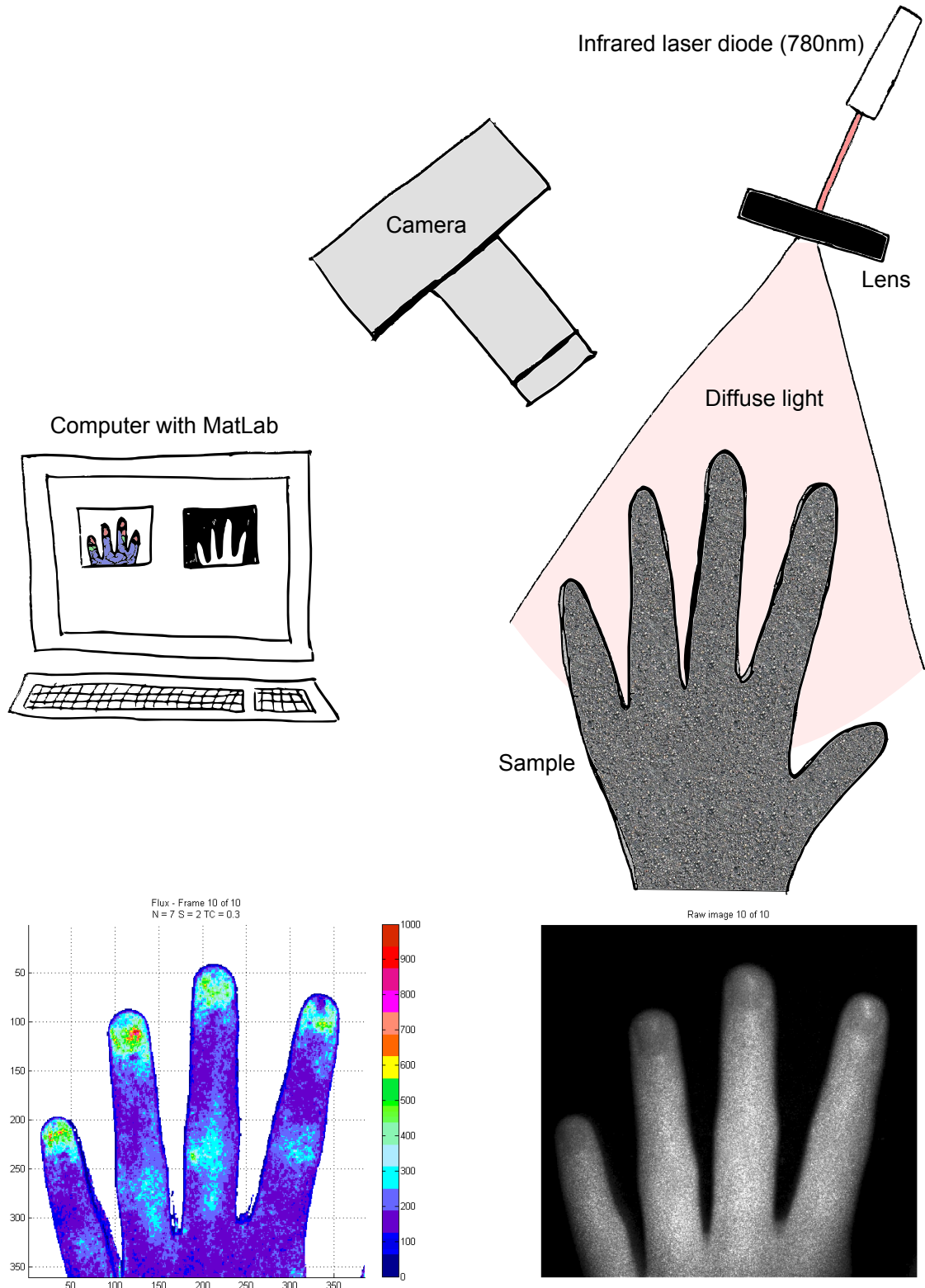


Figure 3.5: Top – diagram of the laser speckle imaging setup. Images were obtained using a Thorlabs DCC1545M camera and a 780nm infrared laser diode. Image processing was performed in MatLab. Bottom – Flux image map of the fingers of the left hand, obtained using an analysis window of 7×7 pixels (left), and the raw image with visible speckles (right). Regions of high perfusion are shown in red, whilst regions of low perfusion are dark blue.

	Spatial resolution	Temporal resolution	Recording depth	Clinical use
Laser Doppler flowmetry (LDF)	Poor	Excellent	Good	Microvascular assessment [273]
Laser Doppler perfusion imaging (LDPI)	Good	Poor	Good	Burn depth [274]
Laser speckle contrast imaging (LSCI)	Good	Excellent	Poor	Pilot neurosurgical procedures [275]

Table 3.1: Overview of techniques for the measurement of blood flow. Specific values depend on the setup used.

saturation of peripheral oxygenation, S_pO_2 , using a probe which is usually placed on the earlobe or fingertip. The pulse oximeter transmits light of two wavelengths into the skin to ascertain absorbance due to arterial blood, whilst correcting for effects from other tissues. Pulse oximetry is particularly useful for detecting systemic alterations in oxygen carriage, for example in hypoxaemia.

Near infrared spectroscopy (NIRS) utilises NIR light to measure relative changes in haemoglobin concentration. In the optical window between 700 and 900nm, biological tissues are considered almost optically transparent; therefore haemoglobin dominates light absorption. Water and other chromophores such as fat and melanin are assumed not to change over time, allowing observed changes to be attributed to haemoglobin. Differences in the absorption spectra of oxygenated and deoxygenated haemoglobin allow the two to be distinguished using at least two light sources of different wavelengths, one above and one below the isosbestic point where the absorption is identical (see Figure 3.6). Some systems incorporate a source at this wavelength to enable calculations of total haemoglobin, to verify the Hb and HbO₂ values. At least two different wavelengths are required for the calculations, with the inclusion of more wavelengths reducing error. Relative concentration is calculated as a function of total photon path length using the modified Beer-Lambert law [276, 277],

$$A = \epsilon cdDPF + G, \quad (3.7)$$

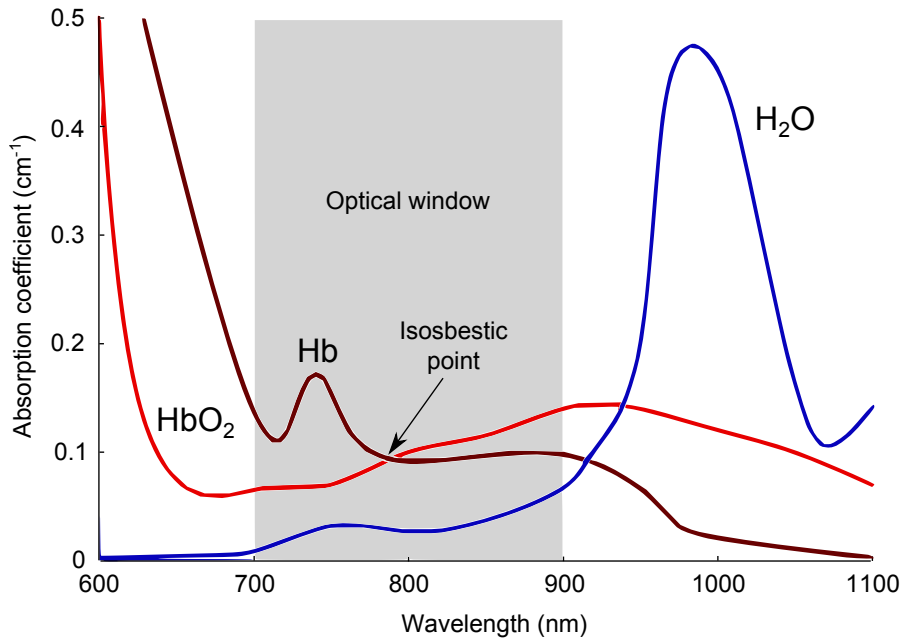


Figure 3.6: Absorption spectra for oxygenated and deoxygenated haemoglobin (red and dark red lines, respectively) and water (blue line). The optical window in which biological tissues are considered almost optically transparent is highlighted in grey (700–900nm).

where A is light attenuation, ϵ is an extinction coefficient, c is substance concentration, d is the distance between source and detector, DPF is the differential path length factor and G is signal loss due to scattering. The Beer-Lambert law is only valid in non-scattering media, and thus is not applicable in biological tissue. NIRS is widely used to monitor haemodynamic responses to brain activation.

3.4 Summary

Constant technological advancement allows continuous improvements in temporal and spatial resolution of existing techniques, whilst making new ones feasible. This is leading to the acquisition of more biological data *in vivo* than ever before, providing the opportunity to view functions within the body without perturbation in both healthy and diseased states. With these new possibilities comes the requirement for new analysis techniques for the optimal extraction of information from this data.

4. Dynamical systems

This chapter comprises three main sections. The first presents the theoretical background of dynamical systems, in particular nonautonomous systems and chronotaxic systems, followed by a review of the inverse approach to dynamical systems in Section 4.2. Methods for the detection of chronotaxic systems via the inverse approach are then reviewed in Section 4.3. Finally, Section 4.4 expands these inverse approach methods to new scenarios using numerical simulations, and the methods are also applied for the first time to brain dynamics using real experimental EEG data.

4.1 Introduction

A dynamical system describes the evolution of a state over time, the simplest case being

$$\frac{dx}{dt} = f(x), \quad (4.1)$$

where the infinitesimal change in x in infinitesimal time intervals t is described by some function f acting on the previous state of x . This differential equation describes the evolution of the system in continuous time. When time is discrete, iterated maps may be used [278], but only continuous time and thus differential equations are considered in this thesis. A dynamical system which explicitly depends on time, as is also the case in most biological systems, is known as *nonau-*

tonomous, with the simplest case being

$$\frac{dx}{dt} = f(x, t). \quad (4.2)$$

Linear dynamical systems, i.e. those with linear output, are exactly solvable. The vast majority of biological systems are nonlinear [7], making their analysis more difficult, but also more interesting. Unlike linear systems, nonlinear dynamical systems may exhibit self-sustained oscillations, and in this case will result in a stable limit cycle in the phase space of the system. A limit cycle is an isolated closed trajectory, which neighbouring trajectories will either spiral towards or away from depending on its stability [278].

These considerations of deterministic models are important in the characterization of the dynamics of biological oscillations.

4.1.1 Nonautonomous systems

The theory of nonautonomous dynamical systems has increasingly been recognised as a necessity in the treatment of the inherent time-variability of biological systems [279]. Closer inspection of the dynamics observed in nature suggests that previous approaches to the characterization of temporal fluctuations in these observations may be insufficient. At first glance, biological fluctuations may appear random, leading to their description by stochastic models [280]. The complexity observed in biological systems has also led to attempts to treat them with chaos theory [281]; however this does not allow for the apparent stability of these systems, irrespective of their initial conditions or perturbations to their trajectories. Such characteristics of biological oscillators suggests underlying determinism or control of both their amplitudes and frequencies even with continuous perturbations. This phenomenon of biological systems resisting a natural tendency to disorder was discussed in terms of free energy minimization [282] and separation of internal and external states, but this approach is still based on random dynamics. A closely related yet more natural

approach is to consider them as nonautonomous systems, which are explicitly time dependent. Approaches based on reformulation of nonautonomous systems as higher dimensional autonomous systems introduce unnecessary complexity whilst failing to describe accurately the dynamics arising from nature, where systems are open and subject to continuously variable external perturbations. Many living systems may be considered as nonautonomous oscillatory systems, with such time-varying dynamics being observed in individual mitochondria [220], the cardio-respiratory system [112, 283], the brain [284] and blood flow [110].

4.1.2 Chronotaxic systems

Although stability of the amplitude dynamics of an oscillator can be achieved with autonomous self-sustained limit cycle oscillators, the frequency of this oscillation could be easily changed by weak external perturbations [285]. To account for a case where this frequency of oscillation is also robust to perturbations, yet time dependent, a completely new approach is required. Thus, nonautonomous systems with stable yet time-varying frequencies were recently addressed, and formulated as chronotaxic systems [285, 286, 287]. Chronotaxic systems possess a time-dependent point attractor provided by an external drive system. This allows the frequency of oscillations to be prescribed externally through this driver and response system, giving rise to determinism even when faced with strong perturbations.

Chronotaxic (*chronos* – time, *taxis* – order) systems were introduced [285, 286, 287] in order to provide a framework in which a nonautonomous dynamical system may possess time-varying amplitudes and frequencies which are stable, i.e. able to resist continuous external perturbations.

Nonautonomous dynamical systems, and thus chronotaxic systems, are defined by the following system,

$$\dot{\mathbf{p}} = \mathbf{f}(\mathbf{p}); \quad \dot{\mathbf{x}} = \mathbf{g}(\mathbf{x}, \mathbf{p}), \quad (4.3)$$

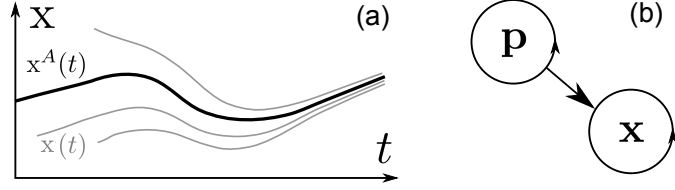


Figure 4.1: (a) Moving point attractor in a chronotaxic system. (b) Simplest case of a chronotaxic system, \mathbf{x} , driven by \mathbf{p}

where $\mathbf{p} \in R^n$, $\mathbf{x} \in R^m$, $\mathbf{f} : R^n \rightarrow R^n$, $\mathbf{g} : R^m \times R^n \rightarrow R^m$, where n and m can be any positive integers. Crucially, the solution $\mathbf{x}(t, t_0, \mathbf{x}_0)$ of Eqs. (4.3) depends on the actual time t as well as on the initial conditions (t_0, \mathbf{x}_0) , whereas the solution $\mathbf{p}(t - t_0, \mathbf{p}_0)$ depends only on initial condition p_0 and on the time of evolution $t - t_0$. The driven system \mathbf{x} is nonautonomous, i.e. it is described by an equation that explicitly depends on time. \mathbf{x} is assumed to be observable, whilst the driving system \mathbf{p} may not be, as is the case in many real systems. Therefore, the observable dynamics of \mathbf{x} are used to infer information about the evolution of the system \mathbf{p} , with the assumptions that in the case of chronotaxicity it will create a time-dependent steady state in the dynamics of \mathbf{x} , (see Figure 4.1(a))

The system \mathbf{x} is considered as a thermodynamically open system, and in addition to the driving \mathbf{p} which makes the system chronotaxic, external perturbations are also considered, arising from everything outside \mathbf{x} and \mathbf{p} which may influence the system. In the absence of external perturbations, the dynamics of \mathbf{x} will reduce to the time-dependent steady state determined by \mathbf{p} . This unperturbed state, also known as a point attractor, is denoted $\mathbf{x}^A(t)$. Assuming that for any initial condition \mathbf{x}_0 at time t_0 the solution of the system asymptotically approaches the time-dependent steady state \mathbf{x}^A , the condition of forward attraction for \mathbf{x}^A is the following,

$$\lim_{t \rightarrow +\infty} |\mathbf{x}(t, t_0, \mathbf{x}_0) - \mathbf{x}^A(t)| = 0, \quad (4.4)$$

which can only be satisfied when the chronotaxic system is not perturbed. Therefore, this condition is not sufficient to define the time-dependent point attractor in a real system, especially when considering the stability of the system at the current

time t , not the infinite future. To resolve this, a condition of pullback attraction must also be satisfied by $\mathbf{x}^A(t)$ in a chronotaxic system,

$$\lim_{t_0 \rightarrow -\infty} |\mathbf{x}(t, t_0, \mathbf{x}_0) - \mathbf{x}^A(t)| = 0. \quad (4.5)$$

Considering the condition 4.5 at all times $t > -\infty$, it follows that \mathbf{x}^A should also satisfy the invariance condition, i.e. the condition that \mathbf{x}^A is a solution of the system 4.3,

$$\mathbf{x}(t, t_0, \mathbf{x}^A(t_0)) = \mathbf{x}^A(t). \quad (4.6)$$

The asymptotic convergence in the infinite future starting from the infinite past allows the dynamics of $\mathbf{x}(t, t_0, \mathbf{x}_0)$ to deviate from \mathbf{x}^A during a certain finite time interval, meaning that during this time interval the ability of the system to resist external perturbations will be absent. Therefore, another condition for chronotaxicity is that the system should satisfy the condition of contraction. This means that in phase space there should be a contraction region $C(t)$ within which any two trajectories $\mathbf{x}_1, \mathbf{x}_2$ of the system inside the contraction region $\mathbf{x}_i(t, t_0, \mathbf{x}_{0i}) \in C(t)$, $i = 1, 2$, can only converge,

$$\frac{d}{dt} |\mathbf{x}_1(t, t_0, \mathbf{x}_{01}) - \mathbf{x}_2(t, t_0, \mathbf{x}_{02})| < 0. \quad (4.7)$$

This contraction region can be finite, and thus trajectories may leave the area. It is therefore required in a chronotaxic system that the contraction region should contain a finite area A' , $A' \subset C$, such that solutions of the system starting in A' never leave it, $\forall t_0 < t, \forall \mathbf{x}_0 \in A'(t_0), \mathbf{x}(t, t_0, \mathbf{x}_0) \in A'(t)$.

Providing the above conditions are met, the dynamics of \mathbf{p} may be stochastic or chaotic, but the dynamics of \mathbf{x} , when unperturbed, will still be deterministic. Real life systems can be modelled by perturbed chronotaxic systems, in which a deterministic and a stochastic component may be observed, but the system will still retain a deterministically defined frequency and resist continuous external perturbations provided that they are not too strong, and will revert to the unperturbed

case in their absence.

The next step following this knowledge of the underlying dynamics of chronotaxic systems is to extract the deterministic components in data from living systems in order to reduce their complexity and study the underlying dynamical processes.

Example chronotaxic systems and their identification via the inverse approach are discussed in Section 4.3.

4.2 Inverse approach to dynamical systems

A wide range of observed properties in living systems can be explained by considering them as nonautonomous. Despite this, difficulties in their analysis as such have led to many unsuccessful attempts to apply methods more suited to autonomous systems. In deterministic systems, phase space analysis is usually the first point of call, i.e. reconstruction of the attractor in phase space. This approach works well for autonomous systems, but does not consider the possibility of time-dependent attractors [279]. To incorporate time-dependence into these systems, extra dimensions in phase space are required, introducing unnecessary complexity to the problem.

Many signal analysis methods assume stationarity of the frequency distribution of the data, but in nonautonomous systems this assumption is not valid. Single variable time-series, particularly those from living systems, must be treated as arising from nonautonomous dynamical systems, due to time-dependent influences of variables other than the one under study. Approaches based on windowing have been applied in order to attempt to treat time-variability in data, but these potentially lose crucial information. For example, in phase space reconstruction, the window may not be of a sufficient size to capture the whole of the attractor, or its variations in time. Application of the Fourier transform to nonstationary data will result in a blurred or misleading power spectra, severely limiting its usefulness. The windowing approach has been applied here with some success,

but the windowed Fourier transform introduces frequency resolution limitations based on window size; the better the time resolution, the worse the frequency resolution (known as the Gabor limit [288]). The fixed time-frequency relationship at all scales in a windowed Fourier transform severely limits its usefulness for the analysis of low frequency oscillations. This problem can be addressed using the continuous wavelet transform, which provides a logarithmic frequency scale (see Section 4.2.3). This simultaneous observation of the time and frequency domains is extremely useful in the visualization of dynamical systems and their time evolution. As a result, development of wavelet-based methods specifically for the treatment of time-dependent dynamics is now a very active field of research [289], including wavelet phase coherence [290], the synchrosqueezed transform [291] and wavelet bispectrum [292].

4.2.1 Time domain

Instantaneous frequency and phase

The instantaneous frequency of an oscillation can be obtained as the time derivative of the phase, assuming that the phase can be defined for each cycle, and that the phase is separable from the amplitude. The calculation of instantaneous frequency via the marked events method has already been discussed in Section 3.1.2. Another method for the calculation of instantaneous phase is the Hilbert transform, which converts a real signal into a complex one known as an analytic signal, containing amplitude and phase information of the oscillation. The Hilbert transform is superior to the marked events method in that it provides a time resolution equal to the sampling frequency, whilst in the marked events method this resolution can only be equal to the frequency of events, which also means that the resolution may vary over time. However, the Hilbert transform is quite limited in terms of the time series to which it can be applied, for example it can only be used in time series in which a single oscillation is present. As previously discussed, extraction of instantaneous phase from time-frequency representations provides

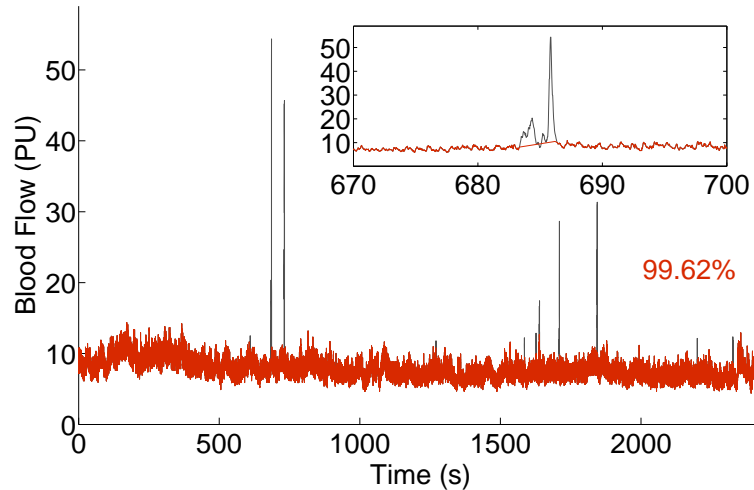


Figure 4.2: Linear interpolation can be used to remove spikes of short duration. As an example, the spike at around 687 seconds can be seen in the inset in black, and the interpolation line across it in red. It is important to retain as much of the original signal as possible, here 99.62% remains.

good resolution whilst allowing the investigation of multi-mode signals.

Preprocessing

Preprocessing of a signal is important to provide optimal conditions for analysis but it is important to keep data manipulation to a minimum. In data recorded from living systems, artefacts may arise from movement or other, non-physical, influences. The characteristics of these artefacts determines how they should be dealt with. If their duration is much shorter than the frequencies of interest, they can be removed by simple linear interpolation across the spike (see Figure 4.2). If there are multiple spikes, or their duration is very long, i.e. comparable to the frequencies being studied, then they should be either cut from the data, if they occur close to either end, or the data should be discarded. Under no circumstances should the data be spliced, i.e. joining non-consecutive intervals of data.

Another thing to consider in preprocessing is filtering. If mean values are to be calculated, or frequency analysis is to be applied to the signal, the data should be detrended to remove trends and effects of frequencies lower than those of interest, which may affect results. Detrending can best be achieved using a moving average method, in which a window of a defined width in time is moved along the signal,

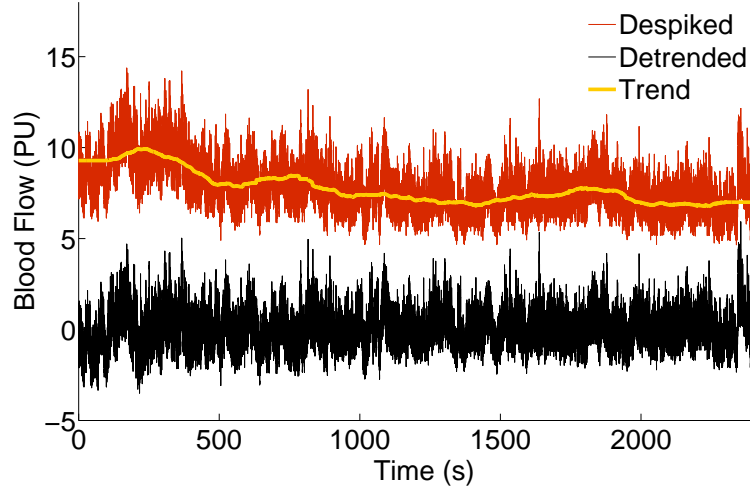


Figure 4.3: A detrended blood flow signal (black). A 200s window was used in a moving average, to calculate the trend (yellow), removing all frequencies below 0.005 Hz. The mean is also subtracted.

and the central value is set to the mean of the window. This can be used to filter or smooth signals, depending on the window size used. For frequency, or time-frequency analysis, it is also necessary to subtract the average of the signal, as shown in Figure 4.3.

Detrended fluctuation analysis

The complexity of a time series can be quantified using fractal analysis. Detrended fluctuation analysis (DFA) is used to determine the statistical self-similarity of a signal at different timescales, with less strict assumptions about the stationarity of a signal than the auto-correlation function. The scaling of these fluctuations is determined by the self-similarity parameter α , where fluctuations at time scales equal to t/a can be made similar to those at the larger time scale t by multiplying with the factor a^α .

In order to calculate α , the time series is integrated in time and divided into sections of length n . For each section the local trend is removed by subtracting a fitted polynomial—usually a first order linear fit [293, 112]. The root mean square

fluctuation for the scale equal to n is then given by

$$F(n) = \sqrt{\frac{1}{N} \sum_{i=1}^N Y_n(t_i)^2}, \quad (4.8)$$

where $Y(t)$ is the integrated and detrended time series and N is its length. The fluctuation amplitude $F(n)$ follows a scaling law if the time series is fractal. By plotting $\log F(n)$ against $\log n$, the value of α is simply the gradient of the line. For completely uncorrelated white Gaussian noise the parameter for α has a value of 0.5, while integrated white Gaussian noise returns a value of 1.5.

4.2.2 Frequency domain

Before analysing a signal in the frequency domain the frequency range which it is possible to observe based on the characteristics of the data must be considered. The maximum observable frequency in a signal is equal to half the sampling frequency, defined as the Nyquist frequency. This limit prevents aliasing. Aliasing occurs when the sampling frequency is not sufficiently high to capture accurate information about the system being observed. The lowest observable frequency is equal to $1/l$, where l is the length of the time series, ensuring that at least one period of oscillation is possible in the measured time series. One also cannot resolve the amplitude of two oscillations which have a difference in frequency of less than $1/l$. In practice, particularly when dealing with signals from living systems, it is more reliable to define the lowest frequency of observation as $1/5l$ [294].

The Fourier transform

Any physical process can be described either in the time domain or in the frequency domain. In the time domain, the values of a quantity f are given as a function of time, $f(t)$, whereas in the frequency domain the process is described as the amplitude of the process F as a function of frequency, $F(f)$. Both are representations of the same function which provide different kinds of information.

If time is measured in seconds, the units of frequency will be Hertz, or cycles per second.

A Fourier series expresses a periodic function as an infinite series of sines and cosines,

$$f(t) = a_0 + \sum_{\omega=1}^{\infty} [a_{\omega} \cos \omega t + b_{\omega} \sin \omega t], \quad (4.9)$$

where ω is the angular frequency and a_0 , a_{ω} and b_{ω} are Fourier coefficients.

Data resulting from biological recordings will involve discrete sampling. For the basis described above, the discrete Fourier transform (DFT) of a signal is given by:

$$F_{\omega} = \sum_{n=0}^{N-1} f(n) e^{\frac{2\pi i \omega n}{N}} \quad (4.10)$$

The Fourier transform will show peaks at frequencies of periodic terms contained in the time series. The Fourier transform is symmetric, with both positive and negative frequencies calculated. However, negative frequency components are usually discarded, and the positive components doubled to compensate.

The Fourier transform assumes that the signal on which it is performed is stationary, i.e. that the frequency components do not vary with time. In the vast majority of biological signals, there is some degree of time variance, which even if deterministic will not be distinguishable from stochastic variations in a basic Fourier transform. The sinusoidal basis of the Fourier transform may also misrepresent oscillations which have more irregular shapes. An example time series containing low frequency oscillations between 0.001 and 0.01 Hz is shown in Figure 4.4. The fast Fourier transform (FFT) of this signal is compared with the FFT of $1/f$ (or pink) noise, demonstrating that it is difficult to distinguish between the deterministic oscillations in the simulated data and the pure noise signal. In contrast, a continuous wavelet transform of the same data reveals a distinct, time-varying oscillation, highlighting the benefits of considering time and frequency information simultaneously.

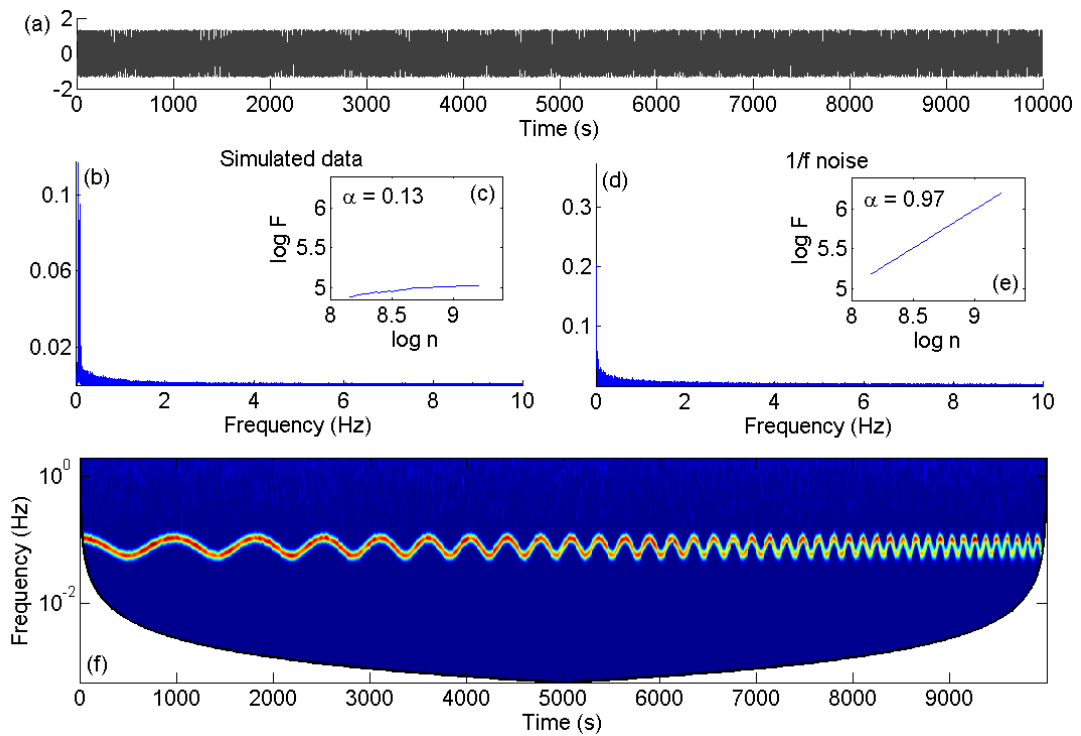


Figure 4.4: Comparison of the Fourier transforms of simulated low frequency oscillations and $1/f$ noise. (a) Simulated data with oscillations varying in frequency between 0.001 and 0.01 Hz. (b) FFT of the data in (a). (c) DFA exponent of the data in (a) suggests anti-correlated. (d) FFT of $1/f$ noise (pink noise). (e) DFA exponent of $1/f$ noise is around 1, as expected. (f) Continuous wavelet transform of the data in (a), shows oscillations are present with varying frequency.

4.2.3 Time-frequency analysis

Short time Fourier transform

The Short Time Fourier Transform (STFT) or windowed Fourier transform (WFT) goes some way to solve the problems with the Fourier transform, by dividing the signal into ‘windows’ within which the signal can be approximated as a stationary one. This method provides a time-frequency representation, in which the FFT is calculated for each window, and the middle value of the window in the STFT representation set to the resultant FFT values.

The STFT still has its limitations. The window size must be decided depending on whether the user requires good time resolution or good frequency resolution, one cannot have both simultaneously [288]. Also, the linear frequency resolution of the STFT means that it performs poorly in resolving separate oscillatory modes when analysing low frequency components in data.

Continuous wavelet transform

The optimal solution to the previously discussed limitations is the wavelet transform. This simultaneously examines the signal in time and frequency, and allows good resolution in both through the use of an adaptive window. If this process is carried out in discrete steps, it is known as a discrete wavelet transform (DWT) which has no overlap between frequency bands. If continuous, it is a continuous wavelet transform (CWT). The superiority of the CWT over the FFT when analysing a chirp signal is demonstrated in Figure 4.5.

The continuous wavelet transform is given by

$$g(s, t) = \frac{1}{\sqrt{s}} \int_{-\infty}^{\infty} \psi\left(\frac{u-t}{s}\right) g(u) du,$$

where s is a scaling factor, t is a location on the signal in time and ψ is the wavelet function. The wavelet transform is obtained by moving a wavelet function along all locations of the signal. For each location, a full range of scales of the wavelet is

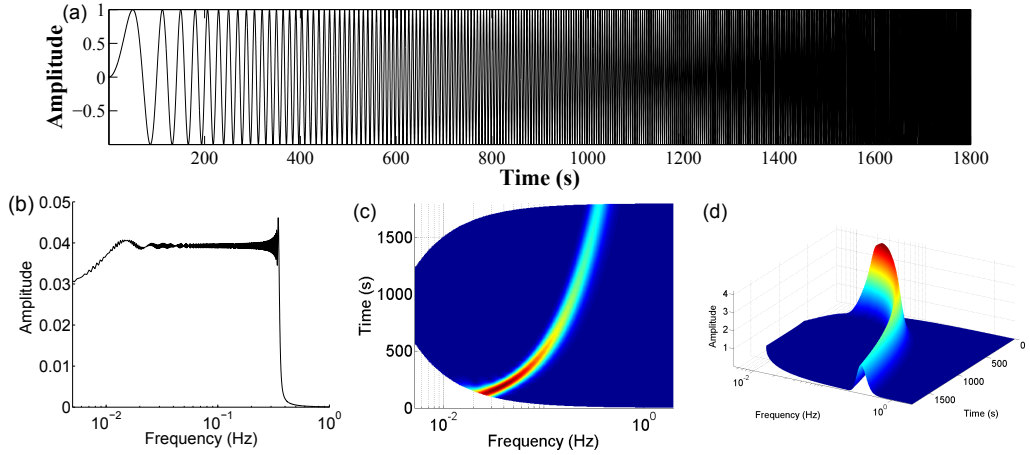


Figure 4.5: (a) Nonlinear chirp signal (quadratic) $\sin(2\pi \times 0.0001 \times \text{time}^2)$ has a frequency which increases with time. (b) The Fourier transform is unable to properly represent the signal in (a) in the frequency domain, due to the time-variation. (c) The continuous wavelet transform in (c) and the 3D version in (d) show how the frequency changes with time using a 3D map showing time and frequency information simultaneously.

used, and can be adjusted depending on the range of frequencies to be investigated. The value obtained from the convolution of the wavelet function with the signal at these times and frequencies will be large if there is a good match (if the signals are out of phase, a large value will still be given but it will vary between real and imaginary parts if a complex wavelet is used). In this way, a whole picture of a signal can be created, with the axes time, frequency and amplitude, which is the value of the transform at each scale as shown in Figure 4.6. The wavelet power spectrum can be calculated as the modulus square of the wavelet transform integrated over frequency [289],

$$P_W(\omega, t) = \int_{\omega - \frac{d\omega}{2}}^{\omega + \frac{d\omega}{2}} |W_T(\omega, t)|^2 d\omega. \quad (4.11)$$

The time average of P_W provides a representation of the whole time series, which can be used to compare between power spectra of different signals. Whilst this may seem to be a reduction to the functionality of the Fourier transform, time-averaged wavelet power provides superior resolution at low frequencies for time-varying oscillations due to the logarithmic frequency scale (see Figure 4.7).

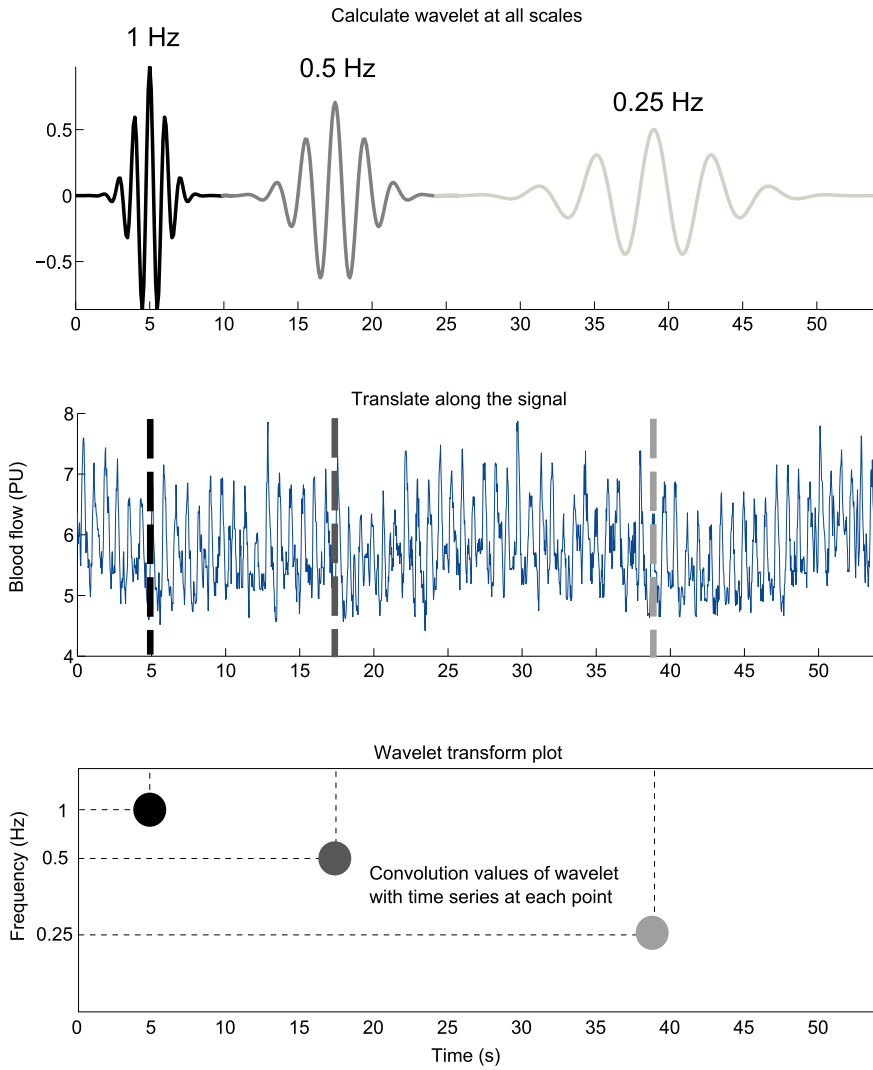


Figure 4.6: Example of the translation of wavelets of different scales (top) across a blood flow signal (middle) in time. The results of the convolution of the wavelet with the time series are plotted for each scale and location (bottom).

Wavelet types

There are many different wavelets, each having its own applications. Particularly useful are complex wavelets, which allow the separation of the phase and amplitude components of a signal. The wavelet used in this thesis is the Morlet wavelet, a complex wave within a Gaussian envelope, which has unit standard deviation. The real and imaginary sinusoids differ in phase by a quarter of a period [295]. The complex Morlet wavelet is defined as

$$\psi(u) = \frac{1}{\sqrt[4]{\pi}} e^{i2\pi f_0 u} e^{-u^2/2}$$

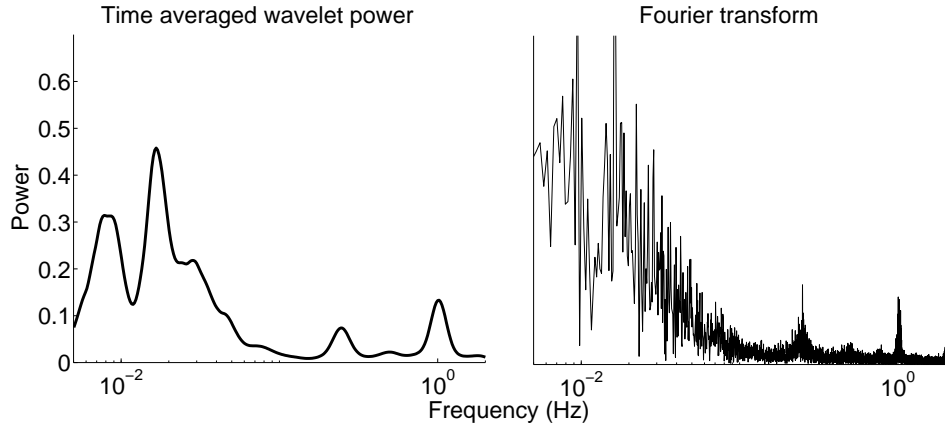


Figure 4.7: Time averaged wavelet transform vs. Fourier transform. Even when time-averaged, the wavelet transform provides superior resolution at lower frequencies for time-varying oscillations.

The wavelet coefficients obtained using the complex Morlet wavelet are complex numbers which define the amplitude and instantaneous phase for each frequency and time [296].

Cone of influence

The CWT integrates over infinite time, but a real data set has finite length. As a result, the wavelet transform becomes ill-defined near the time borders, close to $t = 0$ or when t approaches the length of the time series. To overcome this, the signal can be 'padded', i.e. made longer at both ends during the calculation, and then trimmed to retain only the original time period. Various padding regimes are used, including zero padding, predictive padding and periodic padding [261]. Even with a padding scheme in place, boundary effects are still observed due to the wavelet running over the edge of the time series, with the unaffected portion of the wavelet transform known as the cone-of-influence.

Implementation

An example algorithm for the implementation of the continuous wavelet transform is as follows:

1. Decide the frequency limits within which you require the CWT, and create

a logarithmic scale array, noting that with the Morlet wavelet of $f_0 = 1$, $\text{scale} = 1/\text{frequency}$.

2. Calculate the wavelet for each scale, and implement the convolution with the time series. The finite duration of the time series will result in the wavelet transform becoming ill-defined near the ends of the signal. To tackle this problem, the signal is usually padded (see above).
3. The convolution required in the calculation of the CWT can be implemented using the convolution theorem:

$$g * h \equiv G(f)H(f), \quad (4.12)$$

i.e. the Fourier transform of the convolution is the product of the individual Fourier transforms of the wavelet and the time series [297]. Therefore, the convolution of the signal and the wavelet is equal to the inverse Fourier transform of the product of their individual Fourier transforms.

4.2.4 Interactions

Wavelet phase coherence

When using a complex wavelet such as the Morlet wavelet in the wavelet transform, the wavelet coefficients will also be complex, providing amplitude and phase information at each time and frequency. The differences between instantaneous phases in two signals can be monitored over time using wavelet phase coherence, which may reveal phase relationships between them [298].

Wavelet phase coherence is computed by first calculating instantaneous phases at each time t_n and frequency f_k for both signals $\phi_{1k,n}$ and $\phi_{2k,n}$, and then finding their relative phase differences $\Delta\phi_{k,n} = \phi_{2k,n} - \phi_{1k,n}$. The sine and cosine components of the phase differences are then calculated and averaged in time, and the

phase coherence defined as [298]:

$$C_\phi(f_k) = \sqrt{\langle \cos \Delta\phi_{k,n} \rangle^2 + \langle \sin \Delta\phi_{k,n} \rangle^2}. \quad (4.13)$$

The phase coherence $C_\phi(f_k)$ will have a value between 0 and 1, with a value of zero suggesting that the phase difference changes continuously in time, and thus that the oscillations are likely to be unrelated, whilst a value of 1 is indicative of a phase relationship which remains constant in time. However, wavelet phase coherence values at lower frequencies may be artificially high, due to them being represented by fewer periods of oscillation in the signal. The phase coherence between even two completely unrelated signals will increase at lower frequencies, and tend towards 1. Thus, to distinguish true phase coherence from this low frequency bias, surrogate data can be used to define a boundary above which phase coherence may be considered significant. Surrogate data testing involves the generation of time series which are identical to the one being studied in every way except in the property of interest [299].

Time-localised phase coherence can follow time-variations in the phase relationships between two signals by using a sliding window, which can be scaled to always contain the same number of cycles, thus removing the low frequency bias observed in the time-averaged case [300]. At least 5 cycles of the lowest frequency oscillation are required to calculate windowed phase coherence, which results in the loss of information at low frequencies.

Synchronization

Synchronization is the adjustment of rhythms of oscillators to a state in which the relationship between their phases or amplitudes remains fixed, due to their weak interaction [301]. Here, only phase synchronization is considered, as phase dynamics is the main focus of subsequent chapters.

The simplest representation of synchronization is the synchrogram. Based on the marked events method discussed previously, synchronization can be detected

between two oscillators as follows: the wrapped phase of one oscillator, usually the slowest, is sampled at the times of the marked events of the other oscillator, with the resultant phase values plotted against time. If these events consistently occur at the same point in the cycle of the slow oscillator, the synchrogram will display horizontal lines, which suggests synchronization between the oscillators. The number of horizontal lines determines the synchronization order, for example 2 visible lines when considering one period of the slowest oscillator would mean 2:1 synchronization. Whilst initially useful, synchrograms do not provide a quantifiable measure, and synchronization of higher orders is cumbersome to detect with synchrograms because of having to manually edit the number of cycles over which to wrap the phase.

To obtain a quantifiable measure, the phase synchronization index or phase coherence can be calculated [302]. Dynamical Bayesian inference can also be implemented to detect time-varying synchronization.

Dynamical Bayesian inference

Dynamical Bayesian inference can simultaneously detect time-varying synchronization, directionality of coupling and time-evolving coupling functions [303, 304]. Following the determination of the phases of two time series, for example using the continuous wavelet transform, their dynamics is assumed to be described by [303, 304, 302]

$$\dot{\varphi}_i = \omega_i + f_i(\varphi_i) + g_j(\varphi_i, \varphi_j) + \xi(t), \quad (4.14)$$

where ω_i is the natural frequency of the oscillation, $f_i(\varphi_i)$ are the self-dynamics of the phase, $g_i(\varphi_i, \varphi_j)$ are the cross couplings, and $\xi(t)$ is a two-dimensional white Gaussian noise $\langle \xi_i(t)\xi_j(\tau) \rangle = \delta(t - \tau)E_{ij}$, included to represent a process in a real system. Based on the periodic nature of the system, the coupling terms are

modeled using the Fourier bases

$$f_i(\varphi_i) = \sum_{k=-\infty}^{\infty} \tilde{a}_{i,2k} \sin(k\varphi_i) + \tilde{a}_{i,2k+1} \cos(k\varphi_i), \quad (4.15)$$

and

$$g_i(\varphi_i, \varphi_j) = \sum_{s=-\infty}^{\infty} \sum_{r=-\infty}^{\infty} \tilde{b}_{i,r,s} e^{2\pi i r \varphi_i} e^{2\pi i s \varphi_j}, \quad (4.16)$$

where $k, r, s \neq 0$. In practice, it is reasonable to assume that the dynamics will be well described by a finite number of Fourier terms, denoted $A_{i,k}(\varphi_i, \varphi_j)$. The corresponding parameters from \tilde{a}_i and \tilde{b}_i then form the parameter vector $c_k^{(i)}$. The inference of these parameters utilises Bayes' theorem,

$$p_{\mathcal{X}}(\mathcal{M}|\mathcal{X}) = \frac{\ell(\mathcal{X}|\mathcal{M})p_{prior}(\mathcal{M})}{\int \ell(\mathcal{X}|\mathcal{M})p_{prior}(\mathcal{M})d\mathcal{M}}, \quad (4.17)$$

where $p_{\mathcal{X}}(\mathcal{M}|\mathcal{X})$ is the posterior probability distribution and $\ell(\mathcal{X}|\mathcal{M})$ is the likelihood function for the values of the model parameters \mathcal{M} given the data \mathcal{X} , and $p_{prior}(\mathcal{M})$ is a prior distribution. The negative log-likelihood function is

$$S = \frac{N}{2} \ln |E| + \frac{h}{2} \sum_{n=0}^{N-1} \left(c_k^{(l)} \frac{\partial A_{l,k}(\varphi_{\cdot,n})}{\partial \varphi_l} + [\dot{\varphi}_{i,n} - c_k^{(i)} A_{i,k}(\varphi_{\cdot,n}^*)] (E^{-1})_{i,j} [\dot{\varphi}_{j,n} - c_k^{(j)} A_{j,k}(\varphi_{\cdot,n}^*)] \right), \quad (4.18)$$

with implicit summation over repeated indices k, l, i, j . The log-likelihood is a function of the Fourier coefficients of the phases [303].

Assuming a multivariate normal distribution as the prior for parameters $c_k^{(i)}$ with means \bar{c} and covariances \sum_{prior} , the stationary point of S can be calculated

recursively from

$$\begin{aligned}
E_{i,j} &= \frac{h}{N} [\dot{\varphi}_{i,n} - c_k^{(i)} A_{i,k}(\varphi_{\cdot,n}^*)] [\dot{\varphi}_{j,n} - c_k^{(j)} A_{j,k}(\varphi_{\cdot,n}^*)], \\
c_k^{(i)} &= (\Xi^{-1})_{kw}^{i,l} r_w^{(l)}, \\
r_w^{(l)} &= (\Xi_{prior})_{kw}^{(i,l)} c_w^{(l)} + h A_{i,k}(\varphi_{\cdot,n}^*) (E^{-1})_{ij} \dot{\varphi}_{j,n} - \frac{h}{2} \frac{\partial A_{l,k}(\varphi_{\cdot,n})}{\partial \varphi^l}, \\
\Xi_{kw}^{i,j} &= \Xi_{prior kw}^{i,j} + h A_{i,k}(\varphi_{\cdot,n}^*) (E^{-1})_{ij} A_{j,w}(\varphi_{\cdot,n}^*).
\end{aligned} \tag{4.19}$$

The inferred parameters of the coupling functions can be used to determine whether synchronization results. The presence of synchronization provides evidence that the system could be chronotaxic; however it remains unclear from which coupling function the stability arises without calculating the direction of coupling [305],

$$D = \frac{\epsilon_{12} - \epsilon_{21}}{\epsilon_{12} + \epsilon_{21}}, \tag{4.20}$$

where

$$\begin{aligned}
\epsilon_{12} &= \sqrt{c_2^2 + c_4^2 + \dots}, \\
\epsilon_{21} &= \sqrt{c_1^2 + c_3^2 + \dots},
\end{aligned} \tag{4.21}$$

are the Euclidean norms of the parameters. The odd parameters correspond to the coupling terms inferred for φ_1 in the direction $2 \rightarrow 1$, and the even parameters correspond to the coupling terms inferred for φ_2 in the direction $1 \rightarrow 2$. See [306] for further details and an in depth tutorial on dynamical Bayesian inference and its implementation.

4.3 Identifying chronotaxic systems

Once the properties of an observed system have been recognised as possibly chronotaxic, the next problem is how to infer these dynamics and interactions from direct

observations, i.e. via the inverse approach. In a chronotaxic system, particularly one found in nature, whilst the underlying dynamics is defined by the external driver, the system will likely still be affected by other influences and noise, and these may mask the chronotaxic dynamics if the correct analytical approach is not applied. For example, the inherent time-variability of the frequency of the dynamics arising from a chronotaxic system means that it cannot be characterized accurately by any method based on averaging. This novel class of systems requires new inverse approach methods, with the focus on the extraction and identification of the dynamics of the drive system, and its influence on the response system. Here, the currently available inverse approach methods are demonstrated for the identification of chronotaxicity from a *single time series* of the response system in which the phase and amplitude dynamics are separable. These methods are then applied to numerically simulated and real experimental data.

Two distinct inverse approach methods are utilised in the detection of chronotaxicity [302]: phase fluctuation analysis (PFA) and dynamical Bayesian inference (see previous section on interactions). It should be noted that the current methods are only applicable to phase dynamics, i.e. the focus is on the ability of the time-varying frequency to resist continuous external perturbations. The two methods rely on different inferential bases. Phase fluctuation analysis provides a measure of statistical effects observed in a signal, whilst the dynamical Bayesian inference method infers a model of differential equations and gives a measure of dynamical mechanisms, i.e. the evaluation of chronotaxicity relies on the inferred parameters of the model. PFA is said to infer a functional connectivity, while the dynamical Bayesian inference method infers effective connectivity [307]. The optimal method to use depends on the characteristics of the data, as detailed below.

In order to determine whether a system is chronotaxic, one can observe the distribution of the fluctuations in the system. If the original distribution of the perturbations is known, then the stability of the system can be determined relative to the unperturbed trajectory, which in a chronotaxic system is determined by the

time-dependent point attractor. How these perturbations grow or decay over time will depend on the degree of external influence on the system, or its chronotacticity. Consider a non-chronotactic phase oscillator with noise [308],

$$\dot{\varphi}_{\mathbf{x}} = \omega_0(t) + \eta(t), \quad (4.22)$$

where $\omega_0(t) > 0$ is the time-dependent natural frequency and the observed phase φ_x is perturbed by noise fluctuations $\eta(t)$. If $\eta(t)$ is an uncorrelated Gaussian process, then integrating the system will result in the dynamics of $\varphi_{\mathbf{x}}$ consisting of a monotonically increasing phase perturbed by a random walk noise. However, this is not the case in a chronotactic phase oscillator,

$$\begin{aligned} \dot{\varphi}_{\mathbf{p}} &= \omega_0(t), \\ \dot{\varphi}_{\mathbf{x}} &= \varepsilon \omega_0(t) \sin(\varphi_{\mathbf{p}} - \varphi_{\mathbf{x}}) + \eta(t), \end{aligned} \quad (4.23)$$

where $\varphi_{\mathbf{p}}$ is an external phase and $|\varepsilon| > 0$. Here, the point attractor prevents $\eta(t)$ from being integrated over to the same extent. This will change the distribution of the observed noise from Brownian to something closer to white noise, and it is this difference in the distribution in observed phase fluctuations which is exploited in the inverse approach methods for the detection of chronotacticity.

4.3.1 Extracting the phase estimates

Given a single time series, the first step in determining whether it contains chronotactic phase dynamics is the extraction of the perturbed and unperturbed phases of any oscillatory modes present, as described above. First, when only considering phase dynamics, the amplitude and phase should be separated using time-frequency analysis [289]. Phase information can also be obtained via the analytic signal generated by the Hilbert transform, but this is only applicable when there is only one oscillation in the time series [302, 309, 310], which cannot be assumed in real data. The continuous wavelet transform (see Section 4.2.3) provides an

optimal time-frequency resolution for the required extraction of the instantaneous phases of oscillations in a time series. Oscillations can then be traced in the CWT using a ridge-extraction method [311, 312] or the synchrosqueezed wavelet transform [291]. Following the extraction of the instantaneous frequencies of oscillations via these methods, the phase $\varphi_{\mathbf{x}}$ of the observed system is then $\arg(W_T(s, t))$, where s and t denote the determined positions of the oscillations. Once the estimated perturbed phase $\varphi_{\mathbf{x}}$ has been extracted, the next step is to obtain the estimated unperturbed phase $\varphi_{\mathbf{x}}^{A*}$. In order to separate the dynamics corresponding to $\varphi_{\mathbf{x}}^A$ from the effects of the noise perturbations $\eta(t)$, it can be assumed that the dynamics of $\varphi_{\mathbf{x}}^A$ are confined to timescales larger than a single cycle, and that the noise is weak or comparable in magnitude to this dynamics [302]. Therefore, the estimated unperturbed phase $\varphi_{\mathbf{x}}^{A*}$ can be obtained by filtering out high frequency components of $\varphi_{\mathbf{x}}^*$, taking care to retain the dynamics of $\varphi_{\mathbf{x}}^A$. This can be achieved by smoothing over the instantaneous frequency extracted from the wavelet transform [289]. This can then be integrated over in time to give the estimated driver phase $\varphi_{\mathbf{x}}^{A*}$. For increased precision of phase extraction, and determination of whether an extracted oscillatory mode is physically meaningful, nonlinear mode decomposition may be used [261].

4.3.2 Detecting chronotaxicity

One approach to the detection of chronotaxicity is the application of dynamical Bayesian inference to the extracted perturbed (φ_x) and unperturbed (φ_x^A) phases in order to model their interactions. The characteristics of the coupling functions between φ_x and φ_x^A may reveal the dynamics of the system in terms of chronotaxicity. Bayesian inference is able to track time-dependent system parameters, meaning that it is particularly useful for the detection of chronotaxicity in systems which move in and out of a chronotaxic state. To detect chronotaxicity, Bayesian inference is applied to $\varphi_{\mathbf{x}}^*$ and $\varphi_{\mathbf{x}}^{A*}$ (of which the latter is assumed to follow the same dynamics as $\varphi_{\mathbf{p}}$), following their extraction from the time series. The time-

evolution of the coupling parameters for each phase is inferred and these are used to determine the synchronization state of the system, and the direction of coupling between the phases. In a chronotaxic system we require the driver and response systems to be almost or fully synchronized, and also that the direction of coupling is only from the driver φ_x^A to φ_x .

The basis of this method is the calculation of the synchronization and direction of coupling of the system in order to determine chronotaxicity. However, the more synchronized the driver is with the response system, the less information flow occurs between the two. With less information from which to infer parameters, most directionality methods, including Bayesian inference, become less reliable, and whilst synchronization may still be accurately detected, the direction of coupling will become less accurate the closer the system gets to synchronization. With frequent external perturbations, intermittent transitions, and moderate dynamical noise, there is greater information flow, and thus the inference is more precise, but this cannot be assumed in chronotaxic systems. In real systems, the synchronization state is not known beforehand; thus a more robust method is required, which can identify chronotaxicity even in systems close to synchronization.

Phase fluctuation analysis (PFA) is effective even when $\varphi_{\mathbf{x}}$ and $\varphi_{\mathbf{p}}$ are almost synchronized [302]. Given the estimates of $\varphi_{\mathbf{x}}$ and $\varphi_{\mathbf{x}}^A$, the next step is to analyse the distribution of fluctuations in the system relative to the unperturbed trajectory by calculating the phase fluctuations $\Delta\varphi_{\mathbf{x}} = \varphi_{\mathbf{x}}^* - \varphi_{\mathbf{x}}^{A*}$.

The distribution of these fluctuations will change depending on whether the system is chronotaxic or not. To quantify the distribution of fluctuations, detrended fluctuation analysis (DFA) is performed on $\Delta\varphi_{\mathbf{x}}$ [293, 112]. For uncorrelated white Gaussian noise, as is assumed here to perturb the system, α will have a value of 0.5. Integrated white noise (Brownian noise), which is expected in a non-chronotaxic system, will return a DFA exponent of 1.5. In reality, a chronotaxic system is expected to have a DFA exponent between 0.5 and 1, due to the fact that the decay of perturbations in a chronotaxic system cannot be instantaneous, so some

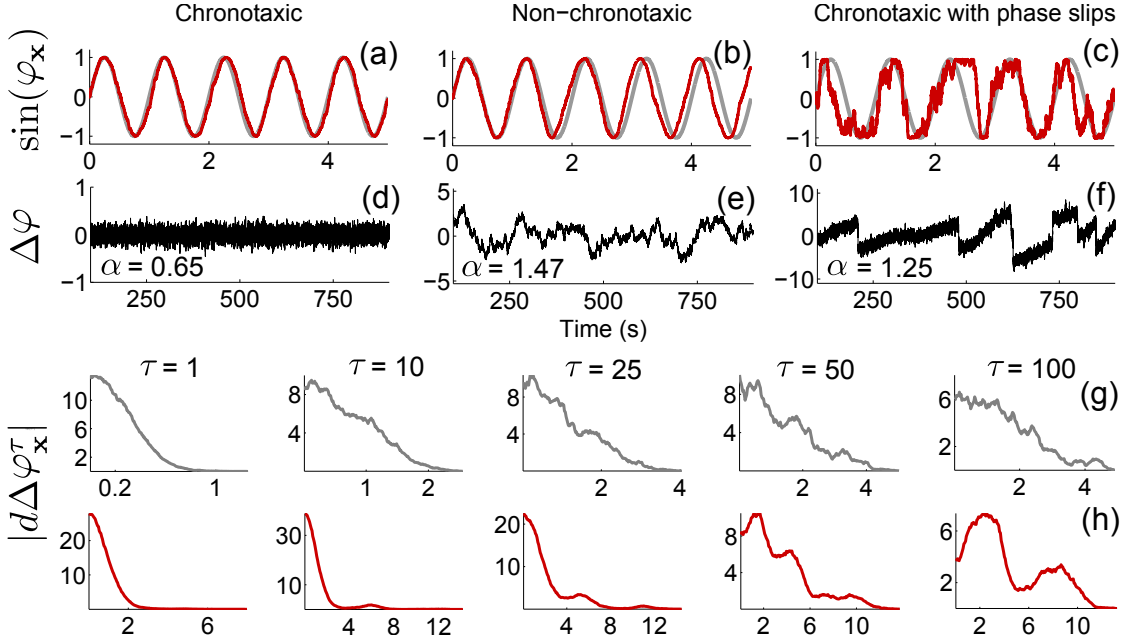


Figure 4.8: (a)–(c) 5-second time series of $\sin(\varphi_x)$ (red line) in 3 cases: chronotaxic, non-chronotaxic, and chronotaxic with phase slips, from Eq. 4.24. The grey line shows φ_p (chronotaxic), and $\omega_x t$ (non-chronotaxic). (d)–(f) $\Delta\varphi_x$ for the whole time series, detrended with a moving average of 200s. In all cases $\omega_{x,p} = 2\pi$, $h = 0.001$, $L = 1000$ seconds and $\sigma = 0.3$. $\varepsilon = 5$ and 0 in the chronotaxic and non-chronotaxic cases, respectively. DFA exponents, α , are shown. The DFA exponent of (f) incorrectly suggests the system is non-chronotaxic. To distinguish between a non-chronotaxic system and a chronotaxic system with phase slips, the delayed distributions were calculated (see Section 4.3.2) in the non-chronotaxic (g) and chronotaxic (h) case.

integration of noise may still occur. These values are presented under the assumption that the noise in the system is not strong enough to cause phase slips, which would cause perturbations to appear over larger timescales even if the system was chronotaxic. In these cases another approach is required [302].

If there are large perturbations which cause the system to move far enough forward or behind the current cycle to be attracted instead by an adjacent cycle, known as a phase slip, this will result in an increased DFA exponent. This can result from large jumps in the extracted phase fluctuations. To distinguish between this case, a chronotaxic system with phase slips, and a non-chronotaxic system, one can consider the fact that in the latter, perturbations may cause $\Delta\varphi_x$ to change by 2π , but these are part of a continuous probability distribution, in contrast to the chronotaxic case. Phase slips can be detected by calculating the distribution of the

difference between the phase fluctuations $\Delta\varphi_{\mathbf{x}}(t)$ and these fluctuations delayed by a timescale τ . $d\Delta\varphi_{\mathbf{x}}^{\tau}(t) = \Delta\varphi_{\mathbf{x}}(t + \tau) - \Delta\varphi_{\mathbf{x}}(t)$ therefore gives information about the perturbations of the system over that timescale. When phase slips are present, the distribution of $|d\Delta\varphi_{\mathbf{x}}^{\tau}|$ changes [302]. An example of this difference is shown in Figure 4.8 (g) & (h), and can also be seen in real biological systems, as previously demonstrated in the heart rate variability [302].

4.4 Further development of the inverse approach to chronotaxic systems

4.4.1 Numerical simulations

The basis of the phase fluctuation analysis (PFA) method is the quantification of the fundamental difference between phase fluctuation distributions in oscillatory systems, depending on their chronotaxicity. Here, this characteristic is illustrated using the simplest realisation of a chronotaxic system, two unidirectionally coupled oscillators (see Figure 4.1(b)):

$$\begin{aligned}\dot{\varphi}_{\mathbf{p}} &= \omega_{\mathbf{p}} \\ \dot{\varphi}_{\mathbf{x}} &= \omega_{\mathbf{x}} - \varepsilon \sin(\varphi_{\mathbf{x}} - \varphi_{\mathbf{p}}) + \eta(t),\end{aligned}\tag{4.24}$$

where $\varphi_{\mathbf{p}}$ and $\varphi_{\mathbf{x}}$ are the instantaneous phases of the driving and the driven oscillators, respectively, $\omega_{\mathbf{p}} > 0$ and $\omega_{\mathbf{x}} > 0$ are the natural frequencies of the oscillators, $\varepsilon > 0$ is the strength of the coupling and η is white Gaussian noise. Note that when $\varepsilon = 0$ the system is reduced to $\dot{\varphi}_{\mathbf{x}} = \omega_{\mathbf{x}} + \eta(t)$ and becomes non-chronotaxic; when $\eta = 0$ and $\varepsilon > |\omega_{\mathbf{x}} - \omega_{\mathbf{p}}|$ the system becomes chronotaxic with $\varphi_{\mathbf{x}}^A(t) = \varphi_{\mathbf{p}}(t) + \arcsin((\omega_{\mathbf{p}} - \omega_{\mathbf{x}})/\varepsilon)$. The system was integrated using the Heun scheme [289], with an integration step of 0.001 and noise strength $\sigma = 0.3$. $\Delta\varphi_{\mathbf{x}}$, shown in Figure 4.8, was obtained by subtracting the unperturbed phase ($\varphi_{\mathbf{x}}^A(t)$ and $\omega_{\mathbf{x}}t$ in the chronotaxic and non-chronotaxic cases, respectively) from

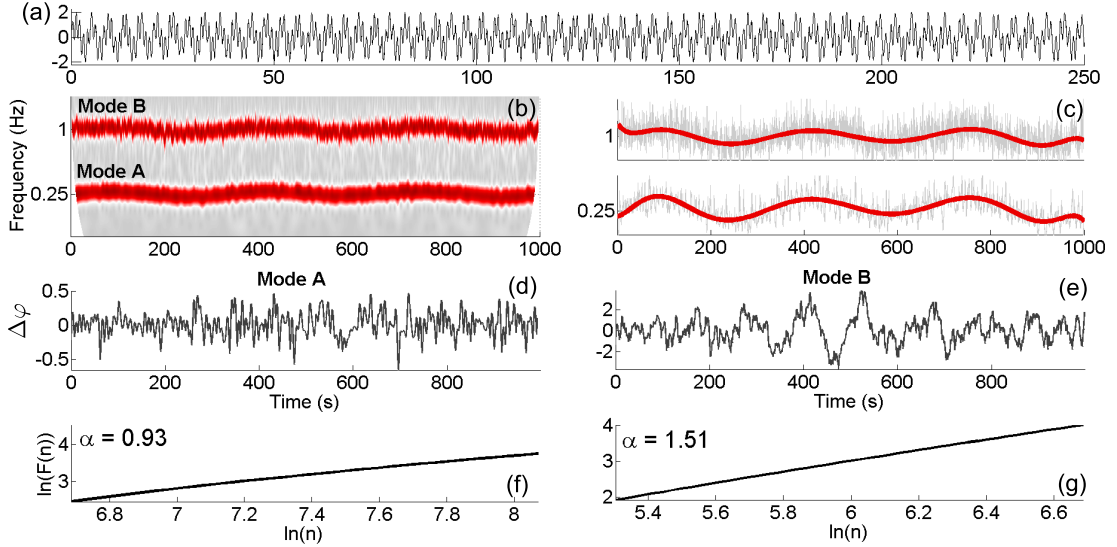


Figure 4.9: Identifying chronotacticity in signals with more than one oscillatory mode. (a) The first 250 seconds of a time series of a simulated signal containing two distinct oscillations, with coupling strengths $\varepsilon = 2$ for mode A (chronotactic) and $\varepsilon = 0$ for mode B (non-chronotactic). (b) The continuous wavelet transform of the signal in (a). (c) The instantaneous frequency (light grey) of both components is extracted from the wavelet transform, with central frequency $f_0 = 0.5$, and smoothed (red), using a polynomial fit. The smoothed frequency is then integrated in time to obtain an estimate of the unperturbed phase, φ_x^{A*} , which is then subtracted from the perturbed phase φ_x^* as extracted directly from the wavelet transform. (d) & (e) show $\Delta\varphi_x = \varphi_x^* - \varphi_x^{A*}$ for each mode. (f) & (g) show the results of DFA analysis on $\Delta\varphi_x$, with DFA exponents α correctly identifying mode A as chronotactic and mode B as non-chronotactic.

the perturbed phase φ_x , as obtained numerically. DFA was then performed on $\Delta\varphi_x$, yielding the exponents shown in Figure 4.8. The values of the exponents demonstrate the differences in the noise distributions between chronotactic and non-chronotactic systems. In the chronotactic case, the noise is closer to white, whereas in the non-chronotactic case it is closer to a random walk. It is this difference which is exploited in the PFA method.

In many systems, particularly those originating from nature, there will be more than one oscillation present in a signal, with different chronotactic characteristics. To test the PFA method in the case of multiple modes, a signal containing two distinct oscillations was simulated, with dynamics as described by Eq. 4.24, with

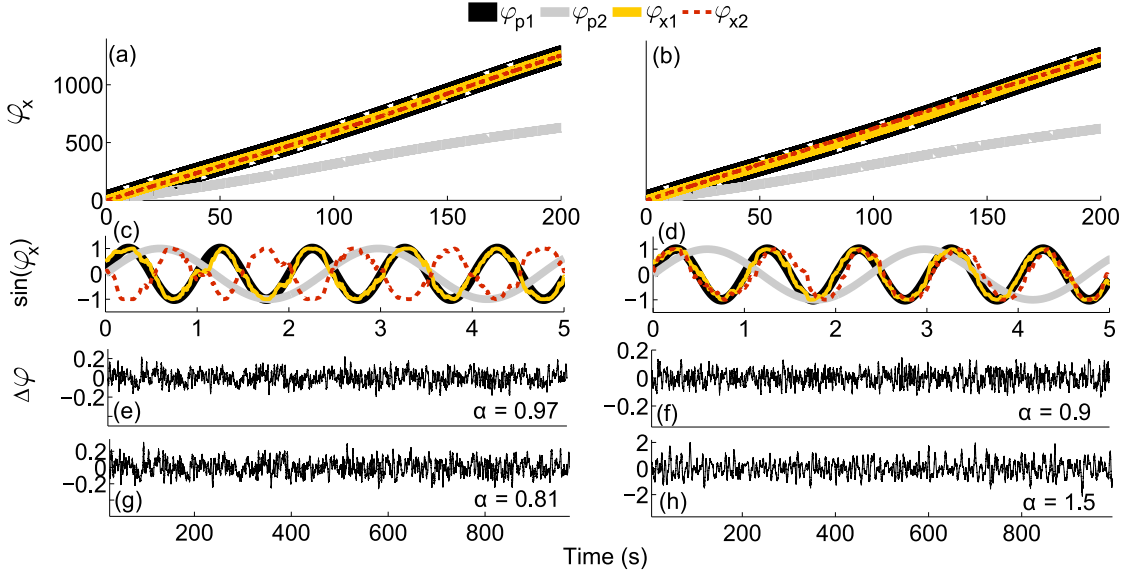


Figure 4.10: Identifying chronotacticity using phase fluctuation analysis in a system of bidirectionally coupled oscillators. The system presented in Eq. 4.26 was simulated in two different states of chronotacticity. (a) phase trajectories for the system when $\varepsilon_1 = 0.1$, $\varepsilon_2 = 20$, $\varepsilon_3 = 0.1$ and $\varepsilon_4 = 10$. (b) phase trajectories of the system with $\varepsilon_1 = 0.5$, $\varepsilon_2 = 0.1$, $\varepsilon_3 = 0.1$ and $\varepsilon_4 = 15$. (c) 5 seconds of the time series of both drivers and oscillators for parameters shown in (a). (d) 5 seconds time series for parameters shown in (b). (e) & (g) phase fluctuations from PFA on $\sin(\varphi_{x1})$ and $\sin(\varphi_{x2})$, respectively. (f) & (h) phase fluctuations extracted with PFA on $\sin(\varphi_{x1})$ and $\sin(\varphi_{x2})$, respectively.

time varying angular frequencies,

$$\begin{aligned}\dot{\omega}_{var}(t) &= A\cos(2\pi f_m t) + \eta(t) \\ \omega_{\mathbf{x},\mathbf{p}}(t) &= 2\pi f_{p,x} + \omega_{var},\end{aligned}\tag{4.25}$$

where $f_{\mathbf{p}}$ and $f_{\mathbf{x}}$ are the average frequencies of oscillation in Hz of the chronotactic and non-chronotactic case, respectively, and f_m is the frequency of variation. Frequencies of oscillation were chosen to vary around 1 and 0.25 Hz in the non-chronotactic and chronotactic cases, respectively, with $f_m = 0.003$. Both systems were perturbed with white Gaussian noise of strength $\sigma = 0.5$. The logarithmic frequency scale of the wavelet transform is very useful for identifying and separating the presence of oscillatory modes, which may otherwise appear as merged in other time-frequency representations, such as the windowed Fourier transform. Figure 4.9 shows the results of PFA on the signal. It correctly identifies mode A

(around 0.25 Hz) as chronotaxic, and mode B (around 1 Hz) as non-chronotaxic.

In single-variable time series obtained from real dynamical systems, it is highly unlikely that the observed dynamics will result from a simple, unidirectional constant coupling as described above. Rather, the system may be influenced by continuous perturbations, couplings to other oscillators, and temporal fluctuations in chronotaxicity. Here, the applicability of the described inverse approach methods to these more complex cases is demonstrated. Consider a system of two bidirectionally coupled oscillators,

$$\begin{aligned}
 \dot{\varphi}_{\mathbf{p}1} &= \omega_{\mathbf{p}1} & (4.26) \\
 \dot{\varphi}_{\mathbf{p}2} &= \omega_{\mathbf{p}2} \\
 \dot{\varphi}_{\mathbf{x}1} &= \omega_{\mathbf{x}1} + \varepsilon_1 \sin(\varphi_{\mathbf{x}1} - \varphi_{\mathbf{x}2}) - \varepsilon_4 \sin(\varphi_{\mathbf{x}1} - \varphi_{\mathbf{p}1}) + \eta(t) \\
 \dot{\varphi}_{\mathbf{x}2} &= \omega_{\mathbf{x}2} + \varepsilon_2 \sin(\varphi_{\mathbf{x}2} - \varphi_{\mathbf{x}1}) - \varepsilon_3 \sin(\varphi_{\mathbf{x}2} - \varphi_{\mathbf{p}2}) + \eta(t),
 \end{aligned}$$

with drivers $\varphi_{\mathbf{p}1}$ and $\varphi_{\mathbf{p}2}$, and $\omega_{\mathbf{p}1}(t) = 2\pi - 0.5 \sin(2\pi 0.005(t))$ and $\omega_{\mathbf{p}2}(t) = \pi - 0.5 \cos(2\pi 0.005(t))$. First, the case of strong influence of the driver $\varphi_{\mathbf{p}1}$ on the system is considered, resulting in chronotaxicity of both oscillators. Phase fluctuation analysis was applied to the system, and successfully identified both $\varphi_{\mathbf{x}1}$ and $\varphi_{\mathbf{x}2}$ as chronotaxic (see Figure 4.10(a)).

Secondly, the case in which $\varphi_{\mathbf{x}1}$ is chronotaxic but $\varphi_{\mathbf{x}2}$ is not is demonstrated. One can observe that despite continuous influences from multiple drivers and other oscillators, single variable time series arising from the same system can be distinguished in terms of their chronotaxic dynamics. Again, PFA correctly distinguishes between the two oscillators. This could be of great importance when investigating composite parts of a larger dynamical system, and seeking to identify causal relationships between observed oscillations. For example, recent advances in cellular imaging are providing the means to observe the dynamics of individual cellular processes in different cellular compartments [313]. Applying inverse approach methods for the detection of chronotaxicity to these dynamics could provide valuable

information on the current state of the cell (see Chapter 7).

So far, only those scenarios in which a system constantly remains as either chronotaxic or non-chronotaxic have been considered. Real dynamical systems may exhibit time variation in their coupling strengths, allowing the system to fluctuate between chronotaxic states. In these cases, it is possible to use dynamical Bayesian inference to track variations of chronotaxicity in time. To demonstrate this, ε_3 was allowed to vary in time in Eq. 4.26, whilst $\varepsilon_1 = \varepsilon_2 = 0.1$ and $\varepsilon_4 = 0$, resulting in intermittent chronotaxicity of the oscillator $\varphi_{\mathbf{x}2}$. $\varphi_{\mathbf{x}2}^{A*}$ and $\varphi_{\mathbf{x}2}^*$ were extracted from the wavelet transform of $\sin(\varphi_{\mathbf{x}2})$. Results of the application of dynamical Bayesian inference to these extracted phases are shown in Figure 4.11. This method is able to track the intermittent changes in chronotaxicity, through changes in synchronization and direction of coupling, demonstrating its usefulness for the detection of chronotaxicity in systems where the interactions between oscillators are time-varying, particularly when the system is intermittently chronotaxic.

4.4.2 Practical considerations

Both presented methods, phase fluctuation analysis and dynamical Bayesian inference, rely on precise phase extraction of the estimated attractor $\varphi_{\mathbf{x}}^{A*}$ and the perturbed dynamics $\varphi_{\mathbf{x}}^*$. Therefore, the parameters in the respective methods must be carefully selected depending on the characteristics of the given data.

The continuous wavelet transform provides an optimal compromise between time and frequency resolution. In the majority of examples used here, $f_0 = 1$ has been used. However, the wavelet central frequency, f_0 , can be altered to suit specific needs. For example, in a case where there are many phase slips, it may be necessary to extract the estimate of the attractor, $\varphi_{\mathbf{x}}^{A*}$, with a higher f_0 to obtain a better frequency resolution and smoother dynamics, whilst the perturbed phase $\varphi_{\mathbf{x}}^*$ is extracted using a lower f_0 , leading to an increased time resolution for the purpose of locating each phase slip. The parameter f_0 may also be increased

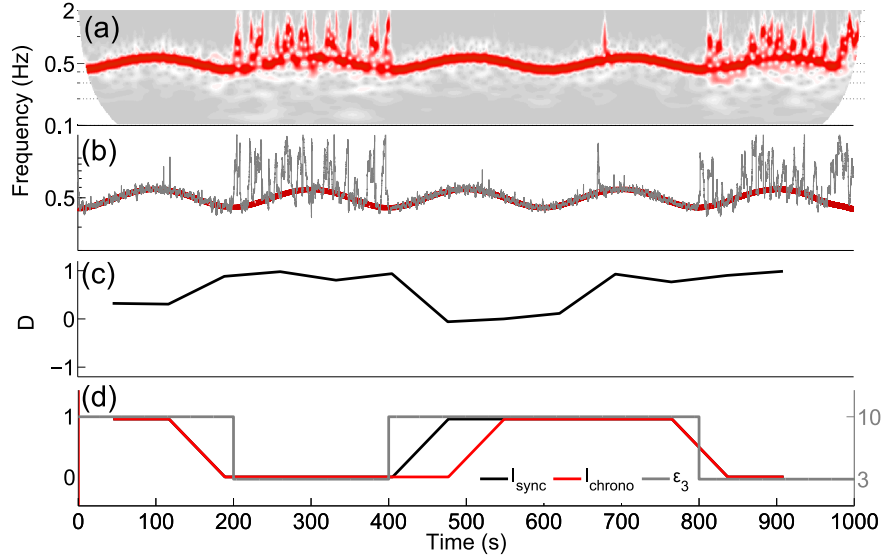


Figure 4.11: Identifying intermittent chronotaxicity using dynamical Bayesian inference. Bayesian inference was performed on φ_{x2}^* and φ_{x2}^{A*} extracted from $\sin(\varphi_{x2})$ (Eqs. 4.26) with ε_3 varying as shown in (d). (a) the CWT of $\sin(\varphi_{x2})$. (b) Instantaneous frequencies extracted from the wavelet transform. φ_{x2}^{A*} was extracted with $f_0 = 2$ and smoothed using a polynomial fit (red line), whilst φ_{x2}^* was extracted from the CWT with $f_0 = 0.5$ (grey line). Bayesian inference was applied, using a time window of 90 seconds. The inferred direction of coupling D can be seen in (c). Positive values show coupling from the driver to the oscillator only. (d) I_{sync} was calculated and shows excellent agreement with changes in ε_3 . I_{chrono} was also calculated, and was slightly less accurate due to the direction of coupling becoming negative very briefly, due to reduced information flow between systems to accurately infer parameters during synchronization.

to provide greater distinction between oscillatory modes, but this will be at the expense of time resolution. It should be noted that modes must be separable in time-frequency representations in order for these inverse approach methods to be applicable.

One fundamental assumption of chronotaxicity is that the system under consideration is oscillatory. Although the presented methods can be applied to any extracted phases, one should take great care to ensure that these phases correspond to a true oscillatory mode, otherwise all results will be meaningless. In the numerical simulations presented here, the characteristics of the oscillations which are present are predetermined, and not concealed by noise, allowing their successful extraction directly from the wavelet transform. These extracted phases can be verified using the specified parameters as a reference signal, and thus the reliability

of the final results can be verified. On the contrary, in real experimental data, the first question must be whether the signal contains any significant oscillations at all. To determine whether this is the case, the recently developed method of nonlinear mode decomposition (NMD) may be used. NMD is an adaptive, time-frequency representation based decomposition tool, which decomposes any given signal into a set of physically meaningful oscillations (if present) and residual noise. In the detection of chronotacticity, the crucial advantage of NMD over other decomposition methods, such as empirical mode decomposition (EMD) or bandpass filtering, is its use of surrogate data testing in order to distinguish between deterministic and random activity [261]. The success of surrogate testing for the identification of nonlinear oscillatory modes in neural data has also been demonstrated previously [314], and more generally in [315]. By verifying the presence of oscillations, and their underlying nature, e.g. whether they are nonlinear, these methods reliably inform the user which analysis approach to take. In this way, it is ensured that any oscillatory modes extracted from real experimental data are physically meaningful, and that their characteristics, including their instantaneous phases, are accurately determined. Once a significant oscillatory mode has been located and extracted using NMD, its smoothed instantaneous frequency provides $\varphi_{\mathbf{x}}^{A*}$ for use in phase fluctuation analysis, $\varphi_{\mathbf{x}}^*$ can then be extracted from the wavelet transform as before, with the parameter f_0 chosen to give sufficient time resolution to follow the noise fluctuations which are removed by NMD. An example of the use of NMD in PFA is provided in Figure 4.13, and explained further in the application to brain dynamics below.

The reliability of the presented inverse approach methods increases with data availability, i.e. a longer time series will give a more reliable result. However, when recording data from biological systems, it is not often feasible to collect hundreds of cycles of oscillation. When recording data from live subjects, for example blood flow recordings, the time of recording must be a compromise between long time series and subject comfort. In the case of cellular recordings, such as cell mem-

brane recordings via the patch clamp technique, the health of the cell can rapidly deteriorate, and thus affect the reliability of results. Therefore, it is useful to determine the lowest possible number of recorded oscillations for which we may still reliably test for chronotaxicity.

In order to address this question, two unidirectionally coupled phase oscillators (Eq. 4.24) were simulated for 1000 cycles with frequencies 1 and 0.1 Hz, with $h = 0.01$ and $\sigma = 0.07$. With coupling $\varepsilon = 2$, the system is chronotaxic. The important parameters to consider in DFA are n_{\min} and n_{\max} , the lower and upper values for the range of the first order polynomial fits performed in order to calculate α . The lower value, n_{\min} , is set to be 2 cycles of the slowest oscillation, to ensure observation of the dynamics over a longer range than one cycle. The smallest n_{\max} required to still obtain a reliable DFA exponent was observed to be $n_{\max} = 3$ cycles of oscillation (see Figure 4.12), provided that the time series is sufficiently long. The second test seeks to identify the required length of the whole time series when using these values of n_{\min} and n_{\max} in DFA. The DFA exponent was calculated from varying lengths of the same noise signals, from 3 to 10 times n_{\max} , to identify the point where the result is no longer reliable. It was found that the time series should be at least 8 times n_{\max} in order to obtain a reliable result, therefore at least 24 cycles of the slowest oscillation are required to test for chronotaxicity. However, if possible, the time series should be at least 10 times n_{\max} [316], to reduce noise by providing more data windows. Overlapping within DFA is also possible, and will go some way toward reducing noise, and improve reliability. The results shown in Figure 4.12 were obtained with an overlap of 0.8.

Whilst the value of the DFA exponent α is expected to be around 0.5 in a chronotaxic system, and 1.5 in a non-chronotaxic system, it is unlikely to be so definitive in reality. In fact, the value of α will depend on a number of factors. The type of noise in a real system is not necessarily white; however the point of phase fluctuation analysis is to identify changes in its distribution. α will also vary depending on how strong the chronotaxicity is in the system, i.e. how strongly driven

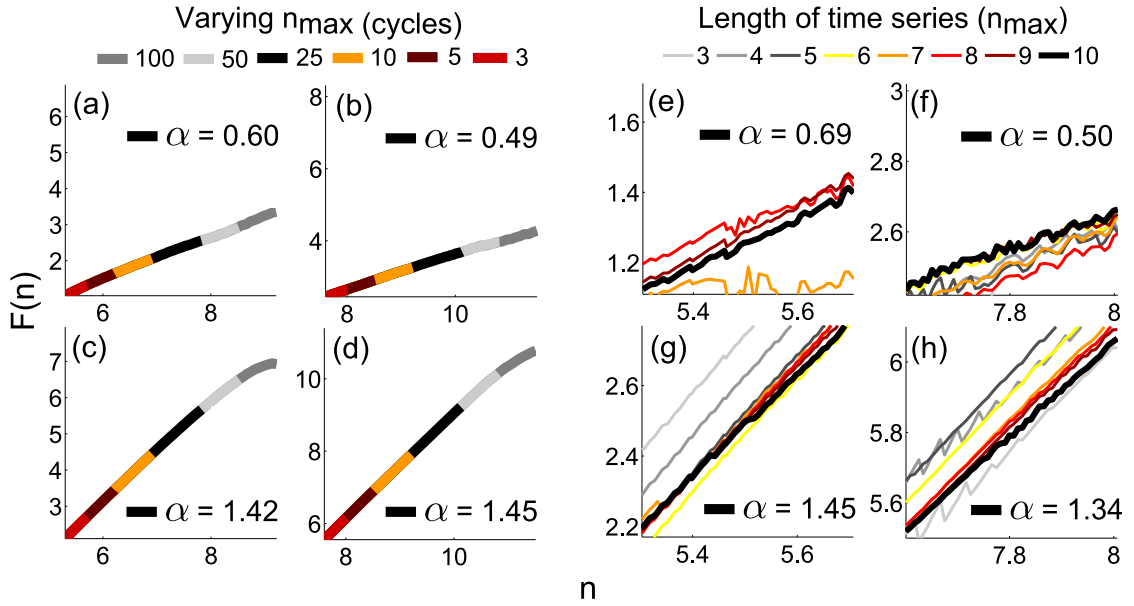


Figure 4.12: In order to test the reliability of the DFA exponent when reducing n_{\max} , the maximum number of cycles of oscillation used in its calculation was varied. (a) chronotaxic oscillation of 1 Hz. (b) chronotaxic oscillation of 0.1 Hz. (c) non-chronotaxic oscillation of 1 Hz. (d) non-chronotaxic oscillation of 0.1 Hz. The same noise signals were then tested with $n_{\max} = 3$ for different lengths of the time series from 10 to 3 times n_{\max} . Based on these results, the time series should be at least 8 times n_{\max} , thus, there should be at least 24 oscillations in the time series. However, to ensure universal applicability, the length of the time series should be at least 10 times n_{\max} , the generally accepted value in DFA [316], resulting in the requirement of 30 cycles.

the observed oscillator is. In the models presented here, this can be represented by varying the coupling strength ε ; weaker coupling will result in a higher DFA exponent as the noise is partially integrated. The ratio of the natural frequency of the chronotaxic oscillator to the frequency of the external driver, or detuning, may also affect the value of α .

4.4.3 Application to brain dynamics

Chronotaxicity will manifest in nature as a result of a driving system which is strong enough such that the oscillatory response system maintains stability in its frequency and amplitude, even when subject to continuous external perturbations. Chronotaxicity was previously demonstrated in the heart rate variability (HRV) [302], when influenced by paced breathing. It has been shown that the main

direction of coupling between the cardiac and respiratory oscillators is the influence of the respiration on the heart rate, known as respiratory sinus arrhythmia (RSA), and this was clearly demonstrated. Here, an example of the application of phase fluctuation analysis to real experimental data is provided, in the form of an electroencephalogram (EEG) recording from an anaesthetised human subject.

Distinct oscillations have long been observed in brain waves, as recorded by EEG. Briefly, from lowest to highest frequency, there are at least 5 frequency bands which have been identified in approximately the following frequency intervals: delta (0.8–4 Hz), theta (4–7.5 Hz), alpha (7.5–14 Hz), beta (14–22 Hz) and gamma (22–80 Hz). Different frequencies of oscillation have been attributed to distinct states of the brain. For example, the alpha and theta bands have been shown to reflect cognitive and memory performance [317]. One active area of research utilising the information provided by these oscillations is in attempts to quantify the depth of anaesthesia based on their temporal evolution in different states of consciousness. Despite the worldwide use of general anaesthesia (GA) daily, the mechanisms leading to this state are still poorly understood in terms of how it truly affects the brain. Thus, brain-state monitoring is still not an accepted practice in GA, due to the lack of reliable markers [318]. However, recent studies in which the spectral power of the oscillations in different frequency bands has been tracked both temporally and spatially during anaesthesia with propofol have shown promising results. For example, it was shown that during consciousness, alpha oscillations are concentrated in occipital channels, whilst during propofol induced anaesthesia, these oscillations are concentrated in frontal channels [318]. An increase in power in the frequency interval 0.1–1 Hz (delta) was also observed in this study during anaesthesia. Understanding the mechanisms underlying these changes in brain function could not only lead to new approaches to anaesthesia monitoring but may be widely applicable in many areas of neuroscience, including in the study of various neurological disorders.

It has been clearly demonstrated that phase interactions are highly important

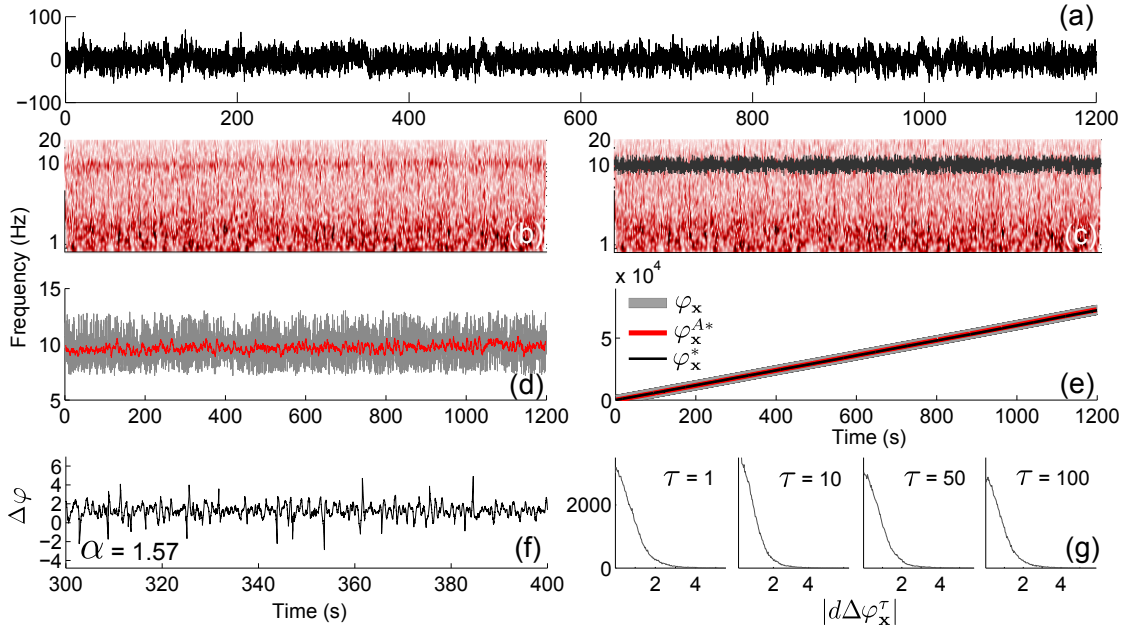


Figure 4.13: Example of the application of phase fluctuation analysis to an EEG signal obtained from the forehead of an anaesthetised patient, shown in (a). (b) The continuous wavelet transform of the EEG signal in (a). (c) Using nonlinear mode decomposition (NMD)(see text), a significant oscillatory mode in the alpha frequency band was identified and extracted (dark grey line). (d) The instantaneous frequency extracted using NMD (grey line), and smoothed using a moving average of 4 seconds (red line). (e) The extracted phases of the mode from NMD (grey), smoothed NMD (red), and from the CWT (black) with $f_0 = 1.5$. (f) $\Delta\varphi_x$ was calculated as $\varphi_x^* - \varphi_x^{A*}$. The DFA exponent was calculated and was 1.57, suggesting that the system is not chronotaxic. Checking for phase slips in (g) shows no change in distribution.

for healthy brain functioning, with by far the most widely reported observations revolving around phase synchronization, which can, as an example, be used to infer information about short and long range behaviours [319]. Brain waves arise from networks of synchronized neurons, and the detected phase of these oscillations determines the degree of excitability of the neurons, and influences precise discharge times of the cells in the network, therefore affecting relative timing of action potentials in different brain regions [320].

The problem of the extraction of phase from EEG data has been approached from many directions, some more physically meaningful than others. Early approaches to the investigation of phase interactions between brain waves used spectral coherence, but this does not separate phase and amplitude components, thus amplitude effects may influence coherence values when only phase locking infor-

mation is required [321]. A widely used phase extraction approach is the use of the Hilbert transform (see above) to obtain the analytic signal [322], usually preceded by band-pass filtering in the frequency interval of interest, highlighting the necessity of the separation of the oscillation of interest from background brain activity, either other oscillations or noise. Lachaux *et al.* recognised the necessity of the separation of amplitude and phase when seeking to detect synchrony between brain waves, introducing phase-locking statistics (PLS) [321] to measure the phase covariance between two signals, verified by surrogate testing. This method also allows for non-stationarity in the signal. However, based on very narrow band-pass filtering, this method does not allow for time-variability in the natural frequency of oscillation, but it did highlight the usefulness of complex wavelets in the extraction of phase dynamics. The Hilbert transform and wavelet convolution methods were compared in the analysis of neural synchrony, and found not to differ substantially [323], but both these methods relied on narrow band-pass filtering beforehand. However, the use of band-pass filtering to extract an oscillatory EEG component with a time-varying frequency has limited usefulness. An instantaneous frequency defined from the analytic signal obtained from band-passing in a particular frequency range in a real signal containing multiple spectral components and noise may be ambiguous and meaningless [319]. To address this problem, ridge extraction methods [311] applied to the complex wavelet transform were used to track the instantaneous frequency of a single oscillatory mode [319], providing a much higher precision of phase extraction, and importantly allowing the phase dynamics of nonautonomous systems to be traced accurately in time. Another, rarely considered, issue when tracing instantaneous frequencies in time is the presence of high harmonics in the signal. Narrow restriction of the frequency range will remove these harmonics, and thus remove valuable intra-cycle phase information. This issue has been addressed directly by the introduction of nonlinear mode decomposition [261]. The inverse approach methods applied here take into account all these issues in order to extract accurately the instantaneous phase of brain

oscillations.

In order to demonstrate the method and search for evidence of chronotaxicity in the phase dynamics of brain waves, phase fluctuation analysis was applied to a real EEG signal. The EEG of an anaesthetised subject was recorded for 20 minutes at 1200 Hz (Figure 4.13 (a)) by researchers involved in a previous study - Brain, Respiration And Cardiac Causalities In Anaesthesia (BRACCIA) (see ethics declaration). The signal was resampled to 100 Hz by splitting the time series into windows, and setting their mid-point to their mean. As expected, strong oscillations were observed in the alpha and delta frequency bands. Nonlinear mode decomposition extracted the oscillatory mode around 10 Hz in the alpha frequency band and identified it as physically meaningful through surrogate testing (Figure 4.13 (c)). The instantaneous frequency of this mode was then smoothed using a moving average of 4 seconds. This value was chosen to provide the best match between the instantaneous phase of the extracted nonlinear mode $\varphi_{\mathbf{x}}$ and its smoothed version $\varphi_{\mathbf{x}}^{A*}$. As NMD by nature removes the noise from the modes which it extracts, $\varphi_{\mathbf{x}}^*$ must then be extracted from the continuous wavelet transform with a time resolution which will allow the noise fluctuations to be included in the extracted mode. Here, it is very important to check that the extracted phase corresponds to that extracted using NMD (see Figure 4.13 (e)). Once the viability of the extracted fluctuations is confirmed, $\Delta\varphi_{\mathbf{x}}$ can be calculated as $\varphi_{\mathbf{x}}^* - \varphi_{\mathbf{x}}^{A*}$. The DFA exponent of $\Delta\varphi_{\mathbf{x}}$ was then calculated, and was 1.57. The distribution $|d\Delta\varphi_{\mathbf{x}}^{\tau}|$ was calculated to check for phase slips in the extracted phase fluctuations, but the distribution did not change over any timescale, τ .

The analysis suggests that the alpha oscillation as extracted is not chronotaxic. However, the current inverse approach methods are based on a single point attractor and single response system. As discussed by Sheppard *et al.* [324], the spectral peaks observed in the EEG, including those observed in the alpha band, result from frequency synchronization between thousands of neurons. In this sense, the observed phase is in fact only a statistical measure, highlighting the preferred phase

of the underlying ensemble of neurons. A method to quantify this was provided by the mean-field variability index, κ , which changes depending on the interactions in the observed network of oscillators [324]. For a non-interacting network, with purely random phasors, κ will converge to 0.215, whereas in a state of complete phase synchronization, κ will tend to zero. Based on the current assumptions of the inverse approach methods, if the detection of chronotaxicity relied only on phase dynamics, we would expect the value of κ to tend to zero in a chronotaxic system. However, when applied to real EEG data, κ was actually greater than 0.215 in most cases, suggesting amplitude synchrony (possibly intermittent), intermittent phase coherence, or both. Therefore, it is apparent that in the case of brain dynamics, to truly test for chronotaxicity, it must be reconsidered within a network of many oscillators, as known to be present in the brain, rather than the relatively low numbers of coupled oscillators considered here. Here, the driving system may be a subnetwork of synchronized oscillators or the mean-field or mean-phase of ensembles of neurons, influencing other areas of the brain in complex ways, with both temporal and spatial dynamics to take into account.

The presented methods are also restricted by the fact that they are currently only applicable to determining chronotaxicity in phase dynamics. Traditionally, in brain dynamics, it is the amplitude of the oscillations observed in the distinct frequency bands which receives the most attention, although consideration of phase dynamics is gaining popularity [325]. In addition to the dynamics within individual frequency bands, there are also interactions between frequency bands [326], known as cross frequency coupling (CFC). CFCs have not only been observed manifesting themselves as phase-phase interactions [327], but also as amplitude-phase [328] and amplitude-amplitude interactions [329]. Whilst some efforts have been made to isolate phase information in neural oscillations [330], the importance of amplitude-phase interactions cannot be ignored, for example the observed modulation of gamma amplitude by the phase of theta oscillations has been identified as a code utilised in multi-item formation in the brain [331]. Other functional roles

of amplitude-phase coupling have also been highlighted [332]; thus it is clear that both amplitude and phase must be considered simultaneously to characterise brain dynamics accurately. Indeed, phase-amplitude coupling has been demonstrated during anaesthesia [333], meaning that the current inverse approach methods may be insufficient to determine chronotaxicity in this system.

4.5 Summary

The recent formulation of chronotaxic systems provided a completely novel approach to the characterisation of time-varying dynamics in real data. Crucially, it provides a framework in which systems may be time-varying, both in terms of their amplitude and phase dynamics, continuously perturbed, and yet still exhibit determinism. Whilst the apparent complexity of some real time-varying oscillatory systems previously led to their consideration as stochastic or chaotic, chronotaxicity facilitates a much more natural approach to the description of their dynamics. The introduction of this approach required the development of new inverse approach methods for the detection of chronotaxicity in time series arising from dynamical systems. Here, the currently available methods for the identification of chronotaxicity from a single time series were reviewed, and various issues regarding their implementation were expanded, in order to facilitate the application of the methods to any data set containing at least one oscillatory component. This ability to characterise oscillations in terms of their chronotaxicity, i.e. to determine whether the observed dynamics arise as a result of influence from an external driver, provides the potential to unlock new information about dynamical systems and their interactions with their environment.

As they currently stand, the inverse approach methods for the detection of chronotaxicity are only applicable in systems in which the amplitude and phase dynamics are separable, as they are applied directly to the extracted phases of the system, and all amplitude information is discarded. This assumption is valid if one is considering that the amplitude dynamics of a chronotaxic system corresponds

to the convergence of the system to the limit cycle, influenced only by a negative Lyapunov exponent and external perturbations, whilst the phase dynamics corresponds to convergence to the time-dependent point attractor, which is also characterized not only by a negative Lyapunov exponent and external perturbations, but also by the motion of the point attractor itself [302]. As it is this point attractor in phase dynamics which we are interested in, separation of amplitude and phase follows naturally. Using this approach, an example of chronotaxic dynamics was successfully demonstrated in a real system, in the case of heart rate variability [302]. However, in generalized chronotaxic systems [287], the amplitude and phase are not required to be separable, providing even greater applicability to real systems, allowing amplitude-amplitude and amplitude-phase interactions, in addition to the phase-phase dynamics considered in [285, 286]. Therefore, the incorporation of the ability to identify these new possibilities for chronotaxicity is crucial in the further development of these inverse approach methods. This will then provide the means to detect chronotaxicity in systems where amplitude and phase are not separable, as previously discussed in the case of brain dynamics. The current definition of chronotaxicity is based on a time-varying point attractor, exerting influence over a system such that it can remain stable despite continuous external perturbations. Numerical results presented here assume that this point attractor results from a single oscillatory drive system, acting on a maximum of two coupled oscillators. However, as highlighted in the brain dynamics example, in reality it must be considered that this point attractor could result from multiple interacting influences, for example a network of oscillators, perhaps acting as one synchronized drive system.

Regardless of the mechanisms of the underlying oscillations, if they manifest as a point attractor, characterisation of their chronotaxicity necessitates the application of methods which can extract both their phase and amplitude dynamics with utmost accuracy. Methods reliant on averaging do not provide the required precision. Both amplitude and phase information can be extracted from the con-

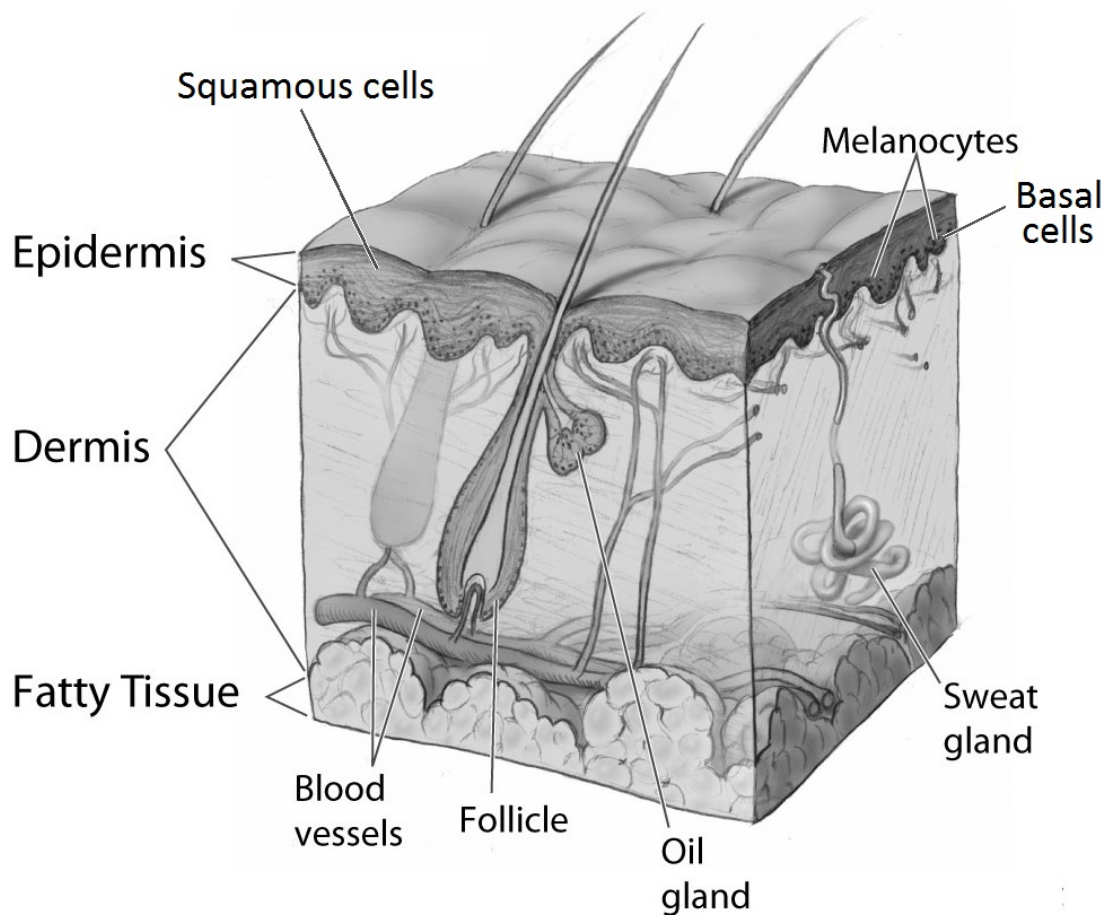
tinuous wavelet transform, a fact which may be utilised in the further development of inverse approach methods for the detection of chronotoxicity. Extending these methods to simultaneously take into account both phase and amplitude dynamics, whilst incorporating the effects of their couplings, may lead to a method based on an optimal combination of time-frequency representations and effective connectivity methods such as dynamical Bayesian inference. This will then provide even wider applicability to real oscillatory systems such as those observed in brain dynamics.

5. Blood flow dynamics in skin melanoma

Skin melanoma provides a unique opportunity to monitor the blood flow of a malignant tumour *in vivo*. In this chapter, it will be described how blood flow data obtained from the Hospital of Pisa, Italy, were analysed using the techniques discussed previously to investigate whether blood flow dynamics is altered in skin malignant melanoma. The results provide insights into the physiological mechanisms of melanoma vasculature, and were used in the development of a noninvasive diagnostic test which may prevent many unnecessary biopsies if verified in a larger study.

5.1 Cancer

In cancer research, attempts to reduce problems to their smallest possible constituents has provided a wealth of new knowledge in fields such as molecular biology and genetics, but a general cure for all cancers seems unfeasible when viewed from these angles, due to their huge variability between cancer types. New collaborations with scientists from increasingly varying fields is leading to exciting new perspectives on old problems, with attempts to quantify and understand the characteristics that all cancers have in common, in addition to how they vary. These ‘hallmarks of cancer’ are: self sufficiency in growth signals and insensitivity to anti-growth signals, limitless replicative potential, resistance to cell death, ability to invade tissues and metastasize, and induction of angiogenesis [334]. There



National Cancer Institute

Figure 5.1: Diagram showing the layers, components and different cells types found in the skin. Modified from [335]

are also further emerging hallmarks receiving attention in their own right; the re-programming of energy metabolism and the evasion of immune destruction [134]. This chapter will focus mainly on the effects of angiogenesis, whilst chapter 7 will address the widely observed phenomenon of altered energy metabolism in cancer cells.

5.1.1 Skin cancer

Skin cancers are usually divided into two groups, melanoma and non-melanoma skin cancers (NMSC), of which the latter account for 90% of all skin cancers registered in the UK and Ireland [336]. There are two main layers in the skin, the upper layer, or epidermis, and the layer beneath it, known as the dermis (see

Figure 5.1). The epidermis is made up of three types of cells, squamous cells, basal cells and melanocytes, all of which may become cancerous, with varying prognoses.

Basal cells are located at the bottom of the epidermis and their carcinogenesis results in basal cell carcinoma (BCC). BCC is the most common skin cancer in the UK and Ireland, accounting for 74% of all NMSC diagnoses [336]. It is usually very slow growing, almost never spreading to other parts of the body, although it can, very rarely, spread downwards into deeper tissues, and sometimes bones, causing treatment to be much more difficult. BCC generally begins as a small shiny red spot, that may bleed, or develop into an ulcer that will not heal. When found at an early stage, basal cell carcinoma is most likely to be completely cured, though some may come back after treatment, known as local recurrence.

Squamous cell carcinoma (SCC) is a cancer of the cells called keratinocytes, also found in the epidermis. SCC is the second most common skin cancer in the UK, accounting for 23% of NMSC [336]. Squamous cell carcinoma is a slow growing cancer, and is rarely aggressive, only spreading if left for a very long time. The prognosis for SCC is generally very promising.

In contrast, melanoma is the skin cancer with the worst prognosis. Whilst accounting for only a small proportion of overall incidence, melanoma is responsible for 75% of all skin cancer related deaths in the USA [337]. Melanoma develops from melanocytes, found at the very bottom of the epidermis. Half of all melanomas start in normal skin, with the other half developing from pre-existing moles. New cases of melanoma continue to increase, especially in young women (15-34) [338]. Skin cancer is still most common in older people, however, as the risk of most cancers rises with age. Risk factors for melanoma include fair skin, excessive UV light exposure, sunburn, previous occurrence of melanoma and reduced immunity. Skin cancer is very rare in children under 14, and also in people with black or brown skin, as their higher melanin levels provide more natural protection from the harmful UV rays of the sun. Melanomas grow very quickly, and soon spread to surrounding layers of skin, underlying tissues and then the rest of the body via the

circulatory system. Therefore, early diagnosis is most crucial in melanoma above all skin cancers.

5.1.2 Hypotheses

Combining the aforementioned time-frequency analysis methods and the coupled oscillator model of the cardiovascular system as observed in blood flow provides the tools to test the following hypotheses:

1. Blood flow regulation within a skin malignant melanoma differs from both healthy skin, and other non-cancerous lesions which share similar characteristics, such as atypical naevi, benign naevi and psoriasis.
2. Differences which arise may be used in the development of a diagnostic test which can differentiate between malignant melanoma and atypical naevi.

5.2 Experimental protocol

To test these hypotheses, 94 patients in total were recruited in the dermatology unit of the University Hospital of Pisa from February 1st 2011 to May 30th 2013. 55 of these subjects presented with clinically atypical naevi, suspected as malignant melanoma by a dermatologist, and were sent for excision of the lesion of interest and subsequent histological examination. A clinically atypical naevus was defined as a skin melanocytic lesion which shared at least three of the clinical features of melanoma (asymmetry, border irregularity, colour variability or a diameter greater than 6mm [179]). As a control group, 30 clinically healthy patients were recruited with typical benign naevi, also known as common moles. Nine patients with psoriasis were also included in the study, as further controls. Psoriasis patients were included due to their similar pathology to melanoma, including excessive cell proliferation and angiogenesis [186], in an attempt to isolate the effects of cancer on blood flow regulation from those known to be induced by inflammation [339]. During histological examination, out of the 55 atypical lesions studied,

Lesion type	N ^o cases	Total (Male)	Age range (Median)	Locations
Melanoma				
Super. spread.	6			
Nodular	3	10(4)	39–80 (62)	Abdomen (1), leg (3), flank (1), shoulder (1), arm (2), face (2)
Lentigo	1			
Atypical naevi				
Compound	24			Clavicle (1), leg (6), chest (1), flank (1), shoulder (6), lumbar (2), thorax (7), gluteal (2), abdomen (4), arm (2), foot (1)
Junctional	6	33(18)	17–73 (41)	
Baso. epithel.	1			
Dysplastic	2			
Benign naevi				
Compound	3			Arm (3), ankle (1), shoulder (4), foot (3), leg (6), flank (1), thorax (2), front (1), side (1), abdomen (8), chest (4), breast (2), back (1)
Junctional	4			
Dermal	2	37(18)	21–78 (46)	
Blue	1			
Acral comp.	1			
Clin. benign	26			
Psoriasis				
Clin. diagnosed	9	9(8)	35–76 (63)	Leg (6), shoulder (1), arm (1), flank (1)

Table 5.1: Type, gender, age and location information for all subjects studied.

11 resulted in a positive diagnosis for melanoma, 33 were defined as histologically atypical and 11 were histologically typical. For the purposes of blood flow dynamics analysis, the 11 clinically atypical yet histologically benign lesions are considered in the benign group, whilst during calculation of any diagnostic test they will be considered atypical, due to the initial diagnosis which they received. Patient information can be found in Table 5.1.

Blood flow monitoring was carried out on all recruited subjects using laser Doppler flowmetry (LDF). Recordings occurred in the morning in an air conditioned room (22-24°C), with the subject in supine position, after an acclimatization period of 20 minutes. Subjects were asked to abstain from food, drugs, alcohol, coffee and tea for 8 hours prior to the measurement. Following acclimatization, blood flow was monitored in two locations, at the centre (geometric mean) of the lesion of interest and in the contralateral location on healthy skin. In all cases but psoriasis, a further recording was made immediately following these two, at the

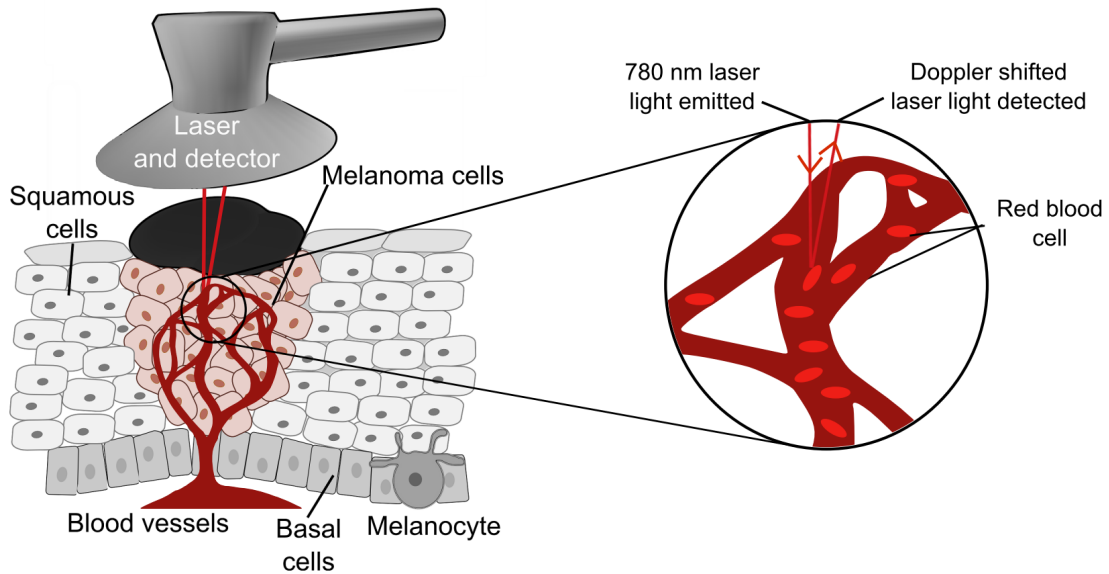


Figure 5.2: Diagram of the laser Doppler probe placed above the lesion of interest, in this case a melanoma lesion.

lesion margin. All recordings were for 30 minutes. Blood flow was measured using single point LDF apparatus (Periflux PF4, Perimed, Jarfalla, Sweden) equipped with an unheated probe (PF408). The probe had a fibre separation of 0.25mm. This allows skin blood flow to be detected in a tissue volume of around 1 cubic millimetre. Blood flow is expressed as arbitrary perfusion units (PU) of output voltage (1 PU = 10mV). The LDF probe was fixed to the lesion of interest using an annular double sided adhesive disc (see Figure 5.2). The laser characteristics were: wavelength – 780nm, bandwidth – 10 Hz-19 kHz, time constant – 0.1s, sampling frequency – 32 Hz. Probe calibration was performed before each session using a specialized device (Perimed, Jarfalla, Sweden) containing colloidal latex particles whose Brownian motion provides standardised values. Blood flow signals were recorded continuously by an interfaced computer (Compaq, Hewlett Packard, Netherlands) equipped with dedicated software (Perisoft, Perimed, Jarfalla, Sweden).

5.2.1 Exclusion criteria

Patients were excluded if they had one or more of the following conditions: age > 80 years, congestive heart failure, recent myocardial infarction, serious cardiac

arrhythmia, chronic inflammatory diseases, other neoplastic diseases, untreated arterial hypertension, severe liver diseases, untreated type 2 diabetes mellitus, type 1 diabetes mellitus, severe renal failure and haemodialysis treatment.

5.3 Analysis

5.3.1 Pre-processing

Signals were inspected for viability prior to analysis. Following this inspection, 5 subjects were removed from the analysis, due to erroneous spikes in the data, most likely an optical effect. Movement artefacts and other obviously non-physical events in the data were removed using either linear interpolation or by trimming the signal. This resulted in a final data set of recordings from 10 melanomas, 33 atypical naevi, 37 benign naevi and 9 psoriasis lesions.

Other artefacts which appeared to be noise could result from different skin types, for example glabrous skin, or heterogeneity of the area under observation, and so were included. Every effort was made to retain as much original data as possible, whilst removing unphysiological artifacts which would greatly alter the results. In a clinical setting, these artefacts could be minimised by producing hardware specifically designed to deal with these skin lesions, for example improved probe attachment.

Prior to analysis all data were detrended using a moving average method to remove low frequency information below the scope of this study, i.e. below the lower limit of the lowest endothelial interval VI at 0.005 Hz, requiring a window size of 200 seconds.

5.3.2 Statistics

The distribution of any group to be compared was tested using the Lilliefors test for normality, which did not consistently find normal distributions of data in any case. Therefore, all statistical tests used were non-parametric, i.e. did not assume

an underlying distribution, facilitating more robust conclusions. When all groups were compared, the Kruskal Wallis ANOVA test was used. The Kruskal Wallis test is used to test whether two or more independent samples originate from the same distribution, and does not assume a normal distribution. If significance was found by this, then pairs of groups were then tested using either the Wilcoxon signed rank test for paired data, or the Wilcoxon rank sum test for unpaired data [340]. The signed rank test is used to test whether two matched samples come from the same distribution, whilst the rank sum test does not require that the samples are matched. For example, to compare two groups of simultaneous blood flow recordings within a group, recorded on opposite sides of the body, the signed rank test would be used. In contrast, to compare the blood flow recordings on the left side of the body in one group (e.g. melanoma), to those recorded in another group (e.g. benign), the rank sum test would be used. Both tests involve the summation of ranks. Linear regression was computed using the Theil-Sen estimator [341, 342] which is a nonparametric method for simple linear regression which is very robust to outliers, and correlation quantified by Kendall's τ [343], which is a measure of rank correlation (the similarity of the orderings of the data when ranked). Significance was considered as $p < 0.05$. All boxes in box and whisker plots demonstrate the median and 25th and 75th percentiles of the data. The lowest point of the whiskers is located at $q_1 - w(q_3 - q_1)$ and the highest point at $q_3 + w(q_3 - q_1)$ where q_1 and q_3 are the 25th and 75th percentiles, respectively. w was 1.5 by default [344]. Points outside this range were classed as outliers.

5.3.3 Time domain analysis

Heart rate and heart rate variability

Instantaneous heart rates were calculated by extracting the cardiac oscillation from the blood flow signals recorded in each subject using nonlinear mode decomposition. Mean heart rates were calculated as the mean of these extracted signals. Significant differences in mean heart rate were found between groups ($p = 0.0049$),

Average blood flow (PU)			
	Centre	Margin	Contralateral
Melanoma	126.8 (80.0–158.6)	77.1 (53.4–91.8)	14.2 (11.8–20.6)
Atypical naevi	15.2 (10.1–29.1)	16.6 (10.4–32.5)	12.5 (10.8–16.0)
Benign naevi	18.6 (9.5–23.9)	19.1 (12.2–28.0)	13.9 (11.7–16.9)
Psoriasis	111.3 (85.8–125.6)	N/A	15.7 (9.8–17.5)
<i>p</i>	0.0000	0.0004	0.5662

Table 5.2: Medians (inter quartile range) of the means of all blood flow signals in perfusion units (PU) for lesion centres, lesion margins and contralateral skin. p values are as calculated for each location using the Kruskal Wallis test. $n = 9, 10, 33$ and 37 for psoriasis, melanoma, atypical naevi and benign naevi respectively.

with the melanoma group exhibiting significantly higher heart rates than all other groups except psoriasis (see Figure 5.3). This may be a result of the significant difference in the distribution of ages between groups, with the melanoma and psoriasis groups having a higher median age than the atypical and benign groups. It has previously been shown that mean heart rate increases with age, and also that this effect varies with gender [345]. However, there was no significant correlation between age and mean heart rates when considering all subjects ($\tau = 0.1123$, $p = 0.1230$). Standard deviation of heart rate was calculated from the extracted instantaneous heart rates for each group, and were found not to differ significantly between groups ($p = 0.0622$). A significant negative correlation was observed between age and heart rate variability ($\tau = -0.3234$, $p = 0.0000$). This effect has been previously demonstrated in healthy individuals [112] and therefore cannot be linked to the presence of melanoma or psoriasis.

Mean blood flow

Mean blood flows were calculated for all subjects and locations (Table 5.4). Blood flow recorded at lesion centres differed significantly between groups ($p = 0.000$). This significance arose from the increased blood flow in melanoma and psoriasis when compared with both atypical and benign naevi. No difference was found between melanoma and psoriasis ($p = 1$), or atypical and benign naevi ($p = 0.7418$) in terms of mean blood flow recorded in the centre of lesions (see Figure 5.4).

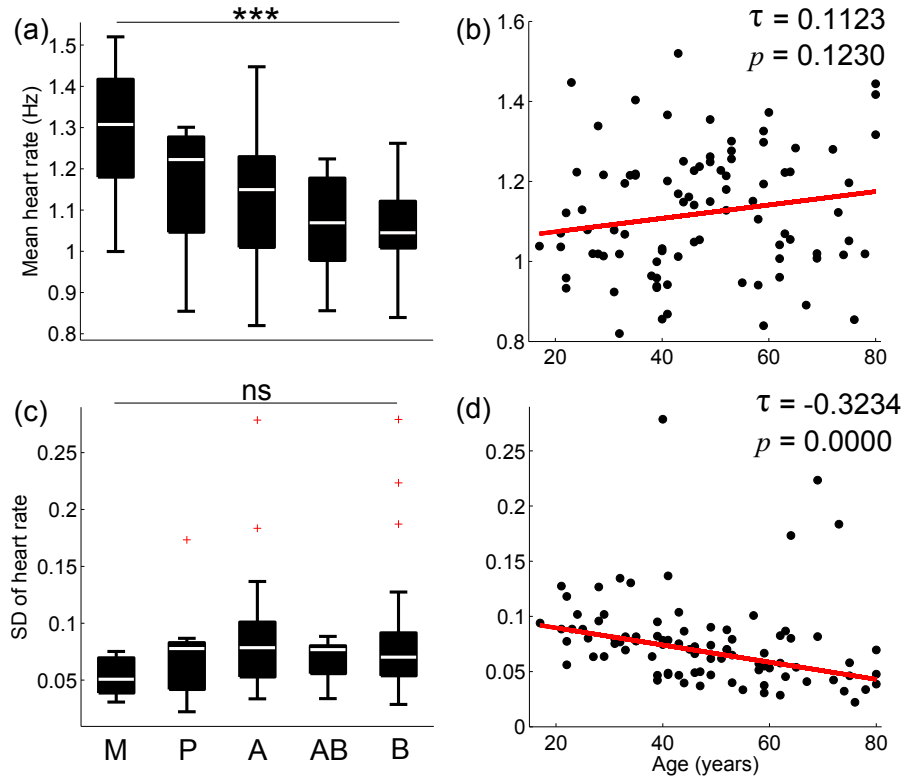


Figure 5.3: (a) Box and whisker plots of mean heart rate for all groups studied. (b) Scatter plots of age vs. mean heart rate (c) Box and whisker plots of standard deviation of heart rate calculated for all groups. (d) Scatter plot of age vs. standard deviation of heart rate for all groups. M – melanoma ($n = 10$), P – psoriasis ($n = 9$), A – atypical naevi ($n = 33$), AB – histologically benign naevi ($n = 11$), B – clinically benign naevi ($n = 26$). Outliers in boxplots are shown as red crosses. ns = not significant. *** = $p < 0.001$. Theil-Sen regression lines are shown in red in (b)&(d).

Blood flow recorded at lesion margins also differed significantly between groups ($p = 0.0004$), with melanoma mean blood flow significantly higher than both atypical ($p = 0.0007$) and benign lesions ($p = 0.0000$). As in lesion centres, blood flow in atypical and benign lesions did not significantly differ at lesion margins ($p = 0.9531$), see Table 5.3. Contralaterally recorded blood flows on healthy skin did not differ between groups ($p = 0.5662$). When comparing blood flows for each subject between sides, i.e. centre vs. contralateral means, central blood flow was significantly higher in melanoma ($p = 0.0020$), psoriasis ($p = 0.0039$) and atypical naevi ($p = 0.0179$), but not in benign naevi ($p = 0.3940$).

Stucker *et al.* quantified the differences in blood flow between malignant melanoma and benign and atypical lesions based on mean blood perfusion values

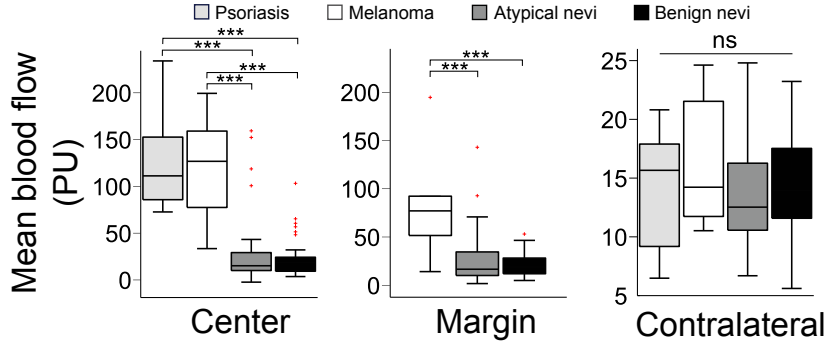


Figure 5.4: Box and whisker plots of mean blood flow calculated for each group and location. Outliers in boxplots are shown as red crosses. ns = not significant. *** = $p < 0.001$. Margin data is not available for psoriasis. $n = 9, 10, 33$ and 37 for psoriasis, melanoma, atypical naevi and benign naevi respectively.

Individual rank-sum results

	P vs. M	P vs. B	P vs. A	M vs. B	M vs. A	B vs. A
Centre	1	0.0000	0.0001	0.0000	0.0000	0.7418
Margin	N/A	N/A	N/A	0.0000	0.0009	0.9531

Table 5.3: Rank sum comparisons of the distribution of mean blood flow between all groups.

of signals recorded using laser Doppler perfusion imaging [11]. They found that the mean blood flow recorded in malignant melanomas was always at least 1.8 times higher than in healthy skin, and used this to develop a diagnostic test with a sensitivity of 100% and sensitivity of 85% when including clinically benign lesions, but this was reduced to 48% when only considering clinically suspicious lesions. Applying this cut off to the results obtained in the current study by comparing blood flow recorded in lesion centres and contralateral skin provides a sensitivity of 100% and a specificity of 70% when considering atypical and benign lesions and 61% when considering only atypical lesions. 10 out of 10 melanoma lesions met the criteria of mean blood flow recorded at lesion centres being at least 1.8 times higher than that recorded in contralateral skin, whilst 17 out of 44 atypical lesions and 4 out of 26 clinically benign lesions also met the criteria and would be diagnosed as melanoma in this test.

This approach was also applied to the blood flow signals recorded at lesion margins in the current study to investigate the effect of a different recording lo-

Subject	Sex	Age (years)	Tumour size (cm)	Clark level	Breslow depth (mm)	Ulceration
1	F	51	1.1 × 0.7	II	0.45	no
2	F	80	2.5 × 2.5 × 1.5	IV	15	yes
3	M	58	1.2 × 0.7 × 0.4	III–IV	3	yes
4	M	58	1.7 × 1.0	III–IV	0.35	no
5	F	80	1.1 × 0.7 × 0.3	IV	3.1	no
6	M	64	0.6 × 0.5	III	0.7	no
7	F	39	0.4 × 0.3	II	0.2	no
8	F	80	1.8 × 1.3	IV	0.8	no
9	M	74	1.5 × 0.9	II	0.45	no
10	F	43	0.5 × 0.4	III	0.4	no

Table 5.4: Histological characteristics of melanoma lesions.

cation on specificity. Sensitivity of 100% was achieved using a cutoff of the mean blood flow at lesion margins being greater than at contralateral locations by at least a factor of 1.26. 21 atypical lesions and 12 benign lesions also met this criterion, resulting in sensitivity of 52% when considering only atypical lesions and 53% when also including benign lesions. These values are not an improvement on the specificity achieved using dermoscopy [182]. This highlights the necessity of further investigation beyond average perfusion values in the characterization of melanoma blood flow for the purposes of diagnosis.

5.3.4 Histological results

All lesions diagnosed as clinically atypical underwent histological examination at the 3rd Pathology Unit of Pisa University Hospital, for diagnostic purposes and to examine the surrounding vasculature. Intra- and peri-lesional vessels were highlighted with anti CD34 Mab (Ventana Medical System). Each sample was examined under low power to identify the region with the highest number of microvessels, or ‘hot spot’. Two 250× fields (25× objective lens and 10× ocular lens) were evaluated to assess the number of microvessels, or microvessel density. Figure 5.5 shows highlighted intra- and peri-lesional vessels in a malignant melanoma. Table 5.4 shows diagnostic information for the confirmed melanoma cases. Intra-lesional

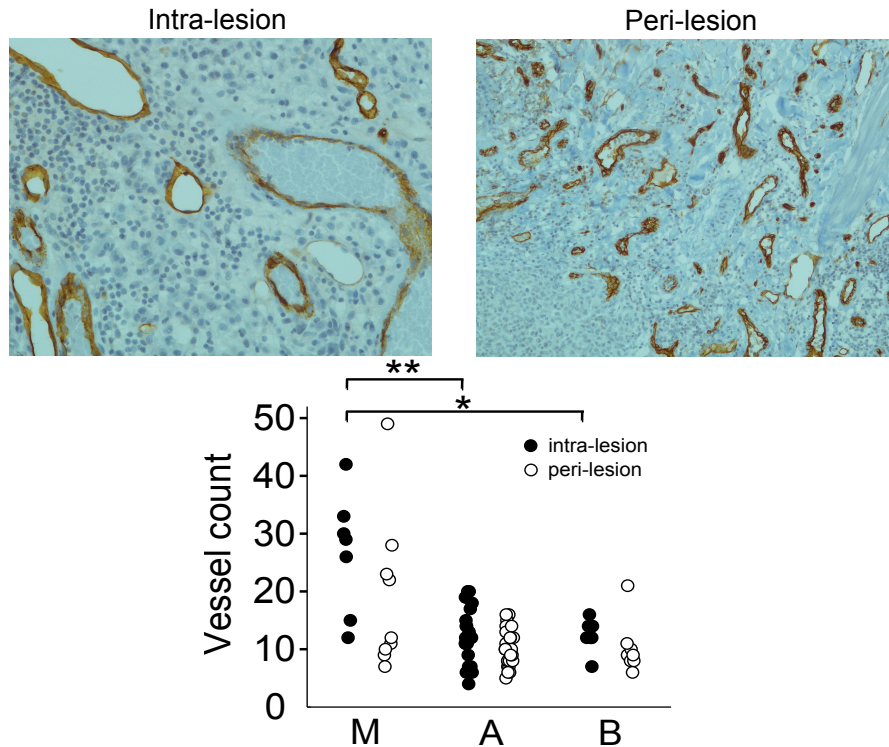


Figure 5.5: Top – Anti CD34 Mab highlighted vessels in a malignant melanoma lesion. Provided by Marco Rossi. Each sample was examined to find the region with the highest number of microvessels, or ‘hot spot’. Bottom – Vessel counts in the ‘hot spot’ in all histologically examined lesions. M – melanoma ($n = 7$ intra, 9 peri), A – atypical naevi ($n = 23$ intra, 27 peri), B – histologically benign naevi ($n = 7$ intra, 8 peri). ** = $p < 0.01$, * = $p < 0.05$.

microvessel density was significantly higher in melanoma than in atypical naevi ($p = 0.0006$), but this was not the case for peri-lesional vessels ($p = 0.2131$) (Figure 5.5). When including all lesions which underwent histological examination, a significant, positive correlation was found between mean blood flow at centres and intra-lesional vessel counts ($\tau = 0.2360$, $p = 0.0470$) (see Figure 5.6). However, no correlation was found between mean blood flows at margins and peri-lesional vessel counts ($\tau = 0.0329$, $p = 0.7679$). A significant positive correlation was found between mean blood flow at centres and lesion area ($\tau = 0.3165$, $p = 0.0009$), an effect that is explained by another significant positive correlation found between lesion area and intra-lesional vessel count ($\tau = 0.4136$, $p = 0.0005$). This provides evidence that, as expected, larger lesions have more blood vessels and are more perfused.

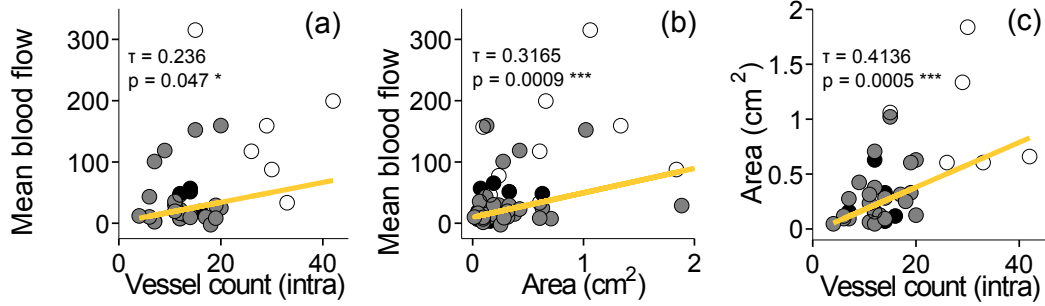


Figure 5.6: Correlations between histological parameters and mean blood flows. (a) Intra-lesion vessel count vs. mean blood flow. (b) Lesion area vs. mean blood flow. (c) Intra-lesion vessel count vs. area. White – melanoma ($n = 7$), grey – atypical ($n = 23$), benign – black ($n = 7$). $*$ = $p < 0.05$, $***$ = $p < 0.001$. Theil-Sen regression line is shown in yellow.

5.3.5 Time-frequency analysis

Wavelet analysis was performed on the signals using custom MatLab codes (see Chapter 4), with a Morlet wavelet of central frequency $f_0 = 1$. Time-averaged wavelet power was calculated for all signals. Absolute power values were significantly higher in both psoriasis and melanoma when compared to atypical and benign naevi. However, in contrast to their mean flows, the spectra of melanoma and psoriasis highlight differences between the groups at some frequencies in the neurogenic and myogenic intervals, whereas the power spectra of atypical and benign naevi do not differ at any frequency (Figure 5.7). The clear differences between the power spectra at lower frequencies between psoriasis and melanoma were investigated in order to find out whether they could be used to discriminate between groups. Figure 5.7(c) shows the calculated ratios between the total power in the cardiac interval and the sum of the power in all low frequency intervals (III, IV, V & VI). To obtain a sensitivity of 100%, a cut-off of 0.56 is required for this data set, as this is the lowest value for this ratio that was observed in melanoma. Using this as a test gave sensitivities of 55.6%, 63.6% and 84.6% for psoriasis, atypical naevi and benign naevi, respectively. Whilst promising, this test alone does not provide adequate specificity.

The global differences in power between groups result in difficulty in the com-

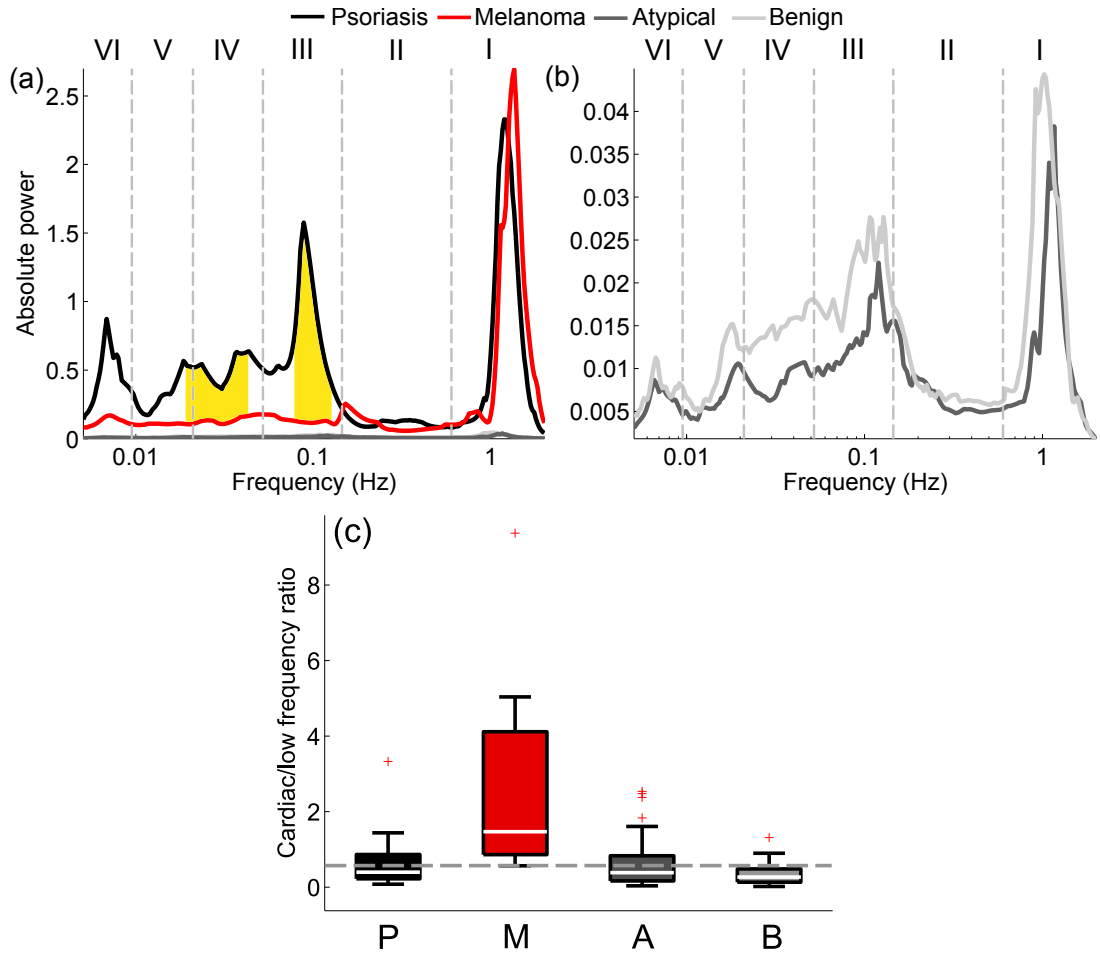


Figure 5.7: Absolute power spectra for all groups, highlighting the necessity of normalization. Power of melanoma and psoriasis (a) is much higher than atypical and benign naevi (b). Significant differences are highlighted in yellow. (c) Ratios between total power in the cardiac interval and the sum of the total power in frequency intervals III, IV, V & VI were calculated and compared between groups. Boxplot outliers are shown as red crosses. The grey dotted line shows the threshold set by the lowest value of the ratio in melanoma. $n = 9, 10, 33$ and 37 for psoriasis, melanoma, atypical and benign naevi, respectively.

parison of specific oscillatory components, also demonstrated in Figure 5.7. Due to the lesion specific nature of this study, lesions were located at widely varying sites on the body, which has been shown to have significant effect on microvascular blood flow recordings [93]. For both of these reasons, normalization is required to create an accurate picture of blood flow dynamics. All wavelet power spectra were normalized through division by their total powers. These were then compared at all frequencies from 0.005 - 2 Hz (Figure 5.8 (a)–(c)). To quantify spectral differences within intervals, and thus allow comparison of oscillations attributable to

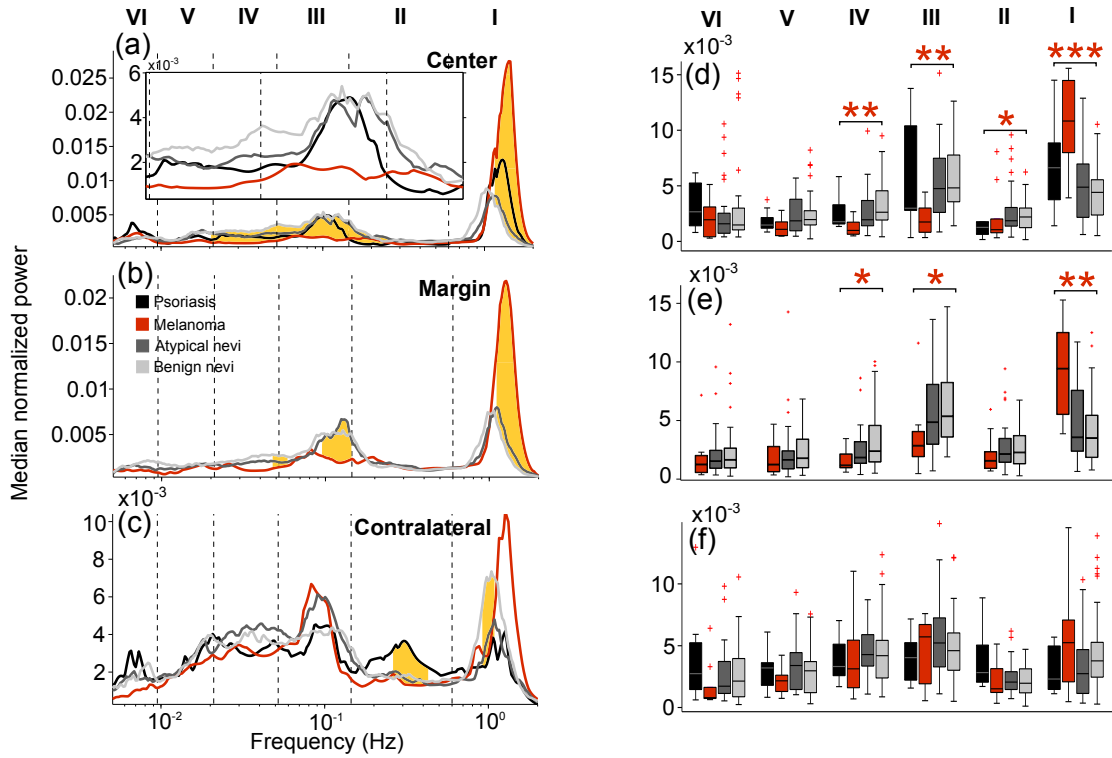


Figure 5.8: (a)–(c) Normalized wavelet power for all groups, with significant differences as determined by the Kruskal Wallis test highlighted in yellow. (d)–(f) Boxplots of normalized wavelet power in the known frequency intervals. Outliers are shown as red crosses. *** = $p < 0.001$, ** = $p < 0.01$, * = $p < 0.05$. $n = 9, 10, 33$ and 37 for psoriasis, melanoma, atypical and benign naevi, respectively.

specific physiological processes, the normalized wavelet powers were divided into six intervals, as defined previously (see Chapter 2). Normalized powers in intervals are shown in Figure 5.8 (d)–(f) and Table 5.5.

At lesion centres, melanomas had significantly lower normalized power in the frequency intervals associated with myogenic (III) and neurogenic (IV) activity, and a significantly higher normalized power in the cardiac frequency interval, when compared to both atypical and benign naevi. At lesion margins, melanoma showed significantly lower normalized power in intervals III and IV when compared to benign naevi, but only in interval IV when compared to atypical naevi. As was the case for lesion centres, normalized power in interval I was significantly higher in melanoma at margins than both atypical and benign naevi. Melanoma also showed significantly lower normalized power in the frequency intervals associated with myogenic, neurogenic and NO-dependent endothelial activity (III, IV & V)

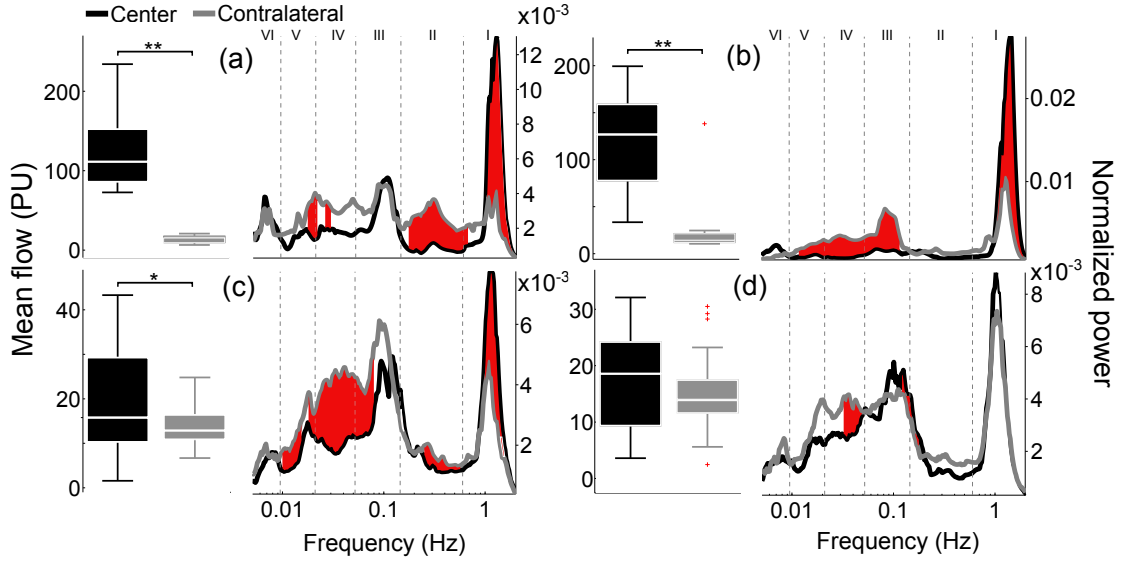


Figure 5.9: Comparison of mean blood flows and normalized wavelet power spectra between lesion centres and contralateral skin in (a) psoriasis, (b) melanoma, (c) atypical naevi and (d) benign naevi. Significant differences ($p < 0.05$) are highlighted in red. Boxplot outliers are shown as red crosses. $** = p < 0.01$, $* = p < 0.05$. $n = 9, 10, 33$ and 37 for psoriasis, melanoma, atypical and benign naevi, respectively.

when compared to contralateral skin in the same subjects, whilst exhibiting an increase in normalized cardiac power (interval I). The same comparison in atypical naevi revealed significantly lower power in intervals IV and V in lesion centres, and significantly higher power in interval I. In contrast, centre and contralateral powers only differed significantly in interval IV (the centre being lower) in typical benign naevi, and psoriasis differed only in intervals I (centre significantly higher) and the interval associated with respiration, II (centre significantly lower) (see Figure 5.9).

Comparison of centrally recorded normalized power between atypical and benign naevi revealed no significant differences in any interval except the neurogenic interval IV (center lower), while no differences were found during the same comparison for data recorded at margins.

5.3.6 Wavelet phase coherence

Wavelet phase coherence was calculated between wavelet transforms calculated from blood flow signals recorded at lesion centres and in contralateral skin, to in-

Normalized power in intervals

I	MM	AN	BN	P	<i>p</i>
Cent	10.8 (8.2–14.3)	4.9 (2.2–7.3)	4.4 (2.4–5.5)	6.6 (3.8–8.3)	0.0003
Marg	9.4 (5.8–12.2)	3.6 (2.4–6.7)	3.5 (1.9–5.4)		0.0034
Cont	5.2 (2.7–7.1)	2.8 (1.2–4.8)	3.8 (2.6–5.7)	2.3 (1.6–4.7)	0.1331
<i>p</i>	0.0020	0.0004	0.7229	0.0078	

II					
Cent	1.0 (0.8–1.8)	1.8 (1.3–3.0)	2.2 (1.3–3.0)	1.3 (0.7–1.8)	0.1571
Marg	1.6 (0.9–2.3)	2.1 (1.4–3.5)	2.3 (1.3–3.7)		0.5163
Cont	1.5 (1.2–2.8)	1.9 (1.5–2.8)	2.0 (1.2–3.1)	2.8 (2.2–4.4)	0.6101
<i>p</i>	1	0.6877	0.3305	0.0039	

III					
Cent	1.7 (0.9–2.7)	4.7 (2.6–7.5)	4.8 (3.6–7.6)	3.0 (2.8–10.3)	0.0006
Marg	2.8 (2.0–4.0)	4.8 (3.0–8.0)	5.3 (3.6–8.2)		0.0230
Cont	5.7 (2.1–6.7)	4.7 (3.2–7.0)	4.6 (3.0–6.0)	4.0 (2.2–5.0)	0.7257
<i>p</i>	0.0020	0.9501	0.1184	0.2500	

IV					
Cent	1.0 (0.6–1.7)	1.9 (1.4–3.5)	2.6 (1.9–4.3)	1.8 (1.6–3.0)	0.0005
Marg	1.2 (1.0–2.0)	1.8 (1.3–3.1)	2.4 (1.5–4.5)		0.0408
Cont	3.1 (1.8–5.1)	3.9 (3.3–5.7)	4.2 (2.5–5.4)	3.3 (2.6–4.8)	0.4845
<i>p</i>	0.0020	0.0001	0.0074	0.0977	

V					
Cent	1.0 (0.6–1.7)	1.8 (1.0–3.7)	2.0 (1.5–2.6)	1.5 (1.2–1.8)	0.0746
Marg	1.2 (0.7–2.5)	1.6 (0.9–2.3)	1.8 (1.0–3.4)		0.6096
Cont	2.2 (1.4–2.5)	3.4 (1.5–4.4)	3.0 (1.2–3.7)	3.2 (2.1–3.5)	0.3417
<i>p</i>	0.0039	0.0049	0.1868	0.0547	

VI					
Cent	1.9 (0.6–3.0)	1.5 (0.8–2.4)	1.5 (1.1–2.7)	2.6 (1.4–4.9)	0.8659
Marg	1.2 (0.6–1.9)	1.5 (0.9–2.4)	1.6 (1.0–2.6)		0.5098
Cont	0.8 (0.7–1.4)	1.6 (1.1–3.4)	2.1 (0.9–3.9)	2.8 (1.6–5.2)	0.1867
<i>p</i>	0.6953	0.4915	0.7229	0.9102	

Table 5.5: Normalized power values for all studied frequency intervals. Results of significance testing from the Kruskal Wallis test (between groups) and the sign rank test (between centres and contralateral) are shown. Significant differences ($p < 0.05$) are highlighted in grey.

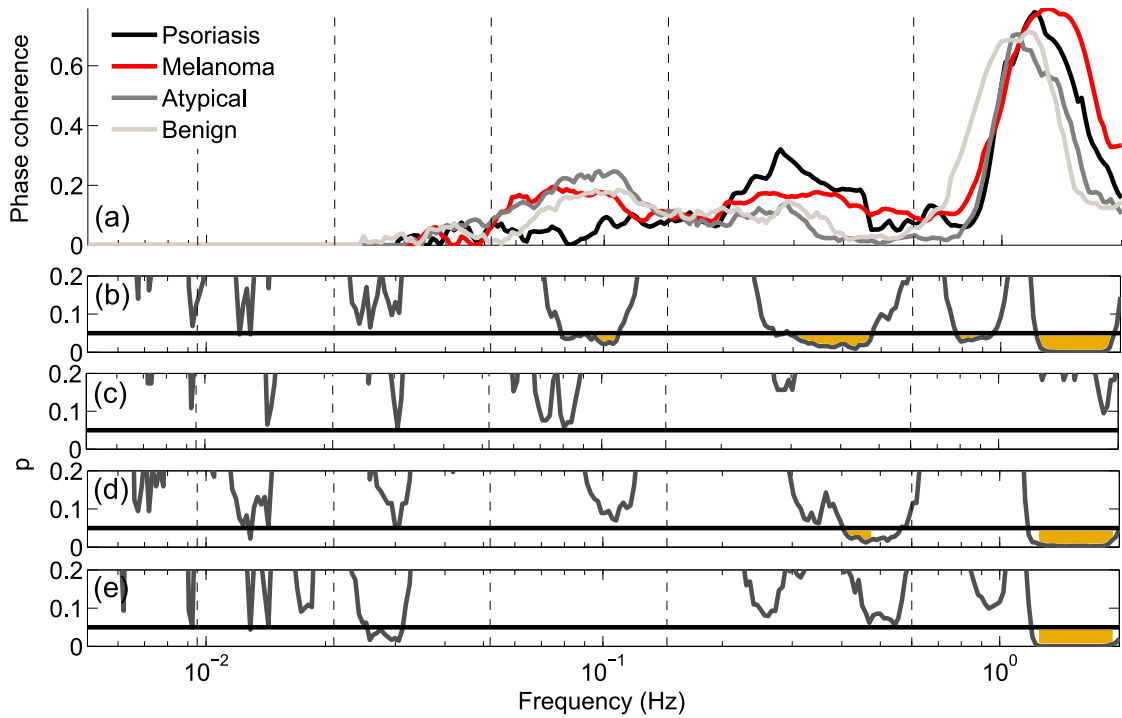


Figure 5.10: Significant wavelet phase coherence calculated by subtracting the 95th percentile of 100 IAAFT surrogates per subject. (a) Phase coherence between recordings from lesion centres and contralateral skin. (b) ANOVA results for all groups. (c) p values from the ranksum test between melanoma and psoriasis. (d) p values between melanoma and atypical naevi. (e) p values between melanoma and benign naevi. Significant differences ($p < 0.05$) are highlighted in yellow. $n = 9, 10, 33$ and 37 for psoriasis, melanoma, atypical and benign naevi, respectively.

investigate whether the phase relationships of the observed oscillatory components differ between groups [298]. Wavelet phase coherence could not be calculated between blood flow at lesion margins and contralateral skin because these signals were not recorded simultaneously. Significant coherence was defined as coherence values above the 95th percentile of 100 IAAFT surrogates. Significant phase coherence was found in all groups, in intervals I, II, III & IV (see Figure 5.10). However, whilst coherence differed significantly between groups according to the Kruskal Wallis test, this difference was mainly as a result of differences between psoriasis and benign naevi. Melanoma differed from atypical naevi at a very small number of frequencies in the respiration interval and differed from atypical naevi and benign naevi in the upper part of the cardiac interval, as a result of the higher heart rate demonstrated in melanoma subjects.

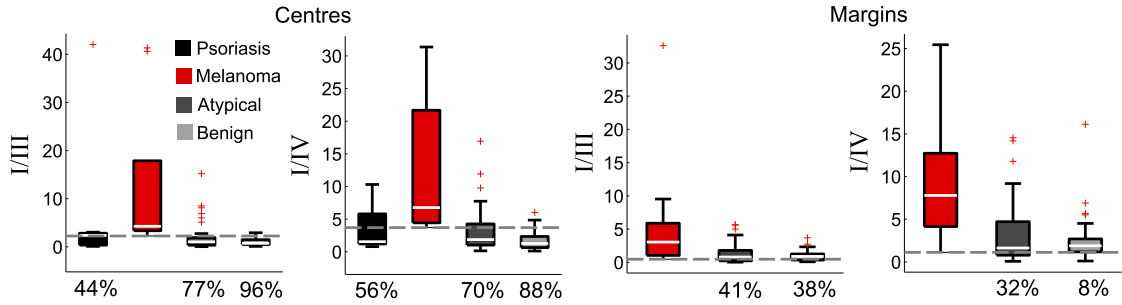


Figure 5.11: Evaluation of the discriminatory power of ratios between cardiac and myogenic/neurogenic power. I/III and I/IV Ratios are shown for lesion centres and margins, with sensitivities shown based on a cut-off of the lowest value observed in melanoma (shown by grey dashed line). Boxplot outliers are shown as red crosses. $n = 9, 10, 44$ and 26 for psoriasis, melanoma, atypical and benign naevi, respectively.

5.3.7 Non-invasive diagnosis of melanoma

For the development of a diagnostic test, it is important that the differences observed are not only significant, but that they are sufficiently discriminatory to provide a cut-off point which can be used to distinguish between groups. The main significant differences observed in this study arise from differences in mean blood flow, differences in normalized cardiac power in lesion centres and margins, and differences in normalized myogenic and neurogenic power in lesion centres and margins. As melanoma exhibits a significant increase in normalized cardiac power at centres and margins when compared to all other groups, and a decrease in normalized power in the neurogenic and myogenic frequency, the ratio between these two parameters is likely to be higher in melanoma than in other groups. Therefore, the ratios of I/III and I/IV power were calculated for centres and margins for all groups and compared in order to assess their success in discriminating between groups. As shown in Figure 5.11, these ratios are much more successful in lesion centres than in lesion margins, and the I/III ratio alone provides better specificity than the I/IV ratio. Differences in normalized cardiac power were also compared between groups in order to ascertain whether the diagnostic test could be improved further. A minimum normalized cardiac power of 0.0038 was found for both lesion centres and lesion margins, and used as a cut-off. In lesion centres,

this cut-off provided a specificity of 43% in atypical and 50% in benign lesions. At lesion margins these values were 59% and 50%, respectively, showing that this test is more successful at lesion margins. Using these three tests, mean blood flow ratio, cardiac/myogenic and cardiac/neurogenic ratio and normalized cardiac power, the combination which gave the highest specificity overall was revealed to be, for melanoma:

1. Mean blood flow recorded at margin/ mean blood flow at the contralateral location > 1.26 ,
2. Normalized cardiac power at the lesion margin > 0.0038 and
3. Total power in I / total power in IV in wavelet power spectrum calculated from blood flow recorded in lesion centres > 3.7 .

Combining these characteristics results in a sensitivity of 100% and a specificity of 90.9% in discriminating between melanoma and atypical naevi, based on the available data (see Figure 5.12). Values for all parameters for each subject are shown in Table A.1.

5.4 Summary

With respect to the hypotheses presented previously, clear differences have been demonstrated in blood flow dynamics between melanoma, psoriasis, atypical naevi and benign naevi, contributing to our understanding of the physiological processes occurring within melanoma microvasculature. In addition, a diagnostic test has been developed based on LDF recordings and wavelet analysis which differentiates between melanoma and atypical naevi with sensitivity 100% and specificity 90.9%, based on the presented data. As demonstrated in previous studies on melanoma blood flow [346], it was observed in this study that melanomas had significantly higher blood flow when compared with atypical and benign naevi, both in lesion centres and at lesion margins, and also when compared to contralateral healthy

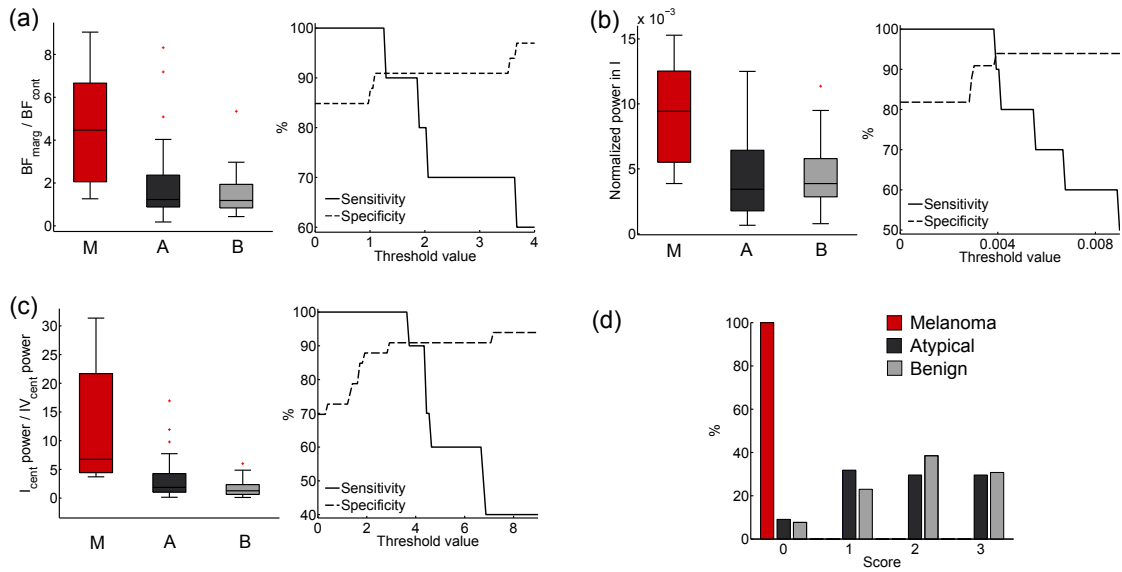


Figure 5.12: Sensitivity and specificity ranges for the diagnostic parameters based on the available data. (a) Ratio between mean blood flow at the margin and mean blood flow in contralateral skin. (b) Normalized wavelet power in the cardiac interval. (c) Ratio between the power in the cardiac interval and the power in the neurogenic interval. (d) Results of diagnostic test for all naevi. The score is how many of the criteria were met by the lesion being tested. Boxplot outliers are shown as red crosses. M – melanoma ($n = 10$), A – atypical naevi ($n = 44$), B – benign naevi ($n = 26$).

skin. The latter was also the case for atypical naevi and psoriasis, but not for benign naevi. Histological examination of melanoma showed an increased number of blood vessels in lesion centres compared to atypical naevi, which can be attributed to the increased angiogenesis occurring within the melanoma vasculature [153, 193]. A significant positive correlation between intra-lesional vessel density and blood flow at the centres of melanomas was found, which is in agreement with the fact that it is not only the number and velocity of erythrocytes in microvessels, but also vessel density which influences microcirculatory blood flow [346]. Though significant, this correlation was not as strong as expected, likely due to the fact that melanomas are characterized by irregularly shaped microvessels which also exhibit increases in cross sectional area, features which are not quantified through the vessel count performed in this study. This correlation was not found between blood flow at margins and peri-lesional vessel count, due to the heterogeneity of melanoma vasculature, and it being unlikely that the margin signals were recorded

in the same place as the vessel count was performed. In terms of blood flow dynamics, melanomas, despite their increased blood flow, had significantly reduced power in the frequency intervals associated with myogenic and neurogenic activity, when compared to atypical naevi and benign naevi. This abnormality in melanoma has important relevance from a pathological and a therapeutic point of view, in light of results of recent experimental and human studies [77, 84] suggesting that blood flow dynamics is essential for efficient nutrient delivery and removal of waste from tissues. In fact, without adequate removal of the by-products of glycolysis, such as lactic acid, the tumour microenvironment becomes more acidic [198], with consequent reduction in vessel reactivity [257]. It has also been shown that many cancer treatments fail due to hypoxia induced by the inadequacy of the blood perfusion to the tumour site [202]. In addition, significantly lower normalized power in the frequency intervals related to myogenic, neurogenic and NO dependent endothelial activity (III, IV & V) was observed in melanoma when compared to healthy skin in the same subjects. This was also observed in intervals IV & V in atypical naevi and interval IV in benign naevi. Taking into account that atypical naevi are more prone to development into malignant melanoma than benign naevi [179], this similarity in blood flow dynamics between melanomas and atypical naevi suggests that the transformation from benign melanocytic lesion to melanoma could be a gradual process.

Due to the large number of false positives in the clinical identification of melanoma, a number of non-invasive approaches have been developed over the years to provide an objective means of evaluating and diagnosing skin melanoma. However, the current gold-standard in melanoma diagnosis is still examination of a skin lesion by the trained eye of a physician, followed by histological examination of an invasive excisional biopsy of the skin specimen. Therefore, the diagnosis of melanoma by non-invasive methods remains an active area of research. In line with this aim, a cut-off was developed based on differences in blood flow dynamics between melanomas and atypical naevi, with a sensitivity of 100% and specificity

90.9%. Considering that the clinical accuracy of diagnosing melanoma in this study was around 20%, the cut-off appears to be very promising as a complementary method to biopsy. Psoriasis was also chosen as a control lesion in this study, due to its similarity to malignant melanoma in terms of angiogenesis and microvasculature characteristics, including elongated and dilated vessels and increased endothelial cell proliferation [186]. In agreement with this similarity, no significant differences in mean blood flow between melanoma and psoriasis lesions were found. On the contrary, melanomas and psoriasis lesions differed in terms of their blood flow dynamics in frequency intervals I & IV. The rhythmical behaviour of blood flow in psoriasis lesions was previously studied and compared to that in skin basal cell carcinomas [186]. Similarly to the melanoma group in our study, basal cell carcinomas differed from psoriasis lesions in terms of blood flow dynamics, showing a reduction in power of the neurogenic dependent frequency interval compared to healthy skin, a finding which was not observed in psoriasis lesions in the same study. However, basal cell carcinomas have been shown to be less perfused than melanomas [184].

A limitation of this study was the variations in age distribution between groups, with the melanoma and psoriasis patients being significantly older. It has been shown previously that physiological processes, such as heart rate and heart rate variability, and microvascular responses to vasoactive substances, change with increasing age. To completely rule out the effects of age on results, further recruitment of age matched melanoma or atypical naevi patients would be required. Another possible limitation of this study is that many of the subjects (6 out of 10 melanoma and 6 out of 9 psoriasis) had arterial hypertension, a pathological condition which has been shown to reduce skin vasoreactivity and to perturb blood flow dynamics [10]. However, all hypertensive patients enrolled in this study had normal blood pressure values due to antihypertensive treatment, a condition which was shown to normalize blood flow dynamics in hypertensive patients in a previous study [10]. Consistent with normalization of blood flow dynamics in treated

hypertensives, significant differences between hypertensive and non-hypertensive subjects in spectral power were not observed in any frequency intervals analysed in healthy skin. A further limitation of this study is the relatively low reproducibility of single point LDF measurements that was observed in studies averaging relatively short time segments. However, in this study, recordings were for 30 minutes, allowing more reliable characterization of the signal, including its time-variability [76]. Furthermore, this limitation of LDF measurements was less important here, due to the fact that blood flow signals were analysed in terms of their frequency components, through the use of the continuous wavelet transform. Now that the diagnostic markers have been identified, recording time may be reduced to 15 minutes, enhancing the clinical applicability of the method.

In conclusion, this study showed changes in both mean blood flow, and blood flow dynamics in melanomas, in comparison to atypical naevi, benign naevi and psoriasis lesions, allowing a better understanding of melanoma microvascular physiology. A diagnostic cut-off for the differentiation of melanoma from atypical naevi is presented, developed based on differences observed in both blood flow, and blood flow dynamics, extracted through wavelet analysis. Whilst this method is very promising, further research is necessary before it can be recommended in the replacement of biopsy for the diagnosis of melanoma.

6. Oxygenation and blood flow dynamics

As discussed previously, blood flow dynamics has been used as a model for microvascular health, and has been shown to be altered in various pathologies. This chapter aims to assess whether simultaneously recorded skin blood flow and oxygenation are altered in terms of their dynamics during dry static apnoea using free diver data recorded in a previous study [347], and age and sex matched control data recorded in non-divers specifically for this thesis. In addition to the comparison of the divers with controls, new analysis on data recorded during apnoea provides further insights into the local effects of hypoxia on blood flow and oxygen dynamics. This may provide information about blood flow and oxygen dynamics during hypoxia, and thus may provide clues to the behaviour of the vasculature in tumours.

6.1 Hypothesis

This study aims to investigate blood flow and oxygen dynamics during dry static apnoea in trained free divers. The extensive training of these divers provides longer breath-holds than are possible with normal untrained humans. It may therefore be possible to observe previously unseen dynamics during this prolonged oxygen deprivation, i.e. whether this induces hypoxia in these subjects, and how this affects their physiological regulation of blood flow and blood oxygenation, in particular the *dynamics* of these parameters. Observations in this scenario may be applicable

to the state of hypoxia in general.

6.2 Experimental protocol

In a previous study [347], 16 free divers were monitored according to the following protocol. Sensors were attached to the skin of each subject as shown in Figure 6.1 and explained in detail below. The protocol involved a period of 30 minute resting recordings of all physiological parameters. The divers were then asked to follow a further protocol involving breathe-ups, breath-holds and one short rest period. The structure of this protocol is shown in Figure 6.10 and explained further in Section 6.3.3. Before investigating whether blood flow and oxygen dynamics are altered during apnoea, it is necessary to find out whether the apnoea training regularly performed by free divers has permanently altered their physiology. To investigate the similarities and differences between divers and non-trained individuals, the previous study based on this data used control subjects from [86], but this study did not use the TOSCA500 (see below), so arterial oxygen saturation and transcutaneous carbon dioxide could not be compared. These data sets also differed in that all data recorded by the O2C device were recorded in different locations. In the study in [86], they were placed on the right shinbone and centre of the inner right forearm, whilst in the divers they were placed on the right foot dorsum and the volar aspect of the right arm, approximately 70mm from the elbow [347]. To provide the possibility of a more accurate comparison of physiological data during the rest period, 16 age- and sex-matched, healthy controls were recruited, following the exact protocol of the free divers at rest, with the addition of 10 extra minutes of recording time. As in the diver group the controls were recruited provided they met the following criteria: they had not consumed caffeine on the day of the experiment, alcohol in the 24 hours prior to the experiment, or food within the previous 4 hours, they were healthy as determined by a medical questionnaire, they had normal blood pressure (i.e. did not exceed 150 mm Hg), and their body mass index did not exceed 30.

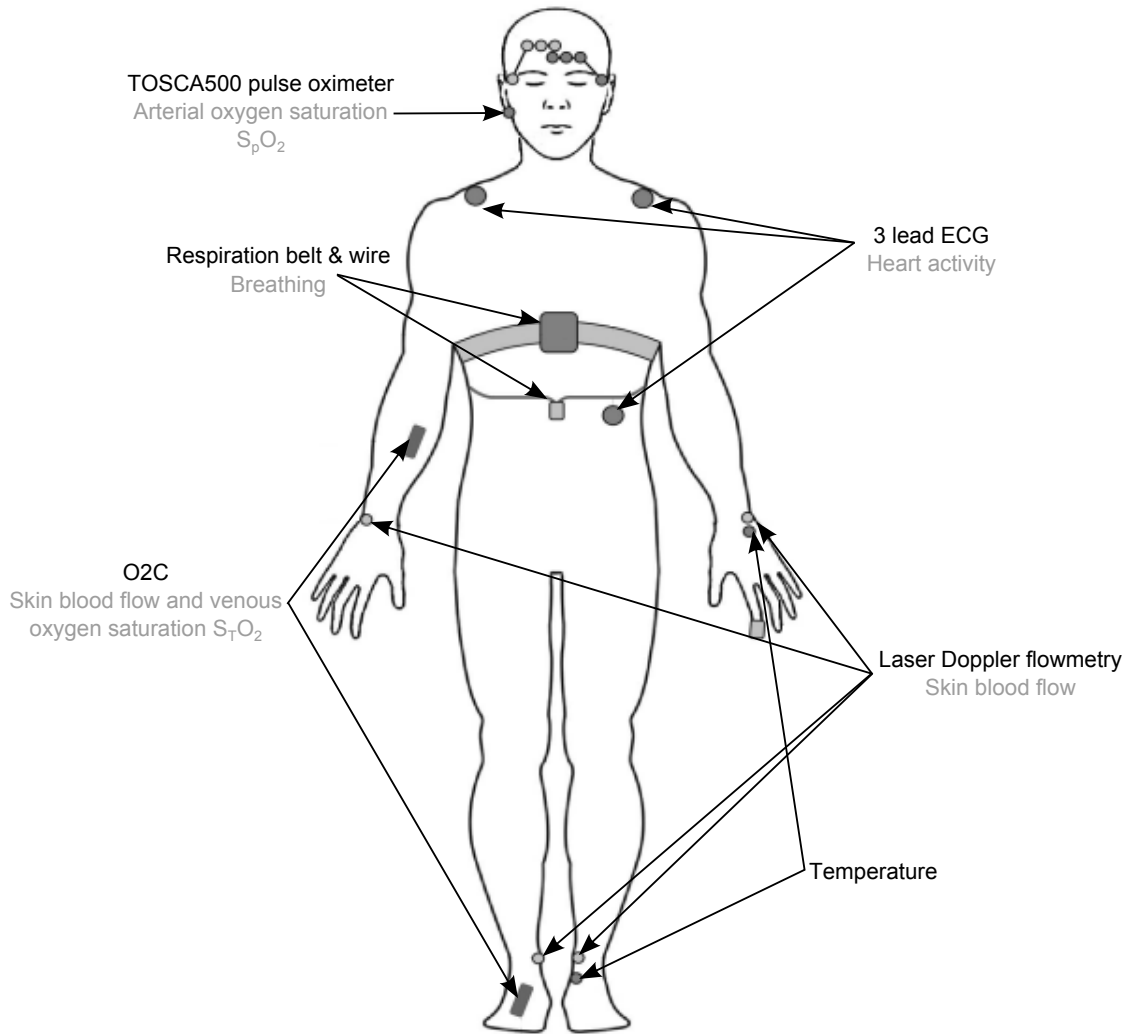


Figure 6.1: Location and function of probes in the apnoea study and in the control group. EEG was not measured in the control group. Modified from [347]

6.2.1 Measured parameters

Electrocardiogram

ECG was measured at 1200 Hz, using a three lead setup, with one electrode on each shoulder and one on the lowest left rib. The electrodes used were disposable Ag/AgCl electrodes (40493D)(Philips Healthcare, UK).

Arterial oxygen saturation

Based on the differences in absorption of light by oxyhaemoglobin and deoxyhaemoglobin, and pulsatile changes in blood volume, the arterial oxygen satura-

Subject	1	2	3	4	5	6	7	8
Age (D C)	21 20	29 28	31 32	34 33	39 38	45 45	25 25	28 28
Sex	F	F	F	F	F	F	M	M
Subject	9	10	11	12	13	14	15	16
Age (D C)	31 30	34 34	35 34	36 36	38 38	38 40	39 41	41 42
Sex	M	M	M	M	M	M	M	M

Table 6.1: Free divers were age matched (± 2 years) and sex matched. D = Divers, C = controls.

tion, S_pO_2 , can be measured using pulse oximetry. In this study, S_pO_2 was measured at the right ear lobe, using the TOSCA500 (Radiometer, UK), which uses a two-wavelength pulsatile system of LEDs to distinguish between oxygenated and deoxygenated blood [348]. Red (658nm) and infrared (880nm) light are passed through the capillary bed of the earlobe to a photodetector, connected to the TOSCA500 where parameters are calculated based on the absorption of light in the tissue. The TOSCA500 calculates functional saturation, the amount of oxygenated haemoglobin as a percentage of the haemoglobin that can carry oxygen, and does not include dysfunctional haemoglobin, e.g. carboxyhaemoglobin. Unlike some other pulse oximeters, the TOSCA500 corrects the S_pO_2 signal by subtracting contributions arising from venous blood movement [348].

Respiration

In free divers, respiration was measured using two different methods, due to difficulties with accommodating the range required during apnoea. Respiration was measured in terms of chest volume changes using either a respiration wire (not available for some divers) or a Velcro belt consisting of a TSD201 conductance transducer [347]. It is the latter method that was used in the control group presented here.

Blood flow

Skin blood flow was measured using laser Doppler flowmetry in eight locations on each subject. Four of the measured signals were recorded using Moor In-

struments (UK) LDF recording equipment, consisting of one DRT4 laser Doppler monitor with two channels, and two Moor Servers with one channel each. The Moor Doppler probes 1 and 2 were placed on the medial malleolus of the left and right ankles, respectively. Moor probes 3 and 4 were placed over the protrusion of the ulna on the left and right wrists, respectively. These locations were chosen to ensure that the measurement area consists only of microvasculature, and not larger vessels such as arterioles, whose large volume lead to different blood flow dynamics than that observed in the microvessels. The other four LDF signals were recorded using the O2C (LEA Medizintechnik, Germany), which allows simultaneous recording of blood flow at two depths in the same location (see Figure 6.2). O2C probe 1 was placed on the top of the right foot, and O2C probe 2 on the right forearm as described previously.

Oxygenation parameters

Relative amount of haemoglobin (rHb) and venous oxygen saturation ($S_{T}O_2$) were measured by the O2C device, in the same locations as the O2C blood flow described above. Each O2C probe provides recordings from two tissue depths, due to two different separations of emitters and detectors. One set of signals, recorded with a fibre separation of 2mm, arises from shallow tissue, whilst simultaneous recording with a fibre separation of 8mm also allows the observation of physiological parameters from deeper tissue.

6.3 Results

6.3.1 Statistics

The distribution of any group to be compared was tested using the Lilliefors test for normality, which did not consistently find normal distributions of data in any case. Therefore, all statistical tests used were non-parametric, i.e. did not assume an underlying distribution. Comparisons within the diver group were made using

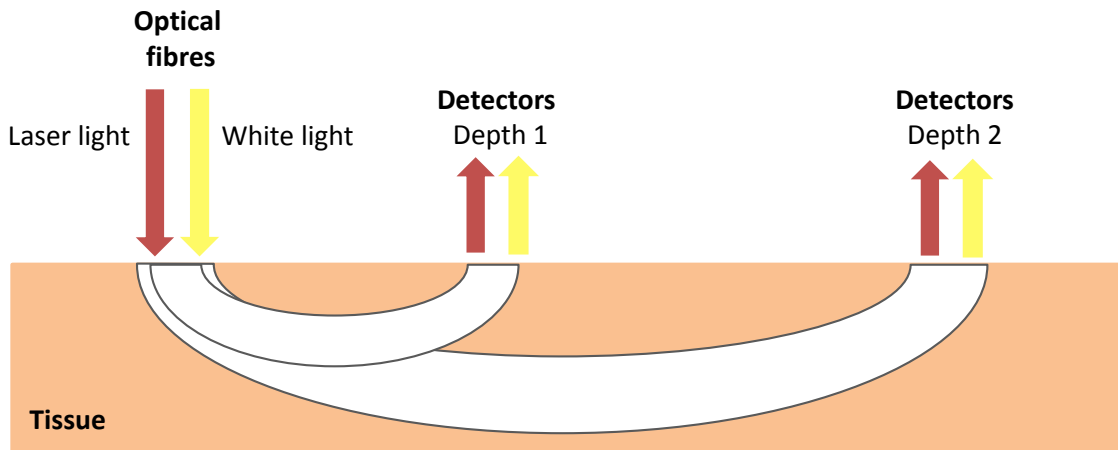


Figure 6.2: Diagram of the two tissue depths measured by the O2C. The depth of recording depends on the spacing between the light source and the detector. Larger spacing will result in deeper recordings. The laser light is used to measure blood flow and blood velocity, whilst the white light is used to measure venous oxygen saturation ($S_T O_2$) and relative haemoglobin (rHb).

the Wilcoxon signed rank test, and comparisons between the divers and control group were made using the Wilcoxon rank sum test. Significance was considered as $p < 0.05$.

6.3.2 Comparison of divers and controls at rest

Sixteen age and sex matched controls were recruited in order to compare the resting state in non freediver controls with that of the previously measured freedivers. This was to ascertain whether the regular training undergone by free divers affects their physiological parameters, in particular their resting blood flow and oxygenation dynamics. Information on the two groups of subjects can be found in Table 6.1.

Systemic comparisons

Heart rate, heart rate variability (HRV), respiration and arterial oxygen saturation ($S_p O_2$) were compared between groups at rest. Mean heart rate was found by extracting the instantaneous frequency of the heart activity from the ECG signal, and calculating the mean. To ensure the extracted heart rate signals were correct, they were also compared with the heart rate recorded by the TOSCA 500 at the ear lobe. Both methods were found to provide the same results. Mean heart

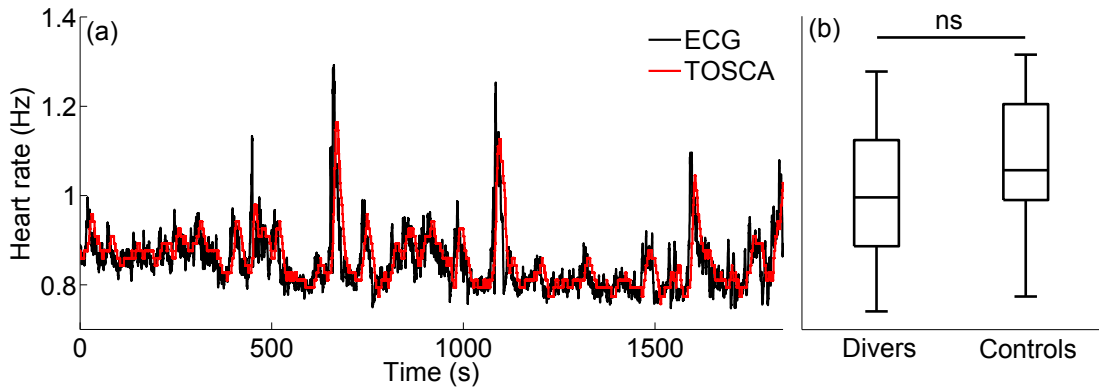


Figure 6.3: (a) Example instantaneous heart rate as extracted from the ECG (black line), and as recorded by the TOSCA 500 (red line). (b) Mean heart rates were found not to differ significantly between divers and controls using the rank sum test ($p_{\text{ECG}} = 0.25$, $p_{\text{TOSCA}} = 0.15$). $n = 16$ for both groups.

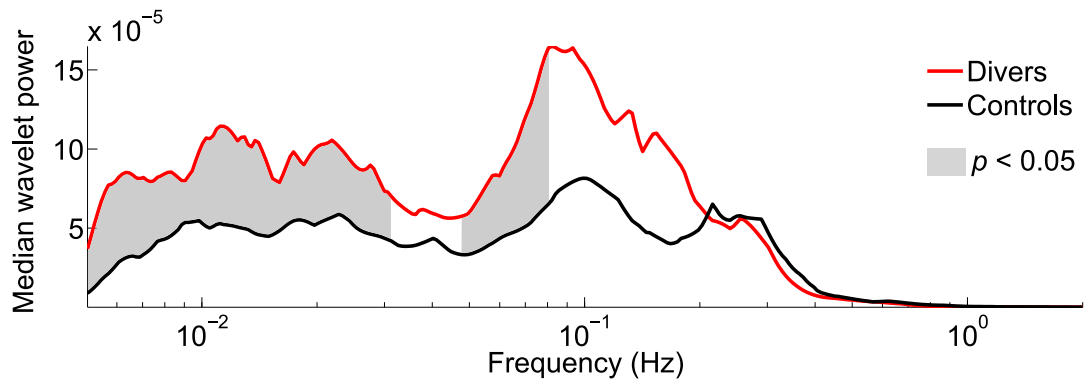


Figure 6.4: Median time averaged wavelet power of heart rate variability (HRV). Significant differences between divers and controls are highlighted in grey. $n = 16$ for both groups.

rates are shown in Figure 6.3. No significant differences in heart rate were found between the divers and the controls ($p_{\text{ECG}} = 0.25$, $p_{\text{TOSCA}} = 0.15$), confirming the result obtained in [347] with a different control group. Heart rate variability was investigated using peak detection of the R-peaks (see Section 4.2.1) in the ECG signal before resampling (1200 Hz), to provide precise temporal resolution. Heart rate variability signals were calculated based on the varying time intervals between R-peaks (see Chapter 3.1.2), and their wavelet transform calculated. Time averaged wavelet power of heart rate variability was compared between divers and controls, with significant differences found at frequencies below around 0.08 Hz, with the exception of the interval 0.031–0.048 Hz (see Figure 6.4).

This is a similar result to the previous study involving this data, where differ-

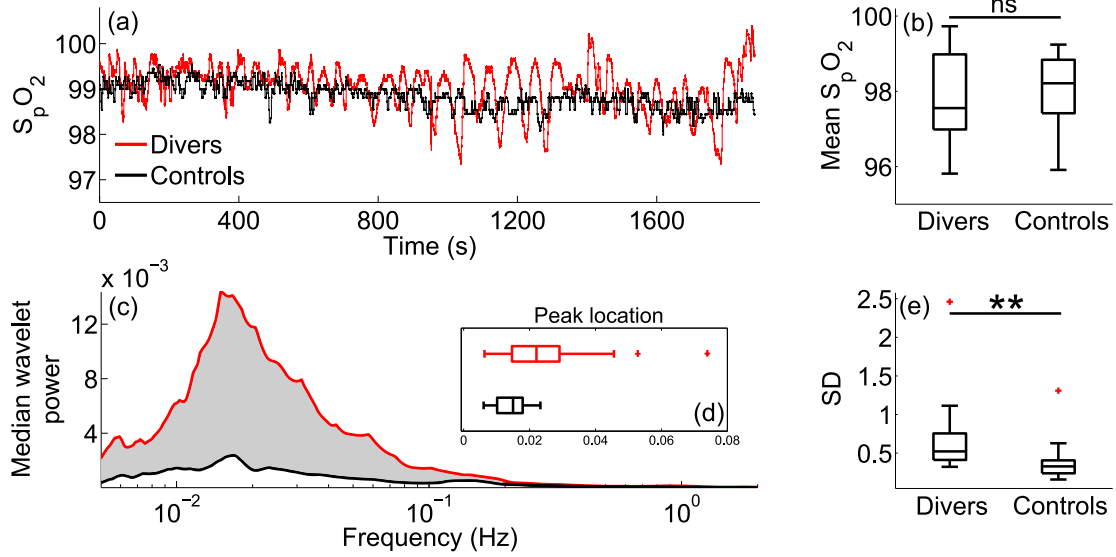


Figure 6.5: (a) Example arterial oxygen saturation, S_pO_2 , time series recorded from the right earlobe of a diver (red line) and a control subject (black line) using the TOSCA500. (b) Mean S_pO_2 did not differ significantly between groups ($p = 0.6109$). (c) Median wavelet power of S_pO_2 for both groups. Significance was tested at each frequency, significant differences are highlighted in light grey. (d) Peak locations compared between divers (red) and controls (black). Peak locations were significantly higher frequency in divers ($p = 0.0348$). Outliers are shown as red crosses, one outlier not shown. (e) Standard deviation of S_pO_2 differed significantly between groups ($p = 0.0021$). $n = 16$ in all cases. $** = p < 0.01$.

ences in HRV were found below 0.04 Hz [347]. Respiration rates were calculated from signals from either the respiration belt or wire, depending on which gave clearer peaks. These signals were then smoothed to facilitate peak detection, and the differences between peaks calculated to provide the respiration rate variability. Respiration rates could only be recovered from 14 out of 16 divers, thus their matched controls were also not used in this comparison. Mean respiration rates did not differ significantly between groups ($p = 0.9817$), with a median respiration rate of 0.24 Hz in both groups.

Arterial oxygen saturation S_pO_2 was recorded at the right earlobe using the TOSCA500 device. No significant differences in mean S_pO_2 were found between the divers and their controls ($p = 0.6109$). However, a significant difference was observed in the standard deviation, with the divers exhibiting higher variability in their S_pO_2 levels ($p = 0.0021$). Comparisons were also made between absolute minimum and maximum values, which were found not to differ significantly (p

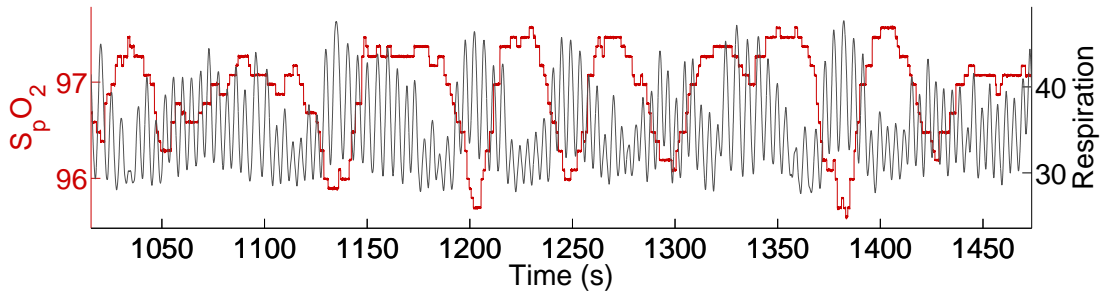


Figure 6.6: Respiration responds to reductions in S_pO_2 . Troughs in the arterial oxygen saturation appear to induce an increase in the amplitude of the respiration to compensate.

= 0.0678 and $p = 0.2828$, respectively). The observed differences in standard deviation highlighted the necessity of further investigation into the time-dependent dynamics of S_pO_2 in both groups. Wavelet transforms of the S_pO_2 signals were calculated, and their time-averages compared between groups. As the TOSCA500 provides absolute values of S_pO_2 , the spectra were not normalized. Significant differences were found across the frequency spectrum, as demonstrated in Figure 6.5(c), with a clear peak in the median wavelet power around 0.016 Hz visible in both groups. This low frequency peak was observed in all subjects, at varying peak frequencies, shown in Figure 6.5(d). If more than one peak was present in the spectrum, the peak with the highest magnitude was considered. The locations of this peak differ significantly between groups, with the controls demonstrating peak S_pO_2 power at lower frequencies ($p = 0.0348$).

It is well known that breathing is closely linked with changes in arterial blood oxygenation. Blood oxygen levels are continuously monitored within the carotid body, a small cluster of chemoreceptors situated at the bifurcation of the carotid artery. Even very small decreases in blood oxygenation are sensed immediately, and this leads to cardiovascular and respiratory reflexes, including variations in breathing rate or amplitude to compensate [349]. Figure 6.6 demonstrates that in the case of decreasing S_pO_2 , the breathing pattern alters to normalize S_pO_2 levels. Therefore, to investigate the relationship between S_pO_2 and respiration at rest, and whether this relationship is altered in freedivers, wavelet phase coherence was calculated between the two signals for both groups. Figure 6.7(a) shows the re-

sults of wavelet phase coherence calculations between S_pO_2 and respiration for the divers and their controls. The bias at low frequencies of wavelet phase coherence calculations (see Chapter 4.2.4) was accounted for by calculating 100 iterative amplitude adjusted Fourier transform (IAAFT) surrogate data sets [299] per subject and considering all phase coherence above the 95th percentile of the surrogate data set as statistically significant. This allowed comparison of wavelet phase coherence between groups, and it was found that there were no significant differences in total phase coherence between respiration and S_pO_2 in divers and controls ($p = 0.3462$). However, comparisons of significant phase coherence between groups at each frequency revealed significant differences around 0.015 and 0.093 Hz, with the divers exhibiting lower coherence in both cases. The difference around 0.015 Hz is likely due to the previously discussed higher frequency of oscillations of S_pO_2 . The median phase coherence appears to show a double peak in both groups, but inspection of the coherence in individual subjects shows that this is not a universal observation. Comparison of the phase coherence between S_pO_2 and respiration in divers and their matched control shows a narrower range of coherence in divers in the majority of cases.

Another well known phenomenon is respiratory sinus arrhythmia, where the heart rate varies depending on the phase of the respiration cycle (see Section 3.1.2) [350]. This cardio-respiratory interaction was also investigated using wavelet phase coherence between the respiration and heart rate variability at rest in both groups. No significant differences in total phase coherence were observed ($p = 0.6625$), but significant differences were observed at the individual frequencies highlighted in Figure 6.7(b), with divers showing higher phase coherence at lower frequencies.

Local comparisons

Eight blood flow signals were recorded in total, one on each wrist, one on each ankle, two from the right forearm, and two from the top of the right foot, as shown in Figure 6.1. Mean blood flows are compared between divers and controls

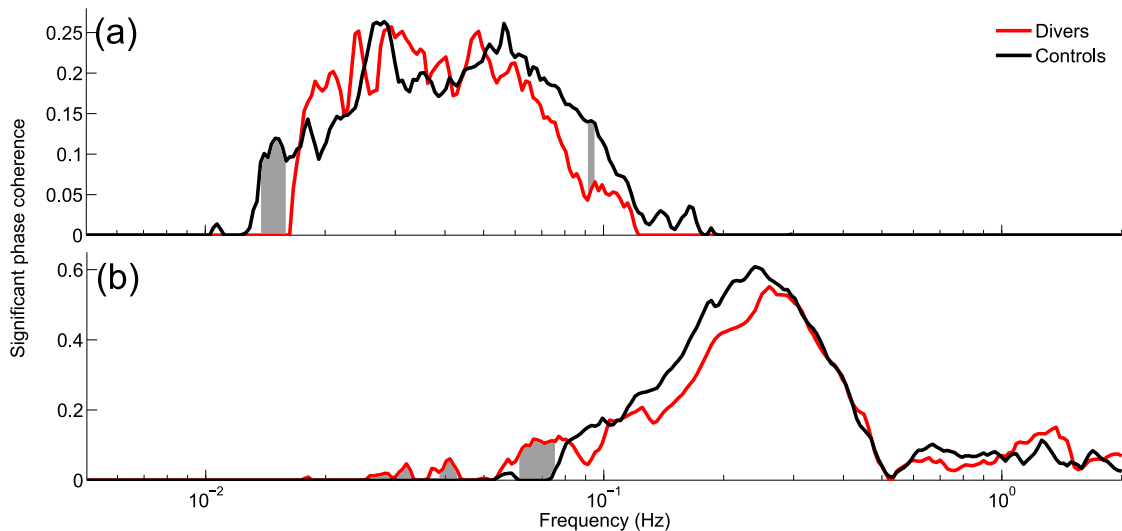


Figure 6.7: (a) Median wavelet phase coherence between S_pO_2 and respiration for divers and controls. (b) Median wavelet phase coherence between respiration and heart rate variability. Only significant coherence is shown, as calculated from subtracting the 95th percentile of 100 IAAFT surrogates. Total coherence did not differ significantly between groups, but significant differences ($p < 0.05$) were found at some frequencies using the rank sum test, highlighted in grey. $n = 14$ in both cases.

in Table 6.2.

Significant differences in mean blood flow were observed only in the right and left wrists. Interestingly, the difference in the left wrist is due to the divers having a significantly lower mean blood flow, whilst the difference in the right wrist is the opposite; the divers have higher mean blood flow.

To investigate the time-dependent dynamics of blood flow, and whether these vary between groups, wavelet transforms were calculated for all blood flows, and their time-averaged wavelet power compared between groups. To take into account the fact that blood flow is not an absolute value, and possible small variations in recording location, the power spectra were normalized by dividing them by their total power. Comparisons were made at each frequency using the Wilcoxon rank sum test, and significant differences were revealed in all cases (see Figure 6.8). In addition to testing the whole spectrum, the total power in each of the previously defined frequency intervals was calculated and compared, to look for trends in the differences between groups. Differences in normalized power were observed in 5 out of 8 blood flow recording locations in the cardiac interval (I), with the power

Location	Blood flow (PU)		<i>p</i>
	Divers	Controls	
Left ankle	10.33 (9.08–11.56)	10.99 (8.19–14.61)	0.4178
Right ankle	9.76 (8.02–12.79)	12.87 (9.15–14.90)	0.3365
Left wrist	10.20 (8.15–19.66)	19.54 (14.00–25.67)	0.0167
Right wrist	15.24 (14.09–25.41)	12.15 (10.10–15.55)	0.0365
Right foot (S)	6.49 (3.92–10.30)	10.11 (4.76–28.95)	0.2662
Right foot (D)	37.37 (18.89–45.60)	48.20 (35.27–70.09)	0.1092
Right arm (S)	17.35 (12.45–25.51)	19.48 (13.86–33.67)	0.5095
Right arm (D)	42.87 (24.96–102.65)	65.85 (45.98–96.08)	0.3179

Table 6.2: Mean blood flows calculated for all locations and compared between divers and controls. Values shown are medians and inter-quartile ranges of the means. Significance was tested using the Wilcoxon rank sum test. Significant differences are highlighted. Grey – significant increase in controls, pink – significant decrease in controls. S – shallow, D – deep. $n = 16$.

in the divers significantly lower in all of these cases. In the respiration interval (II), differences in normalized power were observed in half of the recording locations, and again power was lower for the divers than the controls. The myogenic interval (III) displayed significant differences in only 3 out of 8 recording locations. In two locations (right ankle and left wrist), the myogenic power was lower in the diver group, in contrast to the right arm where it was higher in the diver group. In 5 of 8 locations changes in normalized power were observed in the neurogenic interval (IV). In all cases the power was higher in the diver group. Power in interval V (endothelial), differed significantly in 4 out of 8 recording locations, with divers showing higher power in all cases. Finally, in the lower endothelial interval (VI) differences were revealed in 5 out of 8 recording locations, with divers again showing higher power across all cases. All these differences are shown in Figure 6.8 and Table 6.3.

Mean venous oxygenation values ($S_{T}O_2$) and relative haemoglobin (rHb) values as measured using the O2C can be seen in Table 6.4. Only values recorded from shallow tissue are considered, as testing of the equipment revealed characteristic peaks in the signal which records oxygenation in deeper layers even when attached to the calibration standard. These signals were therefore deemed unreliable and

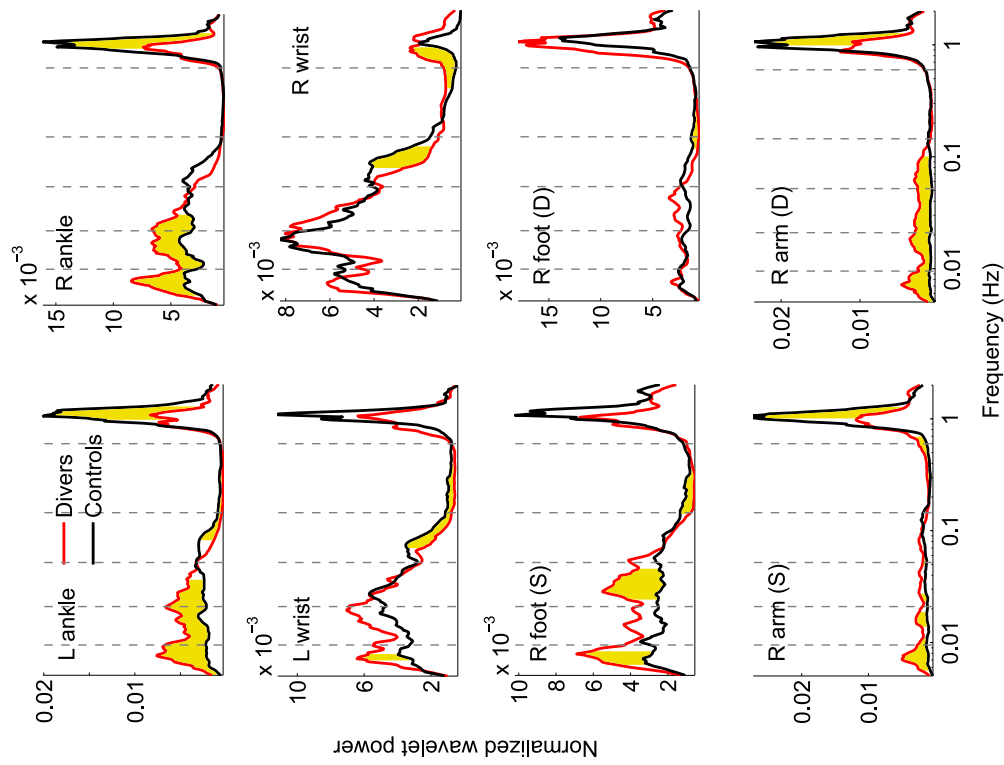
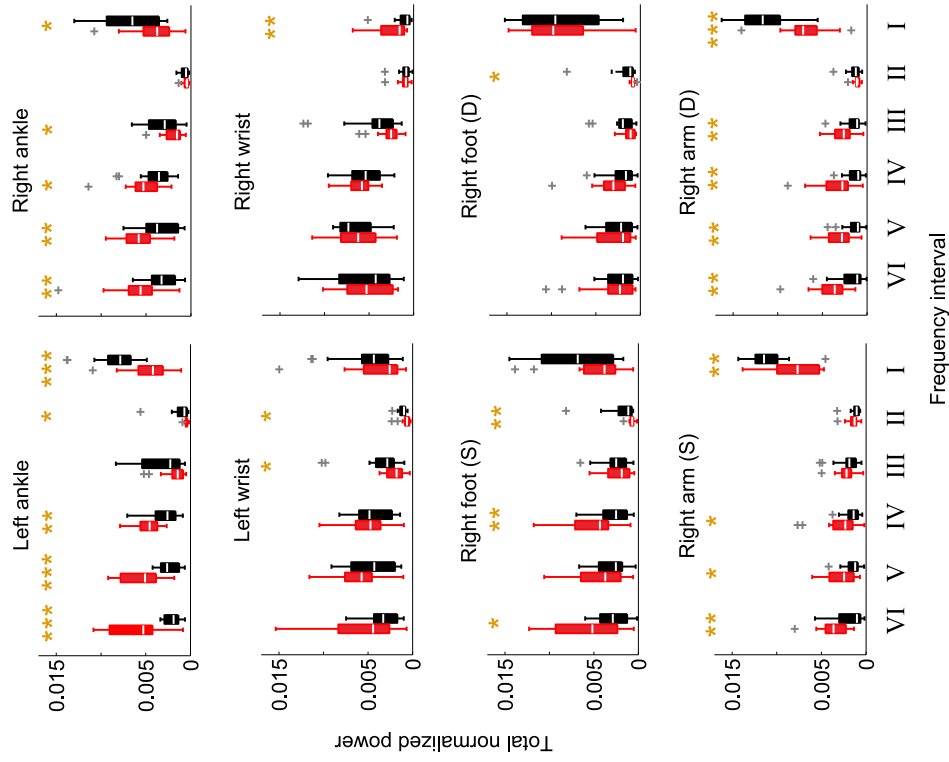


Figure 6.8: Normalized wavelet power for all recorded blood flow signals, compared between divers (red lines) and controls (black lines). Distributions were tested at each frequency, with significant differences between groups highlighted in yellow ($p < 0.05$). Frequency intervals are shown by grey dashed lines. Boxplots of normalized wavelet power in the predetermined frequency intervals for all recorded blood flow signals, compared between divers (red) and controls (black). Statistical significance is denoted with yellow asterisks. * = $p < 0.05$, ** = $p < 0.01$, *** = $p < 0.001$. Outliers are shown as grey crosses. All comparisons used the rank sum test. $n = 16$ in both groups.



Location	<i>p</i> value					
	I	II	III	IV	V	VI
Left ankle	0.0005	0.0400	0.1011	0.0039	0.0000	0.0000
Right ankle	0.0185	0.3558	0.0332	0.0302	0.0039	0.0035
Left wrist	0.3365	0.0167	0.0205	0.5591	0.1269	0.0621
Right wrist	0.0079	0.7774	0.1092	0.3179	0.8653	0.8065
Right foot (S)	0.1576	0.0063	0.6923	0.0098	0.2662	0.0400
Right foot (D)	0.9850	0.0167	0.1689	0.0864	0.5847	0.6647
Right arm (S)	0.0021	0.0864	0.3558	0.0302	0.0185	0.0050
Right arm (D)	0.0006	0.2067	0.0063	0.0021	0.0035	0.0013

Table 6.3: Results of significance testing of the total normalized power in frequency intervals on blood flow intervals between divers and controls (see Figure 6.8) using the Wilcoxon rank sum test. Significant differences are highlighted. Grey – significant increase in controls, pink – significant decrease in controls. $n = 16$ for both groups.

Location	$S_{T}O_2$ (%)		<i>p</i>
	Divers	Controls	
Right foot (S)	29.52 (18.48–37.53)	47.18 (35.75–55.98)	0.0027
Right arm (S)	52.94 (40.89–56.86)	52.43 (44.47–56.12)	0.9850
Location	rHb (%)		<i>p</i>
	Divers	Controls	
Right foot (S)	52.40 (46.95–62.75)	57.25 (50.52–64.57)	0.4624
Right arm (S)	44.62 (36.16–52.75)	49.09 (44.37–56.20)	0.1011

Table 6.4: $S_{T}O_2$ and rHb means calculated for both locations and compared between divers and controls. Values shown are medians and inter-quartile ranges of the means. Significance was tested using the Wilcoxon rank sum test. Significant differences are highlighted in grey. S – shallow. $n = 15$.

have been excluded from the analysis. Mean $S_{T}O_2$ values differed significantly between divers and controls in the right foot (controls higher, $p = 0.0027$), but not in the right arm. Standard deviations of $S_{T}O_2$ did not differ significantly between divers and controls at the right foot or the right arm ($p = 0.0734$ & 0.4397 , respectively). Mean rHb values did not differ significantly between groups in either recording location ($p = 0.4624$ & 0.1011 , respectively). Standard deviation of rHb did not differ significantly at the right foot ($p = 0.4856$), but was significantly higher in controls in the right arm ($p = 0.0010$).

Wavelet transforms of the $S_{T}O_2$ signals were calculated. One $S_{T}O_2$ signal recorded contained sustained unphysiological peaks, thus was removed from the

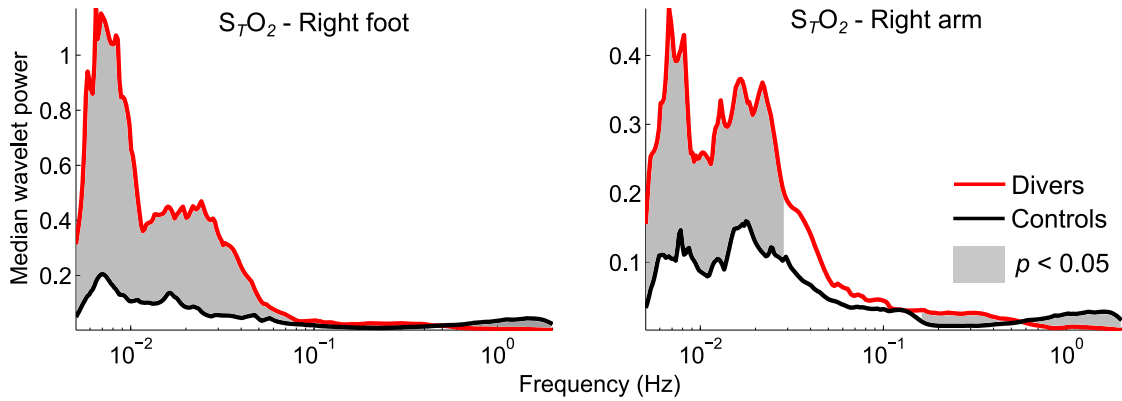


Figure 6.9: Comparison of $S_{T}O_2$ wavelet power between groups and locations. Significant differences are highlighted in grey. $n = 15$ for both groups.

following analysis, in addition to its counterpart from the control group. Differences in $S_{T}O_2$ are shown in Figure 6.9 for the remaining 15 divers and their controls. Significant differences between $S_{T}O_2$ wavelet power in divers and controls was observed below 0.026 Hz at both locations and below 0.4 Hz in the right foot.

6.3.3 Blood flow and oxygen dynamics during apnoea

Following the comparison of the freedivers with non-diving controls, it is apparent that the blood flow and oxygen dynamics of people trained to regularly deal with hypoxemia and hypoxia differ from those who are untrained. In order to assess the underlying mechanisms of this altered physiological state, here the blood flow and oxygenation signals of the freedivers are characterised during and between breath-holds, to ascertain how their bodies respond to oxidative stress. The results presented in this section cannot be compared with a control group, as it would be physically impossible and dangerous for the non-divers to attempt such long periods of apnoea. Therefore, controls are provided in the form of rest periods within the apnoea protocol.

Data were recorded from the free divers [347] as shown in Figure 6.10. The volunteers were supine and asked to remain as still as possible throughout. A sequence of instructions was played to the volunteers from a pre-recorded cassette tape. The volunteers were advised that they should breath normally if they felt

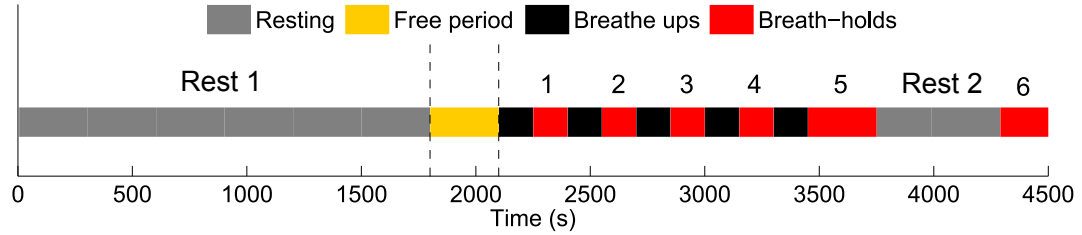


Figure 6.10: Timeline of free diver breath-hold protocol for the data previously recorded in [347]. The breath-hold portion of the protocol begins after 2100 seconds. Breath-holds are numbered. The length of breath-holds 5 & 6 varied between subjects. The 30 minute relaxed period and the breath-hold period were separated by a five minute free period in which the subjects were able to move.

any discomfort.

The resting period shown in the first 30 minutes is that investigated in Section 6.3.2. This was followed by a five minute period of free breathing in which movement was allowed; this section is not analysed. The breath-hold protocol was then applied, beginning with 4 consecutive sets of 150 seconds breathe-up, followed by 150 seconds of breath-hold. These were followed by another 150 second breathe-up before a ‘best endeavours’ breath-hold, subject to safety constraints. A period of relaxed breathing for approximately 540 seconds followed, before a final naive ‘best endeavours’ breath-hold. No countdown warning was given for the final breath-hold. The heart rate, arterial blood oxygen saturation and transcutaneous carbon dioxide were monitored throughout, to maintain safe levels. These were determined as a heart rate of 35 to 135 beats per minute, arterial oxygen saturation $> 75\%$ and transcutaneous partial pressure of carbon dioxide within the range 3kPa to 8kPa. This protocol provides 6 breath-holds per subject for analysis, with breath-holds 5 & 6 varying in length between subjects (see Table 6.9).

The experiments were undertaken within the Physics Department at Lancaster University. Each volunteer was required to provide certification from a physician confirming a recent examination of cardiovascular and respiratory health.

Example signals as recorded from one subject are shown in Figure 6.11, and example wavelet transforms of a respiration, blood flow and $S_{T}O_2$ signal are shown in Figure 6.12. The data are considered in two parts. The first part consists of

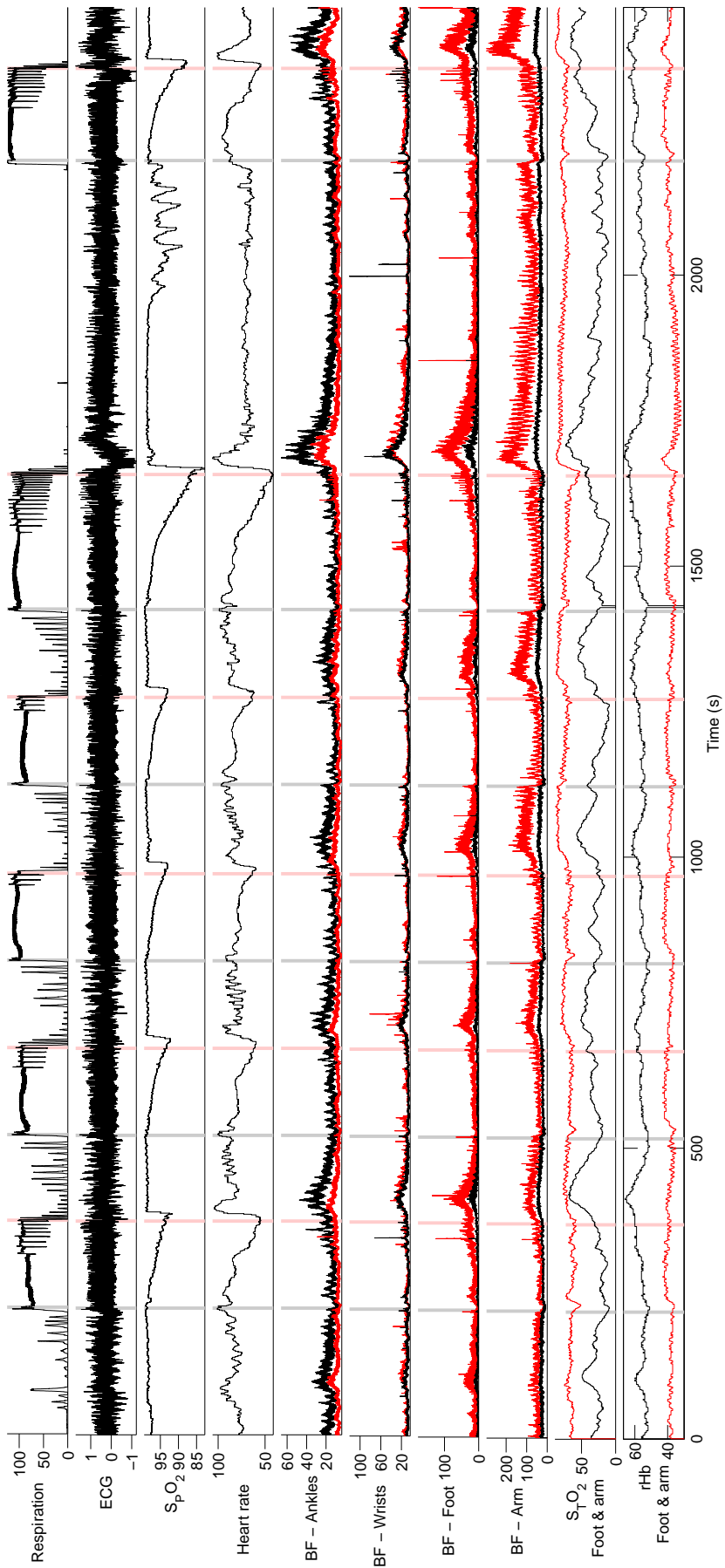


Figure 6.11: Example of physiological signals recorded from a free diver during the breath-hold protocol. BF = Blood Flow (PU). Beginning of breath-holds are marked with light grey lines and the ends are marked with pink lines. BF - ankles & wrists, black = left, red = right. BF - foot & arm, black = shallow, red = deep. SO_2 and rHb - black = foot, red = arm.

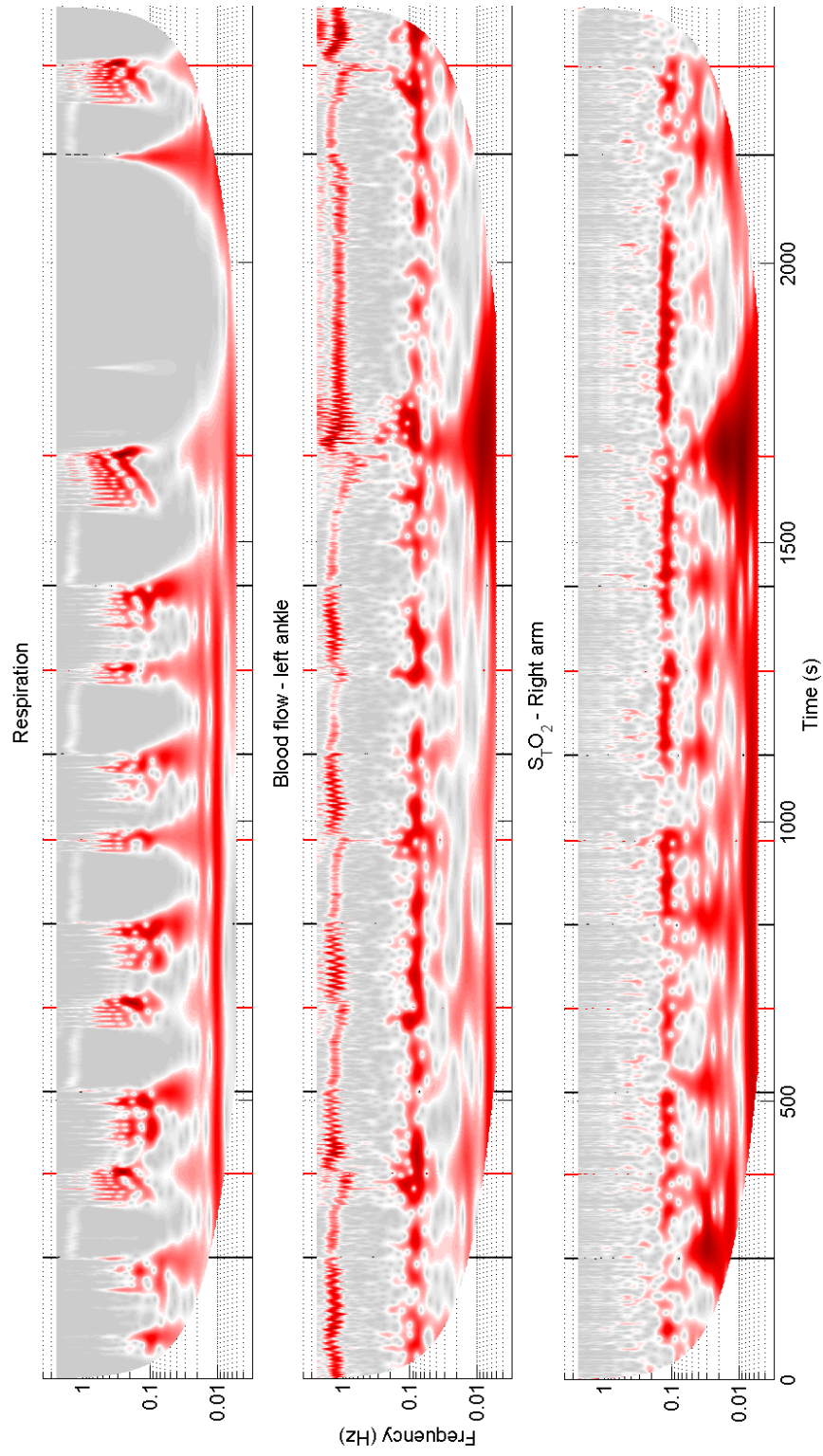


Figure 6.12: Example wavelet transforms of respiration, blood flow and S_TO₂ signals recorded from a free diver during the breath-hold protocol. The beginning of breath-holds are shown with black lines, and the ends shown with red lines.

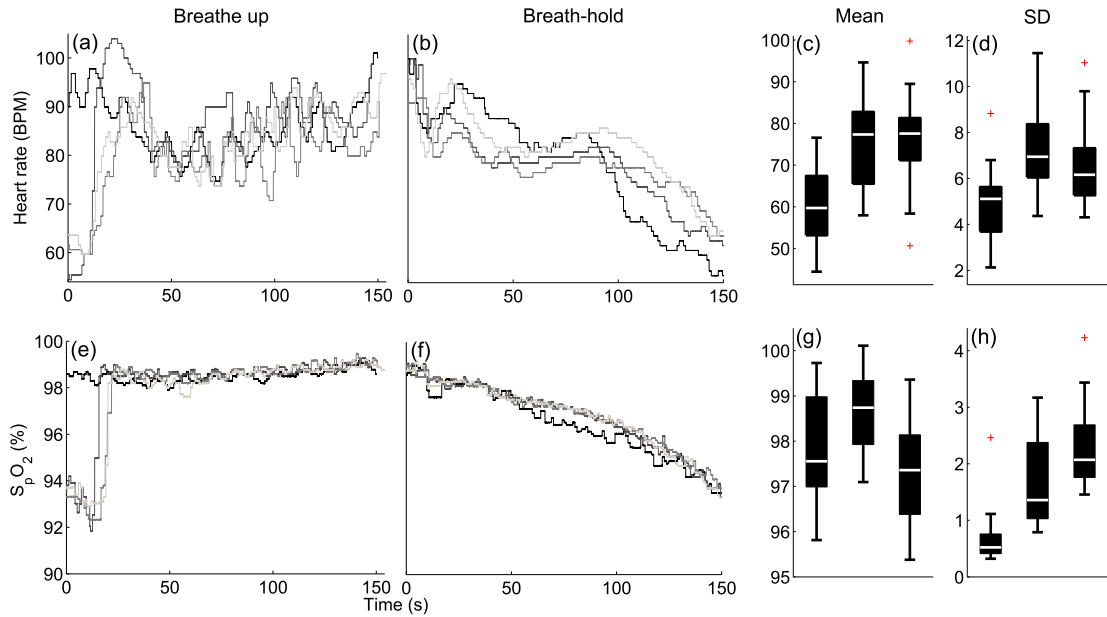


Figure 6.13: (a) Example heart rate signals from four breathe-up periods from one free diver. (b) Example heart rate signals from four breath-hold periods for the free diver in (a). (c) Boxplots of mean heart rates for all free divers during rest (R), breath ups (BU) and breath-holds (B). (d) Boxplots of standard deviation of heart rates for all free divers during the three states. (e) Example S_pO_2 signals from four breathe-up periods from one free diver. (f) Example heart rate signals from four breath-hold periods for the free diver in (e). (g) Boxplots of mean S_pO_2 for all free divers the three states. (h) Boxplots of standard deviation of S_pO_2 for all free divers during the three states. Outliers are shown as red crosses. Significant differences were found in both mean and standard deviation of heart rate and S_pO_2 , and are discussed in detail in Section 6.3.3 of the text. $n = 16$ for all comparisons, which were performed with the Kruskal Wallis test.

the first five breathe-up periods and the breath-hold which immediately followed them. The second part, consisting of the longest resting period in the breath-hold protocol for which breathe-ups were not permitted, followed by the only naive breath-hold, provides an opportunity to compare data in a more natural scenario.

Systemic changes during apnoea

First, the signals were investigated in the first part of the breath-hold period, as described above, in terms of their average values, and compared between the resting state, the breathe-up state, and during breath-holds. For the breathe-up and breath-hold periods, five data sets were available for each subject. These data sets were averaged for each subject, ensuring that a paired signed-rank significance

test could be performed on the data to account for baseline perfusion differences between subjects. Mean heart rate as measured by the TOSCA500 differed significantly between the three states ($p = 0.0003$). Further inspection highlighted that this difference arose from the resting heart rate being significantly lower than in both the breathe-up and breath-holds periods ($p = 0.0004$ in both cases). However, heart rate did not significantly differ between the breathe-up and breath-hold periods ($p = 0.4691$). Similarly, the standard deviation of the heart rate differed significantly between groups ($p = 0.0020$), and again the values at rest were lower than in both breathe-ups and breath-holds ($p = 0.0008$ & $p = 0.0016$, respectively). The standard deviation of the heart rate did not significantly differ between the breathe-up and breath-hold states ($p = 0.1477$) (see Figure 6.13).

S_pO_2 was compared between the same three states, at rest, during breathe-ups and during breath-holds, and significantly differed in terms of both mean ($p = 0.0200$) and standard deviation ($p = 0.0000$). Mean resting S_pO_2 was significantly lower than during breathe-ups ($p = 0.0061$), but did not significantly differ to S_pO_2 during breath-holds ($p = 0.2343$). Mean S_pO_2 also significantly differed between the breathe-up and breath-hold periods ($p = 0.0006$), with breath-holds exhibiting lower mean S_pO_2 . Standard deviation of S_pO_2 was significantly lower in the resting period than during breathe-ups ($p = 0.0038$) and breath-holds ($p = 0.0005$). S_pO_2 during breathe-ups showed significantly lower standard deviation of S_pO_2 than during breath-holds ($p = 0.0023$).

Systemic changes during naive apnoea

To investigate how heart rate and S_pO_2 changes during a naive breath-hold, these parameters were also compared between the 30 minute rest period (rest 1), the short rest period during the breath-hold protocol (rest 2) and breath-hold 6 which immediately follows it, importantly after no breathe-ups. An example of the signals from these groups is shown in Figure 6.14. Mean heart rate differed significantly between these groups ($p = 0.0010$) with mean heart rate during the breath-hold

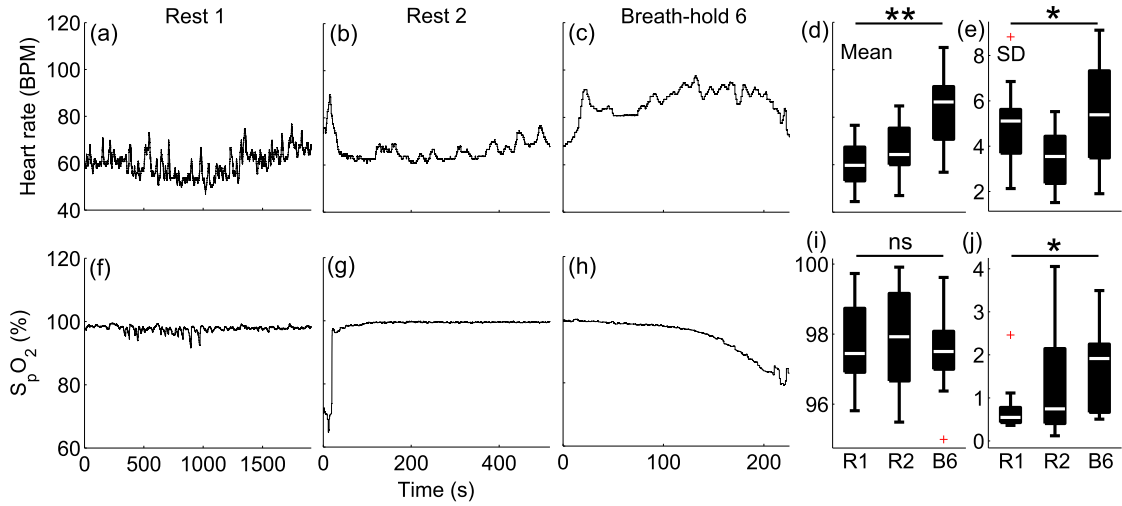


Figure 6.14: (a)–(c) Example heart rate signals recorded from one subject using the TOSCA500 during rest 1, rest 2 and breath-hold 6. (d) Boxplots of mean heart rates, which differed significantly between groups ($p = 0.0010$). (e) Boxplots of standard deviation of heart rate, which differed significantly between groups ($p = 0.0162$). (f)–(h) Example S_pO_2 signals from one subject during the three states. (i) Boxplots of mean S_pO_2 , which did not differ significantly ($p = 0.5933$). (j) Boxplots of standard deviation of S_pO_2 which differed significantly between groups ($p = 0.025$). Outliers are shown as red crosses. $n = 16$ for all comparison, which were performed with the Kruskal Wallis test.

higher than both rest 1 ($p = 0.0000$) and rest 2 ($p = 0.0003$). Heart rate during rest 2 was also significantly higher than rest 1 ($p = 0.0002$). Standard deviation also significantly differed between groups ($p = 0.0162$). SD of heart rate during rest 2 was significantly lower than in rest 1 ($p = 0.0125$) and breath-hold 6 ($p = 0.0084$). Standard deviation of heart rate did not differ significantly between rest 1 and breath-hold 6 ($p = 0.3894$). Mean S_pO_2 did not differ significantly between groups ($p = 0.5933$), but standard deviation did ($p = 0.025$), with SD of S_pO_2 significantly higher in B6 than rest 1 ($p = 0.0034$), but not rest 2 ($p = 0.7615$). SD of S_pO_2 did not significantly differ between R2 and R1 ($p = 0.0730$).

Local changes during apnoea following breathe-up

Blood flows recorded from all eight locations were compared in terms of mean flows and standard deviation of flow, between resting, breathe-up and breath-hold states. The results of significant tests between groups for all locations and all divers are shown in Table 6.5. The significance values reported under the heading ‘All’ are

the results of the Kruskal Wallis ANOVA test on all groups, which does not find significant differences in most cases. This is likely due to the fact that different mechanisms and conditions are being tested between groups, and therefore the test may not be appropriate in this context, but is included for completeness. Based on the results of the signed-rank paired test between groups it was found that at all blood flow recording locations, mean blood flow is significantly lower during breath-holds than during breathe-ups. In five out of eight recording locations mean blood flow is also significantly lower than that recorded at rest. Even in the three cases which were not significant (left ankle, right wrist and right arm (deep)), the median blood flow was lower during breath-holds than at rest.

Location	Mean blood flow (PU)(Median(IQR))			All	p value		
	Resting	Breathe-up	Breath-hold		R vs. BU	R vs. BH	BU vs. BH
Left ankle	10.33 (9.08–11.56)	9.79 (8.59–13.33)	7.95 (7.53–10.70)	0.1302	0.4380	0.1208	0.0004
Right ankle	9.76 (8.02–12.79)	10.51 (8.05–15.38)	7.88 (6.47–12.68)	0.2062	0.5349	0.0061	0.0004
Left wrist	10.20 (8.15–19.66)	11.19 (8.52–19.23)	9.04 (6.52–14.67)	0.4068	0.0494	0.0229	0.0004
Right wrist	15.24 (14.09–25.41)	20.29 (13.80–54.36)	13.84 (12.15–33.50)	0.3094	0.0703	0.8767	0.0004
Right foot (S)	6.49 (3.92–10.30)	7.13 (4.06–10.46)	5.36 (2.67–8.56)	0.3160	0.6051	0.0016	0.0004
Right foot (D)	37.37 (18.89–45.60)	37.65 (18.95–47.94)	27.04 (15.80–38.62)	0.3166	0.8767	0.0005	0.0004
Right arm (S)	17.35 (12.45–25.51)	25.27 (13.56–28.88)	10.56 (6.57–19.40)	0.0157	0.0151	0.0262	0.0004
Right arm (D)	42.87 (24.96–102.65)	73.76 (28.42–135.98)	35.74 (12.39–79.60)	0.2871	0.0032	0.2553	0.0004

Location	SD blood flow (PU)(Median(IQR))			All	p value		
	Resting	Breathe-up	Breath-hold		R vs. BU	R vs. BH	BU vs. BH
Left ankle	2.41 (1.75–3.04)	3.95 (2.07–6.68)	2.36 (1.68–3.40)	0.2002	0.0097	0.9176	0.0131
Right ankle	2.47 (1.92–3.81)	4.08 (2.29–5.92)	2.90 (1.58–4.51)	0.3510	0.1477	0.7174	0.0200
Left wrist	3.19 (2.41–4.57)	4.70 (3.04–7.37)	2.86 (2.01–5.08)	0.1738	0.0038	0.9588	0.0008
Right wrist	5.81 (3.75–9.31)	7.04 (4.71–16.63)	5.04 (3.01–9.27)	0.3464	0.3011	0.5014	0.0013
Right foot (S)	3.35 (2.30–5.94)	5.40 (3.53–6.88)	2.77 (1.83–5.56)	0.1940	0.2343	0.3520	0.0084
Right foot (D)	17.10 (8.83–21.97)	18.43 (12.04–22.35)	13.41 (7.67–17.54)	0.1607	0.6417	0.0340	0.0004
Right arm (S)	5.27(3.85–7.67)	5.80 (4.99–6.51)	3.69 (3.34–4.83)	0.0190	0.7960	0.0023	0.0004
Right arm (D)	14.18 (11.04–39.05)	19.45 (12.29–36.42)	12.11 (8.97–22.96)	0.2278	0.3520	0.0174	0.0004

Table 6.5: Top - Comparison of all mean blood flows at all recording locations. Bottom - Comparison of standard deviations of blood flows. Medians and inter-quartile ranges are shown during rest, during the breathe-up period and during breath-holds. Results of significance tests between all groups (Kruskal Wallis) and between individual groups (signed rank) are shown. R = resting, BU = breathe-ups, BH = breath-holds. Significant differences ($p < 0.05$) are highlighted. Grey – significant increase, pink – significant decrease. $n = 16$.

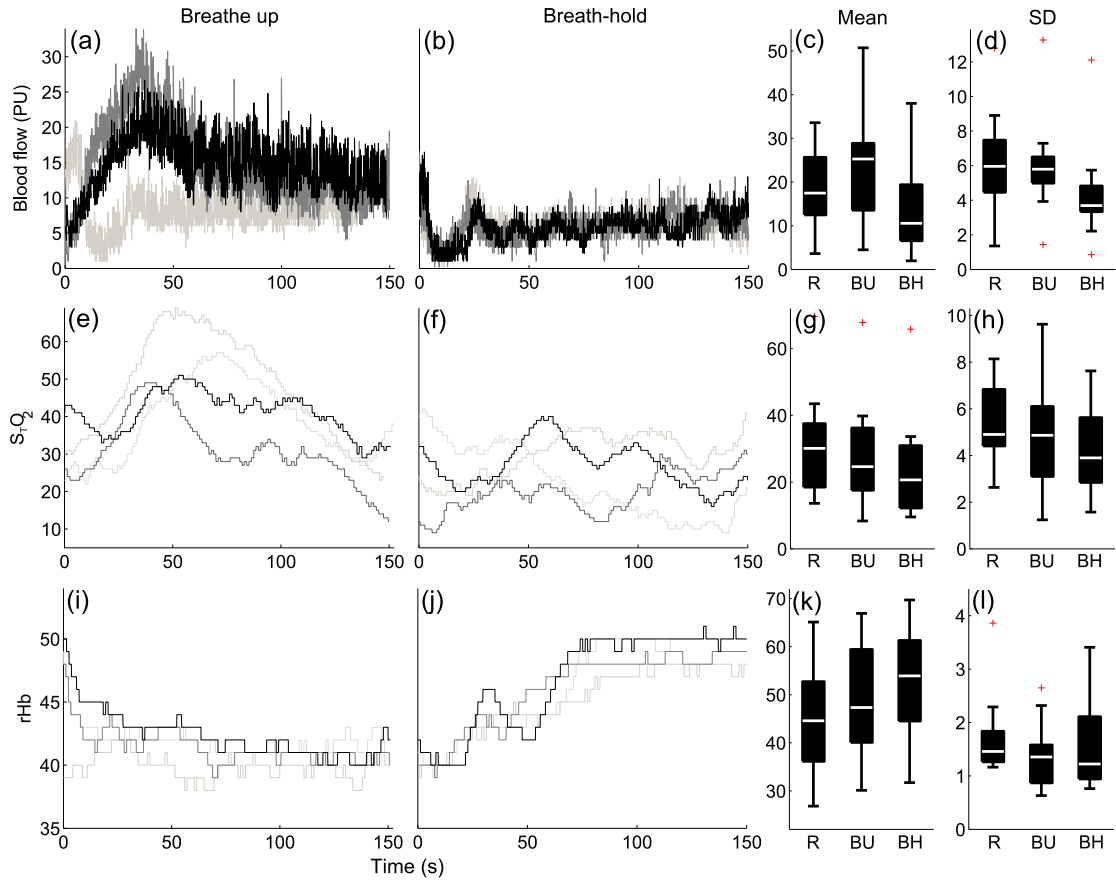


Figure 6.15: Example blood flow, $S_{T}O_2$ and rHb signals, during the breathe-up period and during breath-holds. Signals are not all from the same subject, but were chosen to represent cases in which significant differences were revealed. (a)&(b) Example blood flow signals from the right arm (shallow) of one diver during breathe-ups and breath-holds. (c)&(d) Boxplots of mean and standard deviation of blood flow for all subjects at the right arm (shallow). (e)&(f) Example $S_{T}O_2$ signals from the right foot (shallow) of one diver during breathe-ups and breath-holds. (g)&(h) Boxplots of mean and standard deviation of $S_{T}O_2$ for all subjects at the right foot (shallow). (i)&(j) Example rHb signals from the right arm (shallow) of one diver during breathe-ups and breath-holds. (k)&(l) Boxplots of mean and standard deviation of rHb for all subjects at the right arm (shallow).

Standard deviation of blood flow was found to be significantly lower during breath-holds than during breathe-ups at all recording locations. In three out of eight locations standard deviation of blood flow is also significantly lower during breath-holds than at rest.

Mean values of $S_{T}O_2$ and rHb signals were compared between the same three states. Results are shown in Table 6.6. In both recording locations, on the right foot and right arm, mean $S_{T}O_2$ was significantly lower during breath-holds than during breathe-ups. On the right foot, $S_{T}O_2$ was also significantly lower during

Location	Mean $S_{T}O_2$ (%) (Median (IQR))			All	p value		
	Resting	Breathe-up	Breath-hold		R vs. BU	R vs. BH	BU vs. BH
Right foot	30.08 (18.47–37.52)	24.62 (17.55–36.19)	20.66 (12.22–30.92)	0.1942	0.0299	0.0008	0.0009
Right arm	51.53 (38.59–55.73)	54.93 (42.16–61.51)	46.67 (35.12–55.94)	0.2976	0.1208	0.1089	0.0004
Location	Mean rHb (%) (Median (IQR))			All	p value		
	Resting	Breathe-up	Breath-hold		R vs. BU	R vs. BH	BU vs. BH
Right foot	52.38 (46.24–62.71)	55.39 (49.36–62.45)	55.79 (50.46–63.45)	0.8209	0.0980	0.2146	0.2146
Right arm	44.58 (36.15–52.73)	47.34 (40.09–59.42)	53.92 (44.53–61.30)	0.1230	0.0005	0.0004	0.0004

Location	SD $S_{T}O_2$ (%) (Median (IQR))			All	p value		
	Resting	Breathe-up	Breath-hold		R vs. BU	R vs. BH	BU vs. BH
Right foot	4.90 (4.41–6.83)	4.86 (3.10–6.10)	3.90 (2.84–5.62)	0.3545	0.2553	0.0113	0.2146
Right arm	4.72 (3.76–5.68)	3.89 (3.19–5.01)	3.15 (2.84–4.00)	0.0123	0.3520	0.0006	0.0038
Location	SD rHb (%) (Median (IQR))			All	p value		
	Resting	Breathe-up	Breath-hold		R vs. BU	R vs. BH	BU vs. BH
Right foot	1.84 (1.49–2.63)	0.94 (0.70–1.61)	1.36 (0.78–6.80)	0.0423	0.0437	0.7960	0.1208
Right arm	1.46 (1.26–1.84)	1.35 (0.87–1.58)	1.22 (0.94–2.11)	0.2218	0.1208	0.3011	0.1961

Table 6.6: Top - Comparison of means of the parameters $S_{T}O_2$ and rHb between the three states, resting (R), breathe-ups (BU) and breath-holds (BH). Bottom - Comparison of standard deviations of the parameters $S_{T}O_2$ and rHb between the three states. Significant differences ($p < 0.05$) are highlighted. Grey - significant increase, pink - significant decrease.

breathe-ups and breath-holds than during rest. On the right arm, mean rHb values significantly increased during breathe-ups when compared to rest, and during breath-holds when compared to rest and breathe-ups. In contrast, no significant changes in mean rHb were observed on the right foot. The standard deviation of $S_{T}O_2$ differed significantly on the right arm, with reduced SD during breathe-ups and breath-holds when compared to rest, but not on the right foot. Only one significant difference in the standard deviation of rHb values was observed, with a lower SD of rHb during breathe-ups than during rest on the right foot. Example signals can be seen in Figure 6.15.

Local changes during naive apnoea

Comparisons of mean blood flow between the initial 30 minute rest period (R1), and the approximately 540 second rest period (R2), showed significant differences in 3 out of 8 recording locations, with the right foot exhibiting lower mean blood flow ($p = 0.0032$) whilst the two recordings from the right arm showed an increase ($p = 0.0340$ & $p = 0.0113$). Standard deviation of blood flow did not differ significantly between states R1 and R2 except in the shallow recording of the right foot ($p = 0.0437$). Mean blood flow was significantly reduced in 2 out of 8 locations (right ankle & right foot (S)) when comparing R1 with breath-hold 6 (B6) (see Table 6.7), whilst the standard deviation of blood flow was significantly reduced in half of all locations. When comparing R2 with B6, mean blood flow was revealed to be significantly reduced in 3 out of 8 locations. The standard deviation of flow in this case differed in only 2 locations.

Oxygenation parameters were also compared between R1, R2 and B6 (see Table 6.8). Mean $S_{T}O_2$ only significantly differed on the right foot, where it was lower in B6 than in R1. Standard deviation of $S_{T}O_2$ significantly differed in both locations between R1 and R2, with a decrease observed in both. SD of $S_{T}O_2$ also significantly differed on the right arm between R1 and B6 (decrease) and R2 and B6 (increase). Mean rHb values significantly increased on the right arm, in all tested comparisons,

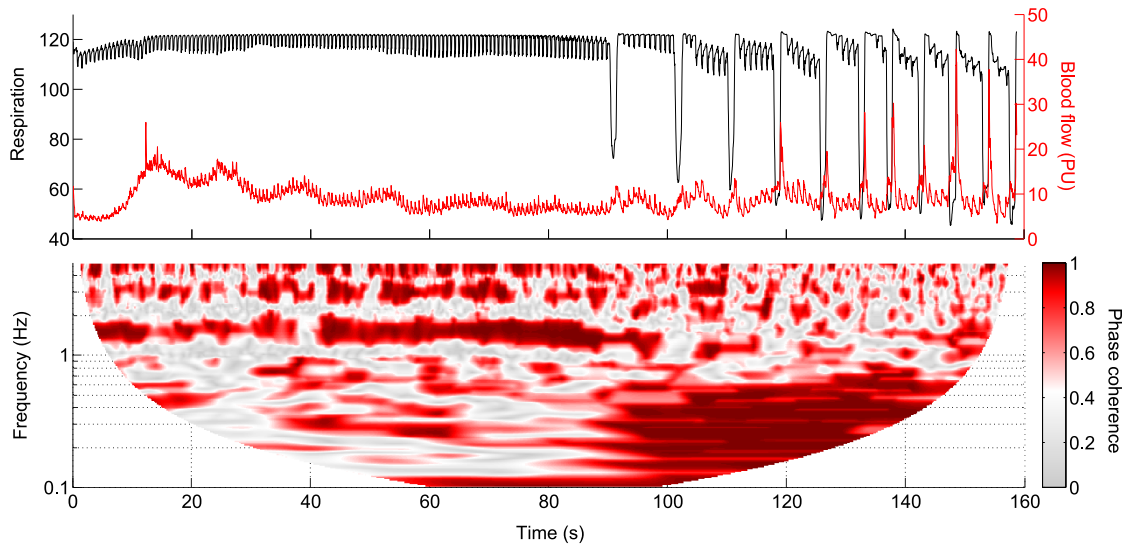


Figure 6.16: Example of the effect of involuntary contractions on LDF signals. Top - Large deviations in the respiration signal (black line) are observed during the latter part of the breath-hold, caused not by breathing but by involuntary chest contractions, which directly affect the blood flow signal (red line) recorded at the left wrist. Bottom - windowed phase coherence demonstrates very high coherence between the respiration and blood flow signals once contractions begin.

whilst on the right foot the only significant difference was an increase in B6 from R2. Standard deviation of rHb did not differ in the right foot, but decreased in R2 when compared to R1 on the right arm, and increased in B6 when compared to R2.

Involuntary chest contractions

In the majority of subjects, involuntary chest contractions were observed during the latter part of breath-holds. These phenomena, and many physiological parameters related to them were studied in [347]. These physical movements of the chest directly affect many of the recorded signals, with those most sensitive to movement, including LDF, most affected. Therefore great care must be taken when interpreting signals recorded during this period. An example of involuntary contractions, and their effect on a blood flow signal, is shown in Figure 6.16. It is clear that any time-frequency analysis on these affected signals may lead to unreliable results. Therefore, the influence of the contractions must be removed from the signals, either by subtraction of their effect on the blood flow, or removal of the

Location	Mean blood flow (PU)(Median(IQR))			All	<i>p</i> value		
	Resting 1	Resting 2	Breath-hold 6		R1 vs. R2	R1 vs. B6	R2 vs. B6
Left ankle	10.33 (9.08–11.56)	8.43 (7.54–11.08)	8.06 (6.76–10.88)	0.2913	0.5695	0.3520	0.1477
Right ankle	9.76 (8.02–12.79)	8.36 (6.44–11.64)	8.65 (6.25–10.74)	0.2774	0.0787	0.0084	0.2775
Left wrist	10.20 (8.15–19.66)	9.67 (5.58–18.36)	9.23 (5.39–12.47)	0.7640	0.7960	0.0557	0.0494
Right wrist	15.24 (14.09–25.41)	18.32 (14.12–39.99)	19.13 (13.61–35.50)	0.6500	0.0879	0.1208	0.2146
Right foot (S)	6.49 (3.92–10.30)	6.51 (2.98–8.64)	5.92 (3.59–7.73)	0.6710	0.0032	0.0072	0.1089
Right foot (D)	37.37 (18.89–45.60)	38.44 (18.55–50.58)	29.38 (20.89–42.18)	0.8862	0.2146	0.1627	0.3259
Right arm (S)	17.35 (12.45–25.51)	22.55 (13.45–30.50)	11.20 (6.75–17.42)	0.0512	0.0340	0.1337	0.0016
Right arm (D)	42.87 (24.96–102.65)	68.90 (32.49–131.98)	29.44 (15.20–89.97)	0.3112	0.0113	0.2775	0.0011

Location	SD blood flow (PU)(Median(IQR))			All	<i>p</i> value		
	Resting 1	Resting 2	Breath-hold 6		R1 vs. R2	R1 vs. B6	R2 vs. B6
Left ankle	2.41 (1.75–3.04)	1.67 (1.47–2.77)	1.68 (1.35–2.63)	0.2871	0.6417	0.0879	0.1208
Right ankle	2.47 (1.92–3.81)	2.09 (1.32–2.96)	1.67 (1.34–2.16)	0.0752	0.0627	0.0061	0.4691
Left wrist	3.19 (2.41–4.57)	2.69 (1.45–4.18)	2.85 (1.87–3.64)	0.6820	0.3011	0.3794	0.1961
Right wrist	5.81 (3.75–9.31)	4.81 (2.78–9.26)	5.89 (3.00–9.90)	0.8256	0.5695	0.6791	0.3259
Right foot (S)	3.35 (2.30–5.94)	3.16 (1.77–4.85)	2.67 (1.67–5.26)	0.5503	0.0437	0.0151	0.6051
Right foot (D)	17.10 (8.83–21.97)	16.87 (9.30–22.32)	14.68 (7.75–18.01)	0.5088	0.1627	0.0174	0.0879
Right arm (S)	5.27 (3.85–7.67)	4.48 (3.54–6.72)	4.32 (2.99–5.16)	0.2746	0.8361	0.0229	0.0340
Right arm (D)	14.18 (11.04–39.05)	18.11 (9.82–36.39)	12.90 (6.97–29.61)	0.4226	0.9176	0.0299	0.0200

Table 6.7: Comparison of mean and standard deviation of blood flow at all locations recorded in divers during the initial long rest period (Rest 1), the short rest period (Rest 2) and during breath-hold 6. Significant differences are highlighted. Grey – Significant increase, pink – significant decrease. $n = 16$.

Location	Mean $S_{T}O_2$ (%) (Median (IQR))			p value			
	Resting 1	Resting 2	Breath-hold 6	All	R1 vs. R2	R1 vs. B6	R2 vs. B6
Right foot	29.52 (18.48–37.53)	26.17 (15.86–35.58)	23.33 (16.08–29.90)	0.4143	0.1337	0.0200	0.0787
Right arm	51.55 (38.60–55.74)	49.31 (41.32–61.81)	45.27 (34.47–53.96)	0.4860	0.3259	0.2553	0.0032
Location	Mean rHb (%) (Median (IQR))			p value			
	Resting 1	Resting 2	Breath-hold 6	All	R1 vs. R2	R1 vs. B6	R2 vs. B6
Right foot	52.40 (46.92–62.75)	53.29 (47.83–62.03)	56.78 (50.01–64.12)	0.6556	1.000	0.0703	0.0005
Right arm	44.62 (36.16–52.75)	46.44 (38.78–59.52)	55.42 (44.37–61.36)	0.1886	0.0023	0.0004	0.0004

Location	SD $S_{T}O_2$ (%) (Median (IQR))			p value			
	Resting 1	Resting 2	Breath-hold 6	All	R1 vs. R2	R1 vs. B6	R2 vs. B6
Right foot	4.75 (4.34–5.76)	3.83 (3.23–4.38)	4.22 (2.68–6.10)	0.1346	0.0174	0.5014	0.1627
Right arm	4.59 (3.65–5.67)	2.38 (2.04–2.82)	3.59 (2.55–3.92)	0.0002	0.0004	0.0174	0.0131
Location	SD rHb (%) (Median (IQR))			p value			
	Resting 1	Resting 2	Breath-hold 6	All	R1 vs. R2	R1 vs. B6	R2 vs. B6
Right foot	1.27 (0.97–1.68)	0.87 (0.63–1.64)	0.91 (0.73–1.89)	0.2445	0.4691	0.3259	0.7174
Right arm	1.35 (1.18–1.71)	0.98 (0.55–1.21)	1.19 (0.91–2.24)	0.0220	0.0084	0.8361	0.0174

Table 6.8: Comparison of mean and standard deviation of $S_{T}O_2$ and rHb at all locations recorded in divers during the initial long rest period (Resting 1), the short rest period (Resting 2) and during breath-hold 6. Significant differences are highlighted. Grey – Significant increase, pink – significant decrease. $n = 16$.

latter part of the signal. Attempts were made to extract the effects of respiration from the LDF signals using nonlinear mode decomposition, using the respiration signal as a reference, but this was unsuccessful in the majority of cases. When an extraction was successful, NMD returned a sinusoidal waveform, which is not precise enough for this purpose. Wavelet phase coherence was calculated between respiration and all blood flow signals during breath-hold six. Although significant coherence was not found in all instances during contractions, the uncertainty of how much each LDF signal is affected by the involuntary contractions necessitates the exclusion of all data recorded for their whole duration. Therefore, only the periods before they begin are considered. Updated signal lengths are presented in Table 6.9.

Blood flow and oxygenation dynamics during naive apnoea

It is clear from the presented results that there is a huge difference in the way the body reacts to apnoea depending on whether it follows a period of breathe-ups or not. Thus, only signals recorded during the naive breath-hold (B6) are considered in this section. Whilst the investigation of the studied parameters in terms of average values has revealed insights into systemic and local physiological behaviour, these do not provide any information regarding the time-evolution of these parameters, and whether this varies between states. To extract this information from the data, time-frequency analysis methods are required. The rest period of approximately 540s allows the observation of oscillatory activity down to the neurogenic interval to be studied, but not all breath-holds are long enough to allow the neurogenic interval to be studied. In most cases, this rest period contained a large peak at the beginning, as the parameters recovered from the previous breath-hold. This peak was removed for time frequency analysis to avoid the increased power at lower frequencies in which this would result. The lengths of breath-holds five and six for each subject are recorded in Table 6.9, with and without periods involving chest contractions.

Subject	B5 length (s)	B6 length (s)	B5 length BC (s)	R length (s)	B6 length BC (s)
1	183.6	161.2	114.7	574.0	94.2
2	168.6	41.1	157.5	597.3	41.1
3	210.6	192.8	124.4	550.3	83.9
4	232.7	158.8	131.3	541.1	90.2
5	294.3	216.9	240.2	470.3	157.5
6	225.6	159.8	87.6	540.4	71.7
7	247.8	225.4	176.5	515.4	192.3
8	338.2	105.3	166.0	423.4	100.6
9	248.6	266.7	248.6	524.1	206.1
10	127.2	82.4	113.7	651.3	79.8
11	245.1	260.0	209.0	519.0	210.5
12	234.3	199.9	114.0	536.2	87.3
13	212.8	221.9	146.1	561.7	134.5
14	398.1	350.2	246.3	386.7	244.7
15	240.3	293.6	150.2	528.4	137.4
16	194.8	189.5	157.9	569.0	138.3

Table 6.9: Lengths of breath-holds five and six for all subjects, and their lengths after removing periods affected by involuntary contractions (BC).

The varying length of breath-hold 6 led to varying lower limits of frequencies observable in the wavelet transform. To allow reliable comparisons between groups in different frequency intervals, spectra were required to span the whole frequency interval to be included in the calculations for that interval, for example, to be included in comparisons in the neurogenic interval, data must be available in the frequency spectrum down to at least 0.021 Hz. Breath-hold 6 for subject 2 was very short (41 seconds) and so subject 2 was removed from the analysis. Many signals from subject 10 contained unphysiological spikes, thus subject 10 was also removed from this analysis. Based on these constraints, the following data are calculated from 14 subjects in frequency intervals I, II & III, and 4 subjects in intervals I, II, III & IV. Due to this small sample size available in the neurogenic interval, care must be taken with interpretation of the results. Before analysis, signals were detrended with a moving average with a window size of 50 seconds. Wavelet transforms of blood flows were calculated for all recording locations, and their time-averages compared between R2 and B6.

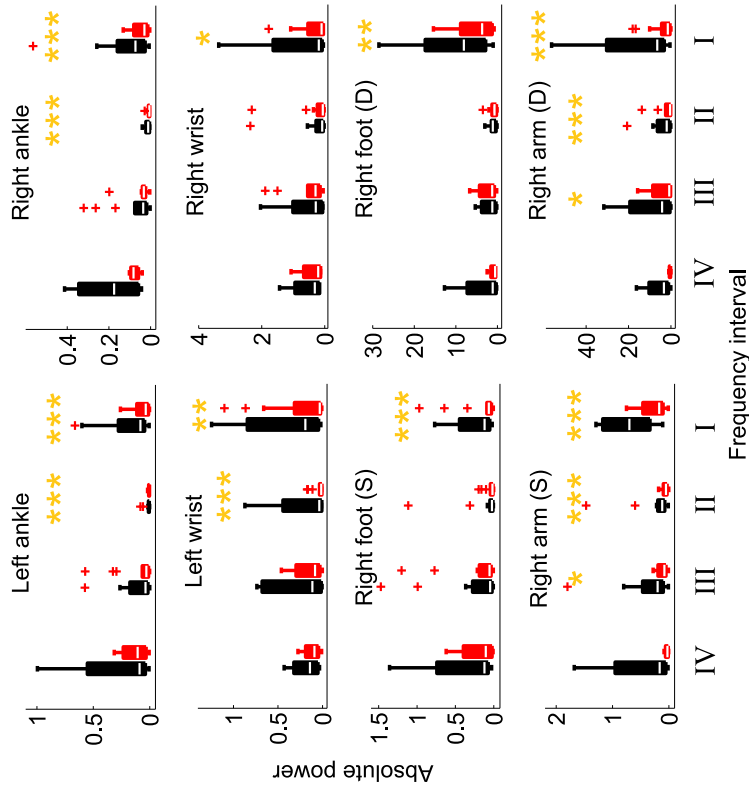
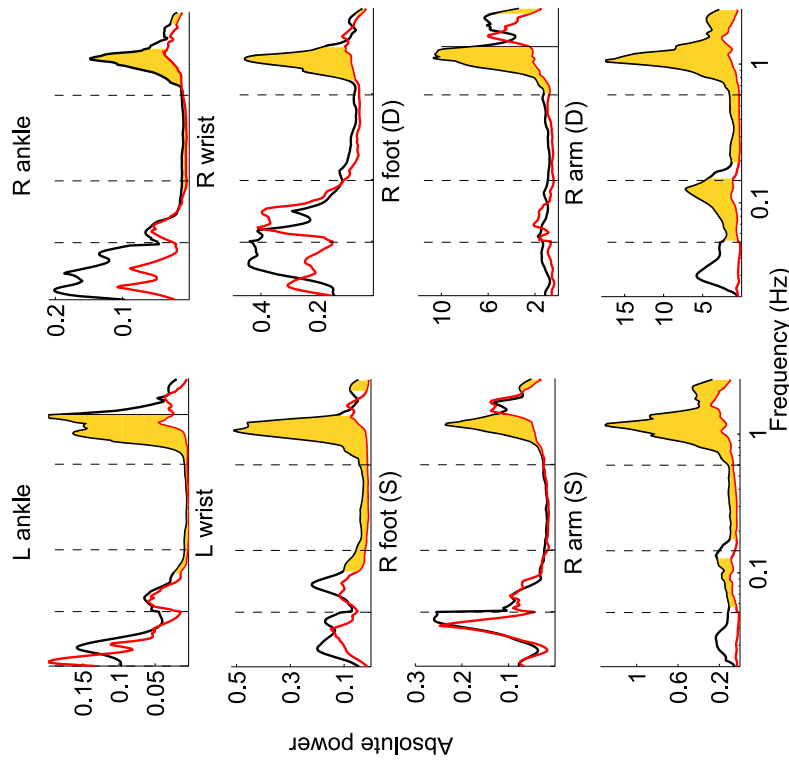


Figure 6.17: Time averaged wavelet power of blood flow compared during rest (black line) and the final breath-hold (red line) for all recording locations in 14 subjects down to the myogenic interval and 4 subjects down to the neurogenic interval. Frequency intervals are shown down to the neurogenic interval with grey dashed lines. Significant differences are highlighted in yellow. Boxplots of absolute wavelet power in frequency intervals I-IV during rest (black) and during breath-hold 6 (red) for all blood flow recording locations in 14 subjects down to the myogenic interval and 4 subjects down to the neurogenic interval. Statistically significant differences are denoted with yellow asterisks. * = $p < 0.05$, ** = $p < 0.01$, *** = $p < 0.001$. Outliers are shown in red.

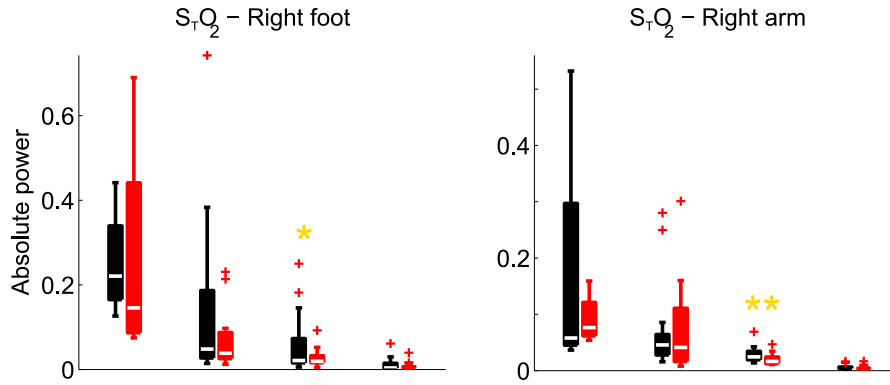


Figure 6.18: Boxplots of absolute wavelet power in frequency intervals I–IV during rest (black) and during breath-hold 6 (red) for both $S_T O_2$ recording locations in 14 subjects down to the myogenic interval and 4 subjects down to the neurogenic interval. Statistically significant differences are denoted with yellow asterisks. * = $p < 0.05$, ** = $p < 0.01$, *** = $p < 0.001$. Outliers are shown in red.

Significant differences were revealed in all locations, as shown in Figure 6.17. Comparisons of power in individual frequency intervals revealed significant differences in cardiac power in all locations, with a lower power observed during B6 than in R2 in all cases. In the respiration interval, 5 out of 8 locations showed significant differences in power, with the power being lower during breath-hold, as expected. Only blood flow recordings from the right arm showed significant differences in the myogenic interval ($p = 0.0134$ (shallow), $p = 0.0419$ (deep)), whilst no differences were observed in the neurogenic interval. Comparisons of $S_T O_2$ recorded at the right foot and right arm revealed significant differences only in the respiration interval ($p = 0.0134$ and 0.0009 , respectively).

This approach to the characterization of blood flow dynamics, i.e. applying statistical tests at all frequencies for all subjects, may not be optimal if the natural frequencies of vasomotion varies between subjects, as is likely the case. Whilst this spectral averaging approach would highlight any systematic, large differences between states, it may cause small variations to be overlooked, due to averaging over many different frequencies and subjects. To ensure that individual differences in blood flow dynamics were taken into account, all blood flow signals were inspected for signatures of vasomotion, and their characteristics recorded. Using again the blood flow signals recorded during the rest period R2 and the naive breath-hold

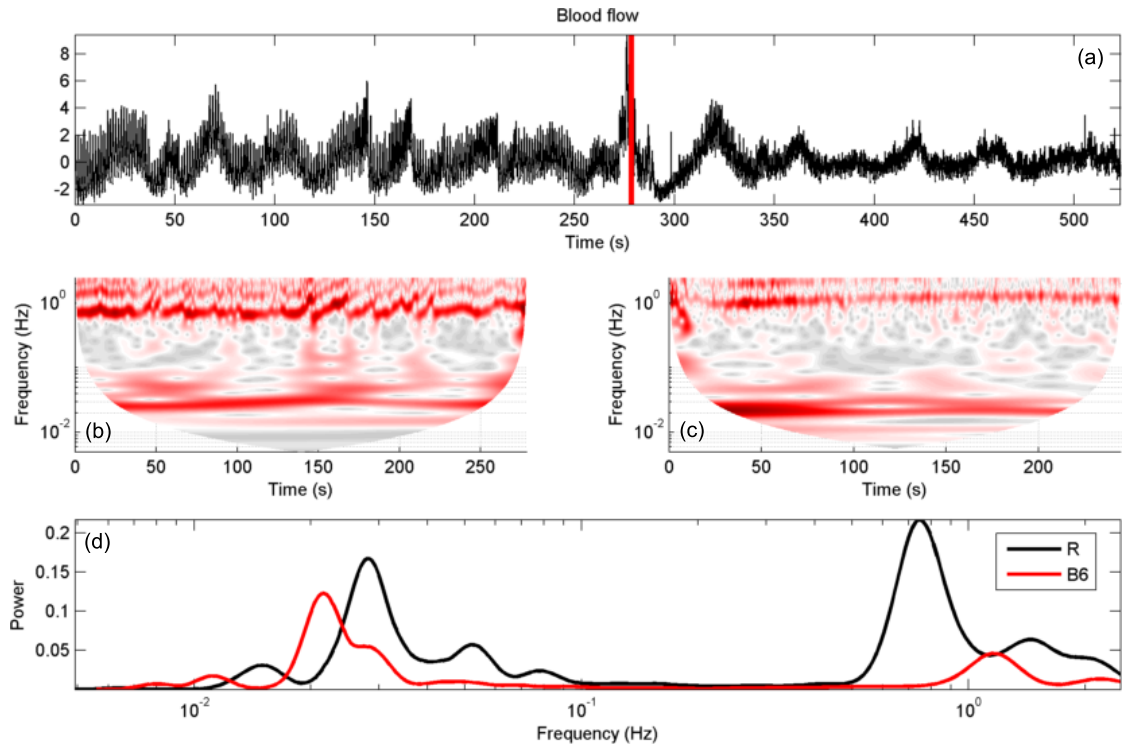


Figure 6.19: Example blood flow signal recorded during rest and breath-hold 6. (a) Blood flow recorded in subject 14, during R2 and B6, the beginning of the breath-hold is shown by a red line. (b) Continuous wavelet transform of R2. (c) CWT of B6. (d) Time averaged wavelet power spectra for the rest period (black line) and breath-hold 6 (red line). In this case the power and frequency of low frequency oscillations are reduced during breath-hold.

B6, signals were investigated provided that they met the following criteria: 1) sustained oscillations were present in the resting portion of the signal, 2) the length of B6 is long enough to include at least two of these oscillations, 3) there is no transient present at the start of B6, or if there is, it does not completely dominate the spectrum. An example of one of the tested blood flow signals is shown in Figure 6.19. In this case, the oscillations present during R2 are reduced in both power and frequency during breath-hold. The peaks of oscillatory activity were recorded for all signals which met the criteria in order to ascertain whether there were any common effects of apnoea on blood flow dynamics. In total, 39 data sets met the above criteria. Power and frequency of the dominant peaks were recorded in each data set during R2 and B6. To allow the observation of lower frequencies, the wavelet transform was calculated with a less strict cone of influence, at the expense of reducing accuracy. All signals were carefully inspected to ensure that

recorded peaks were real. Based on individual differences in power and frequency, no distinct patterns arose for the alterations in vasomotion during apnoea. During apnoea, the power of oscillations increased in 18 out of 39 cases, and decreased in 21. The frequency of oscillations increased in 14 out of 36 cases and decreased in 20, with no change in 2 cases, showing a slight preference for a decrease in frequency of oscillations.

6.4 Summary

This chapter aimed to determine whether blood flow and oxygenation dynamics are altered during apnoea. Apnoea provides an opportunity to study physiological parameters during a state of oxygen deprivation. In a previous study, free divers were recruited and requested to follow a protocol involving periods of rest and breath-holds. The very nature of the training practised by the free divers means that their physiology may be permanently altered in order to adapt to the demands of long periods of apnoea. To investigate the extent of these alterations, a control group of age- and sex-matched, healthy, non-divers were recruited. Clear differences were found between divers and controls. Whilst mean heart rate did not vary between the groups, heart rate variability significantly varied below 0.04 Hz, with the divers showing more variability in their heart rates. This could indicate that their hearts are much more efficient at responding to the needs of their bodies, an adaptation that could have arisen from their apnoea training. Similarly, arterial oxygen saturation recordings showed no difference in mean values between divers and controls but significantly higher variability in divers.

Wavelet phase coherence analysis between respiration and S_pO_2 showed significant coherence in both groups, showing that the observed peaks in S_pO_2 are related to respiration, and this coherence differed significantly between divers and controls, with coherence in divers occurring in a slightly narrower range. Phase coherence was also calculated between respiration and heart rate variability, to investigate whether respiratory sinus arrhythmia is altered in divers. The results suggest that

this phase coherence significantly differs between groups at lower frequencies, with divers demonstrating higher coherence, perhaps due to their increased heart rate variability. Comparisons of blood flow between divers and controls did not reveal a global difference in mean blood flows, with significant differences found only in the right and left wrists, which are only two out of eight recording locations. In contrast, significant differences were found in the time-averaged normalized wavelet power spectrum in all recording locations, at varying frequencies between groups. The blood flow dynamics results show that the normalized power spectra of the divers differ in that they generally show a decrease in power in the cardiac frequency interval, and an increase in power in the lower frequency intervals IV, V, and VI. This again points to an increased efficiency in free divers, this time at a local level. As vasomotion is beneficial to tissue perfusion, an increase in vasomotion in divers could suggest that their mechanism of substrate delivery is optimised due to their apnoea training. However, the normalization of these blood flow spectra necessitates careful interpretation of the results. The differences seen could also arise from the observed reduction in cardiac power, which may not be related to the efficiency of tissue perfusion, but the elasticity and regulation of the vessels themselves. It has previously been shown that vessel elasticity reduces with age [351], and that this may cause the cardiac component of an LDF signal to dominate the spectrum. This is because of a gradual decline in the health of the blood vessels, but may be applicable here. It is possible that the divers may have healthier, more efficient vasculature in general than their counterparts; this may also manifest as the result seen here. Another possibility is that the vasomotion in the control group is less synchronized, and thus the power at each frequency would be more variable and lead to lower power overall.

Signals recorded during apnoea were used to characterise blood flow and oxygenation dynamics during a period of reduced oxygen intake. The most interesting states to consider would be hypoxaemia, a systemic low concentration of oxygen in the blood, or hypoxia, a local reduction in oxygen. Unfortunately, whilst hy-

poxaemia did occur during some breath-holds, it corresponded to the periods in which involuntary chest contractions were observed in some divers, meaning that the data recorded during these periods was not reliable. Hypoxia, a local lack of oxygen, was also observed very rarely, defined for the O2C device as an oxygen saturation of $<10\%$. The values recorded by the O2C are relative however, so the *differences* in local oxygenation were considered, rather than considering this possibly unreliable marker of hypoxia.

The data recorded during the apnoea protocol were considered in two parts. Part 1 consisted of data recorded in breath-holds following breathe-ups, and part 2 considered naive breath-holds. Part 1 compared physiological parameters during the 30 minute rest period (R1), the breathe-up periods (BU) and the breath-holds following them (BH), whilst part 2 compared the long rest period (R1), short rest period preceding breath-hold 6 (R2) and breath-hold 6 (B6). In both parts, systemic differences were observed between R1 and breath-hold. Mean heart rate was significantly increased during breath-hold in both parts, as was standard deviation of S_pO_2 . However, whilst standard deviation of heart rate was increased in breath-holds during part one, there was no significant difference in part 2. Mean S_pO_2 did not change in either part between R1 and breath-holds, but differences were observed when taking into account the intermediate signals from the breathe-up period in part 1 and the R2 period in part 2. This highlights the fact that neither period BU nor R2 can be considered as a true rest period, as they differ significantly from the data recorded in R1. This leads to the question of whether the breath-holds following these periods would be affected by such changes. The closest to rest is the period R2, as there is no artificial breathing for the purposes of lung packing, and thus breath-hold 6 is the closest to a natural breath-hold available in this data.

Mean blood flows were calculated for each part. The differences found between mean blood flows in breath-holds and rest periods heavily depended on whether they were preceded by a breathe-up period or not. In part 1, mean blood flow

significantly decreased during breath-hold in five out of eight recording locations when comparing to R1 and in all recording locations when comparing to BU. In contrast, in part 2, mean blood flow was only significantly reduced in two recording locations when comparing to R1 and 3 recording locations when comparing to R2. This highlights the effect breathe-ups can have on the mean blood flow of the subsequent breath-hold. In terms of mean $S_{T}O_2$, the results were similar between part 1 and part 2, with a decrease in mean $S_{T}O_2$ observed on the right foot but not the right arm in both parts, when comparing the breath-hold to the true rest period R1. Mean rHb showed a significant increase on the right arm but not on the right foot in both cases.

In light of the differences introduced to blood flow and oxygenation recordings by breathe-ups, blood flow and oxygenation dynamics analyses were only performed for naive breath-holds. In order to observe directly the differences induced by apnoea, the power spectra of R2 and B6 were compared for each subject. The short time periods of available data, made shorter by removal of data recorded during involuntary chest contractions, limit the information available at lower frequencies. All included subjects could be compared down to the myogenic frequency interval, whilst 4 subjects provided recordings long enough for the neurogenic interval to be compared. Possibly as a result of this small sample size, no significant differences were found in interval IV for any recording location. Significant differences in the myogenic interval (III) were only observed in the right arm, at both shallow and deep recording locations. In both cases, the power in interval III is significantly lower during breath-hold than during rest. Cardiac power decreased significantly during breath-hold in all recording locations. These results suggest that apnoea does not have a significant effect on local blood flow dynamics overall, at least in free divers. However, this does not mean that there would not be a significant effect in untrained individuals.

Inspection of the data from each subject revealed unique responses for each individual, with some signals showing barely any difference during apnoea, whilst

others showed significant alterations in their oscillatory activity. Therefore, each data set was individually inspected for evidence of vasomotion, i.e. sustained oscillations, in the rest period R2. If these were found, the absolute power and the frequency of the most prominent peak in the spectrum was recorded, both during R2 and B6 to see if this activity was altered during apnoea. Results from this analysis proved to be inconclusive, with no significant trends revealed, other than a slight preference for a decrease in frequency of oscillations during apnoea.

The main results of this chapter reveal the physiological differences between normal healthy humans and free divers, in terms of systemic and local dynamics of blood flow and oxygenation. Differences likely arise from increased efficiency of delivery of nutrients as a direct result of the training of the divers, possibly coupled with a genetic predisposition to be able to deal with such conditions. Whilst a very interesting state to observe, it is clear that divers possess very specific physiological responses, and thus no conclusions can be drawn about blood flow and oxygenation dynamics in normal humans from these data. Further research would be necessary to enable the same observations in non-divers. As it would be impossible for untrained individuals to follow a protocol involving such long periods of apnoea, the desired state of oxygen deprivation could be achieved using an altitude simulation device, which simulates the reduced oxygen partial pressures found at high altitudes. In a carefully controlled environment, this protocol could provide the opportunity to safely study the hypoxic state, and also provide much more opportunity to ensure the protocol for each individual was identical, rather than the varying breath-hold lengths studied here.

In summary, this chapter demonstrates the following:

- The physiology of free divers is permanently altered when compared to non-diving controls, in terms of heart rate variability and arterial oxygen variability.
- Wavelet phase coherence analysis showed that divers exhibit higher phase coherence between respiration and heart rate variability at frequencies around

0.025–0.075 Hz.

- Comparisons of mean blood flow between divers and controls at rest showed no global differences, whilst the time-averaged normalized wavelet power spectra were significantly different in all recording locations, generally showing a decrease in power in the cardiac frequency interval and an increase in intervals IV, V & VI in divers when compared to controls. This suggests an increased efficiency in local blood flow regulation in divers.
- These results suggest that the training undertaken by free divers has significantly altered their physiology, to meet the demands of regular oxygen deprivation.
- Breathe-ups significantly alter the physiological response in the subsequent breath-hold, and thus cannot be used as a rest period for accurate comparisons.
- During apnoea, in general, mean heart rate increases, the cardiac contribution to blood flow decreases, mean blood flow decreases and mean $S_{T}O_2$ decreases.
- In cases where sustained oscillations were present, indicating the presence of vasomotion, the frequency of these oscillations decreased in the majority of cases during apnoea. This agrees with the model presented by Goldman and Popel [82], in that low frequency oscillations appear to be most useful for effective tissue oxygenation.
- The results presented in this chapter from the apnoea protocol go into more detail than previously [347] regarding the blood flow dynamics observed during breath-holds. The previous study only considered vasomotion in one volunteer during apnoea.

7. Modelling metabolic oscillators

Energy production within a living cell is far from constant. Variations in supply and demand may result in continuous fluctuations of adenosine triphosphate (ATP) concentration. Recently developed experimental techniques for the observation of cellular metabolism, including fluorescence microscopy [232, 220] and fluorescence resonance energy transfer (FRET) biosensors [219], clearly illustrate metabolic fluctuations, though sometimes they are overlooked due to averaging [352] or considered as purely stochastic [353]. However, whilst their existence is not universally accepted, metabolic oscillations have been observed in many studies in the mitochondria [245, 241, 220], in glycolysis [243, 227, 354, 219] and in both simultaneously [1].

Thus, both glycolysis and oxidative phosphorylation (OXPHOS) can be considered as biological oscillators with variable frequencies depending upon external concentrations of oxygen and glucose [241, 239]. Moreover, they are coupled and can drive and modulate each other [226, 1, 227], which is essential to the maintenance of sufficient ATP levels. It is these interactions which determine the metabolic state of a cell. When the conditions within a system change (e.g. in hypoxic or cancerous cells), the interactions between metabolic oscillators also change [1, 227], thus changing the oscillatory dynamics of metabolism. These changes are complex and not well understood.

In addition to being oscillatory, energy production in a cell is inherently time-dependent. Taking a single snapshot in time of a system with time-varying dynamics, be it a single cell or a whole organ, cannot provide sufficient information

about its past or future evolution, or its interactions with its environment. Instead, it must be considered as a non-autonomous dynamical system [355, 289] to fully gain a realistic understanding of its behaviour. Thus, in this chapter, cellular metabolism is modelled using non-autonomous oscillatory dynamical systems, with the aim of characterizing these oscillations in healthy and altered metabolic states. More specifically, coupled chronotaxic phase oscillators were used to investigate the interplay between glycolytic and mitochondrial involvement in ATP production in the presence of glucose and oxygen. It is demonstrated that using this model it is possible, in different scenarios, to identify which metabolic pathway plays the dominant role. In particular, the metabolic dysfunction which is well known to be present in cancer is considered. It is shown that chronotaxicity may change during the transition from the normal to cancerous state, and be used to detect this transition. Finally, it is demonstrated how this method could lead to the observation and identification of these states experimentally. This could provide an opportunity to follow the temporal evolution of metabolic dysfunction, and its possible links to carcinogenesis.

7.1 Modelling cellular energy metabolism

A simple diagram of cellular energy metabolism was presented in Fig. 2.4. Here, cellular energy metabolism is modelled using the following assumptions, based on the observed characteristics of cellular energy metabolism discussed previously:

1. Energy metabolism in a cell consists of two main processes, glycolysis and mitochondrial respiration.
2. Oscillations have been observed in both glycolysis and mitochondrial respiration.
3. ATP is produced within a cell through a combination of these pathways, depending on the state of the cell.

-
4. Cellular energy metabolism responds to environmental changes, up or down-regulating glycolysis as necessary, through sensing of ATP levels.
 5. Glycolytic oscillations have been shown to depend on sugar transport, and mitochondrial membrane potential oscillations have been associated with cycles of oxidation, in addition to plasma membrane potential oscillations and Ca^{2+} .

Characteristics 1 & 2 are represented by two phase oscillators. Glycolysis is considered as one oscillator, the glycolytic oscillator (GO). Mitochondrial respiration, i.e. the Krebs cycle and OXPHOS, is represented by another oscillator, the mitochondrial oscillator (MO). The output of both the GO and MO is oscillatory ATP, denoted ATP_{GO} and ATP_{MO} , respectively. In accordance with 3 & 4, these oscillators are bidirectionally coupled. The dependence of the GO on the MO is represented by a repulsive coupling, to replicate the downregulation, via inhibition of phosphofructokinase (PFK) [226], of ATP produced by glycolysis when mitochondrial ATP output is high. Glycolysis is not completely suppressed, but remains at a level which is sufficient to provide the substrates required for the MO to remain the dominant pathway. Based on this coupling, reduction of ATP_{MO} , as expected in the transition towards cancer, will reverse the inhibition of PFK in the GO, causing increased ATP_{GO} . Thus, oscillations in metabolism would be driven by glycolysis, due to it becoming the primary producer of ATP. This is exactly what has been observed experimentally at near anoxia [227], as well as under semi-anaerobic conditions [1]. In this case however, it also has to be considered that glycolysis will be more responsive to ATP_{MO} oscillations, as they provide glycolysis with information on the current status of the mitochondria. Taking this into account, the MO has an increased ability to modulate the GO in this state.

The dependence of the MO on the GO is represented by an attractive coupling due to the dependence of mitochondrial respiration on the products of glycolysis. Here, nicotinamide adenine dinucleotide (NADH) is considered as the primary influencing factor of the MO, representing glycolytic output. Considering this cou-

pling in an altered state [211], increasing NADH levels from up-regulated glycolysis will positively affect the ATP_{MO} production. Here, it must also be considered that the mitochondrial oscillator has a finite ability to utilise NADH, which will be lowered if the mitochondria are damaged, even if all required substrates are available. This is represented as a saturation of the response, and thus in ATP_{MO} output. As the system moves towards this saturation, the influence of glycolysis on the MO decreases, until being completely lost at saturation. This is in contrast to a state with lower NADH concentration, where the GO is capable of modulating the MO.

Requirement 5 is represented in the model by two further oscillators, introducing external substrate availability in the form of oxygen for the MO and glucose for the GO. These drivers unidirectionally influence the GO and MO with variable coupling strengths.

Taking all of the above interactions into account leads to a phase oscillator model of cellular metabolism,

$$\begin{aligned}\dot{\varphi}_g &= \omega_g + \varepsilon_1 \sin(\varphi_g - \varphi_m) - \varepsilon_4 \sin(\varphi_g - \varphi_{gluc}); \\ \dot{\varphi}_m &= \omega_m - \varepsilon_2 \sin(\varphi_m - \varphi_g) - \varepsilon_3 \sin(\varphi_m - \varphi_{ox}),\end{aligned}\tag{7.1}$$

where φ_g , φ_m , φ_{gluc} and φ_{ox} are the phases of the GO, the MO, the glucose driver and the oxygen driver, respectively, ε_1 is the strength of the coupling from the MO to the GO, ε_2 the coupling strength of the GO to MO, ε_3 the strength of the oxygen driver on the MO and ε_4 the strength of the glucose driver on the GO (see Figure 7.1). Parameters ω_g and ω_m in (7.1) represent the natural frequencies of GO and MO, respectively, and may be time-varying. φ_{gluc} and φ_{ox} may also be time-varying.

Only the interactions discussed above are included in the model, as shown in Figure 2.4; other possible interactions between the GO and MO are neglected. Changes in the strength of these interactions define changes in the global dynamics

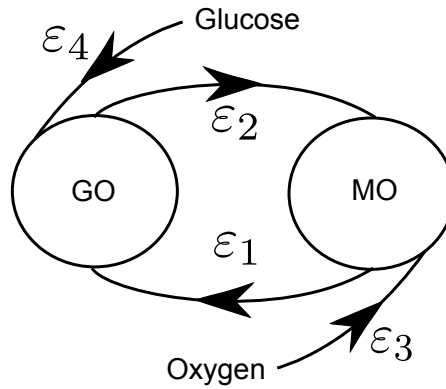


Figure 7.1: Model (7.1) of metabolic oscillations in a cell. The glycolytic and mitochondrial oscillators (GO and MO, respectively) are represented by two phase oscillators coupled to each other via repulsive ϵ_1 (due to the inhibitory nature of the influence of the MO on the GO) and attractive coupling ϵ_2 (due to the excitatory influence of the GO on the MO). Oscillators may be made chronotaxic due to attractive couplings ϵ_3 and ϵ_4 to the glucose and oxygen drivers. The GO and MO oscillators are chronotaxic when synchronised to an external driver directly or via another oscillator.

of the system. Thus, despite its simplicity, the level of detail in the model is sufficient to describe changes in metabolic states.

7.1.1 Determining metabolic states through chronotaxicity

When observing the frequency or amplitude of metabolic oscillations, it is difficult to deduce any information about the metabolic state of the cell from a single time series, as their variability may seem negligible [352]. The nonautonomous nature of the system means that these frequencies or amplitudes can fluctuate irrespective of the current metabolic conditions, making it difficult to study state transitions. In this case, a parameter which changes exclusively during metabolic transitions is needed. As it is expected that the *interactions* within the system will change during transitions, a measure of these changes will allow the observation of switches between metabolic states.

Metabolic oscillations as observed experimentally appear to be time-variable yet very stable. Indeed, several studies of mitochondrial and glycolytic oscillations demonstrate that metabolic fluctuations within a cell are not fully stochastic, but they appear to have non-autonomous and deterministic oscillatory components,

e.g. [232, 220, 1]. This suggests that although they exhibit time-dependent dynamics, these dynamics are stable and resistant to external continuous perturbations within certain ranges. Therefore, these oscillations may reflect underlying deterministic processes, which may be used to identify the state of a cell. The stability of the observed dynamics will change as the interactions in the system change, therefore making it possible to observe metabolic transitions. This property of stability, or ability to resist external perturbations, is described by the recently introduced theory of chronotaxic systems [285, 286, 302, 287] (see Section 4.1.2). Based on measurements from healthy cells and those with altered metabolism, the apparent stability of glycolytic and mitochondrial oscillations suggests that they may have chronotaxic properties. Chronotaxicity may exist when oscillations are modulated [1, 227]; thus changes in the modulation, which will occur during a transition to an altered metabolic state such as that observed in a cancer cell, will be reflected in chronotaxicity.

7.2 Numerical simulations

The phase oscillator model presented above was simulated numerically with varying parameters using the Heun integration scheme with a time step of 0.1s and white Gaussian noise added to the right hand side of Equations 7.1. Each parameter set was simulated for a period of 10,000 seconds. For each set of parameters, the chronotaxicity of both the GO and the MO were tested. An oscillator was considered to be chronotaxic if it was synchronized with an external driver, either glucose or oxygen. Oscillators were considered synchronized if their phase difference remained within a 2π interval during the second half (5,000 seconds) of the full time-series (10,000 seconds). This condition restricts oscillators from making phase slips, after allowances for transient effects.

Synchronization to the unidirectionally coupled driver results in the existence of a point attractor, a key component of a chronotaxic system. In more complex configurations of this system, it is possible that a point attractor during synchro-

	Glycolytic	Mitochondrial
A	ω_{gluc}	ω_{ox}
B	ω_{gluc}	ω_{gluc}
C	ω_g	ω_m
D	ω_{ox}	ω_{ox}
E	ω^*	ω^*
F	ω_{gluc}	ω^{**}
G	ω^{**}	ω_{ox}

Table 7.1: Approximate characteristic frequencies of GO and MO in the regions shown in Figure 7.3. In A, B & D each oscillator is synchronized to either its driver or to the other oscillator. In these cases, frequencies are influenced by the driving oscillators. In C, the oscillators are not synchronized to anything, hence the characteristic frequencies are determined by the natural frequencies of the oscillators. In E oscillators are synchronized to each other only, hence the frequency ω^* corresponds to the frequency of a synchronized state assuming $\varepsilon_* = \varepsilon_4 = 0$, and it can be found from the condition of synchronization $\dot{\phi}_m - \dot{\phi}_g = 0$, $\omega^* = (\varepsilon_1\omega_m - \varepsilon_2\omega_g)/(\varepsilon_1 - \varepsilon_2)$. In F & G one oscillator is synchronized to its driver whilst the other is somewhere between the two drivers.

nization sometimes does not satisfy the contraction condition, Equation 4.7. In this case, there is at least one direction in phase space where trajectories temporarily diverge and deviate from the point attractor. However, as this is a temporal deviation, it is unlikely to influence the observed dynamics. Therefore, the synchronization of oscillators in the model presented is studied and considered as approximate chronotacticity. Example phase trajectories for each region are shown in Figure 7.2 and explained below. Seven different types of dynamics were revealed, shown in Figure 7.3. Approximate frequencies of these oscillations in different regions are summarised in Table 7.1.

The characteristics of the observed regions are as follows:

A – GO synchronized with glucose, MO synchronized with oxygen, GO & MO not synchronized. Both GO & MO are chronotactic.

B – GO synchronized with MO, both synchronized with glucose. Both GO & MO are chronotactic.

C – No synchronization. Neither GO nor MO are chronotactic.

D – GO synchronized with MO, both synchronized with oxygen. Both GO & MO are chronotaxic.

E – GO synchronized with MO. Both oscillators experience multiple phase slips. Neither GO nor MO are chronotaxic.

F – GO synchronized with glucose, MO not synchronized with oxygen, GO & MO not synchronized. GO is chronotaxic, MO is not chronotaxic.

G – GO not synchronized with glucose, MO synchronized with oxygen, GO & MO not synchronized. GO is not chronotaxic, MO is chronotaxic.

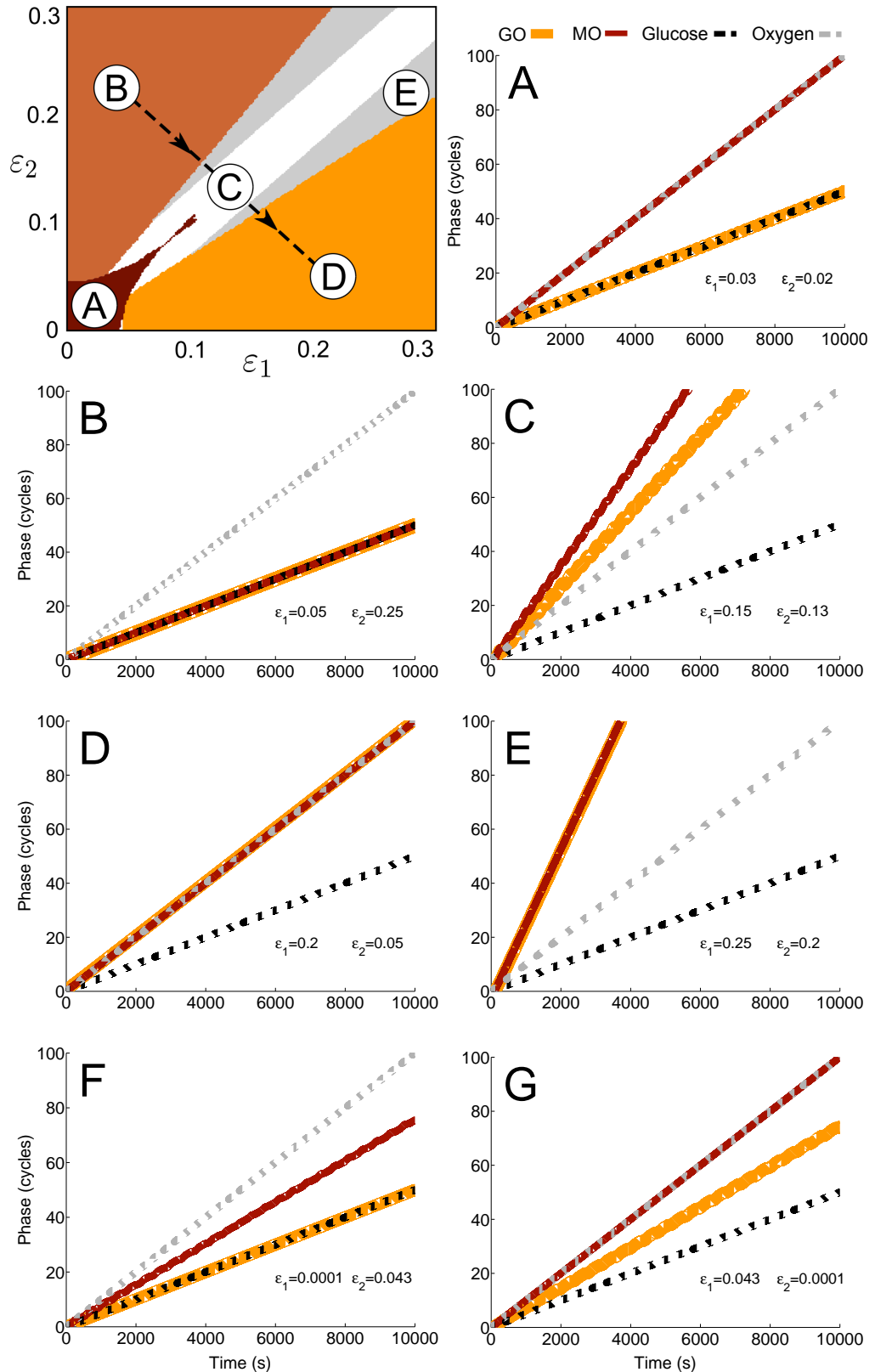


Figure 7.2: Phase trajectories of the 7 types of dynamics which have been observed in the model shown in Equation 7.1. In all cases $\epsilon_3 = \epsilon_4 = 0.025$. Cases A, B, D, F & G show chronotacticity in at least one oscillator, whilst the other cases do not. The transition from the state where the system is chronotactic due to glucose to a state where it is chronotactic due to oxygen is shown with black arrows (top left).

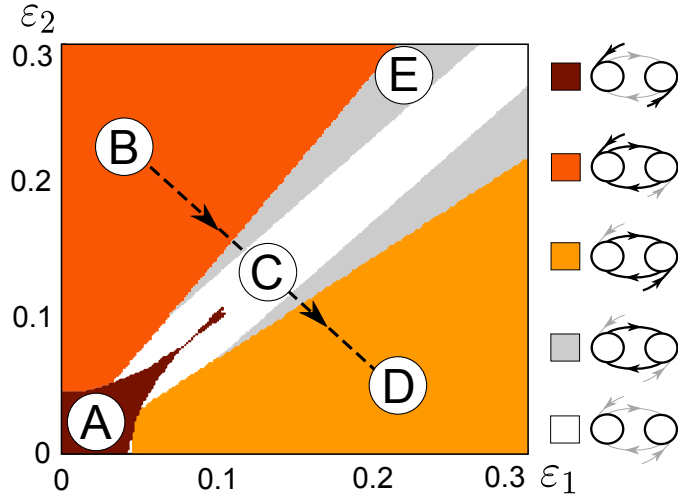


Figure 7.3: Chronotaxicity plot for ε_1 vs. ε_2 with $\varepsilon_3 = \varepsilon_4 = 0.25$. In this example, the model was simulated for varying values of ε_1 vs. ε_2 whilst the influence of the glucose and oxygen drivers remained the same. The type of dynamics observed for each pair of values is shown with the colours shown on the right, showing the GO as a circle on the left, the MO on the right, and their drivers as arrows from the top and bottom, respectively. Dominant couplings are shown in black, whilst absent or weak couplings are shown in grey.

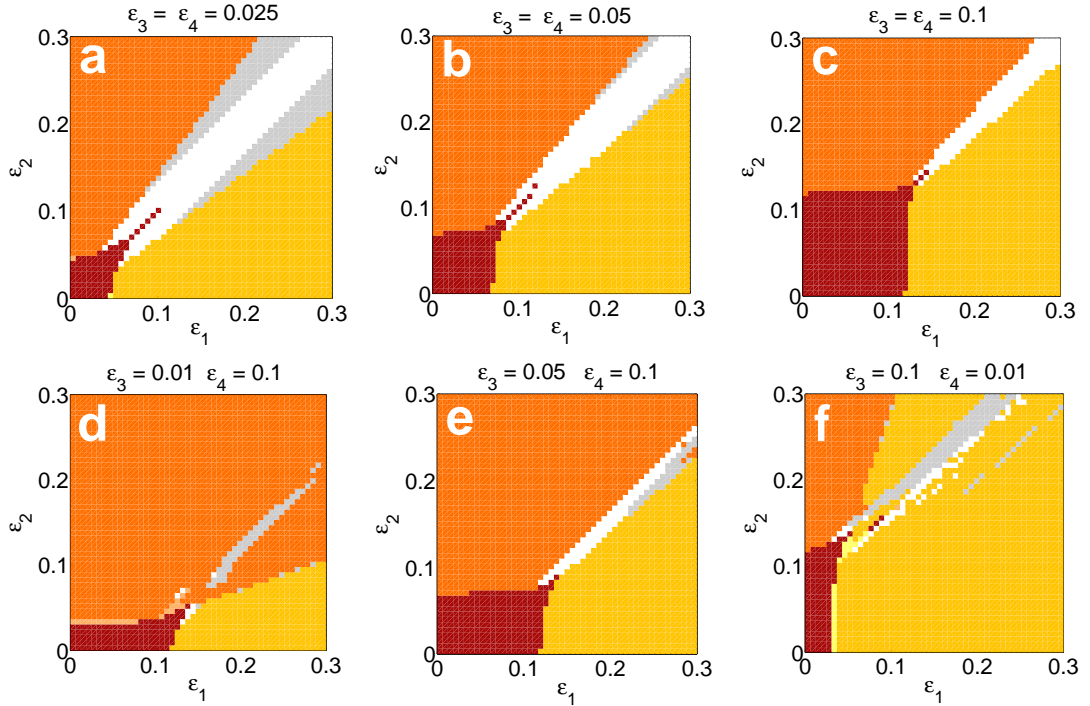


Figure 7.4: Changing modulation from glucose and oxygen, $\varepsilon_3 = \varepsilon_4$. Glucose and oxygen drivers may influence the system equally, as in Figure 7.3, but their values can change. (a) $\varepsilon_3 = \varepsilon_4 = 0.025$. (b) $\varepsilon_3 = \varepsilon_4 = 0.05$. (c) $\varepsilon_3 = \varepsilon_4 = 0.1$. With increasing influence of drivers, chronotaxic areas increase. (d) and (e) represent a state in which the glucose driver has a larger influence on the system than the oxygen driver, i.e. $\varepsilon_4 > \varepsilon_3$. (f) represents a state in which the oxygen driver has a larger influence on the system than the glucose driver. In all cases $\omega_g = 2\pi/200$ and $\omega_m = 2\pi/100$. Colour code as in Figure 7.2 & 7.3.

Figure 7.3 demonstrates the dynamics of the system when the influence from the glucose and oxygen drivers is equal and relatively small. This results in a large range of values for which the system is not chronotaxic. Increasing the influence of glucose and oxygen on the system increases the proportion of cases which are chronotaxic in the range studied (see Figure 7.4). Figure 7.4 also shows the dynamics of the system when ε_3 and ε_4 are not equal.

So far, all simulations have been performed using the natural frequencies $\omega_g = 2\pi/200$ and $\omega_m = 2\pi/100$. Changing these frequencies, and thus the detuning within the system will also have an effect on the dynamics of the system. Figure 7.5 shows the dynamics of the system with changing natural frequencies of the GO and MO, with equal and unequal influences from glucose and oxygen. In a real cell, it is highly unlikely that the natural frequencies of the oscillators or the drivers will be constant. Therefore, in order to check the dynamics of the system in the case of time-varying natural frequencies, the frequencies of the drivers, glucose and oxygen, were allowed to vary in time. Thus, instead of the drivers in Equation 7.1 being $\varphi_{gluc/ox} = \omega_{gluc/ox}t$ they become $\int \omega_{gluc/ox}(t')dt'$. The drivers were modelled as a slow sinusoid modulated by white Gaussian noise, and their periods of oscillation were allowed to vary in the ranges: GO = 4 - 7 minutes and MO = 2 - 3 minutes. This gives ranges for ω_{gluc} of 0.0151 - 0.0264, and ω_{ox} of 0.0352 - 0.0522. The drivers were generated with a modulation frequency of 0.0003 Hz, and are shown in Figure 7.6.

It was demonstrated that chronotaxicity is found in the same regions as in the non-variable case, with slight changes at the boundaries, but this may not hold for very large variations, which may increase the frequency detuning sufficiently to destroy the synchronization and thus the chronotaxicity.

7.2.1 Detection of chronotaxicity via the inverse approach

Following the dynamics of the system in terms of its chronotaxicity, the evolution of the system from the normal to an altered metabolic state can be observed. One

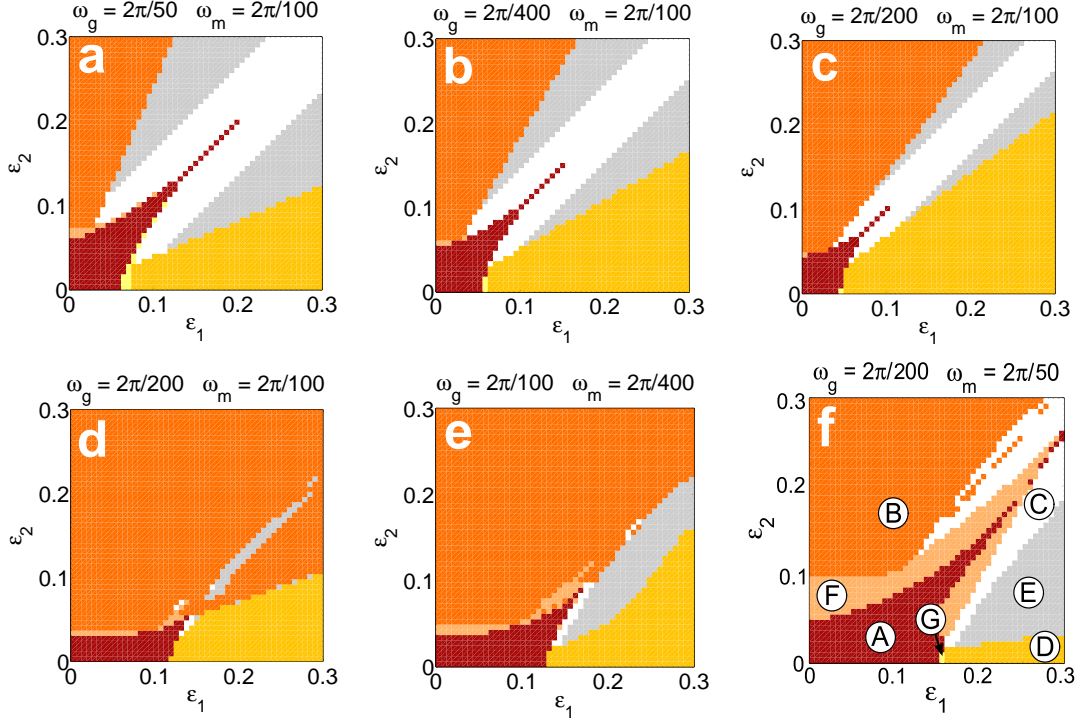


Figure 7.5: Effects of changing frequencies of GO and MO when $\varepsilon_3 = \varepsilon_4$ and $\varepsilon_3 \neq \varepsilon_4$. Different natural frequencies of oscillations may be considered, for example in different cell types. Changing frequency detuning will affect regions of chronotaxicity. In (a)–(c) $\varepsilon_3 = \varepsilon_4 = 0.025$. (c) shows the chronotaxicity plot for the system as considered in the main text, with natural frequencies $\omega_g = 2\pi/200$ and $\omega_m = 2\pi/100$. (a) shows the effects of increasing ω_g . (b) shows the effects of reducing ω_g . In (d)–(f) $\varepsilon_3 = 0.01$ and $\varepsilon_4 = 0.1$. The frequency of GO may increase due to upregulated glycolysis, while the frequency of MO may decrease due to mitochondrial dysfunction. (d) ‘Healthy’ natural frequencies in the case where glucose is the dominant driver. (e) Substrate dependencies as in (d) but with faster glycolytic and slower mitochondrial oscillations. (f) Effect of fixing the glycolytic frequency and increasing the mitochondrial frequency.

pathway considered is the transition of the system from region B (chronotaxic with glucose driver) to region D (chronotaxic, but now with oxygen driver), via regions C and E (both non-chronotaxic). Identification of the chronotaxicity of the system, and its dominant driver, allows the identification of the current status of the metabolism, and whether it is in transition to an unfavourable state. Utilising chronotaxicity as the defining parameter of the system is superior to the consideration of synchronization alone, as it can be identified experimentally from any *single* time series. To demonstrate the applicability of this approach to real metabolic systems, inverse approach methods for the detection of chronotaxicity

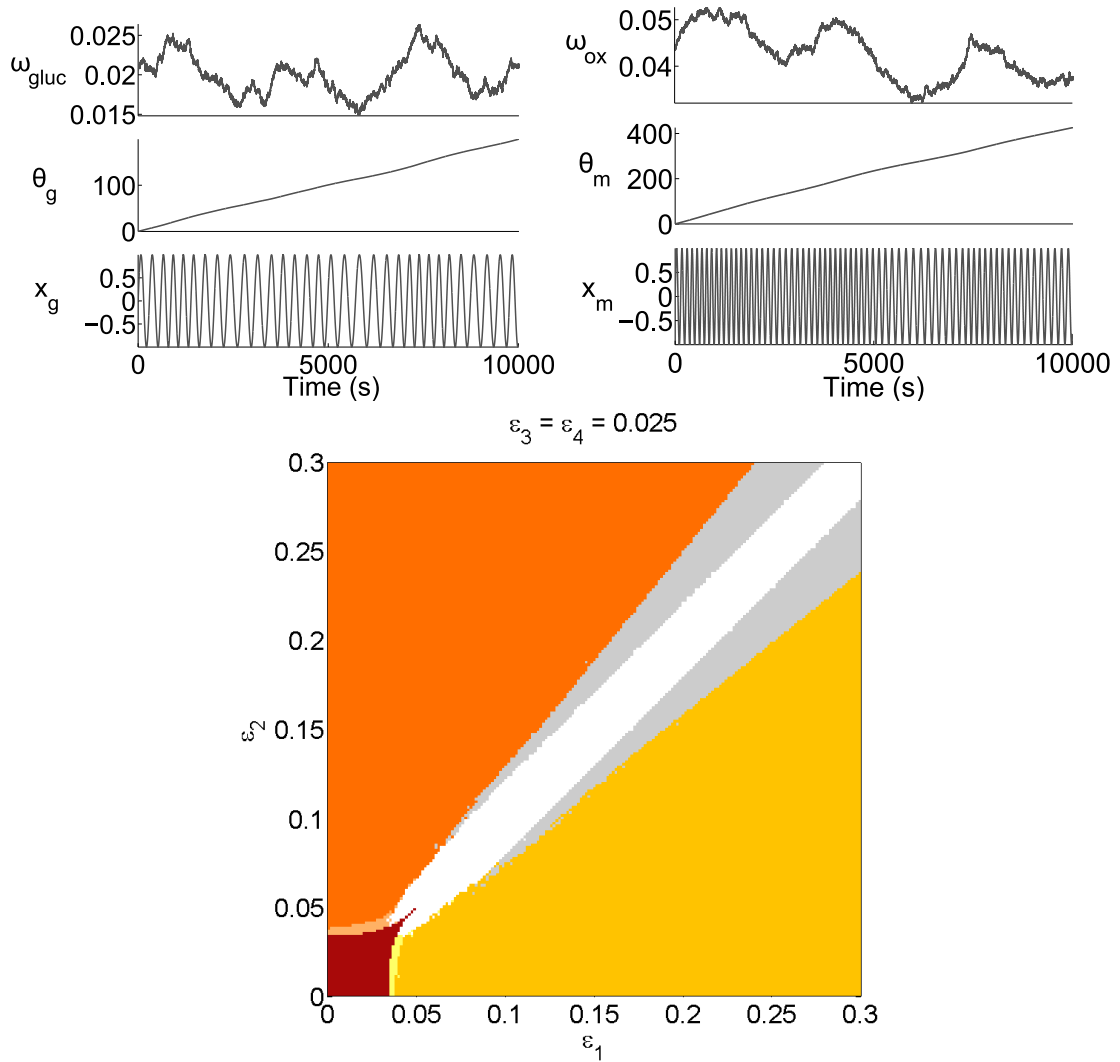


Figure 7.6: Effect of a time-varying driver on the chronotaxic dynamics of the phase oscillator model. The dynamics are very similar, the only difference being that the boundaries between states are not as well defined, due to the slight differences in frequency detuning.

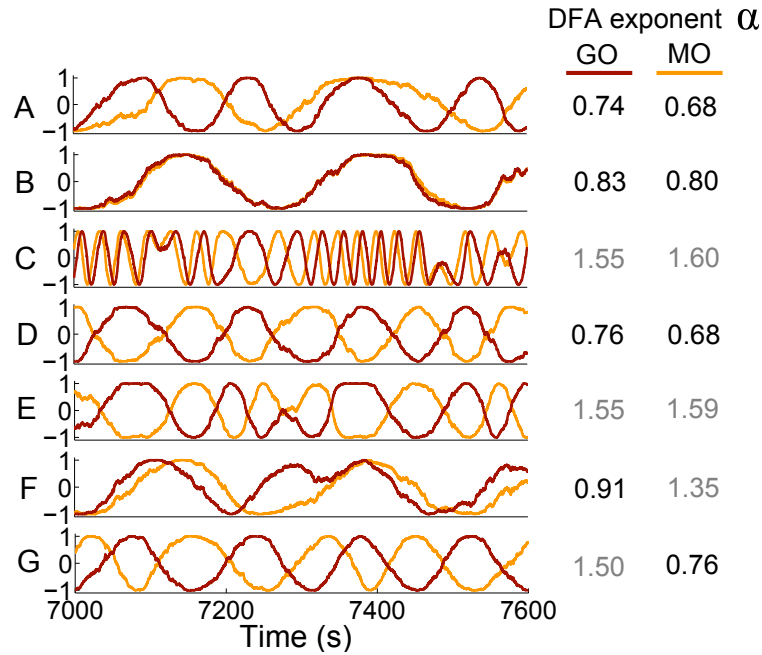


Figure 7.7: Phase fluctuation analysis results from simulated ATP dynamics in all 7 observed regions. PFA was correct in identifying whether the system was chronotaxic or not in all cases. Time series shown are $\sin(\varphi_{g,m})$.

were applied to the dynamic ATP signals arising from the model to ensure that numerical and inverse approach chronotaxicity tests give the same results.

Methods for the detection of chronotaxicity were demonstrated in a complex real life system – the cardiorespiratory system [302]. This study demonstrated evidence of chronotaxicity in the heart rate variability when influenced by paced breathing. In the case of cellular energy metabolism studied here, it would be sufficient to have measurements of only ATP_{GO} and ATP_{MO} to determine the chronotaxicity of each metabolic oscillator. To demonstrate this, inverse approach methods were applied to the signals obtained from the different regions shown in Figure 7.3 to identify their chronotaxicity status (see Figure 7.7). The chronotaxicity of each oscillator was determined separately, using only single time series. Phase fluctuation analysis (PFA) (see Section 4.3.2) was used to distinguish between chronotaxic and non-chronotaxic dynamics. PFA shows very good agreement between the chronotaxicity as calculated by the model using synchronization conditions, and chronotaxicity as calculated via the inverse approach with no prior knowledge. This illustrates that the method is a very promising tool for the ob-

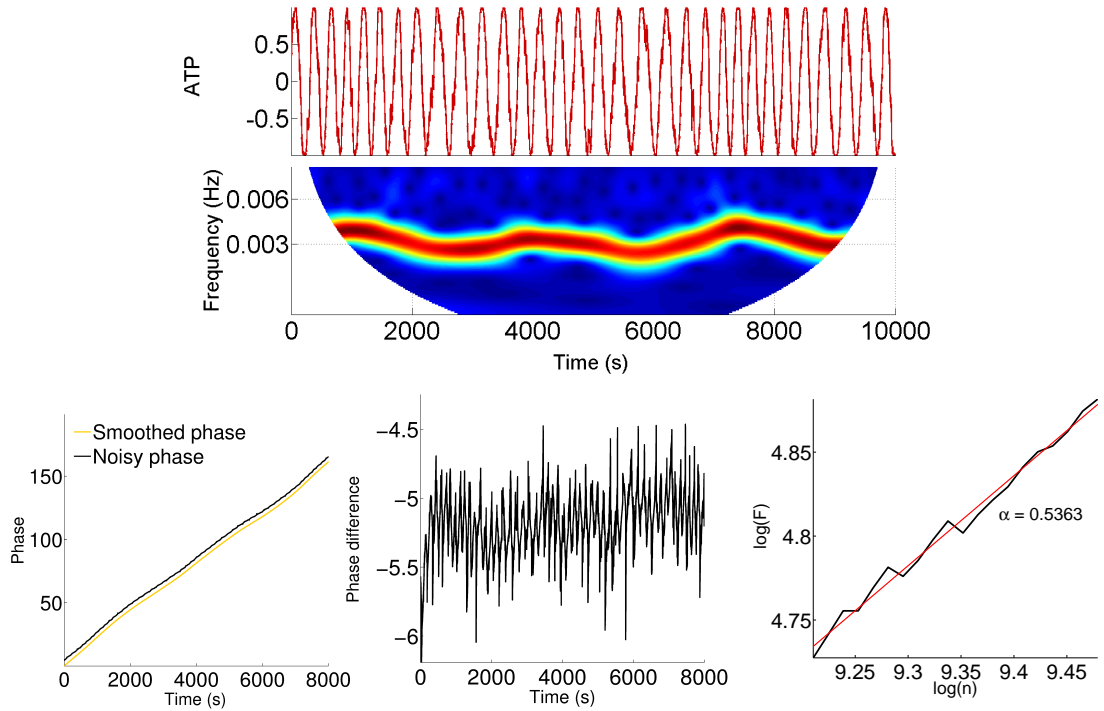


Figure 7.8: Example of the detection of chronotacticity from a single ATP time series using phase fluctuation analysis. (a) Example ATP signal obtained from the model (region B) and its continuous wavelet transform. (b) The phase is extracted twice, one with good frequency resolution (smoothed) and once with good time resolution (noisy). DFA is performed on the difference between these phases (c) and the DFA exponent is obtained (d). In this case, $\alpha = 0.5363$, therefore the signal is chronotactic. From the wavelet transform we can see that the frequency is around that expected during glycolysis, and thus we can say that the system is chronotactic due to the glucose driver.

servation and identification of chronotacticity in real systems, where the dynamics is unknown. A detailed example of PFA as applied to an ATP signal is shown in Figure 7.8.

7.2.2 Experimental verification

In order to measure the required ATP levels as described, FRET-based ATP biosensors could be used, which allow the measurement of ATP levels in different cellular compartments [313], and could therefore be used to isolate the dynamics of each oscillator. The methods described in [247] and [248] could also be used. Applying the inverse approach test for chronotacticity as described above to these data would provide valuable information about the current metabolic state

of the cell, in terms of whether it is externally driven, or attracted to a moving point attractor. In addition, the connection between ATP and cell membrane potential may be utilised. As the intracellular ATP concentration determines the work of ATP-dependent membrane pumps (e.g. Na-K-pumps and H⁺-pumps), it determines the cell membrane potential according to the causal theory of the cell membrane potential [356]. Therefore, oscillations in ATP may be visible in oscillations of cell membrane potential.

7.2.3 Verification of the glycolytic oscillator

Another way to test the chronotoxicity of glycolytic oscillations in particular is to utilise the closely linked dynamics of intracellular ATP and NADH arising from glycolysis. It has been shown previously that both ATP and NADH are oscillatory in yeast cells during glycolytic activity, and that these oscillations have the same frequency but are out of phase by around 180°[248, 249]. This means that measurements of NADH in yeast cells may be used to provide an approximation of ATP dynamics. Although the amplitude of these parameters will differ, their phase relationship will remain the same, and can thus be represented by the phase oscillator model. Using this information, the model can be tested for the case of the glycolytic oscillator based on NADH measurements, which are more readily available. Glycolysis in yeast cells is one of the most widely studied and well characterised biological oscillators. It was previously thought that glycolytic oscillations only arose as a result of synchronization between yeast cells, but recently Gustavsson *et al.* demonstrated glycolytic oscillations in individual isolated yeast cells [357, 358]. Importantly, the observed oscillations, whilst occurring with similar frequencies, were not synchronized. As the external glucose level in these experiments was constant, the oscillations must occur as a result of an internal mechanism, which is a possible cause of chronotoxicity in the model.

Here, data recorded by Gustavsson *et al.* [357] is tested for chronotoxicity, to investigate the applicability of the model to real metabolic oscillators. *Sac-*

Saccharomyces cerevisiae cells were harvested at the time of diauxic shift, starved of glucose for 3 hours and then stored at 0–4°C until use. The cells were then placed in a microfluidic chamber at a distance of $\sim 10\mu\text{m}$ apart using optical tweezers. The cells were covered with 20 mM glucose solution for 4 minutes before flows were increased in order to cover the cells with 20 mM glucose/5 mM KCN solution. NADH fluorescence was monitored for 60 minutes at a sampling frequency of 0.25 Hz. NADH in individual yeast cells was shown to oscillate following starvation and the addition of cyanide. In this state, glycolysis can be the only means of energy production, as cyanide halts respiration, effectively removing the effects of the mitochondrial oscillator. It is therefore expected that the metabolic state induced in this experimental setup should correspond to the ‘altered’ state, i.e. region B in Fig. 7.3, where glycolytic oscillations drive the dynamics of the system, and the GO is chronotaxic.

NADH data was available from 34 yeast cells, 6 of which did not demonstrate visible oscillations so were excluded from the analysis. It was demonstrated in Section 4.4 that at least 30 cycles of oscillation are required to test for chronotaxicity, therefore all cells which did not meet this requirement were excluded. 16 cells met this criteria. PFA was then applied to the remaining NADH signals to determine whether the oscillations observed in these cells exhibited hallmarks of chronotaxicity. The model was used to numerically simulate the GO in a chronotaxic ($\varepsilon_1 = 0, \varepsilon_2 = 0, \varepsilon_3 = 0, \varepsilon_4 = 0.25, \sigma = 0.2$) state using the instantaneous frequency extracted from the real experimental data. To make the system chronotaxic, the extracted frequency was used as the driver ω_{gluc} of the glycolytic oscillator. This provided a chronotaxic oscillator with the same oscillation frequency as the experimental data, allowing the DFA exponent α to be compared between cases (see Fig. 7.9). Due to the relatively short recording time causing variation between simulations, they were repeated 3 times and the average value of α taken. The mean value of α for the 16 included cells was 0.768, compared to $\alpha = 0.772$ in the chronotaxic simulations. The distributions of exponents did not significantly differ

between those calculated in the cells and those calculated in the simulated chronotaxic system ($p = 0.86$) as calculated using the Wilcoxon ranksum test. This shows that the model, although simple, incorporates enough features to allow the calculation of the presented characteristic, chronotaxicity, and that evidence of this characteristic appears to be present in yeast glycolytic dynamics. This verifies the applicability of the model to the glycolytic oscillator. Further investigation is required into the mitochondrial oscillator, and other metabolic states.

7.2.4 Links to carcinogenesis

To link the model to real metabolic dynamics in cancer, evidence provided in the study of cardiomyocytes in a state of metabolic stress [227] is used, as well as in the study of yeast cells under semianaerobic conditions [1]. Yeast cells have been shown to have metabolic similarities with cancer cells [228]. Both studies [1, 227] conclude that glycolysis drives metabolic oscillations, while MO modulates GO. Here, the driving is represented by the fact that glycolysis influences the amount of ATP produced, which determines the amplitude around which oscillations take place. In turn, the modulation of GO by MO manifests as MO influencing the frequency of GO.

Based on previous studies [1, 227], the cancerous state is considered to correspond to the dynamics of the model in which the phase of GO entrains the phase of MO. In the model, the necessary (but not sufficient) condition for entrainment of GO by MO is $\varepsilon_2 > \varepsilon_1$. In contrast, the normal state may correspond to the case where the phase of MO entrains the phase of GO, and consequently the necessary condition of this is $\varepsilon_1 > \varepsilon_2$. However, it may also be possible that in the normal state both oscillators remain driven only by their external drivers, with their mutual interactions not strong enough for entrainment.

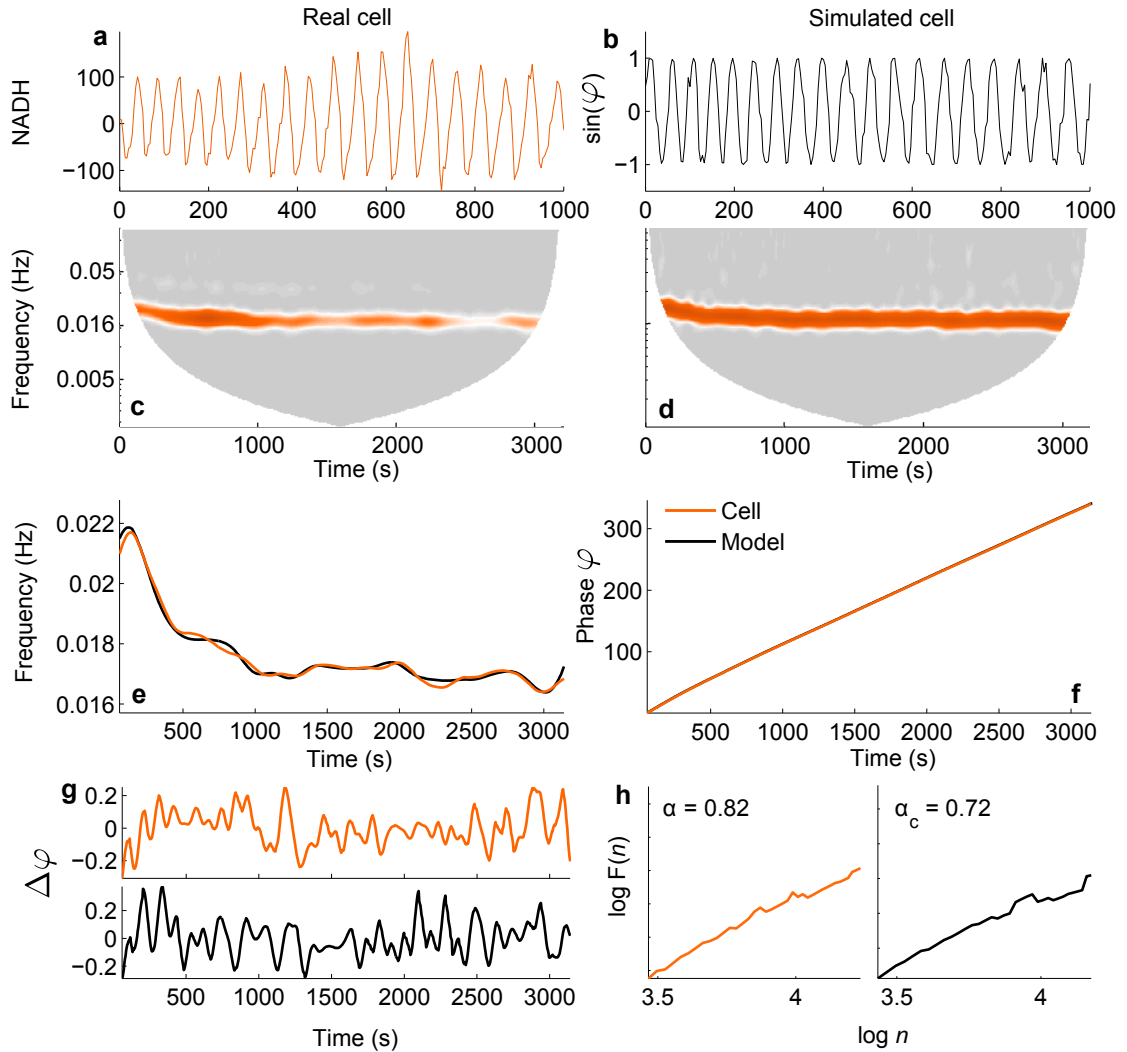


Figure 7.9: Testing real experimental data for chronotacticity. **a** Example NADH signal from an isolated yeast cell, recorded in [357]. **b** Time series of $\sin \varphi_{GO}$ from the model using the instantaneous frequency extracted from **a** as the driver ω_{gluc} . **c** & **d** Continuous wavelet transforms of the time series in **a** & **b**, respectively. **e** The instantaneous frequency of the oscillatory modes were extracted from the wavelet transforms, and smoothed using a moving average. **f** Integrating over the smoothed frequency provides the phase for each case. **g** Subtracting the smoothed phase from the observed phase provides the phase fluctuations, $\Delta\varphi$, in the system. **h** Detrended fluctuation analysis performed on $\Delta\varphi$ suggests that the glycolytic oscillations observed in a real yeast cell (orange line) are chronotactic.

7.3 Summary

This chapter proposes a quantifiable characteristic, chronotoxicity [285, 302, 287], of metabolic oscillations for the purpose of describing the transition of a cell from a state with healthy energy metabolism, to a state where it is altered or abnormal, in particular the metabolic switch to glycolysis observed in many cancer cells. The ability to observe this transition in just a single time series was demonstrated using a very general qualitative model of metabolic oscillations, with the advantage that it captures only the most general and universal oscillatory dynamics and interactions. As a result, this model does not depend on details which vary across cancer states, thus being more likely to be applicable to cancer cells in general.

Oscillations are often overlooked in experimental studies, as if there are several oscillations present in the system, they may cancel each other out [352]. Alternatively, due to their highly complex nature, they are often treated as stochastic, e.g. [353]. Even in cases when oscillations and the interactions between them have been studied, the exact characteristics of their amplitude and phase relations have not been considered. The interactions of oscillatory processes may be amplitude-amplitude, phase-phase, or phase-amplitude, resulting in many possible scenarios of metabolic regulation. Here, for the sake of simplicity, the model is restricted to phase-phase interactions, justifiable by the nature of chronotoxicity relying on phase synchronization in the current case.

Particular attention has been paid to the time-variability of characteristic frequencies of oscillations as one of the key properties of living systems. Namely, the exchange of energy and matter involved in each process is always associated with imperfect timing, or a fundamental inability to instantaneously match supply and demand, resulting in time-varying oscillatory dynamics that is now captured within the theory of chronotaxic systems. Using this simplified version of chronotaxic phase oscillators, a possible new way of studying metabolic processes within a cell has been introduced.

Cellular energy metabolism may be affected by many more processes and interactions than those considered here. The simplicity of the model could easily facilitate the inclusion of further couplings, for example in the consideration of calcium dynamics or genetic factors in energy production. Calcium has been shown to influence mitochondrial dynamics directly via many pathways [359], whilst genetic mutations can have a direct effect on mitochondrial function [360]. These effects could be included in the model as influences to couplings, extra oscillators, or adaptations of the external drivers.

Chronotaxicity in cellular energy metabolism could arise as a result of a number of influences, all of which would require experimental verification. The required drive system could be provided by external oscillatory influences. In the case of glycolysis, the time-varying availability of glucose may be considered as the drive system of the GO. Similarly, the dynamical oxygen availability may be considered as the drive system of the MO. Alternatively, if glucose and oxygen are abundant within the cell, they are unlikely to be the driver for each process. In this case, it is assumed that the inner structure of the oscillator, i.e. finite reaction times, provides the stable, time-dependent point attractor which defines a chronotaxic system. Here, these cases are not considered separately, and the external resources glucose and oxygen are presented as the drivers which define the chronotaxicity of the oscillators, independent of the exact mechanism by which this occurs. As it is only the change in chronotaxicity which is of importance here, knowledge of its specific origins, whilst interesting, is not essential.

The exact shape of the metabolic oscillations is also not described here, as this would not impact the outcome of the chronotaxicity detection methods. Here it is shown that chronotaxicity can identify dynamical changes during the metabolic transition from a normal to an altered metabolic state in the model. Finally, inverse approach methods show that these changes can be measured in the model with no prior knowledge of whether the system is chronotaxic or not, as well as in real complex systems, similarly to the application to the cardio-respiratory system

in [285, 302].

In summary, a simple model of cellular energy metabolism has been introduced with the aim of capturing the oscillatory dynamics of cellular energy metabolism in a healthy cell, and one in which cellular metabolism is altered, for example a cancer cell. Transitions between different types of dynamics, representing different metabolic states, were followed by considering their chronotaxicity. This means that from a single oscillatory ATP time series it can be determined whether the system is driven, i.e. whether its frequencies are prescribed by some deterministic process. It is also possible to extract the characteristics of the driver, and thus these can be compared during metabolic transitions. This information could be used to monitor cells during hypoxia or carcinogenesis. Evidence of chronotaxicity in energy metabolism was shown in real experimental data, in glycolytic oscillations in yeast cells. This demonstrates the applicability of the model to cellular energy metabolism. However, further experimental verification is required for the mitochondrial oscillator.

8. Concluding remarks

8.1 Summary

In brief, the main aspects of this thesis are as follows:

- The physiological background of microvascular flow oscillations in health and disease is reviewed.
- The techniques required for the measurement of the physiological parameters considered are discussed.
- A background to nonautonomous dynamical systems, in particular chronotaxic systems, is presented, and inverse approaches for their detection are elaborated upon.
- The blood flow dynamics of melanoma and control lesions were compared using the presented techniques, and an accurate noninvasive diagnostic test was developed.
- The role of hypoxia in microvascular flow dynamics was explored using data previously recorded during apnoea in free divers, and a control group recruited specifically for this comparison.
- The possible role of altered cellular energy metabolism in cancer on the results observed in the melanoma microvasculature were considered using a coupled chronotaxic phase oscillator model.

-
- The glycolytic oscillator in the phase oscillator model was verified using real experimental data recorded from yeast cells, which demonstrated that the system was chronotaxic.

The primary aim of this thesis was to investigate blood flow dynamics in skin melanoma. Blood flow data recorded using laser Doppler flowmetry were analysed using time series analysis techniques tailored specifically to the underlying properties of these time series, namely that they are oscillatory, nonstationary, nonlinear and nonautonomous. The required analysis techniques were reviewed. These analyses provided new insights into the melanoma vasculature, based on differences in the oscillations present in blood flow as measured in healthy skin and benign moles when compared to cancerous lesions. The previous characterization of these oscillations allows the observed spectral differences to be attributed to the oscillations associated with vasomotion, in both the myogenic and neurogenic frequency intervals. This could be a result of a microvascular detachment from local regulatory mechanisms, a reduction in vessel reactivity due to the harsh tumour microenvironment, or a loss of synchronization between smooth muscle cells. The observed differences in melanoma were large enough to facilitate the development of a set of criteria which have been successfully used in a diagnostic test with a sensitivity of 100% and specificity of 90.9%. Whilst further data collection would be necessary before this technique could be considered for routine clinical practice, this work provides the foundations for the development of a quick, easy, noninvasive diagnostic test which could significantly reduce the number of biopsies required in melanoma diagnosis.

In addition to the investigation into melanoma, blood flow and oxygenation dynamics were explored in data previously recorded from free divers during periods of dry static apnoea and in specifically recruited control subjects at rest, in order to ascertain whether free divers differ from non-trained individuals in terms of their oscillatory physiological signals at rest, and whether the characteristics of these signals are altered in divers when comparing rest periods to those obtained

during breath-holds. The aim of this part of the thesis was to identify whether any differences in blood flow or oxygenation dynamics could be observed as a result of oxygen deprivation, or hypoxia, and to compare them to the changes in blood flow dynamics observed in melanoma lesions. If similar behaviour was found, this could then be considered a hallmark of hypoxia, well known to occur in tumours. Contrary to the observations in melanoma, blood flow dynamics during apnoea did not vary in the frequency intervals associated with vasomotion, but did vary significantly in the cardiac and respiration intervals, as expected. This suggests a much more systemic response than the local effects observed in melanoma lesions. However, it was shown that the divers were physiologically very different to their age and sex matched controls, which may explain the lack of local effects of the oxygen deprivation for which they have likely built up an efficient response.

Another, almost universal, hallmark of cancer was also investigated. Cellular energy metabolism was modelled as a system of coupled chronotaxic phase oscillators, based on experimental observations of metabolic oscillations in many studies. The newly introduced class of chronotaxic systems were considered in this context, and used as a model to explain the underlying stability of metabolic oscillations, and their seemingly intrinsic frequencies. Using this property of chronotaxicity, it was shown that transitions between metabolic states in the model could be identified numerically. It was also shown that chronotaxicity can be identified via the inverse approach from a single time series. This was demonstrated in simulated and real experimental data. Altered cellular energy metabolism can directly affect the tumour microenvironment, and this change is considered as a potential cause of the altered blood flow regulation observed in cancer.

8.2 Original contributions

The original contributions of this work are listed below:

- The inverse approach to chronotaxic systems presented previously has been

developed further in terms of application specifically to signals containing low frequency oscillations, and determining the minimum number of cycles required for successful detection of chronotaxicity.

- These inverse approach methods were also applied for the first time to brain dynamics, with the alpha wave of an anaesthetized patient turning out not to be chronotaxic, highlighting the further developments required for the detection of chronotaxicity in networks of oscillators.
- The blood flow dynamics of melanoma, psoriasis, atypical naevi and benign naevi were compared in the frequency interval 0.005–2 Hz. Time-averaged normalized power significantly differed between groups in the intervals associated with cardiac, myogenic and neurogenic activity.
- The observed differences in blood flow dynamics between melanoma and atypical naevi, the most difficult lesion to distinguish from melanoma, were developed into a diagnostic test with sensitivity of 100% and specificity of 90.9%.
- Significant wavelet phase coherence was observed between blood flow signals recorded in the centre of lesions and on contralateral skin, in intervals I, II & III, but this coherence did not significantly differ between groups, except in the cardiac interval, due to a significant difference in mean heart rate between groups.
- Arterial oxygen saturation was compared between divers and controls and investigated using wavelet analysis. It was found to contain low frequency oscillations which were coherent with respiration, but this coherence did not differ between divers and controls. The peak frequency of these oscillations was higher in divers than in controls at rest, and the standard deviation of arterial oxygen saturation was higher in divers than in controls at rest.
- Normalized wavelet powers calculated from blood flows recorded at rest

showed a significantly lower cardiac power in divers than in controls in 5 out of 8 locations, and increased power at lower frequencies in divers in 5 out of 8 locations when compared to controls.

- Where a change in frequency of vasomotion could be observed during apnoea, it was found to decrease in the majority of cases.
- A model of cellular energy metabolism was developed using chronotaxic phase oscillators, and numerically simulated with varying parameters to represent different metabolic states. Of particular interest was the metabolic switch to glycolysis observed in most cancer cells, which was represented in the model by an upregulation of glycolysis due to a decrease in the ATP produced by the mitochondria. It was shown that this transition may be detected using the inverse approach methods for the detection of chronotaxicity, though this requires experimental verification.
- The inverse approach for the detection of chronotaxicity was applied to real energy metabolism data for the first time. Recorded in yeast cells, results from the analysis of this data provided evidence of chronotaxicity of the glycolytic oscillator during an altered metabolic state.

8.3 Future work

Future directions of this work are expected to include the following:

- Further development of the inverse approach to chronotaxic systems to be applicable to amplitude dynamics in addition to the current applications to phase dynamics.
- Consideration of chronotaxicity in a network of coupled oscillators, for example neurons in the brain.
- Possible use of altitude simulation as a means to induce a more controlled

oxygen deprivation for the study of blood flow and oxygenation dynamics in hypoxia.

- Recruitment of more patients with melanoma, difficult to diagnose lesions and more controls to build up the data set used in the diagnostic test for melanoma.
- Development of a ‘melanometer’, a device which can characterise blood flow dynamics in skin lesions.
- Inclusion of the effects from other important cellular oscillators in the energy metabolism model, especially calcium.
- Acquisition of experimental intracellular ATP recordings and application of the presented inverse approach methods for the detection of chronotoxicity, to verify the mitochondrial oscillator in addition to the glycolytic oscillator.

Appendices

A. Diagnostic test values

Subject	Melanoma			Atypical			Clinically atypical			Benign			Score
	Var 1	Var 2	Var 3	Var 1	Var 2	Var 3	Var 1	Var 2	Var 3	Var 1	Var 2	Var 3	
1	1.2643	0.0041	4.4356	5.0837	0.0108	9.7875	1.2417	0.0125	4.2689	3.3696	0.0021	2.5650	2
2	6.2254	0.0089	21.684	0.9254	0.0025	0.8009	2.3998	0.0012	0.3391	0.9909	0.0035	4.6652	2
3	6.6621	0.0039	6.6690	2.5767	0.0029	7.7403	0.7144	0.0034	4.2647	0.6389	0.0057	3.2909	2
4	3.6643	0.0099	4.6145	0.8163	0.0015	0.1774	0.9396	0.0017	0.1478	1.0104	0.0052	2.3501	2
5	6.7023	0.0067	4.3726	2.2365	0.0102	1.2338	0.9996	0.0019	1.5214	1.8712	0.0080	1.4072	1
6	4.9010	0.0055	20.0700	1.0892	0.0067	5.1212	1.7329	0.0009	0.5758	1.1293	0.0012	1.0817	3
7	9.0407	0.0112	3.7076	1.5986	0.0007	1.0994	0.8527	0.0049	1.9438	1.2395	0.0058	0.6438	2
8	1.8805	0.0125	28.9310	0.8335	0.0012	0.6167	4.0325	0.0014	1.3788	0.7714	0.0008	0.1204	3
9	2.0576	0.0153	31.3570	0.7305	0.0063	1.4063	1.2141	0.0018	2.8379	2.5542	0.0034	1.3377	2
10	4.0369	0.0133	6.8540	8.3143	0.0104	0.3175	0.9094	0.0054	3.7674	0.6335	0.0023	1.5865	3
11				0.9816	0.0117	5.4646	1.6451	0.0054	16.9410	1.6902	0.0044	2.3916	1
12				1.0541	0.0030	1.8687				2.0335	0.0023	1.5865	3
13				0.7315	0.0007	0.2151				0.5927	0.0012	NaN	1
14				0.2881	0.0058	2.6311				2.2280	0.0036	3.0377	2
15				7.1830	0.0065	2.9120				0.8380	0.0029	1.7187	3
16				2.3337	0.0024	1.8560				2.2744	0.0042	1.4581	1
17				3.8104	0.0030	4.3110				1.6672	0.0028	1.2079	2
18				0.3643	0.0035	0.9160				2.9700	0.0022	1.1839	2
19				1.0816	0.0036	5.3285				0.8674	0.0031	0.6887	3
20				0.6175	0.0010	0.1570				2.8752	0.0015	0.2063	2
21				2.5235	0.0028	6.3356				1.9455	0.0065	0.8529	1
22				3.5254	0.0038	7.1479				5.3451	0.0095	6.0078	0
23				0.9691	0.0033	2.8220				0.6871	0.0011	0.1126	3
24				3.6705	0.0112	11.9300				0.8874	0.0020	0.3132	3
25				0.6424	0.0017	1.2743				1.8671	0.0081	0.4148	1
26				1.9413	0.0109	1.6392				0.7794	0.0042	0.3688	2
27				1.4581	0.0057	1.8287				1.9361	0.0043	0.7196	1
28				1.5710	0.0024	3.3210				1.9236	0.0114	4.8610	0
29				2.8634	0.0104	1.6770				0.9805	0.0073	2.1113	2
30				0.1816	0.0036	3.3037				0.4329	0.0034	2.2374	3
31				2.1634	0.0063	1.3712							
32				0.9394	0.0108	3.1974							
33				1.9624	0.0018	0.9502							
< cut-off	0	0	0	16	18	24	7	7	7	14	13	23	24
Sensitivity (%)	100	100	100	48.48	56.82	72.73	63.64	63.64	63.64	53.85	50.00	88.46	92.31
Specificity (%)													

Table A.1: Results of the melanoma diagnostic test for all subjects. Subjects highlighted in red were not included in the analysis.

B. Sample size and statistical power calculations

This appendix considers the statistical power of the diagnostic test for melanoma developed in Chapter 5.

Sample size is rarely reported in diagnostic accuracy studies [361], so no standard treatment of the problem exists. Consider the main hypothesis, that: *statistically significant alterations in skin blood flow dynamics will be observable when comparing skin malignant melanoma with atypical naevi and healthy skin*. Also consider our secondary aim, to consider the utilisation of any observed differences in the noninvasive diagnosis of skin melanoma.

Based on the aims and outcomes of this study, it may be concluded that it is an observational study. Important considerations in sample size calculation are as follows [362]

- The null hypothesis - there is no difference between blood flow dynamics in melanoma and atypical naevi.
- The alternative hypothesis - there is a difference between blood flow dynamics in melanoma and atypical naevi.
- The level at which we wish to avoid a type I error ($p\alpha$) - A type I error is the incorrect rejection of the null hypothesis, i.e. finding differences where there are none, usually set to 0.05.

-
- The level at which we wish to avoid a type II error ($p\beta$) - A type II error in the incorrect acceptance of the null hypothesis, i.e. stating there is no difference when there is, typically 0.8.
 - What difference do we want to detect? What is the magnitude of this difference?
 - Standard deviations of the variables of interest.
 - The distribution of the data. Many statistical tests and sample size calculations are based on assumptions of normal distributions. In our study, the non-normal distribution of data warranted the use of non-parametric tests. The same criteria which caused us to use these tests will apply to sample size calculations, and inevitably lead to the need for larger sample sizes.

Power of significance tests

Statistically significant differences in blood flow were revealed between groups. Here the statistical power of the tests used to obtain these results is assessed. As not all distributions of final test parameters were normal (as determined by the Lilliefors test), these differences were found using non-parametric tests, namely the Wilcoxon rank sum test for unpaired data (the parametric equivalent is the t test for independent samples), and the signed rank test for paired data (parametric equivalent - paired t test). When comparing more than one group, the Kruskal Wallis ANOVA test was used (parametric equivalent - one way analysis of variance, F test). The statistical power of these tests will depend on sample size.

Sample size, effect size, significance level and power are related, and given any three, one can simply calculate the fourth, based on a normal distribution. When a normal distribution cannot be assumed, the situation is more complex. Nevertheless, the required parameters from the existing data are calculated in order to give an estimate of the required sample size, the missing variable. Asymptotic relative efficiency (ARE), loosely describes the ratio of sample sizes required (parametric

to non-parametric) for a parametric procedure to have the same ability to reject a null hypothesis as the corresponding nonparametric procedure. It has been shown that the ARE of the Wilcoxon-Mann-Whitney (rank sum) test is always at least 0.864, regardless of the underlying population [363]. Although this value may increase depending on the data, this worst case scenario will be used in the following calculations, and therefore increase all calculated sample sizes by 15%.

Effect size

Three sets of parameters used in the final test are to be considered. Effect sizes are calculated for all cases, and the smallest effect size will be used in calculations, as this will result in the largest requirement for sample size. In these comparisons, only the difference between parameters in the melanoma and atypical naevi groups are considered, as atypical naevi provide the biggest diagnostic challenge, and from observations are more similar to melanoma in their blood flow characteristics than benign naevi, thus providing a more rigorous test of statistical power.

Test 1 - Ratio of mean blood perfusion at lesion margins and contralateral skin, recorded simultaneously.

Test 2 - Normalized spectral power of cardiac interval at the lesion margin.

Test 3 - Ratio of total spectral power in the cardiac and neurogenic frequency intervals in blood perfusion at lesion centres.

Effect size can be calculated as Cohen's d ,

$$d = \frac{\bar{x}_1 - \bar{x}_2}{s},$$

where s is the standard deviation and $\bar{x}_1 - \bar{x}_2$ is the difference between the two means of the samples. The standard deviation required can be a pooled standard deviation of the two groups, but this should not be used if the two standard deviations are likely to be systematically different. Therefore, the control standard deviation is used in the calculation. Effect sizes are therefore obtained for tests 1,

2 and 3 of 1.393, 1.095 and 3.536, respectively. The effect size of parameter 2, the smallest effect size, is taken forward into the sample size calculation. Sample size was calculated using the 'pwr' package in R, the statistical programming language.

R was used to compute the required sample size of the melanoma group (n_1), to perform a two sample, independent, one tailed, t-test, based on the following input:

n_2 - sample size of the atypical naevi group. There are 33 subjects, but because the tests used are non parametric, this will be reduced according to the extra 15% requirement explained above. The effective sample size thus becomes 28.696 subjects. Rounding down gives $n_2=28$.

d - effect size - the effect size calculated from parameter 2 - 1.095 is used.

sig.level - probability of a type I error, α . As standard, this is set to 0.05

power - the probability that the test will correctly reject the null hypothesis ($1-\beta$, where β is the probability of a type II error). As standard, this is set to 0.8.

alternative - specifies whether the test is two tailed, or one tailed (less or greater). Here, greater is used.

```
pwr.t2n.test(n2=28, power=0.8, d=1.095, sig.level=.05, alternative="greater")
```

```
t test power calculation
```

```
n1 = 6.658445
```

```
n2 = 28
```

```
d = 1.095
```

```
sig.level = 0.05
```

```
power = 0.8
```

```
alternative = greater
```

The test indicates that a sample size of at least 6.658 (rounded up to 7) is required to provide adequate statistical power. Including a further 15% to account for the non-parametric nature of the tests leads to a minimum required sample size of 8.05, which is rounded up to 9. As there are currently 10 subjects in the malignant melanoma group, the null hypothesis that there are no differences in blood flow dynamics in the cardiac interval can be rejected. As all other test parameters resulted in even larger effect sizes, one would expect to also be able to reject the null hypotheses that those parameters do not differ between groups. This is demonstrated by using the effect size from parameter 1 and observing the reduction in n_1 that is required to maintain sufficient statistical power:

```
pwr.t2n.test(n2=28, power=0.8, d=1.393, sig.level=.05, alternative="greater")
```

```
t test power calculation
```

```
n1 = 3.789535
```

```
n2 = 28
```

```
d = 1.393
```

```
sig.level = 0.05
```

```
power = 0.8
```

```
alternative = greater
```

Here it can be seen that increasing the effect size has provided an even lower estimate for the sample size n_1 , and is thus still within the scope of our data collection.

References

- [1] L. F. Olsen, A. Z. Andersen, A. Lunding, J. C. Brasen, and A. K. Poulsen. Regulation of glycolytic oscillations by mitochondrial and plasma membrane H^+ -ATPases. *Biophys. J.*, 96(9):3850–3861, 2009.
- [2] A. Stefanovska. Coupled oscillators: Complex but not complicated cardiovascular and brain interactions. *IEEE Eng. Med. Biol. Mag.*, 26(6):25–29, 2007.
- [3] G. Buzsáki and A. Draguhn. Neuronal oscillations in cortical networks. *Science*, 304:1926–1929, 2004.
- [4] G. Dupont, L. Combettes, G. S. Bird, and J. W. Putney. Calcium oscillations. *Cold Spring Harb. Perspect. Biol.*, 3(3):a004226, 2011.
- [5] I. Goehring, A. A. Gerencser, S. Schmidt, M. D. Brand, H. Mulder, and D. G. Nicholls. Plasma membrane potential oscillations in insulin secreting Ins-1 832/13 cells do not require glycolysis and are not initiated by fluctuations in mitochondrial bioenergetics. *J. Biol. Chem.*, 287(19):15706–15717, 2012.
- [6] H. J. Kwon, Y. Ohmiya, Ki. Honma, S. Honma, T. Nagai, K. Saito, and K. Yasuda. Synchronized ATP oscillations have a critical role in prechondrogenic condensation during chondrogenesis. *Cell Death Dis.*, 3(3):e278, 2012.
- [7] A. Goldbeter. *Biochemical Oscillations and Cellular Rhythms: the Molecular bases of Periodic and Chaotic Behaviour*. Cambridge University Press, 1997.
- [8] L. Bocchi, A. Evangelisti, M. Barrella, L. Scatizzi, and M. Bevilacqua. Recovery of 0.1 hz microvascular skin blood flow in dysautonomic diabetic (type 2) neuropathy by using frequency rhythmic electrical modulation system (fremis). *Med. Eng. Phys.*, 32(4):407–413, 2010.
- [9] M. Rossi, M. Nannipieri, M. Anselmino, M. Pesce, E. Muscelli, G. Santoro, and E. Ferrannini. Skin vasodilator function and vasomotion in patients with morbid obesity: effects of gastric bypass surgery. *Obes. Surg.*, 21(1):87–94, 2011.
- [10] M. Rossi, A. Bradbury, A. Magagna, M. Pesce, S. Taddei, and A. Stefanovska. Investigation of skin vasoreactivity and blood flow oscillations in hypertensive patients: effect of short-term antihypertensive treatment. *J. Hypertens.*, 29(8):1569–1576, 2011.

-
- [11] M. Stücker, M. Esser, M. Hoffmann, U. Memmel, A. Hirschmüller, C. von Bormann, K. Hoffmann, and P. Altmeyer. High-resolution laser Doppler perfusion imaging aids in differentiating between benign and malignant melanocytic skin tumours. *Acta. Derm. Venereol.*, 82:25–29, 2002.
- [12] H. M. Häfner, K. Bräuer, M. Eichner, A. Steins, M. Möhrle, A. Blum, and M. Jünger. Wavelet analysis of cutaneous blood flow in melanocytic skin lesions. *J. Vasc. Res.*, 42(1):38–46, 2005.
- [13] W. Harvey. *On the motion of the heart and blood in animals*, volume 1. Bell, 1889.
- [14] W. C. Aird. Discovery of the cardiovascular system: from Galen to William Harvey. *J. Thromb. Haemost.*, 9(s1):118–129, 2011.
- [15] D. Chillet, J. Jomier, D. Cool, and S. Aylward. Vascular atlas formation using a vessel-to-image affine registration method. In *Medical Image Computing and Computer-Assisted Intervention-MICCAI 2003*, pages 335–342. Springer, 2003.
- [16] D. S. Park and G. I. Fishman. The cardiac conduction system. *Circulation*, 123(8):904–915, 2011.
- [17] S. Tawara. *Das reizleitungssystem des Säugetierherzens*. Fischer, 1906.
- [18] S. Tawara. *The Conduction system of the mammalian heart. English translation*. Imperial College Press, London, 2000.
- [19] A. Keith and M. Flack. The form and nature of the muscular connections between the primary divisions of the vertebrate heart. *J. Anat. Physiol.*, 41(Pt 3):172, 1907.
- [20] P. Safar and P. Kochanek. Cerebral blood flow promotion after prolonged cardiac arrest. *Crit. Care Med.*, 28(8):3104–3106, 2000.
- [21] T. Kalogeris, C. P. Baines, M. Krenz, and R. J. Korthuis. Cell biology of ischemia/reperfusion injury. *Int. Rev. Cell Mol. Biol.*, 298:229, 2012.
- [22] M. S. Olufsen, C. S. Peskin, W. Y. Kim, E. M. Pedersen, A. Nadim, and J. Larsen. Numerical simulation and experimental validation of blood flow in arteries with structured-tree outflow conditions. *Ann. Biomed. Eng.*, 28(11):1281–1299, 2000.
- [23] D. Mehta and A. B. Malik. Signaling mechanisms regulating endothelial permeability. *Physiol. Rev.*, 86(1):279–367, 2006.
- [24] V. Urbančič-Rovan, A. Bernjak, A. Stefanovska, K. Ažman-Juvan, and A. Kocijančič. Macro- and microcirculation in the lower extremities - possible relationship. *Diabetes Res. Clin. Pract.*, 73(2):166–173, 2006.
- [25] J. M. S. Pearce. Malpighi and the discovery of capillaries. *Eur. Neurol.*, 58(4):253–255, 2007.

-
- [26] J. Young. Malpighi's 'De Pulmonibus'. *Proc. R. Soc. Med.*, 23(1):1, 1929.
- [27] A. van Leeuwenhoek. Den waaragtigen omloop des bloeds [on the true circulation of the blood]. *Letter, written to the Royal Society in London*, 1688.
- [28] Kelvinsong. <https://commons.wikimedia.org/wiki/File:Capillary.svg>. [Online; accessed 06-January-2015].
- [29] M. R. Eliseyeva. Endothelium: a long road from mystery to discovery. *Int. J. Biomed.*, 3(1):9–11, 2013.
- [30] W. His. *Die Häute und Höhlen des Körpers: Akademisches Programm*. Schweighauser, 1865.
- [31] G. Favero, C. Paganelli, B. Buffoli, L. F. Rodella, and R. Rezzani. Endothelium and its alterations in cardiovascular diseases: life style intervention. *BioMed Res. Int.*, 2014:801896, 2014.
- [32] L. Florey. The endothelial cell. *Br. Med. J.*, 2(5512):487–90, 1966.
- [33] E. A. Jaffe, R. L. Nachman, C. G. Becker, and C. R. Minick. Culture of human endothelial cells derived from umbilical veins. identification by morphologic and immunologic criteria. *J. Clin. Invest.*, 52(11):2745, 1973.
- [34] R. L. Nachman. Endothelium: from cellophane to orchestral maestro. *J. Clin. Invest.*, 122(3):796, 2012.
- [35] J. R. Vane, E. E. Änggård, and R. M. Botting. Regulatory functions of the vascular endothelium. *N. Engl. J. Med.*, 323(1):27–36, 1990.
- [36] D. B. Cines, E. S. Pollak, C. A. Buck, J. Loscalzo, G. A. Zimmerman, R. P. McEver, J. S. Pober, T. M. Wick, B. A. Konkle, B. S. Schwartz, E. S. Barnathan, K. R. McCrae, B. A. Hug, A. M. Schmidt, and D. M. Stern. Endothelial cells in physiology and in the pathophysiology of vascular disorders. *Blood*, 91(10):3527–3561, 1998.
- [37] O. Cleaver and D. A. Melton. Endothelial signaling during development. *Nat. Med.*, 9(6):661–668, 2003.
- [38] A. P. Fishman. Endothelium: a distributed organ of diverse capabilities. *Ann. N. Y. Acad. Sci.*, 401(1):1–8, 1982.
- [39] A. Hoeben, B. Landuyt, M. S. Highley, H. Wildiers, A. T. Van Oosterom, and E. A. De Bruijn. Vascular endothelial growth factor and angiogenesis. *Pharmacol. Rev.*, 56(4):549–580, 2004.
- [40] S. Moncada, R. J. Gryglewski, S. Bunting, and J. R. Vane. An enzyme isolated from arteries transforms prostaglandin endoperoxides to an unstable substance that inhibits platelet aggregation. *Nature*, 263:663–665, 1976.
- [41] R. F. Furchgott and J. V. Zawadzki. The obligatory role of endothelial cells in the relaxation of arterial smooth muscle by acetylcholine. *Nature*, 288(5789):373–376, 1980.

-
- [42] L. J. Ignarro, G. M. Buga, K. S. Wood, R. E. Byrns, and G. Chaudhuri. Endothelium-derived relaxing factor produced and released from artery and vein is nitric oxide. *Proc. Nat. Acad. Sci.*, 84(24):9265–9269, 1987.
- [43] R. M. J. Palmer, A. G. Ferrige, and S. Moncada. Nitric oxide release accounts for the biological activity of endothelium-derived relaxing factor. *Nature*, 327:524–526, 1987.
- [44] S. G. Taylor and A. H. Weston. Endothelium-derived hyperpolarizing factor: a new endogenous inhibitor from the vascular endothelium. *Trends Pharmacol. Sci.*, 9(8):272–274, 1988.
- [45] G. Chen, H. Suzuki, and A. H. Weston. Acetylcholine releases endothelium-derived hyperpolarizing factor and EDRF from rat blood vessels. *Br. J. Pharmacol.*, 95(4):1165–1174, 1988.
- [46] M. Yanagisawa, H. Kurihara, S. Kimura, Y. Tomobe, M. Kobayashi, Y. Mitsui, Y. Yazaki, K. Goto, and T. Masaki. A novel potent vasoconstrictor peptide produced by vascular endothelial cells. *Nature*, 332(6163):411–415, 1988.
- [47] A. J. Pappano and W. G. Wier. *Cardiovascular Physiology: Mosby Physiology Monograph Series*. Elsevier Health Sciences, 2012.
- [48] G. Siegel, G. Meyer-Rath, E. Ermilov, M. Rodríguez, M. Malmsten, P. Claesson, R. Saunders, R. Hetzer, and B. Lindman. Flow sensing in the cardiovascular system. *Colloids Surf. A Physicochem. Eng. Asp.*, 2015.
- [49] U. Pohl, J. Holtz, R. Busse, and E. Bassenge. Crucial role of endothelium in the vasodilator response to increased flow *in vivo*. *Hypertension*, 8(1):37–44, 1986.
- [50] P. O. Bonetti, L. O. Lerman, and A. Lerman. Endothelial dysfunction a marker of atherosclerotic risk. *Arterioscler. Thromb. Vasc. Biol.*, 23(2):168–175, 2003.
- [51] C. M. Steyers and F. J. Miller. Endothelial dysfunction in chronic inflammatory diseases. *Int. J. Mol. Sci.*, 15(7):11324–11349, 2014.
- [52] D. H. Endemann and E. L. Schiffrin. Endothelial dysfunction. *J. Am. Soc. Nephrol.*, 15(8):1983–1992, 2004.
- [53] C. G. Schalkwijk and C. D. A. Stehouwer. Vascular complications in diabetes mellitus: the role of endothelial dysfunction. *Clin. Sci.*, 109:143–159, 2005.
- [54] F. Stam, C. van Guldener, C. G. Schalkwijk, P. M. ter Wee, A. J. M. Donker, and C. D. A. Stehouwer. Impaired renal function is associated with markers of endothelial dysfunction and increased inflammatory activity. *Nephrol. Dial. Transplant.*, 18(5):892–898, 2003.
- [55] C. Costa and R. Virag. The endothelial–erectile dysfunction connection: An essential update. *J. Sex. Med.*, 6(9):2390–2404, 2009.

-
- [56] X. K. Tong, N. Nicolakakis, A. Kocharyan, and E. Hamel. Vascular remodeling versus amyloid β -induced oxidative stress in the cerebrovascular dysfunctions associated with Alzheimer's disease. *J. Neurosci.*, 25(48):11165–11174, 2005.
- [57] A. M. Germain, M. C. Romanik, I. Guerra, S. Solari, M. S. Reyes, R. J. Johnson, K. Price, S. A. Karumanchi, and G. Valdés. Endothelial dysfunction: A link among preeclampsia, recurrent pregnancy loss, and future cardiovascular events? *Hypertension*, 49(1):90–95, 2007.
- [58] A. Avogaro and S. V. de Kreutzenberg. Mechanisms of endothelial dysfunction in obesity. *Clin. Chim. Acta*, 360(1):9–26, 2005.
- [59] N. Stergiopoulos, C. A. Porret, S. De Brouwer, and J. J. Meister. Arterial vasomotion: effect of flow and evidence of nonlinear dynamics. *Am. J. Physiol. Heart Circ. Physiol.*, 274(6):H1858–H1864, 1998.
- [60] G. Ross, E. Stinson, J. Schroeder, and R. Ginsburg. Spontaneous phasic activity of isolated human coronary arteries. *Cardiovasc. Res.*, 14(10):613–618, 1980.
- [61] D. Hayoz, Y. Tardy, B. Rutschmann, J. P. Mignot, H. Achakri, F. Feihl, J. J. Meister, B. Waerber, and H. R. Brunner. Spontaneous diameter oscillations of the radial artery in humans. *Am. J. Physiol. Heart Circ. Physiol.*, 264(6):H2080–H2084, 1993.
- [62] T. W. Jones. Discovery that the veins of the bat's wing (which are furnished with valves) are endowed with rythmical contractility, and that the onward flow of blood is accelerated by each contraction. *Phil. Trans. R. Soc. Lond.*, 142:131–136, 1852.
- [63] A. G. Kaufman and M. Intaglietta. Automated diameter measurement of vasomotion by cross-correlation. *Int. J. Microcirc.*, 4(1):45–53, 1985.
- [64] S. Hu, K. Maslov, and L. V. Wang. Noninvasive label-free imaging of microhemodynamics by optical-resolution photoacoustic microscopy. *Opt. Express*, 17(9):7688–7693, 2009.
- [65] S. Abuhajar. *Visualizing real time vasomotion in vivo using optical coherence tomography*. PhD thesis, Lancaster University, 2012.
- [66] H. Nilsson and C. Aalkjær. Vasomotion: mechanisms and physiological importance. *Mol. Interventions*, 3(2):79, 2003.
- [67] C. Aalkjaer, D. Boedtkjer, and V. Matchkov. Vasomotion—what is currently thought? *Acta Physiol.*, 202(3):253–269, 2011.
- [68] P. Kvandal, S. A. Landsverk, A. Bernjak, A. Stefanovska, H. D. Kvernmo, and K. A. Kirkebøen. Low frequency oscillations of the laser Doppler perfusion signal in human skin. *Microvasc. Res.*, 72(3):120–127, 2006.

-
- [69] E. Bouskela and W. Grampp. Spontaneous vasomotion in hamster cheek pouch arterioles in varying experimental conditions. *Am. J. Physiol. Heart Circ. Physiol.*, 262(2):H478–H485, 1992.
- [70] D. W. Slaaf, G. J. Tangelder, H. C. Teirlinck, and R. S. Reneman. Arteriolar vasomotion and arterial pressure reduction in rabbit tenuissimus muscle. *Microvasc. Res.*, 33(1):71–80, 1987.
- [71] J. A. Schmidt, P. Borgström, G. P. Firestone, P. von Wichert, M. Intaglietta, and A. Fronek. Periodic hemodynamics (flow motion) in peripheral arterial occlusive disease. *J. Vasc. surg.*, 18(2):207–215, 1993.
- [72] C. Aalkjær and H. Nilsson. Vasomotion: cellular background for the oscillator and for the synchronization of smooth muscle cells. *Br. J. Pharmacol.*, 144(5):605–616, 2005.
- [73] T. Söderström, A. Stefanovska, M. Veber, and H. Svenson. Involvement of sympathetic nerve activity in skin blood flow oscillations in humans. *Am. J. Physiol. Heart Circ. Physiol.*, 284(5):H1638–H1646, 2003.
- [74] A. Colantuoni, S. Bertuglia, and M. Intaglietta. Quantitation of rhythmic diameter changes in arterial microcirculation. *Am. J. Physiol.*, 246(4):H508–H517, 1984.
- [75] S. A. Landsverk, P. Kvandal, A. Bernjak, A. Stefanovska, and K. A. Kirkebøen. The effects of general anesthesia on human skin microcirculation evaluated by wavelet transform. *Anesth. Analg.*, 105(4):1012–1019, 2007.
- [76] A. Stefanovska, L. W. Sheppard, T. Stankovski, and P. V. E. McClintock. Reproducibility of LDF blood flow measurements: Dynamical characterization versus averaging. *Microvasc. Res.*, 82(3):274–276, 2011.
- [77] T. Sakurai and N. Terui. Effects of sympathetically induced vasomotion on tissue-capillary fluid exchange. *Am. J. Physiol. Heart Circ. Physiol.*, 291(4):H1761–H1767, 2006.
- [78] L. W. Sheppard, V. Vuksanović, P. V. E. McClintock, and A. Stefanovska. Oscillatory dynamics of vasoconstriction and vasodilation identified by time-localized phase coherence. *Phys. Med. Biol.*, 56:3583–3601, 2011.
- [79] V. Vuksanović, L. W. Sheppard, and A. Stefanovska. Nonlinear relationship between level of blood flow and skin temperature for different dynamics of temperature change. *Biophys. J.*, 94(10):L78–L80, 2008.
- [80] S. Bertuglia, A. Colantuoni, G. Coppini, and M. Intaglietta. Hypoxia-or hyperoxia-induced changes in arteriolar vasomotion in skeletal muscle microcirculation. *Am. J. Physiol. Heart Circ. Physiol.*, 260(2):H362–H372, 1991.
- [81] M. Rücker, O. Strobel, B. Vollmar, F. Roesken, and M. D. Menger. Vasomotion in critically perfused muscle protects adjacent tissues from capillary perfusion failure. *Am. J. Physiol. Heart Circ. Physiol.*, 279(2):H550–H558, 2000.

-
- [82] D. Goldman and A. S. Popel. A computational study of the effect of vasomotion on oxygen transport from capillary networks. *J. Theor. Biol.*, 209(2):189–199, 2001.
- [83] A. G. Tsai and M. Intaglietta. Evidence of flowmotion induced changes in local tissue oxygenation. *Int. J. Microcirc. Clin. Exp.*, 12(1):75–88, 1993.
- [84] C. E. Thorn, H. Kyte, D. W. Slaff, and A. C. Shore. An association between vasomotion and oxygen extraction. *Am. J. Physiol. Heart Circ. Physiol.*, 301(2):H442–H449, 2011.
- [85] T. Yano, C. Lian, T. Arimitsu, R. Yamanaka, R. Afroundeh, K. Shirakawa, and T. Yunoki. Oscillation of oxygenation in skeletal muscle at rest and in light exercise. *Acta Physiol. Hung.*, 100(3):312–320, 2013.
- [86] A. Bernjak, P. V. E. McClintock, A. Stefanovska, P. J. Owen-Lynch, and P. B. M. Clarkson. Coherence of fluctuations in blood flow with those in tissue oxygen saturation. *Fluct. Noise Lett.*, 11(1):1240013, 2012.
- [87] C. E. Thorn, S. J. Matcher, I. V. Meglinski, and A. C. Shore. Is mean blood saturation a useful marker of tissue oxygenation? *Am. J. Physiol. Heart Circ. Physiol.*, 296(5):H1289–H1295, 2009.
- [88] K. Z. Kuliga, E. F. McDonald, R. Gush, C. Michel, A. J. Chipperfield, and G. F. Clough. Dynamics of microvascular blood flow and oxygenation measured simultaneously in human skin. *Microcirculation*, 21(6):562–573, 2014.
- [89] M. D. Stern. *In vivo* observation of microcirculation by coherent light scattering. *Nature*, 254:56–58, 1975.
- [90] M. D. Stern, D. L. Lappe, P. D. Bowen, J. E. Chimosky, G. A. Holloway, H. R. Keiser, and R. L. Bowman. Continuous measurement of tissue blood flow by laser-Doppler spectroscopy. *Am. J. Physiol. Heart Circ. Physiol.*, 232(4):H441–H448, 1977.
- [91] C. Riva, B. Ross, and G. B. Benedek. Laser Doppler measurements of blood flow in capillary tubes and retinal arteries. *Invest. Ophthalmol.*, 11:936–944, 1972.
- [92] K. Wårdell, A. Jakobsson, and G. E. Nilsson. Laser doppler perfusion imaging by dynamic light scattering. *IEEE Trans. Biomed. Eng.*, 40(4):309–316, 1993.
- [93] J. L. Cracowski, C. T. Minson, M. Salvat-Melis, and J. R. Halliwill. Methodological issues in the assessment of skin microvascular endothelial function in humans. *Trends Pharmacol. Sci.*, 27(9):503–508, 2006.
- [94] M. Roustit and J. L. Cracowski. Non-invasive assessment of skin microvascular function in humans: an insight into methods. *Microcirculation*, 19(1):47–64, 2012.

-
- [95] F. Morales, R. Graaff, A. J. Smit, S. Bertuglia, A. L. Petoukhova, W. Steenberg, P. Leger, and G. Rakhorst. How to assess post-occlusive reactive hyperaemia by means of laser Doppler perfusion monitoring: application of a standardised protocol to patients with peripheral arterial obstructive disease. *Microvasc. Res.*, 69(1):17–23, 2005.
- [96] G. Jörneskog, K. Brismar, and B. Fagrell. Skin capillary circulation severely impaired in toes of patients with IDDM, with and without late diabetic complications. *Diabetologia*, 38(4):474–480, 1995.
- [97] K. Farkas, E. Kolossváry, Z. Járαι, J. Nemcsik, and C. Farsang. Non-invasive assessment of microvascular endothelial function by laser Doppler flowmetry in patients with essential hypertension. *Atherosclerosis*, 173(1):97–102, 2004.
- [98] J. Stewart, A. Kohen, D. Brouder, F. Rahim, S. Adler, R. Garrick, and M. S. Goligorsky. Noninvasive interrogation of microvasculature for signs of endothelial dysfunction in patients with chronic renal failure. *Am. J. Physiol. Heart Circ. Physiol.*, 287(6):H2687–H2696, 2004.
- [99] G. B. Yvonne-Tee, A. H. G. Rasool, A. S. Halim, and A. R. A. Rahman. Reproducibility of different laser Doppler fluximetry parameters of post-occlusive reactive hyperemia in human forearm skin. *J. Pharmacol. Toxicol. Methods*, 52(2):286–292, 2005.
- [100] M. Berghoff, M. Kathpal, S. Kilo, M. J. Hilz, and R. Freeman. Vascular and neural mechanisms of ACh-mediated vasodilation in the forearm cutaneous microcirculation. *J. Appl. Physiol.*, 92(2):780–788, 2002.
- [101] R. M. Rapoport, M. B. Draznin, and F. Murad. Endothelium-dependent relaxation in rat aorta may be mediated through cyclic GMP-dependent protein phosphorylation. 306:174–176, 1983.
- [102] P. Kvandal, A. Stefanovska, M. Veber, H. D. Kvernmo, and K.-A. Kirkebøen. Regulation of human cutaneous circulation evaluated by laser Doppler flowmetry, iontophoresis, and spectral analysis: importance of nitric oxide and prostaglandines. *Microvasc. Res.*, 65(3):160–171, 2003.
- [103] A. Bandrivskyy, A. Bernjak, P. V. E. McClintock, and A. Stefanovska. Role of transdermal potential difference during iontophoretic drug delivery. *IEEE Trans. Biomed. Eng.*, 51(9):1683–1685, 2004.
- [104] M. N. Berliner. Skin microcirculation during tapwater iontophoresis in humans: cathode stimulates more than anode. *Microvasc. Res.*, 54(1):74–80, 1997.
- [105] A. Asberg, T. Holm, T. Vassbotn, A. K. Andreassen, and A. Hartmann. Nonspecific microvascular vasodilatation during iontophoresis is attenuated by application of hyperosmolar saline. *Microvasc. Res.*, 58(1):41–48, 1999.
- [106] N. Charkoudian. Skin blood flow in adult human thermoregulation: how it works, when it does not, and why. In *Mayo Clinic Proceedings*, volume 78, pages 603–612. Elsevier, 2003.

-
- [107] G. A. Tew, M. Klonizakis, J. Moss, A. D. Ruddock, J. M. Saxton, and G. J. Hodges. Reproducibility of cutaneous thermal hyperaemia assessed by laser Doppler flowmetry in young and older adults. *Microvasc. Res.*, 81(2):177–182, 2011.
- [108] C. T. Minson. Thermal provocation to evaluate microvascular reactivity in human skin. *J. Appl. Physiol.*, 109(4):1239–1246, 2010.
- [109] M. Bračič and A. Stefanovska. Wavelet based analysis of human blood flow dynamics. *Bull. Math. Biol.*, 60(5):919–935, 1998.
- [110] A. Stefanovska, M. Bračič, and H. D. Kvernmo. Wavelet analysis of oscillations in the peripheral blood circulation measured by laser Doppler technique. *IEEE Trans. Bio. Med. Eng.*, 46(10):1230–1239, 1999.
- [111] K. Ažman-Juvan, A. Bernjak, V. Urbančič-Rovan, A. Stefanovska, and D. Štajer. Skin blood flow and its oscillatory components in patients with acute myocardial infarction. *J. Vasc. Res.*, 45(2):164–172, 2008.
- [112] Y. Shiogai, A. Stefanovska, and P. V. E. McClintock. Nonlinear dynamics of cardiovascular ageing. *Phys. Rep.*, 488:51–110, 2010.
- [113] A. Bernjak, P. B. M. Clarkson, P. V. E. McClintock, and A. Stefanovska. Low-frequency blood flow oscillations in congestive heart failure and after β 1-blockade treatment. *Microvasc. Res.*, 76(3):224–232, 2008.
- [114] A. Bollinger, A. Yanar, U. Hoffmann, and U. K. Franzek. Is high-frequency flux motion due to respiration or to vasomotion activity? *Prog. Appl. Microcirc.*, 20:52–52, 1993.
- [115] M. E. Mück-Weymann, H. P. Albrecht, D. Hiller, O. P. Hornstein, and R. D. Bauer. [Respiration-dependence of cutaneous laser Doppler flow motion]. *VASA. Zeitschrift für Gefasskrankheiten*, 23(4):299–304, 1993.
- [116] J. Karstrup, J. Bühlow, and N. A. Lassen. Vasomotion in human-skin before and after local heating recorded with laser Doppler flowmetry – A method for induction of vasomotion. *Int. J. Microcirc.: Clin. Exp.*, 8(2):205–215, 1989.
- [117] C. Julien. The enigma of Mayer waves: Facts and models. *Cardiovasc. Res.*, 70(1):12–21, 2006.
- [118] S. C. Malpas. The rhythmicity of sympathetic nerve activity. *Prog. Neurobiol.*, 56(1):65–96, 1998.
- [119] S. A. Landsverk, P. Kvandal, T. Kjelstrup, U. Benko, A. Bernjak, A. Stefanovska, H. Kvernmo, and K. A. Kirkebøen. Human skin microcirculation after brachial plexus block evaluated by wavelet transform of the laser Doppler flowmetry signal. *Anesthesiology*, 105(3):478–484, 2006.
- [120] S. Lehtipalo, O. Winsö, L.-O. D. Koskinen, G. Johansson, and B. Biber. Cutaneous sympathetic vasoconstrictor reflexes for the evaluation of interscalene brachial plexus block. *Acta Anaesthesiol. Scand.*, 44(8):946–952, 2000.

-
- [121] F. Bajrović, M. Čenčur, M. Hožič, S. Ribarič, and A. Stefanovska. The contribution of lumbar sympathetic neurones activity to rat's skin blood flow oscillations. *Pflüg. Arch.: Eur. J. Physiol. Suppl.*, 439(3):R158–R160, 2000.
- [122] H. L. Peng, V. Matchkov, A. Ivarsen, C. Aalkajær, and H. Nilsson. Hypothesis for the initiation of vasomotion. *Circ. Res.*, 88(8):810–815, 2001.
- [123] H. D. Kvernmo, A. Stefanovska, K.-A. Kirkebøen, and K. Kvernebo. Oscillations in the human cutaneous blood perfusion signal modified by endothelium-dependent and endothelium-independent vasodilators. *Microvasc. Res.*, 57(3):298–309, 1999.
- [124] M. Veber, A. Bandrivskyy, P. B. M. Clarkson, P. V. E. McClintock, and A. Stefanovska. Wavelet analysis of blood flow dynamics: effect on the individual oscillatory components of iontophoresis with pharmacologically neutral electrolytes. *Phys. Med. Biol.*, 49:N111–N117, 2004.
- [125] A. Stefanovska and M. Bračič. Physics of the human cardiovascular system. *Contemp. Phys.*, 40(1):31–55, 1999.
- [126] H. D. Kvernmo, A. Stefanovska, and K. A. Kirkebøen. Enhanced endothelial activity reflected in the cutaneous blood flow oscillations of athletes. *Eur. J. Appl. Physiol.*, 90:16–22, 2003.
- [127] M. Rossi, E. Matteucci, M. Pesce, C. Consani, F. Galetta, O. Giampietro, and G. Santoro. Study of skin vasomotion in type 1 diabetic patients and of its possible relationship with clinical and laboratory variables. *Clin. Hemorheol. Microcirc.*, 53(4):357–367, 2013.
- [128] V. Ticcinelli, R. Martini, and A. Bagno. Preliminary study of laser Doppler perfusion signal by wavelet transform in patients with critical limb ischemia before and after revascularization. *Clin. Hemorheol. Microcirc.*, 58(3):415–428, 2014.
- [129] M. Rossi, A. Carpi, F. Galetta, F. Franzoni, and G. Santoro. The investigation of skin blood flowmotion: a new approach to study the microcirculatory impairment in vascular diseases? *Biomed. Pharmacother.*, 60(8):437–442, 2006.
- [130] L. A. Holowatz, C. S. Thompson-Torgerson, and W. L. Kenney. The human cutaneous circulation as a model of generalized microvascular function. *J. Appl. Physiol.*, 105(1):370–372, 2008.
- [131] J. L. Cracowski and M. Roustit. Commentary on viewpoint: The human cutaneous circulation as a model of generalized microvascular function. *J. Appl. Physiol.*, 105:388, 2008.
- [132] D. Rizzoni. Commentary on viewpoint: The human cutaneous circulation as a model of generalized microvascular function. *J. Appl. Physiol.*, 105:383, 2008.

-
- [133] A. Stefanovska. Commentary on viewpoint: The human cutaneous circulation as a model of generalized microvascular function. *J. Appl. Physiol.*, 105:387, 2008.
- [134] D. Hanahan and R. A. Weinberg. Hallmarks of cancer: the next generation. *cell*, 144(5):646–674, 2011.
- [135] R. A. Cairns, I. S. Harris, and T. W. Mak. Regulation of cancer cell metabolism. *Nat. Rev. Cancer*, 11(2):85–95, 2011.
- [136] P. Carmeliet and R. K. Jain. Angiogenesis in cancer and other diseases. *Nature*, 407(6801):249–257, 2000.
- [137] D. H. Ausprunk and J. Folkman. Migration and proliferation of endothelial cells in preformed and newly formed blood vessels during tumor angiogenesis. *Microvasc. Res.*, 14(1):53–65, 1977.
- [138] A. G. Ide, N. H. Baker, and S. L. Warren. Vascularization of the Brown Pearce rabbit epithelioma transplant as seen in the transparent ear chamber. *Am J. Roentgenol.*, 42:891–899, 1939.
- [139] D. Ribatti. Judah Folkman, a pioneer in the study of angiogenesis. *Angiogenesis*, 11(1):3–10, 2008.
- [140] G. H. Algire, H. W. Chalkley, F. Y. Legallais, and H. D. Park. Vascular reactions of normal and malignant tissues *in vivo*. I. vascular reactions of mice to wounds and to normal and neoplastic transplants. *J. Natl. Cancer Inst.*, 6:73–85, 1945.
- [141] M. Greenblatt and P. Shubik. Tumor angiogenesis: transfilter diffusion studies in the hamster by the transparent chamber technique. *J. Natl. Cancer Inst.*, 41(1):111–124, 1968.
- [142] Y. Cao and R. Langer. A review of Judah Folkman’s remarkable achievements in biomedicine. *Proc. Nat. Acad. Sci. U. S. A.*, 105(36):13203, 2008.
- [143] J. Folkman. Tumor angiogenesis: therapeutic implications. *N. Engl. J. Med.*, (285):1182–6, 1971.
- [144] J. Folkman, E. Merler, C. Abernathy, and G. Williams. Isolation of a tumor factor responsible for angiogenesis. *J. Exp. Med.*, 133(2):275–288, 1971.
- [145] H. F. Dvorak, L. F. Brown, M. Detmar, and A. M. Dvorak. Vascular permeability factor/vascular endothelial growth factor, microvascular hyperpermeability, and angiogenesis. *Am. J. Pathol.*, 146(5):1029–1039, 1995.
- [146] D. R. Senger, S. J. Galli, A. M. Dvorak, C. A. Perruzzi, V. S. Harvey, and H. F. Dvorak. Tumor cells secrete a vascular permeability factor that promotes accumulation of ascites fluid. *Science*, 219(4587):983–985, 1983.
- [147] G. Gasparini. Prognostic value of vascular endothelial growth factor in breast cancer. *The Oncologist*, 5(Supplement 1):37–44, 2000.

-
- [148] M. Volm, R. Koomägi, and J. Mattern. Prognostic value of vascular endothelial growth factor and its receptor Flt-1 in squamous cell lung cancer. *Int. J. Cancer*, 74(1):64–68, 1997.
- [149] N. Ferrara and T. Davis-Smyth. The biology of vascular endothelial growth factor. *Endocr. Rev.*, 18(1):4–25, 1997.
- [150] M. Potente, H. Gerhardt, and P. Carmeliet. Basic and therapeutic aspects of angiogenesis. *Cell*, 146(6):873–887, 2011.
- [151] F. Hillen and A. W. Griffioen. Tumour vascularization: sprouting angiogenesis and beyond. *Cancer Metastasis Rev.*, 26(3-4):489–502, 2007.
- [152] B. A. Peters, L. A. Diaz, K. Polyak, L. Meszler, K. Romans, E. C. Guinan, J. H. Antin, D. Myerson, S. R. Hamilton, B. Vogelstein, K. W. Kinzler, and C. Lengauer. Contribution of bone marrow-derived endothelial cells to human tumor vasculature. *Nat. Med.*, 11(3):261–262, 2005.
- [153] J. Folkman. Angiogenesis in cancer, vascular, rheumatoid and other disease. *Nat. Med.*, 1(1):27–30, 1995.
- [154] A. J. Maniotis, R. Folberg, A. Hess, E. A. Seftor, L. M. G. Gardner, J. Pe’er, J. M. Trent, P. S. Meltzer, and M. J. C. Hendrix. Vascular channel formation by human melanoma cells *in vivo* and *in vitro*: vasculogenic mimicry. *Am. J. Pathol.*, 155(3):739–752, 1999.
- [155] M. G. Tonnesen, X. Feng, and R. A. F. Clark. Angiogenesis in wound healing. In *J. Invest. Derma. Symp. P.*, volume 5, pages 40–46. Nature Publishing Group, 2000.
- [156] D. J. Collinson and R. Donnelly. Therapeutic angiogenesis in peripheral arterial disease: can biotechnology produce an effective collateral circulation? *Eur. J. Vasc. Endovasc. Surg.*, 28(1):9–23, 2004.
- [157] A. Breslow. Thickness, cross-sectional areas and depth of invasion in the prognosis of cutaneous melanoma. *Ann. Surg.*, 172(5):902, 1970.
- [158] Cancer Research UK/ Wikimedia Commons. https://commons.wikimedia.org/wiki/File:Diagram_showing_the_T_stages_of_melanoma_CRUK_373.svg. [Online; accessed 06-January-2015].
- [159] G. H. Mahabeleshwar and T. V. Byzova. Angiogenesis in melanoma. *Semin. Oncol.*, 34(6):555–565, 2007.
- [160] R. Ria, A. Reale, A. Castrovilli, G. Mangialardi, F. Dammacco, D. Ribatti, and A. Vacca. Angiogenesis and progression in human melanoma. *Dermatol. Res. Pract.*, 2010, 2010.
- [161] J. Marcoval, A. Moreno, J. Graells, A. Vidal, J. M. Escribà, M. Garcia-Ramirez, and A. Fabra. Angiogenesis and malignant melanoma. Angiogenesis is related to the development of vertical (tumorigenic) growth phase. *J. Cutan. Pathol.*, 24(4):212–218, 1997.

-
- [162] M. Kashani-Sabet, R. W. Sagebiel, C. M. M. Ferreira, M. Nosrati, and J. R. Miller. Tumor vascularity in the prognostic assessment of primary cutaneous melanoma. *J. Clin. Oncol.*, 20(7):1826–1831, 2002.
- [163] M. Streit and M. Detmar. Angiogenesis, lymphangiogenesis, and melanoma metastasis. *Oncogene*, 22(20):3172–3179, 2003.
- [164] Rakesh K Jain. Determinants of tumor blood flow: a review. *Cancer Res.*, 48(10):2641–2658, 1988.
- [165] I. S. Haldorsen, I. Stefansson, R. Grüner, J. A. Husby, I. J. Magnussen, H. M. J. Werner, Ø. O. Salvesen, L. Bjørge, J. Trovik, T. Taxt, L. A. Akslen, and H. B. Salvesen. Increased microvascular proliferation is negatively correlated to tumour blood flow and is associated with unfavourable outcome in endometrial carcinomas. *Br. J. Cancer*, 110(1):107–114, 2014.
- [166] S. Goel, D. G. Duda, L. Xu, L. L. Munn, Y. Boucher, D. Fukumura, and R. K. Jain. Normalization of the vasculature for treatment of cancer and other diseases. *Physiol. Rev.*, 91(3):1071–1121, 2011.
- [167] D. Fukumura, D. G. Duda, L. L. Munn, and R. K. Jain. Tumor microvasculature and microenvironment: Novel insights through intravital imaging in pre-clinical models. *Microcirculation*, 17(3):206–225, 2010.
- [168] C. J. Eskey, A. P. Koretsky, M. M. Domach, and R. K. Jain. ^2H -nuclear magnetic resonance imaging of tumor blood flow: spatial and temporal heterogeneity in a tissue-isolated mammary adenocarcinoma. *Cancer Res.*, 52(21):6010–6019, 1992.
- [169] H. Hashizume, P. Baluk, S. Morikawa, J. W. McLean, G. Thurston, S. Roberge, R. K. Jain, and D. M. McDonald. Openings between defective endothelial cells explain tumor vessel leakiness. *Am. J. Pathol.*, 156(4):1363–1380, 2000.
- [170] T. P. Padera, B. R. Stoll, J. B. Tooredman, D. Capen, E. di Tomaso, and R. K. Jain. Pathology: cancer cells compress intratumour vessels. *Nature*, 427(6976):695–695, 2004.
- [171] T. P. Padera, A. Kadambi, E. di Tomaso, C. M. Carreira, E. B. Brown, Y. Boucher, N. C. Choi, D. Mathisen, J. Wain, E. J. Mark, L. L. Munn, and R. K. Jain. Lymphatic metastasis in the absence of functional intratumor lymphatics. *Science*, 296(5574):1883–1886, 2002.
- [172] D. M. McDonald and A. J. E. Foss. Endothelial cells of tumor vessels: Abnormal but not absent. *Cancer Metast. Rev.*, 19(1-2):109–120, 2000.
- [173] B. St. Croix, C. Rago, V. Velculescu, G. Traverso, K. E. Romans, E. Montgomery, A. Lal, G. J. Riggins, C. Lengauer, B. Vogelstein, and K. W. Kinzler. Genes expressed in human tumor endothelium. *Science*, 289(5482):1197–1202, 2013.

-
- [174] A. Srivastava, P. Laidler, L. E. Hughes, J. Woodcock, and E. J. Shedden. Neovascularization in human cutaneous melanoma: A quantitative morphological and Doppler ultrasound study. *Eur. J. Cancer. Clin. Oncol.*, 22(10):1205–1209, 1986.
- [175] H. Ishida, T. Andoh, S. Akiguchi, T. Kyoden, and T. Hachiga. Observation of tumor microvessels that are controlled by blood flow in breast cancer. *Appl. Phys. Lett.*, 106(17):173703, 2015.
- [176] M. K. Schilling, C. Redaelli, H. Friess, B. Blum, C. Signer, C. A. Maurer, and M. W. Bächler. Evaluation of laser doppler flowmetry for the study of benign and malignant gastric blood flow *in vivo*. *Gut*, 45(3):341–345, 1999.
- [177] S. Fujimori, T. Kishida, Y. Yoshida, and M. Kobayashi. Superficial blood flow, blood volume, and blood velocity in colorectal tubular adenomas and adenocarcinomas. *J. Gastroenterol.*, 34(4):467–473, 1999.
- [178] M. Kragh, B. Quistorff, and P. E. G. Kristjansen. Quantitative estimates of angiogenic and anti-angiogenic activity by laser Doppler flowmetry (LDF) and near infra-red spectroscopy (NIRS). *Eur. J. Cancer*, 37(7):924–929, 2001.
- [179] R. J. Friedman, M. J. Farber, M. A. Warycha, N. Papathasis, M. K. Miller, and E. R. Heilman. The “dysplastic” nevus. *Clin. Dermatol.*, 27(1):103–115, 2009.
- [180] J. I. Van Der Rhee, W. Bergman, and N. A. Kukutsch. The impact of dermoscopy on the management of pigmented lesions in everyday clinical practice of general dermatologists: a prospective study. *B. J. Dermatol.*, 162(3):563–567, 2010.
- [181] M. E. Vestergaard, P. Macaskill, P. E. Holt, and S. W. Menzies. Dermoscopy compared with naked eye examination for the diagnosis of primary melanoma: a meta-analysis of studies performed in a clinical setting. *Br. J. Dermatol.*, 159(3):669–676, 2008.
- [182] H. Kittler, H. Pehamberger, K. Wolff, and M. Binder. Diagnostic accuracy of dermoscopy. *Lancet Oncol.*, 3(3):159–165, 2002.
- [183] J. K. Patel, S. Konda, O. A. Perez, S. Amini, G. Elgart, and B. Berman. Newer technologies/techniques and tools in the diagnosis of melanoma. *Eur. J. Dermatol.*, 18(6):617–631, 2008.
- [184] M. Stücker, I. Horstmann, C. Nüchel, A. Röchling, K. Hoffmann, and P. Altmeyer. Blood flow compared in benign melanocytic naevi, malignant melanomas and basal cell carcinomas. *Clin. Exp. Dermatol.*, 24(2):107–111, 1999.
- [185] A. M. Enejder, C. af Klinteberg, I. Wang, S. Andersson-Engels, N. Bendsoe, S. Svanberg, and K. Svanberg. Blood perfusion studies on basal cell carcinomas in conjunction with photodynamic therapy and cryotherapy employing laser-Doppler perfusion imaging. *Acta Derm. Venereol.*, 80(1):19–23, 2000.

-
- [186] H. M. Häfner, K. Bräuer, C. Radke, M. Eichner, and A. Strölin. Wavelet analysis of laser Doppler flux time series of tumor and inflammatory associated neoangiogenesis. differences in rhythmical behavior. *Clin. Hemorheol. Micro.*, 43(3):191–201, 2009.
- [187] J. Reyat, N. Lebas, E. Fourme, T. Guihard, C. Vilmer, and P. Le Masurier. Post-occlusive reactive hyperemia in basal cell carcinoma and its potential application to improve the efficacy of solid tumor therapies. *Tohoku J. Exp. Med.*, 227(2):139–147, 2012.
- [188] J. S. Isenberg, F. Hyodo, L. A. Ridnour, C. S. Shannon, D. A. Wink, M. C. Krishna, and D. D. Roberts. Thrombospondin 1 and vasoactive agents indirectly alter tumor blood flow. *Neoplasia*, 10(8):886–896, 2008.
- [189] T. Gambichler, P. Regeniter, F. G. Bechara, A. Orlikov, R. Vasa, G. Moussa, M. Stücker, P. Altmeyer, and K. Hoffmann. Characterization of benign and malignant melanocytic skin lesions using optical coherence tomography *in vivo*. *J. Am. Acad. Dermatol.*, 57(4):629–637, 2007.
- [190] E. L. Psaty and A. C. Halpern. Current and emerging technologies in melanoma diagnosis: the state of the art. *Clin. Dermatol.*, 27(1):35–45, 2009.
- [191] A. Srivastava, L. E. Hughes, J. P. Woodcock, and P. Laidler. Vascularity in cutaneous melanoma detected by doppler sonography and histology: correlation with tumour behaviour. *Br. J. Cancer*, 59(1):89, 1989.
- [192] E. Tur and S. Brenner. Cutaneous blood flow measurements for the detection of malignancy in pigmented skin lesions. *Dermatology*, 184(1):8–11, 1992.
- [193] R. L. Barnhill, K. Fandrey, M. A. Levy, M. C. Mihm Jr, and B. Hyman. Angiogenesis and tumour progression of melanoma. Quantification of vascularity in melanocytic nevi and cutaneous malignant melanoma. *Lab. Invest.*, 67(3):331–337, 1992.
- [194] D. W. Siemann and M. R. Horsman. Vascular targeted therapies in oncology. *Cell Tissue Res.*, 335(1):241–248, 2009.
- [195] A. W. Griffioen and G. Molema. Angiogenesis: potentials for pharmacologic intervention in the treatment of cancer, cardiovascular diseases, and chronic inflammation. *Pharmacol. Rev.*, 52(2):237–268, 2000.
- [196] D. Mooney. Cancer: One step at a time. *Nature*, 436(7050):468–469, 2005.
- [197] R. Bar, A. Netzer, D. Ostrovsky, M. Daitzchman, and A. Golz. Abrupt tonsillar hemorrhage from a metastatic hemangiosarcoma of the breast: Case report and literature review. *ENT-Ear Nose Throat*, 90(3):116 – 120, 2011.
- [198] I. F. Tannock and D. Rotin. Acid pH in tumors and its potential for therapeutic exploitation. *Cancer Res.*, 49(16):4373–4384, 1989.

-
- [199] S. Rockwell, I. T. Dobrucki, E. Y. Kim, S. T. Marrison, and V. T. Vu. Hypoxia and radiation therapy: past history, ongoing research, and future promise. *Curr. Mol. Med.*, 9(4):442, 2009.
- [200] J. T. Lee and M. Herlyn. Microenvironmental influences in melanoma progression. *J. Cell. Biochem.*, 101(4):862–872, 2007.
- [201] M. C. Brahimi-Horn, J. Chiche, and J. Pouyssegur. Hypoxia and cancer. *J. Mol. Med.*, 85(12):1301–1307, 2007.
- [202] P. Vaupel, O. Thews, and M. Hoeckel. Treatment resistance of solid tumors. *Med. Oncol.*, 18(4):243–259, 2001.
- [203] G. Danza, C. Di Serio, M. R. Ambrosio, N. Sturli, G. Lonetto, F. Rosati, B. J. Rocca, G. Ventimiglia, M. T. del Vecchio, I. Prudovsky, N. Marchionni, and F. Tarantini. Notch3 is activated by chronic hypoxia and contributes to the progression of human prostate cancer. *Int. J. Cancer*, 133(11):2577–2586, 2013.
- [204] G. L. Semenza. Regulation of mammalian O₂ homeostasis by hypoxia-inducible factor 1. *Annu. Rev. Cell Dev. Biol.*, 15(1):551–578, 1999.
- [205] G. L. Semenza and G. L. Wang. A nuclear factor induced by hypoxia via de novo protein synthesis binds to the human erythropoietin gene enhancer at a site required for transcriptional activation. *Mol. Cell. Biol.*, 12(12):5447–5454, 1992.
- [206] A. L. Harris. Hypoxia—a key regulatory factor in tumour growth. *Nat. Rev. Cancer*, 2(1):38–47, 2002.
- [207] Z. Ovadia-Blechman, A. Meilin, N. Rabin, M. Eldar, and D. Castel. Noninvasive monitoring of peripheral microcirculatory hemodynamics under varying degrees of hypoxia. *Respir. Physiol. Neurobiol.*, 216:23–27, 2015.
- [208] N. C. Denko. Hypoxia, HIF1 and glucose metabolism in the solid tumour. *Nat. Rev. Cancer*, 8(9):705–713, 2008.
- [209] I. F. Robey, A. D. Lien, S. J. Welsh, B. K. Baggett, and R. J. Gillies. Hypoxia-inducible factor-1 α and the glycolytic phenotype in tumors. *Neoplasia*, 7(4):324–330, 2005.
- [210] S. J. Ralph, S. Rodriguez-Enriquez, J. Neuzil, E. Saavedra, and R. Moreno-Sánchez. The causes of cancer revisited: ‘Mitochondrial malignancy’ and ROS-induced oncogenic transformation – Why mitochondria are targets for cancer therapy. *Mol. Aspects Med.*, 31(2):145–170, 2010.
- [211] C. Frezza, L. Zheng, D. A. Tennant, D. B. Papkovsky, B. A. Hedley, G. Kalna, D. G. Watson, and E. Gottlieb. Metabolic profiling of hypoxic cells revealed a catabolic signature required for cell survival. *PLoS One*, 6(9):e24411, 2011.

-
- [212] M. G. Vander Heiden, L. C. Cantley, and C. B. Thompson. Understanding the Warburg effect: the metabolic requirements of cell proliferation. *Science*, 324(5930):1029–1033, 2009.
- [213] S. M. Evans, A. E. Schrlau, A. A. Chalian, P. Zhang, and C. J. Koch. Oxygen levels in normal and previously irradiated human skin as assessed by EF5 binding. *J. Invest. Dermatol.*, 126(12):2596–2606, 2006.
- [214] B. Bedogni and M. B. Powell. Hypoxia, melanocytes and melanoma—survival and tumor development in the permissive microenvironment of the skin. *Pigment Cell Melanoma Res.*, 22(2):166–174, 2009.
- [215] A. E. Adams, Y. Chudnovsky, and P. A. Khavari. Oxygen deprivation provokes melanoma. *Nat. Med.*, 12(2):168–169, 2006.
- [216] S. Törnroth-Horsefield and R. Neutze. Opening and closing the metabolite gate. *Proc. Nat. Acad. Sci.*, 105(50):19565–19566, 2008.
- [217] G. Azarias and J. Y. Chatton. Selective ion changes during spontaneous mitochondrial transients in intact astrocytes. *PLoS One*, 6(12):e28505, 2011.
- [218] B. Rieger, W. Junge, and K. B. Busch. Lateral pH gradient between OXPHOS complex IV and F0F1 ATP-synthase in folded mitochondrial membranes. *Nat. Commun.*, 5:3103, 2014.
- [219] M. J. Merrins, A. R. Van Dyke, A. K. Mapp, M. A. Rizzo, and L. S. Satin. Direct measurements of oscillatory glycolysis in pancreatic islet β -cells using novel fluorescence resonance energy transfer (FRET) biosensors for pyruvate kinase M2 activity. *J. Biol. Chem.*, 288(46):33312–33322, 2013.
- [220] F. T. Kurz, M. A. Aon, B. O’Rourke, and A. A. Armoundas. Wavelet analysis reveals heterogeneous time-dependent oscillations of individual mitochondria. *Am. J. Physiol. Heart Circ. Physiol.*, 299:H1736–H1740, 2010.
- [221] K. Furuya, M. Sokabe, and R. Grygorczyk. Real-time luminescence imaging of cellular ATP release. *Methods*, 66(2):330–344, 2014.
- [222] S. M. Cloonan and A. M. K. Choi. Mitochondria: commanders of innate immunity and disease? *Curr. Opin. Immunol.*, 24(1):32–40, 2012.
- [223] G. Kroemer and J. Pouyssegur. Tumor cell metabolism: Cancer’s Achilles’ heel. *Cancer Cell*, 13:472, 2008.
- [224] T. N. Seyfried and L. M. Shelton. Cancer as a metabolic disease. *Nutr. Metab.*, 7:7, 2010.
- [225] D. C. Wallace. Mitochondria and cancer. *Nat. Rev. Cancer*, 12:685, 2012.
- [226] R. Bertram, L. S. Satin, M. G. Pedersen, D. S. Luciani, and A. Sherman. Interaction of glycolysis and mitochondrial respiration in metabolic oscillations of pancreatic islets. *Biophys. J.*, 92(5):1544–1555, 2007.

-
- [227] V. Ganitkevich, V. Mattea, and K. Benndorf. Glycolytic oscillations in single ischemic cardiomyocytes at near anoxia. *J. Gen. Physiol.*, 135(4):307–319, 2010.
- [228] R. Diaz-Ruiz, S. Uribe-Carvajal, A. Devin, and M. Rigoulet. Tumor cell energy metabolism and its common features with yeast metabolism. *Biochim. Biophys. Acta*, 1796(2):252–265, 2009.
- [229] O. Warburg. Metabolism of tumours. *Biochem. Z.*, 142:317–33, 1923.
- [230] W. H. Koppenol, P. L. Bounds, and C. V. Dang. Otto Warburg’s contributions to current concepts of cancer metabolism. *Nat. Rev. Cancer*, 11:325–337, 2011.
- [231] M. A. Kluge, J. L. Fetterman, and J. A. Vita. Mitochondria and endothelial function. *Circ. Res.*, 112(8):1171–1188, 2013.
- [232] M. A. Aon, S. Cortassa, E. Marbán, and B. O’Rourke. Synchronized whole cell oscillations in mitochondrial metabolism triggered by a local release of reactive oxygen species in cardiac myocytes. *J. Biol. Chem.*, 278(45):44735–44744, 2003.
- [233] J. Higgins. A chemical mechanism for oscillation of glycolytic intermediates in yeast cells. *PNAS*, 51(6):989–994, 1964.
- [234] H. F. Chou, N. Berman, and E. Ipp. Oscillations of lactate released from islets of Langerhans: evidence for oscillatory glycolysis in beta-cells. *Am. J. Physiol. Endoc. M.*, 262(6):E800–E805, 1992.
- [235] S. Kar and D. S. Ray. Sustained simultaneous glycolytic and insulin oscillations in β -cells. *J. Theor. Biol.*, 237(1):58–66, 2005.
- [236] L. N. M. Duysens and J. Ames. Fluorescence spectrophotometry of reduced phosphopyridine nucleotide in intact cells in the near-ultraviolet and visible region. *Biochim. Biophys. Acta*, 24:19–26, 1957.
- [237] A. Ghosh and B. Chance. Oscillations of glycolytic intermediates in yeast cells. *Biochem. Biophys. Res. Commun.*, 16(2):174–181, 1964.
- [238] B. Hess. The glycolytic oscillator. *J. Exp. Biol.*, 81(1):7–14, 1979.
- [239] K. A. Reijenga, J. L. Snoep, J. A. Diderich, H. W. van Verseveld, H. V. Westerhoff, and B. Teusink. Control of glycolytic dynamics by hexose transport in *Saccharomyces cerevisiae*. *Biophys. J.*, 80(2):626–634, 2001.
- [240] K. Tornheim, V. Andrés, and V. Schultz. Modulation by citrate of glycolytic oscillations in skeletal muscle extracts. *J. Biol. Chem.*, 266(24):15675–15678, 1991.
- [241] M. A. Aon, S. Cortassa, and B. O’Rourke. Mitochondrial oscillations in physiology and pathophysiology. *Adv. Exp. Med. Biol.*, 641:98–117, 2008.
- [242] B. Chance and T. Yoshioka. Sustained oscillations of ionic constituents of mitochondria. *Arch. Biochem. Biophys.*, 117(2):451–465, 1966.

-
- [243] B. O'Rourke, B. M. Ramza, and E. Marban. Oscillations of membrane current and excitability driven by metabolic oscillations in heart cells. *Science*, 265(5174):962–966, 1994.
- [244] F. T. Kurz, M. A. Aon, B. O'Rourke, and A. A. Armoundas. Spatio-temporal oscillations of individual mitochondria in cardiac myocytes reveal modulation of synchronized mitochondrial clusters. *PNAS*, 107(32):14315–14320, 2010.
- [245] S. Cortassa, M. A. Aon, R. L. Winslow, and B. O'Rourke. A mitochondrial oscillator dependent on reactive oxygen species. *Biophys. J.*, 87(3):2060–2073, 2004.
- [246] E. K. Ainscow and G. A. Rutter. Glucose-stimulated oscillations in free cytosolic ATP concentration imaged in single islet β -cells evidence for a Ca^{2+} -dependent mechanism. *Diabetes*, 51(suppl 1):S162–S170, 2002.
- [247] C. K. Ytting, A. T. Fuglsang, J. K. Hiltunen, A. J. Kastaniotis, V. C. Özalp, L. J. Nielsen, and L. F. Olsen. Measurements of intracellular ATP provide new insight into the regulation of glycolysis in the yeast *Saccharomyces cerevisiae*. *Integr. Biol.*, 4(1):99–107, 2012.
- [248] V. C. Özalp, T. R. Pedersen, L. J. Nielsen, and L. F. Olsen. Time-resolved measurements of intracellular ATP in the yeast *Saccharomyces cerevisiae* using a new type of nanobiosensor. *J. Biol. Chem.*, 285(48):37579–37588, 2010.
- [249] H. S. Thoke, A. Tobiesen, J. Brewer, P. L. Hansen, R. P. Stock, L. F. Olsen, and L. A. Bagatolli. Tight coupling of metabolic oscillations and intracellular water dynamics in *Saccharomyces cerevisiae*. *PLOS ONE*, 1:16, 2015.
- [250] D. Ziech, R. Franco, A. Pappa, and M. I. Panayiotidis. Reactive Oxygen Species (ROS)-induced genetic and epigenetic alterations in human carcinogenesis. *Mut. Res.*, 711(1):167–173, 2011.
- [251] S. Fulda, L. Galluzzi, and G. Kroemer. Targeting mitochondria for cancer therapy. *Nat. Rev. Drug Discovery*, 9(6):447–464, 2010.
- [252] P. Sonveaux, F. Végran, T. Schroeder, M. C. Wergin, J. Verrax, Z. N. Rabhani, C. J. De Saedeleer, K. M. Kennedy, C. Diepart, B. F. Jordan, M. J. Kelley, B. Gallez, M. L. Wahl, O. Feron, and M. W. Dewhirst. Targeting lactate-fueled respiration selectively kills hypoxic tumor cells in mice. *J. Clin. Invest.*, 118(12):3930, 2008.
- [253] P. Vaupel, F. Kallinowski, and P. Okunieff. Blood flow, oxygen and nutrient supply, and metabolic microenvironment of human tumors: a review. *Cancer Res.*, 49(23):6449–6465, 1989.
- [254] P. A. Schornack and R. J. Gillies. Contributions of cell metabolism and H^+ diffusion to the acidic pH of tumors. *Neoplasia*, 5(2):135–145, 2003.
- [255] E. K. Rofstad, B. Mathiesen, K. Kindem, and K. Galappathi. Acidic extracellular pH promotes experimental metastasis of human melanoma cells in athymic nude mice. *Cancer Res.*, 66(13):6699–6707, 2006.

-
- [256] W. H. Gaskell. On the tonicity of the heart and blood vessels1. *J. Physiol.*, 3(1):48–92, 1880.
- [257] A. C. Celotto, V. K. Capellini, C. F. Baldo, M. B. Dalio, A. J. Rodrigues, and P. R. B. Evora. Effects of acid-base imbalance on vascular reactivity. *Braz. J. Med. Biol. Res.*, 41(6):439–445, 2008.
- [258] O. Baretella, A. Xu, and P. M. Vanhoutte. Acidosis prevents and alkalosis augments endothelium-dependent contractions in mouse arteries. *Pflügers Arch. Eur. J. Physiol.*, 466(2):295–305, 2014.
- [259] P. Sonveaux. Provascular strategy: targeting functional adaptations of mature blood vessels in tumors to selectively influence the tumor vascular reactivity and improve cancer treatment. *Radiother. Oncol.*, 86(3):300–313, 2008.
- [260] S. Meek and F. Morris. ABC of clinical electrocardiography: introduction. II—basic terminology. *Brit. Med. J.*, 324(7335):470, 2002.
- [261] D. Iatsenko, P. V. E. McClintock, and A. Stefanovska. Nonlinear mode decomposition: a noise-robust, adaptive decomposition method. *Submitted*, 2015.
- [262] P. G. Katona and J. Felix. Respiratory sinus arrhythmia: noninvasive measure of parasympathetic cardiac control. *J. Appl. Physiol.*, 39(5):801–805, 1975.
- [263] R. E. Kleiger, J. P. Miller, J. T. Bigger Jr., and A. J. Moss. Decreased heart rate variability and its association with increased mortality after acute myocardial infarction. *Am. J. Cardiol.*, 59(4):256–262, 1987.
- [264] N. J. Stapelberg, I. Hamilton-Craig, D. L. Neumann, D. H. K. Shum, and H. McConnell. Mind and heart: Heart rate variability in major depressive disorder and coronary heart disease - a review and recommendations. *Aust. NZ. J. Psychiat.*, 46(10):946–957, 2012.
- [265] M. B. Lotrič and A. Stefanovska. Synchronization and modulation in the human cardiorespiratory system. *Physica A*, 283(3-4):451–461, 2000.
- [266] Moor Instruments Ltd Axminster, UK. Basic theory and operating principles of laser Doppler blood flow monitoring and imaging (LDF & LDI), Issue 1.
- [267] V. Rajan, B. Varghese, T. G. van Leeuwen, and W. Steenbergen. Review of methodological developments in laser Doppler flowmetry. *Lasers Med. Sci.*, 24(2):269–283, 2009.
- [268] J. D. Briers. Laser speckle contrast imaging for measuring blood flow. *Opt. Appl.*, 37(1/2):139, 2007.
- [269] D. Briers, D. D. Duncan, E. Hirst, S. J. Kirkpatrick, M. Larsson, W. Steenbergen, T. Stromberg, and O. B. Thompson. Laser speckle contrast imaging: theoretical and practical limitations. *J. Biomed. Opt.*, 18(6):066018, 2013.

-
- [270] A. F. Fercher and J. D. Briers. Flow visualization by means of single-exposure speckle photography. *Opt. Commun.*, 37(5):326–330, 1981.
- [271] Moor Instruments. moorFLPI user manual. 2012.
- [272] L. M. Richards, S. M. Kazmi, J. L. Davis, K. E. Olin, and A. K. Dunn. Low-cost laser speckle contrast imaging of blood flow using a webcam. *Biomed. Opt. Express*, 4(10):2269–2283, 2013.
- [273] Z. Stoyneva. Clinical application of laser Doppler flowmetry in neurology. *Perspect. Med.*, 1(1):89–93, 2012.
- [274] P. Gill. The critical evaluation of laser Doppler imaging in determining burn depth. *Int. J. Burns Trauma*, 3(2):72, 2013.
- [275] S. M. S. Kazmi, L. M. Richards, C. J. Schrandt, M. A. Davis, and A. K. Dunn. Expanding applications, accuracy, and interpretation of laser speckle contrast imaging of cerebral blood flow. *J. Cereb. Blood Flow Metab.*, 2015.
- [276] D. T. Delpy, M. Cope, P. van der Zee, S. R. Arridge, S. Wray, and J. S. Wyatt. Estimation of optical pathlength through tissue from direct time of flight measurement. *Phys. Med. Biol.*, 33(12):1433, 1988.
- [277] A. Villringer and B. Chance. Non-invasive optical spectroscopy and imaging of human brain function. *Trends Neurosci.*, 20(10):435–442, 1997.
- [278] S. H. Strogatz. *Nonlinear Dynamics and Chaos*. Westview Press, Boulder, 2001.
- [279] P. E. Kloeden and C. Pöetzche. Eds. *Nonautonomous Dynamical Systems in the Life Sciences*. Springer, 2013.
- [280] R. Friedrich, J. Peinke, M. Sahimi, and M. R. R. Tabar. Approaching complexity by stochastic methods: From biological systems to turbulence. *Phys. Rep.*, 506(5):87–162, 2011.
- [281] N. Wessel, M. Riedl, and J. Kurths. Is the normal heart rate “chaotic” due to respiration? *Chaos*, 19(2):028508, 2009.
- [282] K. Friston. A free energy principle for biological systems. *Entropy*, 14(11):2100–2121, 2012.
- [283] D. Iatsenko, A. Bernjak, T. Stankovski, Y. Shiogai, P. J. Owen-Lynch, P. B. M. Clarkson, P. V. E. McClintock, and A. Stefanovska. Evolution of cardiorespiratory interactions with age. *Phil. Trans. R. Soc. A*, 371(1997):20110622, 2013.
- [284] C. J. Stam. Nonlinear dynamical analysis of EEG and MEG: review of an emerging field. *Clin. Neurophysiol.*, 116(10):2266–2301, 2005.
- [285] Y. F. Suprunenko, P. T. Clemson, and A. Stefanovska. Chronotaxic systems: a new class of self-sustained nonautonomous oscillators. *Phys. Rev. Lett.*, 111(2):024101, 2013.

-
- [286] Y. F. Suprunenko, P. T. Clemson, and A. Stefanovska. Chronotaxic systems with separable amplitude and phase dynamics. *Phys. Rev. E*, 89(1):012922, 2014.
- [287] Y. F. Suprunenko and A. Stefanovska. Generalized chronotaxic systems: time-dependent oscillatory dynamics stable under continuous perturbation. *Phys. Rev. E*, 90(3):032921, 2014.
- [288] D. Gabor. Theory of communication. *J. IEEE*, 93:429–457, 1946.
- [289] P. T. Clemson and A. Stefanovska. Discerning non-autonomous dynamics. *Phys. Rep.*, 542(4):297–368, 2014.
- [290] L. W. Sheppard, A. Stefanovska, and P. V. E. McClintock. Detecting the harmonics of oscillations with time-variable frequencies. *Phys. Rev. E*, 83:016206, 2011.
- [291] I. Daubechies, J. Lu, and H.-T. Wu. Synchrosqueezed wavelet transforms: An empirical mode decomposition-like tool. *Appl. and Comput. Harmon. Anal.*, 30(2):243–261, 2011.
- [292] J. Jamšek, M. Paluš, and A. Stefanovska. Detecting couplings between interacting oscillators with time-varying basic frequencies: Instantaneous wavelet bispectrum and information theoretic approach. *Phys. Rev. E*, 81(3):036207, 2010.
- [293] C. K. Peng, S. V. Buldyrev, S. Havlin, M. Simons, H. E. Stanley, and A. L. Goldberger. Mosaic organisation of DNA nucleotides. *Phys. Rev. E*, 49(2):1685–1689, 1994.
- [294] L. Keselbrenner and S. Akselrod. Selective discrete Fourier transform algorithm for time-frequency analysis: method and application on simulated and cardiovascular signals. *IEEE Trans. Biomed. Eng.*, 43(8):789–802, 1996.
- [295] P. S. Addison. *The Illustrated Wavelet Transform Handbook: Introductory Theory and Applications in Science, Engineering, Medicine and Finance*. IOP Publishing, Bristol, 2002.
- [296] G. Kaiser. *A Friendly Guide to Wavelets*. Birkhäuser, Boston, 1994.
- [297] W. H. Press. *Numerical Recipes 3rd Edition: The Art of Scientific Computing*. Cambridge University Press, 2007.
- [298] A. Bandrivskyy, A. Bernjak, P. V. E. McClintock, and A. Stefanovska. Wavelet phase coherence analysis: Application to skin temperature and blood flow. *Cardiovasc. Eng.*, 4(1):89–93, 2004.
- [299] T. Schreiber and A. Schmitz. Surrogate time series. *Physica D*, 142(3-4):346–382, 2000.
- [300] L. W. Sheppard, A. Stefanovska, and P. V. E. McClintock. Testing for time-localised coherence in bivariate data. *Phys. Rev. E*, 85:046205, 2012.

-
- [301] A. Pikovsky, M. Rosenblum, and J. Kurths. *Synchronization – A Universal Concept in Nonlinear Sciences*. Cambridge University Press, Cambridge, 2001.
- [302] P. T. Clemson, Y. F. Suprunenko, T. Stankovski, and A. Stefanovska. Inverse approach to chronotaxic systems for single-variable time series. *Phys. Rev. E*, 89(3):032904, 2014.
- [303] T. Stankovski, A. Duggento, P. V. E. McClintock, and A. Stefanovska. Inference of time-evolving coupled dynamical systems in the presence of noise. *Phys. Rev. Lett.*, 109:024101, 2012.
- [304] A. Duggento, T. Stankovski, P. V. E. McClintock, and A. Stefanovska. Dynamical bayesian inference of time-evolving interactions: From a pair of coupled oscillators to networks of oscillators. *Phys. Rev. E*, 86(6):061126, 2012.
- [305] M. G. Rosenblum and A. S. Pikovsky. Detecting direction of coupling in interacting oscillators. *Phys. Rev. E.*, 64(4):045202, 2001.
- [306] T. Stankovski, A. Duggento, P. V. E. McClintock, and A. Stefanovska. A tutorial on time-evolving dynamical Bayesian inference. *Eur. Phys. J. Special Topics*, 223(13):2685–2703, 2014.
- [307] K. J. Friston. Functional and effective connectivity: A review. *Brain Connect.*, 1(1):13–36, 2011.
- [308] Y. Kuramoto. *Chemical Oscillations, Waves, and Turbulence*. Springer-Verlag, Berlin, 1984.
- [309] A. V. Oppenheim, R. W. Schaffer, and J. R. Buck. *Discrete-Time Signal Processing*. Prentice-Hall, Upper Saddle River, 1999.
- [310] B. Kralemann, L. Cimponeriu, M. Rosenblum, A. Pikovsky, and R. Mrowka. Phase dynamics of coupled oscillators reconstructed from data. *Phys. Rev. E*, 77(6, Part 2):066205, 2008.
- [311] N. Delprat, B. Escudie, P. Guillemain, R. Kronland-Martinet, P. Tchamitchian, and B. Torrèsani. Asymptotic wavelet and Gabor analysis: Extraction of instantaneous frequencies. *IEEE Trans. Inf. Theory*, 38(2):644–664, 1992.
- [312] R. A. Carmona, W. L. Hwang, and B. Torrèsani. Characterization of signals by the ridges of their wavelet transforms. *IEEE Trans. Sig. Proc.*, 45(10):2586–2590, 1997.
- [313] H. Kioka, H. Kato, M. Fujikawa, O. Tsukamoto, T. Suzuki, H. Imamura, A. Nakano, S. Higo, S. Yamazaki, T. Matsuzaki, K. Takafuji, H. Asanuma, M. Asakura, T. Minamino, Y. Shintani, M. Yoshida, H. Noji, M. Kitakaze, I. Komuro, Y. Asano, and S. Takashima. Evaluation of intramitochondrial ATP levels identifies G0/G1 switch gene 2 as a positive regulator of oxidative phosphorylation. *Proc. Nat. Acad. Sci. USA*, 111(1):273–278, 2014.

-
- [314] M. Vejmelka, M. Paluš, and K. Šušmáková. Identification of nonlinear oscillatory activity embedded in broadband neural signals. *Int. J. Neural Syst.*, 20(02):117–128, 2010.
- [315] M. Paluš and D Novotná. Enhanced monte carlo singular system analysis and detection of period 7.8 years oscillatory modes in the monthly NAO index and temperature records. *Nonlinear Proc. Geoph.*, 11(5/6):721–729, 2004.
- [316] R. Hardstone, S-S. Poil, G. Schiavone, R. Jansen, V. V. Nikulin, H. D. Mansvelder, and K. Linkenkaer-Hansen. Detrended fluctuation analysis: a scale-free view on neuronal oscillations. *Front. Physiol.*, 3, 2012.
- [317] W. Klimesch. EEG alpha and theta oscillations reflect cognitive and memory performance: a review and analysis. *Brain Res. Rev.*, 29(2):169–195, 1999.
- [318] P. L. Purdon, E. T. Pierce, E. A. Mukamel, M. J. Prerau, J. L. Walsh, K. F. K. Wong, A. F. Salazar-Gomez, P. G. Harrell, A. L. Sampson, A. Cimenser, S. Ching, N. J. Kopell, C. Tavares-Stoeckel, K. Habeeb, R. Merhar, and E. N. Brown. Electroencephalogram signatures of loss and recovery of consciousness from propofol. *Proc. Nat. Acad. Sci. USA*, 110(12):E1142–E1151, 2013.
- [319] D. Rudrauf, A. Douiri, C. Kovach, J. P. Lachaux, D. Cosmelli, M. Chavez, C. Adam, B. Renault, J. Martinerie, and M. L. Van Quyen. Frequency flows and the time-frequency dynamics of multivariate phase synchronization in brain signals. *Neuroimage*, 31(1):209–227, 2006.
- [320] J. Fell and N. Axmacher. The role of phase synchronization in memory processes. *Nat. Rev. Neurosci.*, 12(2):105–118, 2011.
- [321] J. P. Lachaux, E. Rodriguez, J. Martinerie, and F. J. Varela. Measuring phase synchrony in brain signals. *Human Brain Mapping*, 8(4):194–208, 1999.
- [322] P. Tass, M. G. Rosenblum, J. Weule, J. Kurths, A. Pikovsky, J. Volkmann, A. Schnitzler, and H.-J. Freund. Detection of $n:m$ phase locking from noisy data: Application to magnetoencephalography. *Phys. Rev. Lett.*, 81(15):3291–3294, 1998.
- [323] M. Le Van Quyen, J. Foucher, J. P. Lachaux, E. Rodriguez, A. Lutz, J. Martinerie, and F. J. Varela. Comparison of Hilbert transform and wavelet methods for the analysis of neuronal synchrony. *J. Neurosci. Methods*, 111(2):83–98, 2001.
- [324] L. W. Sheppard, A. C. Hale, S. Petkoski, P. V. E. McClintock, and A. Stefanovska. Characterizing an ensemble of interacting oscillators: The mean-field variability index. *Phys. Rev. E*, 87(1):012905, 2013.
- [325] S. Palva and J. M. Palva. New vistas for α -frequency band oscillations. *Trends Neurosci.*, 30(4):150–158, 2007.

-
- [326] T. Stankovski, V. Ticcinelli, P. V. E. McClintock, and A. Stefanovska. Coupling functions in networks of oscillators. *New J. Phys.*, 17(3):035002, 2015.
- [327] F. Darvas, K. J. Miller, R. P. N. Rao, and J. G. Ojemann. Nonlinear phase-phase cross-frequency coupling mediates communication between distant sites in human neocortex. *J. Neurosci.*, 29(2):426–435, 2009.
- [328] A. B. L. Tort, R. Komorowski, H. Eichenbaum, and N. Kopell. Measuring phase-amplitude coupling between neuronal oscillations of different frequencies. *J. Neurophysiol.*, 104(2):1195–1210, 2010.
- [329] K. J. Friston. Another neural code? *NeuroImage*, 5(3):213–220, 1997.
- [330] J. M. Hurtado, L. L. Rubchinsky, and K. A. Sigvardt. Statistical method for detection of phase-locking episodes in neural oscillations. *J. Neurophysiol.*, 91(4):1883–1898, 2004.
- [331] J. E. Lisman and O. Jensen. The theta-gamma neural code. *Neuron*, 77(6):1002–1016, 2013.
- [332] R. T. Canolty and R. T. Knight. The functional role of cross-frequency coupling. *Trends Cogn. Sci.*, 14(11):506–515, 2010.
- [333] E. A. Mukamel, E. Pirondini, B. Babadi, K. F. K. Wong, E. T. Pierce, P. G. Harrell, J. L. Walsh, A. F. Salazar-Gomez, S. S. Cash, E. N. Eskandar, V. S. Weiner, E. N. Brown, and P. L. Purdon. A transition in brain state during propofol-induced unconsciousness. *J. Neurosci.*, 34(3):839–845, 2014.
- [334] D. Hanahan and R. A. Weinberg. The hallmarks of cancer. *Cell*, 100(1):57–70, 2000.
- [335] Don Bliss/National Cancer Institute. https://commons.wikimedia.org/wiki/File:Skin_%28layers,_glands,_vessels%29.jpg. [Online; accessed 06-January-2015].
- [336] National Cancer Intelligence Network. Non-melanoma skin cancer in England, Scotland, Northern Ireland and Ireland. 2013.
- [337] American Cancer Society. Cancer facts & figures. 2013.
- [338] M. P. Purdue, L. B. Freeman, W. F. Anderson, and M. A. Tucker. Recent trends in incidence of cutaneous melanoma among US caucasian young adults. *J. Invest. Dermatol.*, 128(12):2905, 2008.
- [339] J. R. Jackson, M. P. Seed, C. H. Kircher, D. A. Willoughby, and J. D. Winkler. The codependence of angiogenesis and chronic inflammation. *FASEB J.*, 11(6):457–465, 1997.
- [340] F. Wilcoxon. Individual comparisons by ranking methods. *Biometrics Bull.*, 1(6):80–83, 1945.
- [341] H. Theil. A rank-invariant method of linear and polynomial regression analysis. In *Henri Theil's Contributions to Economics and Econometrics*, pages 345–381. Springer, 1992.

-
- [342] P. K. Sen. Estimates of the regression coefficient based on Kendall's tau. *J. Am. Stat. Assoc.*, 63(324):1379–1389, 1968.
- [343] M. G. Kendall. A new measure of rank correlation. *Biometrika*, 30:81–93, 1938.
- [344] <http://uk.mathworks.com/help/stats/boxplot.html?> [Online; accessed 16-December-2015].
- [345] R. S. de Paula, I. Antelmi, M. A. Vincenzi, C. D. S. André, R. Artes, C. J. Grupi, and A. J. Mansur. Influence of age, gender, and serum triglycerides on heart rate in a cohort of asymptomatic individuals without heart disease. *Int J. Cardiol.*, 105(2):152–158, 2005.
- [346] M. Stücker, C. Springer, V. Paech, N. Hermes, M. Hoffmann, and P. Altmeyer. Increased laser doppler flow in skin tumors corresponds to elevated vessel density and reactive hyperemia. *Skin Res. Tech.*, 12(1):1–6, 2006.
- [347] N. C. Turner. *The Effect of Voluntary Dry Static Apnoea on Cardiovascular Dynamics*. PhD thesis, Lancaster University, 2013.
- [348] Radiometer. *TOSCA500 Operating Manual*. UK, 2010.
- [349] S. Lahiri, A. Roy, S. M. Baby, T. Hoshi, G. L. Semenza, and N. R. Prabhakar. Oxygen sensing in the body. *Prog. Biophys. Mol. Biol.*, 91(3):249–286, 2006.
- [350] F. Yasuma and J. Hayano. Respiratory sinus arrhythmia: why does the heartbeat synchronize with respiratory rhythm? *Chest*, 125(2):683–690, 2004.
- [351] A. R. Smith, F. Visioli, B. Frei, and T. M. Hagen. Age-related changes in endothelial nitric oxide synthase phosphorylation and nitric oxide dependent vasodilation: evidence for a novel mechanism involving sphingomyelinase and ceramide-activated phosphatase 2A. *Aging Cell*, 5(5):391–400, 2006.
- [352] D. G. Spiller, C. D. Wood, D. A. Rand, and M. R. H. White. Measurement of single-cell dynamics. *Nature*, 465:736–745, 2010.
- [353] D. J. Kiviet, P. Nghe, N. Walker, S. Boulineau, V. Sunderlikova, and Sander J. Tans. Stochasticity of metabolism and growth at the single-cell level. *Nature*, 514:376–379, 2014.
- [354] F. A. Chandra, G. Buzi, and J. C. Doyle. Glycolytic oscillations and limits on robust efficiency. *Science*, 333:187–192, 2011.
- [355] P. E. Kloeden and M. Rasmussen. *Nonautonomous Dynamical Systems*. American Mathematical Soc., 2011.
- [356] J. Jäckle. The causal theory of the resting potential of cells. *J. Theor. Biol.*, 249(3):445–463, 2007.
- [357] A.-K. Gustavsson, D. D. van Niekerk, C. B. Adiels, F. B. du Preez, M. Goksör, and J. L. Snoep. Sustained glycolytic oscillations in individual isolated yeast cells. *FEBS J.*, 279(16):2837–2847, 2012.

-
- [358] A.-K. Gustavsson, C. B. Adiels, B. Mehlig, and M. Goksör. Entrainment of heterogeneous glycolytic oscillations in single cells. *Sci. Rep.*, 5(9404), 2015.
- [359] B. Glancy, W. T. Willis, D. J. Chess, and R. S. Balaban. Effect of calcium on the oxidative phosphorylation cascade in skeletal muscle mitochondria. *Biochemistry*, 52(16):2793–2809, 2013.
- [360] M. Brandon, P. Baldi, and D. C. Wallace. Mitochondrial mutations in cancer. *Oncogene*, 25(34):4647–4662, 2006.
- [361] L. M. Bachmann, M. A. Puhan, G. ter Riet, and P. M. Bossuyt. Sample sizes of studies on diagnostic accuracy: literature survey. *BMJ*, 332(7550):1127–1129, 2006.
- [362] S. Jones, S. Carley, and M. Harrison. An introduction to power and sample size estimation. *Emerg. Med. J.*, 20(5):453, 2003.
- [363] J. L. Hodges Jr and E. L. Lehmann. The efficiency of some nonparametric competitors of the t-test. *Ann. Math. Statist.*, pages 324–335, 1956.